

**Deep Subduction in Earth history:
Seeking for traces in the sedimentary record**

Dissertation

for the award of the degree

“Doctor rerum naturalium”

of the Georg-August-Universität Göttingen

within the program “Geosciences”

of the Georg-August University School of Science (GAUSS)

submitted by

Jan Schönig

from Burgwedel (Germany)

Göttingen, 2021

Thesis Committee

Prof. Dr. Hilmar von Eynatten
Department of Sedimentology and Environmental Geology, Geosciences Center,
Georg-August-University Göttingen

Prof. Dr. Guido Meinhold
Department of Exogenous Geology / Sedimentology, Institute for Geology,
TU Bergakademie Freiberg

Dr. Nils Keno Lünsdorf
Department of Sedimentology and Environmental Geology, Geosciences Center,
Georg-August-University Göttingen

Members of the Examination Board

Reviewer: Prof. Dr. Hilmar von Eynatten
Department of Sedimentology and Environmental Geology, Geosciences Center,
Georg-August-University Göttingen

Second Reviewer: Prof. Dr. Guido Meinhold
Department of Exogenous Geology / Sedimentology, Institute for Geology,
TU Bergakademie Freiberg

Additional Reviewer: Prof. Dr. Heinrich Bahlburg
Department of Sedimentology, Institute of Geology and Palaeontology,
University of Münster

Further members of the Examination Board:

Prof. em. Dr. Gerhard Wörner
Department of Geochemistry, Geosciences Center,
Georg-August-University Göttingen

Prof. Dr. Thomas Müller
Department of Mineralogy, Geosciences Center,
Georg-August-University Göttingen

Prof. Dr. Jonas Kley
Department of Structural Geology and Geodynamics, Geosciences Center,
Georg-August-University Göttingen

Dr. István Dunkl
Department of Sedimentology and Environmental Geology, Geosciences Center,
Georg-August-University Göttingen

Date of the oral examination: 14th December 2021

STATUTORY DECLARATION

Statutory Declaration

I declare that I have authored the Dissertation “Deep Subduction in Earth history: Seeking for traces in the sedimentary record” independently, that I have not used other than the declared sources/resources, and that I have explicitly marked all material which has been quoted either literally or by content from the used sources.

Eidesstattliche Erklärung

Ich erkläre an Eides statt, dass ich die vorliegende Dissertation “Deep Subduction in Earth history: Seeking for traces in the sedimentary record” selbstständig verfasst, andere als die angegebenen Quellen/Hilfsmittel nicht benutzt, und die den benutzten Quellen wörtlich und inhaltlich entnommenen Stellen als solche kenntlich gemacht habe.

Göttingen, 3rd November 2021

.....

(Jan Schönig)

PREFACE

This cumulative thesis is composed of eight chapters. In addition to the introductory Chapter 1 and concluding remarks as well as future research directions in Chapter 8, Chapters 2–7 include six *Original Research* manuscripts, and one *Discussion* manuscript (Reply to Comment). Five of the seven manuscripts are published in peer-reviewed journals (Chapters 2–5), one is accepted and in press (Chapter 6), and one is in preparation (Chapter 7). The included manuscripts are identical to their published/accepted versions, with the exception that language (American English), units, symbols, and the reference style have been unified throughout the thesis. A list of the manuscripts, along with Contributor Role Taxonomy (CRediT) author statements, is following:

CHAPTER 2

Schönig J, von Eynatten H, Meinhold G, Lünsdorf NK (2019): Diamond and coesite inclusions in detrital garnet of the Saxonian Erzgebirge, Germany. *Geology* 47, 715–718, <https://doi.org/10.1130/G46253.1>.

JS Conceptualization, Field work, Methodology, Formal analysis, Investigation, Writing – Original draft, Visualization; *HvE* Conceptualization, Field work, Writing – Review and editing, Supervision, Project administration, Funding acquisition; *GM* Conceptualization, Writing – Review and editing, Supervision, Funding acquisition; *NKL* Methodology, Writing – Review and editing.

CHAPTER 3

Schönig J, von Eynatten H, Meinhold G, Lünsdorf NK, Willner AP, Schulz B (2020): Deep subduction of felsic rocks hosting UHP lenses in the central Saxonian Erzgebirge: Implications for UHP terrane exhumation. *Gondwana Research* 87, 320–329, <https://doi.org/10.1016/j.gr.2020.06.020>.

JS Conceptualization, Field work, Methodology, Formal analysis, Investigation, Writing – Original draft, Visualization; *HvE* Conceptualization, Field work, Writing – Review and editing, Supervision, Project administration, Funding acquisition; *GM* Conceptualization, Writing – Review and editing, Supervision, Funding acquisition. *NKL* Methodology, Validation, Writing – Review and editing; *APW* Resources, Writing – Review and editing; *BS* Resources, Writing – Review and editing.

Schönig J, von Eynatten H, Meinhold G, Lünsdorf NK, Willner AP, Schulz B (2021a): Reply to comment on “Deep subduction of felsic rocks hosting UHP lenses in the central Saxonian Erzgebirge: Implications for UHP terrane exhumation”. *Gondwana Research* 98, 320–323, <https://doi.org/10.1016/j.gr.2020.12.029>.

JS Writing – Original draft, Visualization; *HvE* Writing – Review and editing; *GM* Writing – Review and editing; *NKL* Writing – Review and editing; *APW* Writing – Review and editing; *BS* Writing – Review and editing.

CHAPTER 4

Baldwin SL, **Schönig J**, Gonzalez JP, Davies H, von Eynatten H (2021): Garnet sand reveals rock recycling processes in the youngest exhumed high- and ultrahigh-pressure terrane on Earth. *Proceedings of the National Academy of Sciences* 118, e2017231118, <https://doi.org/10.1073/pnas.2017231118>.

SLB Conceptualization, Field work, Resources, Visualization, Writing – Original draft, Supervision; **JS** Methodology, Formal analysis, Investigation, Visualization, Writing – Review and editing; **JPG** Formal analysis, Visualization, Writing – Review and editing; **DH** Field work, Resources, Writing – Review and editing; **HvE** Writing – Review and editing.

CHAPTER 5

Schönig J, von Eynatten H, Meinhold G, Lünsdorf NK (2021b): Life-cycle analysis of coesite-bearing garnet. *Geological Magazine* 158, 1421–1440, <https://doi.org/10.1017/S0016756821000017>.

JS Conceptualization, Field work, Methodology, Formal analysis, Investigation, Writing – Original draft, Visualization; **HvE** Conceptualization, Field work, Writing – Review and editing, Supervision, Project administration, Funding acquisition; **GM** Conceptualization, Writing – Review and editing, Supervision, Funding acquisition; **NKL** Methodology, Writing – Review and editing.

CHAPTER 6

Schönig J, von Eynatten H, Tolosana-Delgado R, Meinhold G (in press): Garnet major-element composition as an indicator of host-rock type: A machine-learning approach using the random forest classifier. *Contributions to Mineralogy and Petrology* (not yet issued), <https://doi.org/10.1007/s00410-021-01854-w>.

JS Conceptualization, Software, Formal Analysis, Investigation, Data Curation, Visualization, Writing – Original Draft; **HvE** Conceptualization, Supervision, Funding Acquisition, Writing – Review & Editing; **RTD** Conceptualization, Software, Formal Analysis, Writing – Review & Editing; **GM** Funding Acquisition, Writing – Review & Editing.

CHAPTER 7

Schönig J, von Eynatten H, Meinhold G, Lünsdorf NK (in preparation): The sedimentary record of ultrahigh-pressure metamorphism: A perspective review. (Planned submission to *Earth-Science Reviews*).

JS Conceptualization, Formal analysis, Investigation, Writing – Original draft, Visualization; **HvE** Conceptualization, Writing – Review and editing, Supervision, Project administration, Funding acquisition; **GM** Conceptualization, Writing – Review and editing, Supervision, Funding acquisition; **NKL** Software, Writing – Review and editing.

ACKNOWLEDGEMENTS

I acknowledge funding since September 2019 until August 2022 by the German Research Foundation (Deutsche Forschungsgemeinschaft); DFG grant EY23/27-1 to Prof. Dr. Hilmar von Eynatten and Prof. Dr. Guido Meinhold. This grant was/is a fundamental prerequisite to enable the extensive work in the field and in the lab during the PhD thesis as well as in the upcoming months to finalize the project.

I am extraordinarily grateful to my main supervisors Prof. Dr. Hilmar von Eynatten and Prof. Dr. Guido Meinhold. After finishing my Master's thesis, I received continuous and endless support for translating my research ideas into reality and for developing a specially tailored PhD project. Without the mentoring, guidance, patience, motivation, and professional knowledge of Hilmar and Guido, none of the lines included in this thesis would have been written down. As well as for the time we spend together in the field and the many fruitful discussions we had, I am additionally thankful for support to facilitate my future career aspirations.

Many thanks to Dr. N. Keno Lünsdorf for supervising the Raman spectroscopy part of this project. Over the years, I was fortunate enough to rub off a small proportion of the in-depth understanding Keno has regarding technical details and how to tune experimental parameters for the optimal outcome. I am also grateful for several scripts Keno wrote and provided, which allowed to organize my analytical work much more efficiently.

Besides my supervisors, I thank all professional colleagues for collaborations on various subprojects during my PhD studies. This includes Dr. Raimon Tolosana-Delgado, Dr. István Dunkl, Prof. Dr. Suzanne L. Baldwin, Dr. Joseph P. Gonzalez, Prof. Dr. Hugh Davies, Dr. Arne P. Willner, Dr. Bernhard Schulz, Yu Pei, Prof. Dr. Joachim Reitner, and Dr. Jan P. Duda. I particularly thank Suzanne L. Baldwin for the fruitful collaboration on a sample from Papua New Guinea, for inviting me to Syracuse to finalize the dataset, and for working together on ongoing and potentially upcoming projects.

I would like to thank all former and present members of the Department of Sedimentology and Environmental Geology. It is a great pleasure to work in such a friendly and positive atmosphere. I am particularly thankful for the many scientific discussion and brainstorming sessions on various topics with Dr. István Dunkl, Prof. Dr. Hilmar von Eynatten, Dr. N. Keno Lünsdorf, Jun. Prof. Dr. Michael Tatzel, Dr. Ingo Hache, Dr. Angana Chaudhuri, and Dr. Volker Karius; but I am also very grateful for the many discussions on miscellaneous topics over coffee.

For the substantial support in sample preparation, many thanks are going to our chemical-technical assistants Judit Dunkelné Nagy, Irina Ottenbacher, and Cornelia Friedrich, as well as our student assistants Jakob Popp and Carsten Benner. I particularly thank Carsten Benner for his work on the samples from Greenland, which contributed essential data to this subproject. Dr. Andreas Kronz, Antje Grebe, and Jochen Gätjen from the Department of Mineralogy are thanked for access to the electron microprobe as well as support during sample preparation, analysis, and data evaluation.

I am incredibly grateful for the support I received from all of my family and friends. Special thanks are going to my parents Simone and Torsten Schönig as well as my sister Lisa. They have been a constant

source of reliable encouragement throughout my entire career in higher education, enabling me to pursue my career aspirations under any circumstances.

Finally, I give my biggest hug and thanks to the most important person in my life, my better half Hannah Schönrock. These thanks are not only for accepting all complications coming along with having a partner with passion for science, not only for commuting large distances in order to spend time together, not only for patient listening to endless research ideas suddenly popping up in my mind, but also for giving me love, enriching my life for 14 years now, keeping me in balance, and for sticking with me in my emotionally most difficult times. I love you!

ABSTRACT

The global-scale horizontal movement of tectonic plates driven by the sinking of cold and dense lithosphere, known as plate tectonics, is a major process linking the Earth's surface with mantle. Thus, plate tectonics strongly affect geochemical cycles, mantle convection, crustal growth rates, as well as thermal and tectonic regimes. Numerous hints, particularly from the detrital zircon record, indicate that plate tectonics operate since at least the Archean–Proterozoic transition, although opposing views persist. How plate tectonics evolved on a global-scale from the onset to the modern-style regime, which includes cold and deep subduction defined by low-temperature/high-pressure and ultrahigh-pressure (UHP) metamorphism, is a highly controversial and hotly debated topic in Earth Sciences. Particularly the lack of blueschists and UHP rocks from the pre-Neoproterozoic record represents a key argument for a late onset of modern-style plate tectonics. A main limitation in the search for modern-style plate tectonic regimes in deep time is the fragmentarily preserved crystalline rock record that may or may not be representative for the respective time interval, and the virtual absence of techniques to make use of the sedimentary record that would enable to more representatively investigate subduction regimes through time on a global scale. Recently, a novel method was introduced to trace the erosion of UHP metamorphic rocks by screening mineral inclusion assemblages of detrital garnet for the presence of coesite, and thus potentially opening new avenues to seek for the operation of deep subduction in deep time. However, these findings are restricted to a small catchment in the Western Gneiss Region of Norway, raising some fundamental question to be addressed before applying the concept to ancient sediments.

This thesis applies the novel detrital approach to two Phanerozoic orogens, demonstrating that: (i) mineral inclusions in detrital garnet are capable to record UHP rock occurrences, also for regional river catchments; (ii) besides coesite, diamond-grade rocks effectively transfer UHP signatures to the sedimentary record in the form of diamond inclusions; and (iii) combining the information from mineral inclusions and garnet chemistry provides new insights regarding the UHP rock cycle of the study areas. For the central Saxonian Erzgebirge of Germany, this includes evidence for a much wider extent of UHP metamorphism than previously assumed and the involvement of mafic as well as felsic rocks in the UHP cycle. This includes felsic country-rock gneisses that underwent partial melting and re-equilibration during exhumation and have previously been supposed to have reached peak conditions below the coesite stability field. It is concluded that previously described UHP lenses and the surrounding country rocks were subducted as a largely coherent slab, which has important implications to understand the buoyancy development of the subducting/exhuming continental crust of UHP terranes. For the D'Entrecasteaux metamorphic complex of Papua New Guinea, detrital garnet chemistry, coesite co-existing with graphite inclusions, melt inclusions, and elastic geothermobarometry reveal, for the first time, a complete UHP rock cycle starting with a metasedimentary protolith that originated from the Earth surface, deep subduction to UHP conditions, exhumation under increasing temperature conditions, and erosion to form the studied beach placer.

In addition, for the Erzgebirge, the large number of monomineralic coesite inclusions and coesite inclusions that partially transformed to quartz enabled a detailed investigation of preservation factors, showing that: (iv) a small size $<9 \mu\text{m}$ and a low frequency of coesite inclusions favors the garnet host

to stay intact in spite of inclusion overpressures developing during exhumation, and thus coesite inclusions are shielded from external conditions and fluids, which enables their monomineralic preservation; (v) bimineralic coesite/quartz inclusions ruptured their host garnet at a late stage during exhumation at temperatures of ~ 330 °C; and (vi) the heterogeneous grain-size distribution of detrital coesite-bearing garnet can be explained by inclusion frequency. Thereby, mafic and felsic UHP garnets are initially large, but mafic garnet contains a low number of inclusions resulting in minor disintegration and enrichment in the coarse fraction, while felsic garnet contains variable amounts of inclusions, whereby coesite-poor grains are enriched in the coarse fraction and coesite-rich grains extensively disintegrated into smaller fragments resulting in an enrichment in the fine fraction.

Furthermore, the thesis presents several technical advancements, which include that: (vii) the 250–500 μm grain-size fraction is most efficient in terms of analytical time to invest compared to information value to gain; (viii) based on a newly developed discrimination scheme using a large database and a machine-learning algorithm, garnet chemistry represents an efficient tool to pre-screen and pre-select grains ahead of the time-consuming inclusion analysis; and (ix) hyperspectral Raman imaging provides an alternative to reduce the user-assisted analytical time.

In main conclusion, analyzing mineral inclusions in detrital garnet represents a robust and efficient approach to capture the distribution and characteristics of UHP rocks exposed at the surface at the time of sediment generation and deposition. The methodological framework is mature and has a high potential to tackle the issue whether modern-style plate tectonics operated on a global scale in pre-Neoproterozoic times.

KURZFASSUNG

Die durch das Absinken von kalter und dichter Lithosphäre angetriebene horizontale Bewegung von tektonischen Platten auf globalem Maßstab ist bekannt als Plattentektonik, ein Hauptprozess der den Austausch zwischen Erdoberfläche und Erdmantel ermöglicht. Demnach hat die Plattentektonik einen starken Einfluss auf geochemische Kreisläufe, die Konvektion des Erdmantels, Wachstumsraten kontinentaler Kruste, sowie thermische und tektonische Regime. Wenn auch unterschiedliche Meinungen vorherrschen, so deuten zahlreiche Hinweise auf die Existenz plattentektonischer Prozesse seit dem Übergang vom Archaikum zum Proterozoikum, vor allem solche die von detritischen Zirkonen abgeleitet wurden. Wie sich jedoch die Plattentektonik von ihrem Beginn zum modernen Regime entwickelt hat, d.h. ab wann kalte und tiefe Subduktion charakterisiert durch Niedrig-Temperatur/Hoch-Druck und Ultrahoch-Druck (UHP) Metamorphose existierte, ist eine stark kontrovers diskutierte Thematik. Insbesondere die Abwesenheit von Blauschiefern und UHP-Gesteinen vom pre-neoproterozoischem Rekord ist ein Hauptargument der Befürworter eines späten Beginns der modernen Plattentektonik. Auf der Suche nach Hinweisen für moderne Plattentektonik in der frühen Erdgeschichte sind wir stark beschränkt durch das lückenhaft erhaltene Archiv von Kristallingesteinen, dessen Repräsentativität für das jeweilig betrachtete Zeitintervall zweifelhaft ist, sowie das Nichtvorhandensein geeigneter Methoden um das sedimentäre Archiv auf moderne Subduktionsprozesse zu ergründen. Vor allem detritische Minerale haben das grundsätzliche Potenzial Zeitscheiben der Erdgeschichte mit höherer Repräsentativität zu beproben. Kürzlich wurde eine neuartige Methode etabliert, welche durch die Analyse von Mineral-Einschlüssen in detritischem Granat ermöglicht, erodiertes Material von UHP-Gesteinen aufzuspüren, mit Coesit-Einschlüssen als Indikator. Potentiell schafft dieser Ansatz einen neuen Zugang, um die frühe Erdgeschichte auf Hinweise für tiefe Subduktion zu untersuchen. Allerdings wurde dessen Funktionalität bisher nur für ein kleines Einzugsgebiet in der Western Gneiss Region von Norwegen demonstriert, was die Klärung einiger fundamentaler Fragen bedarf bevor die Methode auf große Gebiete sowie fossile Sedimente und Sedimentgesteine angewendet werden kann.

Diese Dissertation präsentiert die Anwendung des neuartigen Ansatzes auf zwei phanerozoische Gebirge und demonstriert: (i) Mineral-Einschlüsse in detritischem Granat sind befähigt UHP-Gesteine aufzuspüren, auch in großen Einzugsgebieten von Flüssen; (ii) zusätzlich zu Coesit, hinterlassen auch Diamant-führende Gesteine ihre Spuren im Detritus in Form von Diamant-Einschlüssen in Granat; und (iii) liefert die Kombination von Mineral-Einschlüssen und Granatchemie neue Einblicke in den UHP-Gesteinszyklus der untersuchten Gebiete. Dies beinhaltet Beweise für eine räumlich deutlich weitreichenderes Auftreten von UHP-Gesteinen im zentralen Erzgebirge von Deutschland als zuvor angenommen, sowie die Einbeziehung von sowohl mafischen als auch felsischen Lithologien. Auch die felsischen Nebengesteine wurden mit einbezogen, die nach bisheriger Meinung nie das Coesit-Stabilitätsfeld erreichten. Während der Exhumierung von UHP-Bedingungen wurden diese teilweise aufgeschmolzen und re-equilbrierten. Daraus wird geschlossen, dass die vorherig beschriebenen UHP-Linsen und die umgebenden Nebengesteine gemeinsam als weitgehend zusammenhängende Platte subduziert wurden, was weitreichende Implikationen für das Verständnis der Dichte-Entwicklung von kontinentaler Kruste während der Subduktion bis zu oder der Exhumierung von UHP-Bedingungen hat.

Die Funde von detritischem Coesit-führendem Granat aus dem metamorphen D'Entrecasteaux-Komplex von Papua Neu-Guinea, in Kombination mit co-existierenden Graphit-Einschlüssen, Granatchemie, Schmelzeinschlüssen und elastischer Geothermobarometrie, enthüllen erstmals einen vollständigen UHP-Zyklus. Dieser beinhaltet ein metasedimentäres Ausgangsgestein gebildet an der Erdoberfläche, welches tief subduziert wurde bis zu UHP-Bedingungen unter Bildung der Coesit-führenden Granate, darauffolgende Exhumierung bis zur Erdoberfläche unter zwischenzeitlich ansteigender Temperatur, wo es schließlich erodiert, transportiert, und die Granate als Strandseife abgelagert wurden.

Die große Anzahl an Granaten vom Erzgebirge mit sowohl monomineralischen Coesit-Einschlüssen als auch solchen die teilweise zu Quarz umgewandelt wurden, ermöglichten zudem eine detaillierte Studie der Erhaltungsfaktoren von Coesit. Es wird gezeigt: (iv) eine kleine Einschlussgröße von $<9 \mu\text{m}$ und eine geringe Anzahl pro Granat-Wirtsmineral-Korn reduziert stark das Bruchverhalten des Granats durch sich bildende Überdrücke in den Einschlüssen und somit werden die Einschlüsse von den externen Bedingungen und Fluiden abgeschirmt, was wiederum die monomineralische Erhaltung ermöglicht; (v) bimineralisch erhaltene Coesit/Quarz-Einschlüsse treten durch Bruch des Wirts-Granats spät während der Exhumierung mit Fluiden in Kontakt bei Temperaturen $\sim 330 \text{ }^\circ\text{C}$; und (vi) die heterogene Korngrößenverteilung von detritischem Coesit-führendem Granat kann auf die Einschlusshäufigkeit pro Korn zurückgeführt werden. Demnach haben sowohl Granate die von mafischen als auch solche die von felsische Ausgangsgesteinen stammen ursprünglich eine große Kristallgröße, jedoch weisen mafische Granate eine geringe Anzahl an Einschlüssen auf, wodurch diese kaum zerbrechen, während felsische Granate eine variable Anzahl aufzeigen und Einschluss-reiche Kristalle bevorzugt zu kleinen Fragmenten zerbrechen, welches zu einer Anreicherung im feineren Korngrößenbereich führt.

Des Weiteren zeigt die Dissertation mehrere methodische Weiterentwicklungen auf, einschließlich: (vii) die höchste Effizienz von aufzuwendender Analysezeit im Vergleich zum gewonnen Informationsgehalt für die Korngrößenfraktion $250\text{--}500 \mu\text{m}$; (viii) die effiziente Möglichkeit einer geochemischen Vorauswahl und Selektion einzelner Granatkörner basierend auf einem neu entwickelten Diskriminierungs-Modell unter Verwendung einer großen Datenbank und einem Algorithmus für maschinelles Lernen; und (ix) eine alternative Möglichkeit zur Reduktion der vom Benutzer aufzuwendenden Analysezeit durch hyperspektrale Raman Bildgebungsmethoden.

Insgesamt führt dies zu der Hauptschlussfolgerung, dass die Analyse von Mineral-Einschlüssen in detritischem Granat ein solides und effizientes Konzept repräsentiert, um die Verbreitung und Eigenschaften von UHP-Gesteinen zur Zeit dessen Freilegung an der Erdoberfläche und Generierung sowie Ablagerung von Sedimenten zu erfassen. Dieses Konzept hat großes Potenzial die ungeklärte Problematik anlässlich des Agierens moderner Plattentektonik auf globalem Maßstab in pre-neoproterozoischer Zeit von einer neuen Perspektive zu ergründen.

CONTENTS

STATUTORY DECLARATION	iii
PREFACE	v
ACKNOWLEDGEMENTS	vii
ABSTRACT	ix
KURZFASSUNG	xi
CONTENTS	xiii
LIST OF FIGURES	xix
LIST OF TABLES	xxiii
CHAPTER 1	1
Introduction.....	1
1.1 Plate tectonics through time: state of the art and motivation	1
1.2 Aims and outline	6
CHAPTER 2	11
Diamond and coesite inclusions in detrital garnet of the Saxonian Erzgebirge, Germany	11
2.1 Introduction.....	11
2.2 Samples and Methods	13
2.3 Mineral Inclusions	14
2.4 Garnet Chemistry	15
2.5 Discussion.....	16
2.6 Conclusions.....	17
Acknowledgements.....	17
CHAPTER 3	19
Deep subduction of felsic rocks hosting UHP lenses in the central Saxonian Erzgebirge: Implications for UHP terrane exhumation	19
3.1 Introduction.....	19
3.2 Geological framework and samples.....	21
3.3 Methods	22
3.4 Results.....	23
3.4.1 Coesite-bearing detrital garnet.....	23
3.4.2 Diamond-bearing detrital garnet	26
3.4.3 Cristobalite-, kokchetavite-, and kumdykolite-bearing detrital garnet	27

3.5	Discussion	29
3.6	Geodynamic implications.....	31
3.7	Conclusions.....	32
	Acknowledgements.....	32
	Reply to comment on “Deep subduction of felsic rocks hosting UHP lenses in the central Saxonian Erzgebirge: Implications for UHP terrane exhumation”.....	33
3.8	Reply to comment by Massonne (2021)	33
	Acknowledgements.....	37
CHAPTER 4		39
	Garnet sand reveals rock recycling processes in the youngest exhumed high- and ultrahigh-pressure terrane on Earth.....	39
4.1	Introduction.....	39
4.2	Results.....	43
4.3	Discussion	46
4.4	Materials and Methods.....	49
	Acknowledgements.....	50
CHAPTER 5		53
	Life-cycle analysis of coesite-bearing garnet.....	53
5.1	Introduction.....	53
5.2	Geological framework and sampling locations.....	55
5.3	Methods.....	56
5.4	Results and discussion.....	58
5.4.1	Garnet chemistry compared with grain size.....	58
5.4.2	Frequent mineral inclusion types compared with garnet chemistry and grain size...60	
5.4.3	UHP mineral inclusions compared with garnet chemistry and grain size.....63	
5.4.4	Coesite preservation: the role of inclusion size and fluid availability.....68	
5.4.5	Source-rock- and catchment-specific coesite inclusion characteristics.....72	
5.4.6	A model of coesite-bearing garnet disintegration	75
5.4.7	Selecting the most efficient garnet grain-size fraction.....	79
5.5	Conclusions.....	80
	Acknowledgements.....	82
CHAPTER 6		83

Garnet major-element composition as an indicator of host-rock type: a machine learning approach using the random forest classifier	83
6.1 Introduction.....	83
6.2 Database.....	85
6.3 Model development	87
6.4 Model performance.....	89
6.4.1 Performance of the ‘setting and metamorphic facies’ model.....	89
6.4.2 Performance of the ‘composition’ model.....	91
6.5 Understanding the models.....	93
6.5.1 Variable importance of the ‘setting and metamorphic facies’ model	93
6.5.2 Variable importance of the ‘composition’ model	95
6.5.3 Origin of main discriminators.....	96
6.6 Sensitivity and Applicability.....	99
6.6.1 Sensitivity to P–T changes.....	99
6.6.2 Reflecting catchment specific garnet host-rock characteristics	101
6.6.3 Detecting provenance shifts	102
6.7 The ‘garnetRF’ web application	102
6.8 Conclusions.....	103
6.9 Outlook and call on the community.....	104
Acknowledgements.....	105
CHAPTER 7	107
The sedimentary record of ultrahigh-pressure metamorphism: a perspective review	107
7.1 Introduction.....	107
7.2 Attempts to link sediments to UHP sources.....	108
7.3 UHP mineral inclusions in detrital garnet.....	111
7.3.1 Documented findings.....	111
7.3.2 UHP source rock reconstruction using garnet chemistry and inclusion assemblages	114
7.3.3 Methodological benefits and limits.....	119
7.3.4 Enhancing efficiencies	121
7.4 Other potential UHP host minerals	128
7.4.1 Zircon.....	128
7.4.2 Rutile.....	130

7.4.3	Tourmaline	131
7.5	Fields of application	131
7.5.1	Exhumation history of UHP terranes	131
7.5.2	Modern-style plate tectonics in Earth history	132
7.5.3	Elastic geothermobarometry	134
7.6	Summary	134
	Acknowledgements	135
CHAPTER 8	137
	Concluding Remarks and Future Research Directions	137
8.1	General Conclusions	137
8.2	Outlook.....	139
REFERENCES	141
APPENDIX	xxv
	Supplementary Information – Chapter 2.....	xxv
	Electronic Appendix 2e-A.....	xxv
	Electronic Appendix 2e-B.....	xxv
	Electronic Appendix 2e-C.....	xxv
	Electronic Appendix 2e-D.....	xxv
	Electronic Appendix 2e-E	xxv
	Appendix 2-A.....	xxv
	Samples	xxv
	Raman spectroscopy.....	xxvi
	Electron Microprobe	xxvii
	Supplementary Information – Chapter 3.....	xxix
	Electronic Appendix 3e-A.....	xxix
	Electronic Appendix 3e-B.....	xxix
	Appendix 3-A.....	xxix
	Supplementary Information – Chapter 4.....	xxxi
	Electronic Appendix 4e-A.....	xxxi
	Electronic Appendix 4e-B.....	xxxi
	Electronic Appendix 4e-C.....	xxxi
	Electronic Appendix 4e-D.....	xxxi

Supplementary Information – Chapter 5.....	xxxiii
Electronic Appendix 5e-A	xxxiii
Appendix 5-A	xxxiii
Detailed information on rutile-bearing garnet	xxxiii
Detailed information on omphacite-bearing garnet	xxxiv
Detailed information on graphite-bearing garnet.....	xxxv
Detailed information on quartz- and kyanite-bearing garnet	xxxvi
Appendix 5-B.....	xxxviii
Details of step-wise garnet discrimination.....	xxxviii
Appendix 5-C.....	xli
Appendix 5-D	xlii
Supplementary Information – Chapter 6.....	xliii
Electronic Appendix 6e-A	xliii
Appendix 6-A	xliii
Extended information to Section 6.3	xliii
Appendix 6-B.....	xlvi
Bare-bone version of the code for reproducing the classification models	xlvi
Appendix 6-C.....	xlvii
Performance of the discrimination scheme after Mange & Morton (2007).....	xlvii
Performance of the discrimination scheme after Hardman et al. (2018)	xliv
Performance of the discrimination scheme after Tolosana-Delgado et al. (2018).....	li
Appendix 6-D	liii
Effect of pressure and temperature on votes	liii
Appendix 6-E.....	liv
Consequences on misclassification rates for individual classes of the ‘setting and metamorphic facies’ model by excluding individual oxides.....	liv
Consequences on misclassification rates for individual classes of the ‘composition’ model by excluding individual oxides	lvi
Appendix 6-F	lvii
Detailed exploration of main discriminators for individual subgroups	lvii
Curriculum Vitae	lxiii

LIST OF FIGURES

Figure 1.1-1: Indications for the onset and evolution of plate tectonics through time.	3
Figure 2.1-1: Geological map of the area around the Saidenbach reservoir in the central Erzgebirge with sampling locations.	12
Figure 2.2-1: Coesite and diamond inclusions in detrital garnet.	14
Figure 2.4-1: Chemical composition of detrital garnets in molar proportions of the Mg-, Fe-, and Ca-endmembers.	16
Figure 3.2-1: Maps showing the location and outline of the study area.	21
Figure 3.4-1: Chemistry of coesite-bearing detrital garnet grains.	25
Figure 3.4-2: Chemistry of diamond-bearing detrital garnet grains.	27
Figure 3.4-3: Photomicrographs and Raman images of cristobalite-, kokchetavite-, and kumdykolite-bearing garnet grains.	28
Figure 3.4-4: Chemistry of cristobalite-, kokchetavite-, and kumdykolite-bearing detrital garnet grains.	29
Figure 3.8-1: Composition of (A) diamond- and (B) coesite-bearing detrital garnet summarized after Schönig et al. (2020).	34
Figure 3.8-2: Photomicrograph of banded country rock gneiss sample JS-Erz-11h taken close to a diamond-bearing rock lens (N 50.72694°, E 13.24681°).	35
Figure 4.1-1: (A) Tectonic and geologic setting of the (U)HP terrane in the Woodlark Rift of eastern Papua New Guinea.	41
Figure 4.1-2: Schematic figure illustrating rock (re-)cycling in the eastern Papuan (U)HP terrane where rifting of a subduction complex has exhumed (U)HP rocks since ~8 Ma (i.e., negligible petrologic lag times).	42
Figure 4.2-1: Ternary plots of garnet compositions (molar proportions of Fe+Mn, Ca, and Mg) for metamorphic rocks of the lower plates of the D'Entrecasteaux Islands core complexes, as compared with detrital garnet compositions from the placer deposit.	43
Figure 4.2-2: Representative detrital garnets and inclusion suites and associated Raman spectra.	44
Figure 4.2-3: <i>P-T</i> diagram showing (A) quartz-in-garnet and zircon-in-garnet elastic thermobarometric data for detrital garnets (DGs; this study).	45
Figure 5.1-1: Trends of geometric means of detrital garnet composition from the 63–125 μm fraction (origin of arrow), via the 125–250 μm fraction to the 250–500 μm fraction (head of arrow).	54
Figure 5.2-1: Maps showing the location and outline of the study area, modified after Schönig et al. (2019, 2020).	56
Figure 5.4-1: Composition of inclusion-bearing detrital garnet.	58
Figure 5.4-2: Composition and grain-size distribution of detrital garnet containing specific mineral inclusion types.	61
Figure 5.4-3: Ratios of garnet grains containing specific mineral inclusion types, displayed in ternary diagrams reflecting the three grain size fractions.	63
Figure 5.4-4: Composition, grain-size distribution, and frequency of (a) diamond- and (b) coesite-bearing detrital garnet.	64

Figure 5.4-5: Steps I to IV of the step-wise assignment of coesite-bearing garnet to their most likely source based on garnet composition in molar proportions.....	65
Figure 5.4-6: Steps V and VI of the step-wise assignment of coesite-bearing garnet to their most likely source based on log-ratio plots in comparison with mineral inclusion assemblages.	66
Figure 5.4-7: Grain-size relations and frequency of (a) felsic and (b) mafic coesite-bearing garnet for the individual samples based on the step-wise assignment performed in Figure 5.4-5 and Figure 5.4-6.	67
Figure 5.4-8: Monomineralic coesite and bimineralic coesite/quartz inclusions compared to inclusion size.	69
Figure 5.4-9: Photomicrographs and Raman images of selected garnet grains and coesite inclusions.	71
Figure 5.4-10: Distribution of monomineralic coesite versus bimineralic coesite/quartz inclusions and inclusion frequency with regard to the individual sample and assigned source.	73
Figure 5.4-11: Disintegration model for coesite-bearing garnet from entrapment to exhumation to mid-crustal levels.....	76
Figure 5.4-12: Disintegration model for coesite-bearing garnet from source to sink.	78
Figure 6.4-1: Performance of the ‘setting and metamorphic facies’ model based on the out-of-bag error.	90
Figure 6.4-2: Performance of the ‘composition’ model based on the out-of-bag error.	92
Figure 6.5-1: Variable importance for the ‘setting and metamorphic facies’ model.	94
Figure 6.5-2: Misclassification rates of the ‘setting and metamorphic facies’ model for individual oxides excluded compared to the full model with all oxides used (see Table 6.2-1 for abbreviations).	95
Figure 6.5-3: Variable importance for the ‘composition’ model.	95
Figure 6.5-4: Misclassification rates of the ‘composition’ model for individual oxides excluded compared to the full model with all oxides used (see Table 6.2-1 for abbreviations).	96
Figure 6.5-5: Main discriminators to separate setting (a–c) and metamorphic facies classes (d–f).	97
Figure 6.5-6: Main discriminators to separate composition classes.....	99
Figure 6.6-1: Sensitivity and applicability of the introduced garnet discrimination scheme.	100
Figure 7.2-1: Global map showing locations where detrital approaches have been applied to trace the erosion of UHP rocks.....	109
Figure 7.3-1: Photomicrographs and Raman images of UHP inclusions in detrital garnet.	112
Figure 7.3-2: Discrimination scheme classification for crustal vs. mantle origin of coesite- and diamond-bearing detrital garnet.	115
Figure 7.3-3: Comparison of detrital UHP garnet composition with regard to source-rock composition.	117
Figure 7.3-4: Prediction of metamorphic host-rock facies based on major-element composition of detrital coesite- and diamond-bearing garnet grains.	123
Figure 7.3-5: Prediction of metamorphic host-rock facies based on major-element composition of all individual analyses (9–20 spots per grain) for coesite- and diamond-bearing garnet grains that have not been classified as being sourced from eclogite-facies rocks in Figure 7.3-4.	125
Figure 7.3-6: Discrimination results of all inclusion-bearing garnets from sample JS-Erz-14s after the ‘setting and metamorphic facies’ model after Schönig et al. (in press).	126

Figure 7.3-7: Photomicrograph and three-dimensional hyperspectral Raman images of coesite-bearing garnet.	127
Figure Appendix 2-A 1: Geochemical classification of detrital garnets after Tolosana-Delgado et al. (2018) showing the probabilities of being derived from eclogite-, granulite-, or amphibolite-facies rocks.	xxvii
Figure Appendix 3-A 1: Chemistry of coesite-bearing detrital garnet grains shown in perturbed ternary plots. Perturbation after von Eynatten et al. (2002).	xxix
Figure Appendix 3-A 2: Chemistry of diamond-bearing detrital garnet grains shown in perturbed ternary plots. Perturbation after von Eynatten et al. (2002).	xxx
Figure Appendix 5-A 1: Composition, grain-size distribution, and frequency of rutile-bearing detrital garnet.	xxxiii
Figure Appendix 5-A 2: Composition, grain-size distribution, and frequency of omphacite-bearing detrital garnet.	xxxiv
Figure Appendix 5-A 3: Composition, grain-size distribution, and frequency of graphite-bearing detrital garnet.	xxxv
Figure Appendix 5-A 4: Composition, grain-size distribution, and frequency of (A) quartz- and (B) kyanite-bearing detrital garnet.	xxxvii
Figure Appendix 5-B 1: Biplot showing principal components two and three of the centered log-ratio transformed compositional data of the unassigned coesite-bearing garnet grains after classification step IV.	xxxix
Figure Appendix 5-B 2: Assignment of coesite-bearing garnet to their most likely source after step VI based on log-ratio plots in comparison with mineral inclusion assemblages.	xxxix
Figure Appendix 5-B 3: Theoretical grain-size distribution of felsic and mafic coesite-bearing garnet grains if all unassigned grains after step VI are assigned to a felsic or mafic source, respectively.	xl
Figure Appendix 5-C 1: Monomineralic coesite and bimineralic coesite/quartz inclusions compared to inclusion size.	xli
Figure Appendix 5-D 1: Relation of the number of garnet grains per sample containing UHP mineral inclusions (n) in comparison to the analytical time needed (h) with regard to the grain-size fraction.	xlii
Figure Appendix 6-A 1: Flow chart of a simplified example to create a random forest classification model, inspired by Belgiu & Drăgut (2016).	xliv
Figure Appendix 6-C 1: Performance of the garnet discrimination scheme after Mange & Morton (2007).	xlviii
Figure Appendix 6-C 2: Performance of the graphical mantle-versus-crustal garnet discrimination scheme after Hardman et al. (2018).	l
Figure Appendix 6-C 3: Performance of the garnet discrimination scheme after Tolosana-Delgado et al. (2018) using the prior probability ‘equal-M’.	lii
Figure Appendix 6-D 1: Votes within the individual metamorphic classes as a function of temperature (a, b) or pressure (c, d).	liii
Figure Appendix 6-D 2: Effect of pressure and temperature on geometric mean votes of metamorphic facies classes.	liv

Figure Appendix 6-F 1: Main discriminators to separate individual classes, groups, and subgroups of the ‘setting’ scheme. lvii

Figure Appendix 6-F 2: Main discriminators to separate individual classes, groups, and subgroups of the ‘metamorphic facies’ scheme.....lx

Figure Appendix 6-F 3: Main discriminators to separate individual classes, groups, and subgroups of the ‘composition’ scheme. lxii

LIST OF TABLES

Table 2.2-1: Omphacite-, coesite-, and diamond-bearing garnets from the Saxonian Erzgebirge, Germany.	13
Table 3.4-1: Summary of detrital UHP garnet grains from the central Saxonian Erzgebirge.	24
Table 6.2-1: Number of observations for individual garnet host-rock types (main group), metamorphic facies (group), and composition (subgroup) included in the database.....	86
Table 6.3-1: Classes and parameters of the random forest garnet discrimination models.....	87
Table 6.4-1: Classification rates and confusion matrix of the ‘setting and metamorphic facies’ random forest model based on the out-of-bag estimate.	89
Table 6.4-2: Classification rates and confusion matrix of the ‘composition’ random forest model based on the out-of-bag estimate.	92
Table Appendix 2-A 1: Coordinates of modern sand sampling locations	xxvi

Introduction

1.1 Plate tectonics through time: state of the art and motivation

Plate tectonics is the global-scale horizontal movement of tectonic plates (e.g., McKenzie & Parker 1967; Cawood et al. 2006) driven by the sinking of cold and dense lithosphere into the mantle (e.g., Forsyth & Ueda 1975; Conrad & Lithgow-Bertelloni 2002), which is a unique feature of planet Earth (e.g., Stern 2018; Dewey et al. 2021). Because plate tectonics is a prerequisite for the recycling of surface materials like sediments and volatiles into the mantle via subduction (e.g., Hawkesworth et al. 2016), tracking the operation of plate tectonics back in time has profound implications for the understanding of Earth long-term evolution, including thermal regimes, geochemical reservoirs, and tectonic processes (e.g., Palin et al. 2020). Geodynamics of the Earth probably evolved from a pre-plate-tectonic (stagnant lid) regime, like observed on other rocky planets (e.g., Stern 2018), to a plate-tectonic (mobile lid) regime. The transitional time interval is called the onset of global subduction (e.g., Dhuime et al. 2012) and its placement onto the geological time scale is one of the most controversially discussed topics in Earth Sciences (e.g., Palin et al. 2020), ranging from Hadean (Hopkins et al. 2008) to Neoproterozoic (Stern 2005; Hamilton 2011).

Many observations from Hadean to Paleoproterozoic crystalline rocks have been used to suppose the operation of subduction during the time of rock formation. This includes the geochemical composition of magmatic rocks (Mueller & Corcoran 2001; Parman et al. 2001; Boily & Dion 2002; Barley et al. 2006; Adam et al. 2012; Nagel et al. 2012; Furnes et al. 2015; Keller & Schoene 2018), different types of inclusions in diamond and their composition (MacGregor & Manton 1986; Schulze et al. 2003; Tappert et al. 2005; Shirey & Richardson 2011; Smart et al. 2016; Smit et al. 2019), mélange-like terranes interpreted as accretionary prisms (Mueller et al. 1996; Kusky 1998; Polat & Kerrich 1999; Peng et al. 2020; Kusky et al. 2020), the appearance of paired metamorphic belts (Brown 2006, 2014), and paleomagnetism (Cawood et al. 2006, 2018; Evans & Pisarevsky 2008; Mitchell et al. 2014; Buchan et al. 2016; Lubnina et al. 2017). Besides reasonable concerns raised about the robustness of geochemical discrimination (Pearce 2008; Payne et al. 2010; Condie 2015; Li et al. 2015) and interpretations based on inclusions in diamond (Palin et al. 2020), a major limiting factor is the increasingly incomplete crystalline rock record when going back in time (Goodwin 1996; Figure 1.1-1A, black line). Even when accepting a specific observation to be indicative for subduction, it is still questionable whether the fragmentarily preserved crystalline rock record is suitable for proving the operation of subduction on a global scale, i.e., plate tectonics, or whether it can solely account for local subduction operated in particular regions at particular times. Thus, proposed early onsets in the Hadean to Paleoproterozoic (Komiya et al. 1999; Nutman et al. 2002, 2020; Shirey et al. 2008; Hopkins et al. 2008, 2010; Ernst 2017; Greber et al. 2017; Maruyama et al. 2018; Figure 1.1-1A) have to be considered with caution and interpretations of subduction tectonics in these old terranes are frequently challenged (e.g., Webb et al. 2020). Notably, local subduction does not require the global operation of plate tectonics (Palin et al. 2020). Other possibilities include subduction initiation without subduction stabilization

(Toth & Gurnis 1998; Gurnis et al. 2004) or local plume-induced subduction in an otherwise stagnant lid regime (Ueda et al. 2008; Burov & Cloetingh 2010; Gerya et al. 2015; Davaille et al. 2017). Features observed on Venus indicate that local subduction may be possible in a stagnant lid regime (Sandwell & Schubert 1992; Schubert & Sandwell 1995; Davaille et al. 2017).

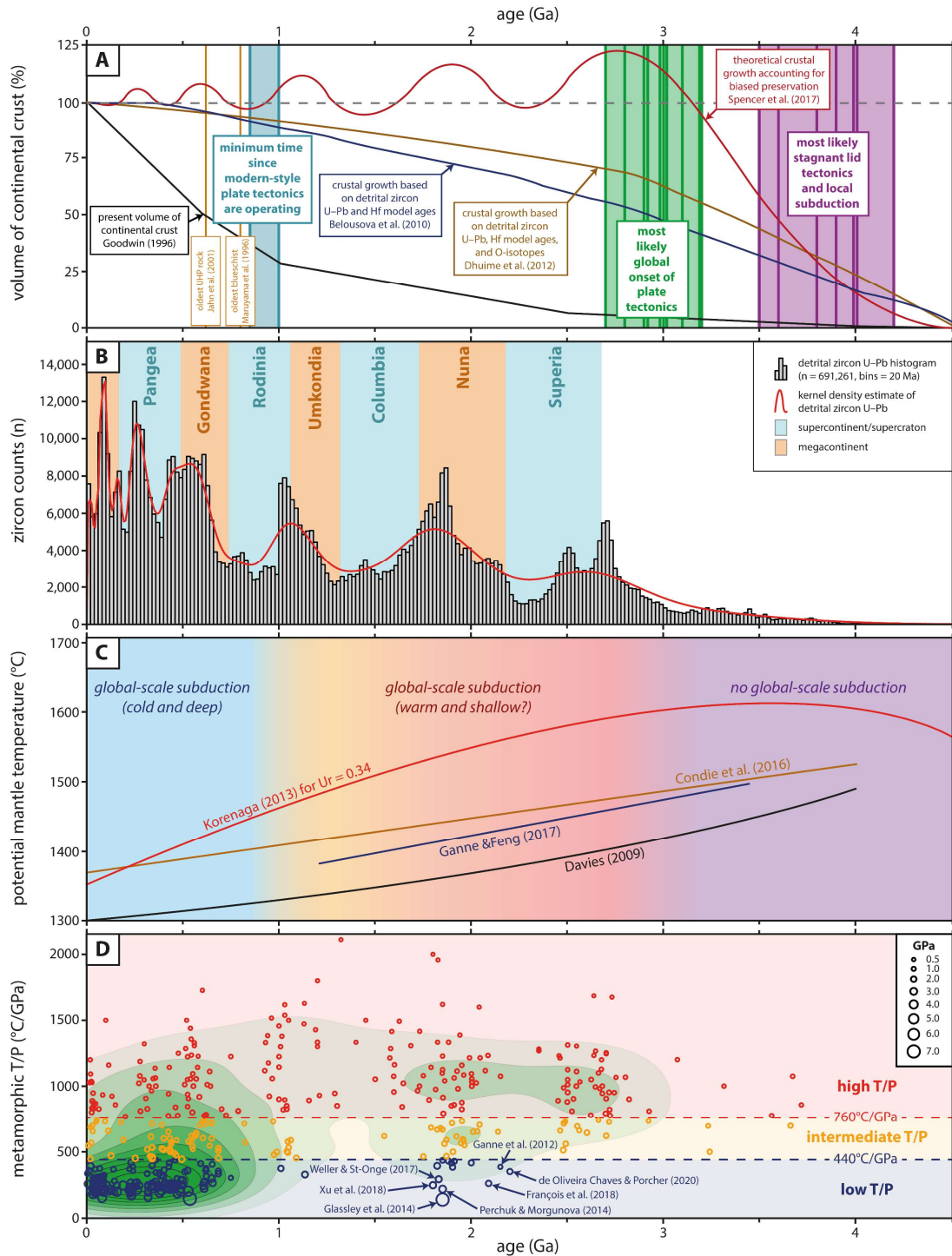


Figure 1.1-1: Indications for the onset and evolution of plate tectonics through time. (A) Present volume of continental crust (Goodwin 1996), crustal growth curves (Belousova et al. 2010; Dhuime et al. 2012; Spencer et al. 2017), and proposed onsets of plate tectonics in the Hadean to Paleoproterozoic as purple lines (Komiya et al. 1999; Nutman et al. 2002; Hopkins et al. 2008; Pease et al. 2008; Shirey et al. 2008; Ernst 2017; Greber et al. 2017; Maruyama et al. 2018; here interpreted as most likely representing stagnant lid tectonics with local subduction), Meso- to Neoproterozoic as green lines (Cawood et al. 2006; van Kranendonk et al. 2007; Condie & Kröner 2008; Dhuime et al. 2012, 2015; Tang et al. 2016; Brown & Johnson 2018; Palin et al. 2020; here interpreted as most likely representing the global onset of plate tectonics), and Neoproterozoic as sky-blue lines (Stern 2005; Hamilton 2011; interpreted as representing the minimum time since modern-style plate tectonics are operating). (B) Global dataset of detrital zircon U–Pb ages (Puetz 2018), shown as histogram and kernel density estimate with bandwidth after Venables & Ripley (2002), and supercontinent/supercraton cycles (Wang et al. 2021). (C) Potential mantle temperature (Davies 2009; Korenaga 2013; Condie et al. 2016; Ganne & Feng 2017). (D) Metamorphic gradients of crystalline rocks after Brown & Johnson 2018, extended by Paleoproterozoic references (Perchuk & Morgunova 2014; François et al. 2018; Müller et al. 2018a, 2018b; de Oliveira Chaves & Porcher 2020). Marker size indicates pressure conditions. Gradient classes after Palin et al. (2020). Green contours show dataset distribution as kernel density estimate map, bandwidth after Venables & Ripley (2002).

A hallmark for understanding the operation of plate tectonics through time on the global-scale is the consideration of the detrital zircon record to estimate crustal growth rates (e.g., Hawkesworth et al. 2013, 2016, and references therein). Large U–Pb databases of detrital zircon cover the entire geological time scale from the oldest known terrestrial material, the Jack Hills zircons with a crystallization age of ~4.4 Ga (Compston & Pidgeon 1986; Wilde et al. 2001; Valley et al. 2014), to present (Puetz 2018, Figure 1.1-1B). Thus, detrital zircon is supposed to be more representative on a global scale compared to zircon from preserved igneous rocks (Hawkesworth et al. 2010). However, due to potential isotopic resetting, isolation of material in the interior of supercontinents, as well as reworking and recycling, U–Pb age distributions are highly biased (Hawkesworth et al. 2017).

To partially tackle the issue of reworking, Belousova et al. (2010) combined U–Pb ages and hafnium model ages, whereby the model ages represent the time since the source of the parental magmas separated from the mantle (e.g., Arndt & Goldstein 1987). By dividing the number of zircons with a specific hafnium model age by the sum of zircons with an identical hafnium model and U–Pb age, Belousova et al. (2010) proposed a crustal growth curve that is more representative for juvenile magma addition than considering U–Pb or hafnium model age distributions alone (Figure 1.1-1A, dark blue line). Dhuime et al. (2012) pointed out that hafnium model age distributions may also be biased by zircons from host magmas having a mixed, hydrothermal or sedimentary source component (reworking). By additional consideration of oxygen isotopes to discriminating pristine mantle zircons from those which crystallized from reworked material, Dhuime et al. (2012) proposed a corrected crustal growth curve (Figure 1.1-1A, brown line). Inversely, higher $\delta^{18}\text{O}$ values of magmatic zircons since the Paleoproterozoic compared to the Archean support an increasing reworking of sediment in igneous regimes, interpreted as a response to collisional tectonics along with supercontinent assembly (Spencer et al. 2014). Nevertheless, the growth curve of Dhuime et al. (2012) has to be evaluated as a minimum of crustal growth, because the volume of crust recycled into the mantle through time is unknown (Spencer et al. 2017). Most of the continental crust is generated in oceanic arcs (Jicha & Jagoutz 2015) but oceanic arcs are thin and prone to be recycled via subduction (Yamamoto et al. 2009). In addition, much of the crust produced in continental arcs prior to continental collision is recycled via tectonic erosion during subduction (collision), leading to a predominant preservation of rocks from the last stage of continental assembly (Spencer et al. 2015). Thus, episodic supercontinent cycles (Figure

1.1-1B) have a strong influence on zircon age distributions and Spencer et al. (2017) proposed a crustal growth curve accounting for biased preservation (Figure 1.1-1A, red line).

Irrespective of the continental growth curve considered, all come to the agreement that the majority of continental crust was generated in the first third of Earth history, and that growth rates substantially decreased afterwards (Figure 1.1-1A). This is further supported by an independent sample-based analysis of a large U–Pb zircon dataset by Reimink et al. (2021), who concluded that continents with mature watersheds emerged globally above sea level at ~ 2.8 Ga. Thus, the global detrital zircon record indicates a major change in the generation and preservation of continental crust at ~ 3 Ga, indicating the global destruction of continental crust via subduction, and thus marking the onset of plate tectonics (e.g., Dhuime et al. 2017).

Commonly, the onset of plate tectonics at ~ 3 Ga is interpreted to be attributed to the evolution of Earth's potential mantle temperature (e.g., Cawood et al. 2018; Palin et al. 2020, and references therein), which directly effects the composition, viscosity, and rigidity of the lithospheric lid (e.g., Rolf et al. 2012). Numerical models indicate that a higher potential mantle temperature leads to a weaker lithospheric lid, which in turn prohibits the stable operation of subduction tectonics (van Hunen & van den Berg 2008; Sizova et al. 2010; van Hunen & Moyen 2012). Estimates of the potential mantle temperature through time vary significantly but provide a general consensus of a hotter mantle in the Archean that secularly cooled to present (Figure 1.1-1C).

The interpretation of an onset of plate tectonics at least since ~ 3 Ga (Mesoarchean) is a widely-held view based on the numerous hints (Figure 1.1-1A, green lines). However, some authors argue for a late onset at some point in the Neoproterozoic between 1 Ga and 0.54 Ga (Stern 2005; Hamilton 2011; Stern et al. 2016; Figure 1.1-1A, sky-blue lines). The key argument for a late onset is the lacking evidence of subduction-related rocks from the geological record prior to that time (e.g., Stern 2005). This means in particular (i) ophiolites, which indicate the generation of oceanic crust (e.g., Stern et al. 2012), (ii) low T/P (temperature/pressure) metamorphic rocks like blueschists (oldest ~ 800 Ma; Maruyama et al. 1996; Figure 1.1-1A), lawsonite-bearing rocks, and jadeites that indicate cold geotherms < 350 °C/GPa characteristic for subduction zones (e.g., Tsujimori & Ernst 2014; Harlow et al. 2015; Palin & White 2016), and (iii) ultrahigh-pressure (UHP) metamorphic rocks (oldest ~ 620 Ma; Jahn et al. 2001; Figure 1.1-1A) indicating pressure conditions of at least 2.6–2.8 GPa at 600–900 °C (e.g., Kitahara & Kennedy 1964; Bohlen & Boettcher 1982) characteristic for cold and deep subduction to depths exceeding ~ 100 km (e.g., Stern 2005). However, local occurrences of Paleoproterozoic ophiolites exist (Scott et al. 1992; Peltonen et al. 1996; Dann 1997) and low T/P as well as UHP rocks are specifically related to modern-style (Phanerozoic) subduction processes. Plate tectonics prior to the Neoproterozoic likely operated under higher potential mantle temperatures, may leading to shallow subduction at higher T/P conditions (Sizova et al. 2010; Hawkesworth et al. 2016; Ernst 2017; Figure 1.1-1C). This is supported by the secular evolution of peak metamorphic T/P gradients, that evolved to lower average T/P from ~ 2.5 Ga to present (Brown 2014; Brown & Johnson 2018; Holder et al. 2019; Figure 1.1-1D). Consequently, a distinction between the onset of plate tectonics, i.e., global-scale subduction, and the onset of modern-style plate tectonics, i.e., global-scale cold and deep subduction, is necessary.

A Neoproterozoic onset of modern-style plate tectonics based on the virtual lack of pre-Neoproterozoic low T/P and UHP rocks is increasingly challenged. On the one hand, their absence may be strongly related to biased preservation due to erosion, retrograde metamorphism, and supercontinent cycles (e.g., Wei & Clarke 2011; Cawood & Hawkesworth 2014; Weller & St-Onge 2017; Keller & Schoene 2018; Chowdhury et al. 2021), restriction of lawsonite-bearing rocks to extremely cold conditions (Penniston-Dorland et al. 2015; Hernández-Uribe & Palin 2019), variations in protolith composition through time (Palin & Dyck 2018; Palin et al. 2021), as well as their general rare occurrence in the geological record (Palin et al. 2020). On the other hand, a growing number of local Paleoproterozoic low T/P rocks is getting reported, which includes the Belomorian Belt of Russia (Mints et al. 2010; Dokukina et al. 2014; Perchuk & Morgunova 2014; partially maybe Mesoarchean), the Usagaran Belt of Tanzania (Möller et al. 1995; Collins et al. 2004), the West African Craton of Burkina Faso (Ganne et al. 2012), the Kasai Block of the Democratic Republic of Congo (François et al. 2018), the Nagssugtoqidian Orogen of Greenland (Glassley et al. 2014; Müller et al. 2018a, 2018b), the Trans-Hudson Orogen of Canada (Weller & St-Onge 2017), the North China Craton of China (Xu et al. 2018), and the São Francisco Craton of Brazil (de Oliveira Chaves & Porcher 2020; Figure 1.1-1D).

Although the above-mentioned observations indicate the operation of modern-style plate tectonics in pre-Neoproterozoic times, at least on the local scale, all hints are restricted to the fragmentary and probably biased crystalline rock record (Figure 1.1-1A, black line), which is obvious from the kernel density maps of the metamorphic T/P dataset (Figure 1.1-1D, green contours). This raises the controversial and seemingly unresolvable question: “Are these local observations representative for modern-style plate tectonics on a global scale?” In addition, irrefutable evidence for one characteristic feature of modern-style plate tectonics, the operation of deep subduction to UHP conditions, by findings of coesite is lacking. So far, UHP conditions have only been suspected for the western part of the Nagssugtoqidian Orogen of Greenland (Glassley et al. 2014). However, this is mainly based on interpreted exsolution textures in a rock type of exotic composition, leading to estimates of extreme pressure conditions (Glassley et al. 2014; Figure 1.1-1D), which are even in Phanerozoic environments rarely reported and where the formation/exhumation mechanism is still a puzzle (Agard et al. 2009; Palin et al. 2020). In order to get from local to global indications for modern-style plate tectonics through time, there is a high demand for new techniques that are able to make use of the sedimentary archive, which has already been proven to be powerful in examining the onset of plate tectonics on a global scale (see above). Currently, two different approaches were introduced using detrital garnet (Schönig et al. 2018a) and rutile (Pereira et al. 2021).

Pereira et al. (2021) investigated detrital rutile by combining single-grain chemistry (Agangi et al. 2019; Pereira et al. 2019), U–Pb dating, zirconium thermometry (Kohn 2020) and consideration of the rutile stability field (Angiboust & Harlov 2017). A zirconium content of 100 ppm in rutile corresponds to ~550 °C at 1.3 GPa, which is at the given temperature the minimum pressure necessary to stabilize rutile. For lower zirconium contents (lower temperature), higher pressure conditions are necessary. Thus, any rutile containing ≤ 100 ppm zirconium crystallized at geotherms of ≤ 423 °C/GPa (≤ 550 °C/1.3 GPa), which is characteristic for low T/P modern-style subduction regimes based on the plagioclase-out/omphacitic-pyroxene-in transition for mafic protoliths (Palin et al. 2020). By applying this concept to a dataset consisting of compiled literature and newly obtained data, Pereira et al. (2021) found few

rutile grains pointing to low T/P metamorphism in the Meso- to Paleoproterozoic, and thus supporting modern-style subduction prior to the Neoproterozoic.

Following first findings of coesite-bearing detrital zircon in the Hefei Basin in China (Chen et al. 2005), a novel method has been developed using Raman spectroscopy to systematically screen detrital mineral grains for the presence of coesite inclusions with a focus on garnet (Schönig et al. 2018a). The authors investigated detrital garnet of a modern-sand sample from a small catchment ($<1 \text{ km}^2$) in the Western Gneiss Region of Norway. By a systematic analysis of mineral-inclusion assemblages in 732 grains, six grains containing a total of 13 monomineralic coesite inclusions have been found, directly reflecting UHP conditions of the source rock. Garnet chemistry and mineral inclusions co-existing with coesite in the same grains call for mafic as well as felsic source rocks for individual grains. Besides being the first direct evidence for the erosion of UHP metamorphic rocks from detrital garnet single grains, particularly the small size $<12 \text{ }\mu\text{m}$ (often not studied), the monomineralic character (lacking typical petrographic features of biminerallitic coesite/quartz inclusions), and indications for a felsic source (often not investigated due to intense overprinting), imply that the usual approach tracking UHP metamorphism by studying thin-sections of point-sampled eclogites from available outcrops and looking for radial fractures resulting from the partial coesite-to-quartz transformation suffers in several respects (Schönig et al. 2018a). This is further supported by recent findings of subduction-related UHP peridotites in the Western Gneiss Region (Spengler et al. 2021), which occur outside/between the UHP domains defined by investigations of eclogite (Root et al. 2005). In contrast, the detrital garnet approach enables to systematically screen entire catchments on the occurrence of UHP rocks by making use of the natural processes of erosion and sedimentary transport to sample a mixture of garnet grains sourced from a much larger volume of garnet-bearing rocks (Schönig et al. 2018a).

1.2 Aims and outline

The preliminary work by Schönig et al. (2018a) opened new avenues for the prospective exploration of UHP metamorphism in Earth's geological record by analyzing mineral inclusion in detrital garnet. A great advantage is the potential to apply this concept to pre-Neoproterozoic terranes in order to efficiently screen large rock volumes for the presence of UHP rocks, and consequently on the operation of deep subduction. In addition, considering that the oldest garnets date back to $\sim 2.8\text{--}3.2 \text{ Ga}$ (Kruger et al. 1998; Smit et al. 2013; Cutts et al. 2014; Maneiro 2016), the detrital approach forms the theoretical foundation to sample and investigate a representative number of grains ranging in age from the onset of plate tectonics to Present, including sedimentary material from eroded orogens. However, the findings by Schönig et al. (2018a) are restricted to a small catchment ($<1 \text{ km}^2$) from a single locality, raising some fundamental questions:

1. Is the preservation of coesite in detrital garnet a local phenomenon or can the results be reproduced in other UHP terranes?
2. Is the developed method also capable to trace UHP rocks of diamond grade?
3. Can the technique be applied to larger catchments?

4. Do UHP mineral inclusions in detrital garnet provide new insights in well-studied Phanerozoic terranes, particularly regarding felsic UHP rocks?
5. Are UHP inclusions preserved in detrital garnet sourced from crystalline rocks that underwent high-temperature metamorphism and diffusional modification of garnet composition during exhumation?
6. How important is the choice of the considered garnet grain size?
7. What is the role of source-rock lithology, inclusion size, inclusion frequency, and fluid availability on the preservation of detrital coesite-bearing garnet?
8. How can technical efficiencies be enhanced and is the chemical composition of garnet useful to pre-select grains?

Manuscripts included in this thesis tackle the above-mentioned questions by detailed investigation of detrital garnet grains from modern-sand samples taken in the Carboniferous central Saxonian Erzgebirge of Germany and the Neogene D'Entrecasteaux metamorphic complex in eastern Papua New Guinea. Field work in the Erzgebirge was performed in June 2018 by Hilmar von Eynatten and Jan Schönig, in preparation of the PhD project which began in November 2018. In the course of a collaboration, the studied samples from Papua New Guinea were provided by Suzanne L. Baldwin from Syracuse University, New York, and jointly investigated.

Chapter 1 provides an introduction to plate tectonics through time, addressing what we know, which indications we have, which techniques exist to trace plate tectonics, what the difference is between plate tectonics and modern-style plate tectonics, and how detrital approaches can contribute.

Chapter 2 (Schönig et al. 2019) focusses on answering questions 1 to 4 by combining inclusion identification using Raman spectroscopy and garnet major-element chemistry using electron microprobe analysis (EMPA). In total, 700 inclusion-bearing garnet grains from the 125–250 μm grain-size fraction of seven modern sands from the Erzgebirge are studied. This includes samples representing small (<1 km^2) and large (>500 km^2) catchments as well as catchments with previously reported and (so far) unreported coesite- and diamond-bearing rock occurrences. Besides the technical questions 1 to 3, the chapter addresses whether UHP metamorphism is restricted to few crystalline rock lenses, as expected from literature (Nasdala & Massonne 2000; Massonne 2001; O'Brien & Ziemann 2008; Marschall et al. 2009), or whether the extent is much wider.

Chapter 3 (Schönig et al. 2020) sheds light on questions 4 to 6. The Erzgebirge garnet dataset of inclusion assemblages and chemical composition (Schönig et al. 2019; Chapter 2) is extended by 700 inclusion-bearing grains from both the 63–125 μm and 250–500 μm grain-size fraction, resulting in a merged dataset of 2100 inclusion-bearing garnets (Schönig et al. 2020). By focusing on coesite-, diamond-, and melt-bearing garnet, by performing spectral Raman imaging, and by application of statistical tools like confidence ellipses/ellipsoids, multivariate discrimination (Tolosana-Delgado et al. 2018), and perturbation on the simplex (von Eynatten et al. 2002), this chapter addresses a fundamental question to the Erzgebirge that also applies to many UHP terranes worldwide (e.g., Liou et al. 2009): “Are UHP lenses and the surrounding high- to medium-pressure (HP/MP) felsic country rocks are a

product of different peak metamorphic conditions corresponding to different maximum depth of subduction or did the country rocks also experienced UHP conditions but equilibrated and/or re-equilibrated at a different metamorphic stage?” Answering this question based on the new results raised a new discussion on the geodynamic context of the central Saxonian Erzgebirge (Comment by Massonne 2021; Reply by Schönig et al. 2021a), which forms the second part of Chapter 3.

Chapter 4 (Baldwin et al. 2021) takes advantage of the knowledge gained in the previous chapters, and applies the combination of Raman inclusion identification and imaging as well as EMPA to garnet from a beach placer of a remote island in eastern Papua New Guinea. The regional setting is of particular interest as the metamorphic complex represents the youngest and actively exhuming HP to UHP terrane on Earth (Baldwin et al. 2012). However, UHP conditions are solely recorded by coesite in a single eclogite lens from a single outcrop (Baldwin et al. 2008), whereby it is open for interpretation whether this eclogite originates from the crust or the mantle (e.g., Zirkparvar et al. 2011; Baldwin & Das 2015). Consequently, the fulfillment of the definition of UHP metamorphism, i.e., crustal rocks which experienced P - T conditions high enough for the formation of coesite (e.g., Carswell & Compagnoni 2003), is equivocal. This chapter particularly focuses on the identification of detrital UHP garnet sourced from felsic source rocks, shedding further light on question 4. In addition, elastic geothermobarometry (Angel et al. 2017a, 2019; Mazzucchelli et al. 2021) is applied for the first time to detrital garnet grains that contain quartz inclusions (pressure sensitive) co-existing with zircon inclusions (temperature sensitive), to further explore the metamorphic path during exhumation and heating recorded by detrital garnet (question 5).

Chapter 5 (Schönig et al. 2021b) addresses questions 6 and 7 in detail. For this purpose, the large dataset of inclusion assemblages and garnet chemistry ($n = 2,100$) acquired from the Erzgebirge (Schönig et al. 2019, 2020; Chapters 2 and 3) is used. The distribution and composition of coesite-bearing garnet compared to rutile-, omphacite-, graphite-, quartz-, and kyanite-bearing garnet as well as Raman imaging of a decent number of coesite inclusions ($n = 193$) is investigated by statistical data evaluation using multivariate discrimination (Tolosana-Delgado et al. 2018), confidence ellipsoids, kernel density estimates, and principal component analysis (Schönig et al. 2021b). This provides new insights in understanding the grain-size distribution of detrital coesite-bearing garnet, which is influenced by a complex interaction of factors occurring from inclusion entrapment, over exhumation to Earth's surface, to erosion and sedimentary transport. Additionally, Raman spectroscopy is used to estimate peak temperature conditions of carbonaceous material (Lünsdorf et al. 2017) occurring in bimineralic coesite/quartz inclusions, interpreted as reflecting the temperature of garnet host fracturing and fluid infiltration during exhumation.

Chapter 6 (Schönig et al. in press) forms the basis to address question 8. Garnet major-element composition is a widely used tool in sedimentary provenance analysis, applied to gain source rock information, in particular regarding metamorphic rocks. While classical schemes are using strict compositional fields and mainly show insufficient classification success or non-detailed prediction classes (e.g., Krippner et al. 2014), novel discrimination schemes use multivariate statistics to make use of all available variables (e.g., Tolosana-Delgado et al. 2018). However, these still have a high potential to be improved by increasing the database, by more detailed prediction classes, and by applying statistical methods with high flexibility to disentangle the strongly overlapping compositional

signatures of various garnet types. A large database ($n = 13,615$) of major-element garnet compositions from specific host rocks is presented, which was compiled by an extensive literature survey. The database is split into provenance informative classes that form the basis to predict the host-rock setting, metamorphic facies, and composition. A novel discrimination scheme is presented that was developed by the usage of the random forest machine-learning algorithm, and available via a worldwide accessible web application.

Chapter 7 (Schönig et al. in preparation) reviews previous attempts to link clastic sediments to the erosion of UHP rocks and the novel technique of analyzing mineral inclusions in detrital, as well as the new insights the method provided regarding UHP metamorphism in the Western Gneiss Region of Norway (Schönig et al. 2018a), the central Saxonian Erzgebirge of Germany (Schönig et al. 2019, 2020; Chapters 2 and 3), and the D'Entrecasteaux metamorphic complex of Papua New Guinea (Baldwin et al. 2021; Chapter 4). Technical advancements are highlighted (question 8), including recommendations with regard to enhance efficiencies by the choice of the grain size (Schönig et al. 2021b; Chapter 5), chemical pre-screening by the developed garnet discrimination scheme (Schönig et al. in press; Chapter 6) to reduce the number of garnets to be analyzed by time-consuming inclusion analysis, and by hyperspectral Raman imaging to reduce the user-assisted analytical time. In addition, the potential of host minerals other than garnet is addressed. Finally, a number of perspective applications is given and their importance for tackling major issues in Earth Sciences is addressed.

Chapter 8 summarizes the main conclusions of the thesis and gives an outlook of future research directions.

Diamond and coesite inclusions in detrital garnet of the Saxonian Erzgebirge, Germany

Jan Schönig¹, Hilmar von Eynatten¹, Guido Meinhold^{1,2}, and N. Keno Lünsdorf¹

¹*Geosciences Center Göttingen, University of Göttingen, Germany*

²*School of Geography, Geology and the Environment, Keele University, United Kingdom*

published 22th May 2019

Geology 47, 715–718

<https://doi.org/10.1130/G46253.1>

Local occurrences of coesite- and diamond-bearing rocks in the central Erzgebirge reveal ultrahigh-pressure (UHP) metamorphic conditions during the Variscan Orogeny. Although UHP metamorphism supposedly affected a wider area, implying that rocks which equilibrated under UHP conditions occur dispersed in large volumes of high-pressure country rock gneisses, mineralogical evidence is scarce. Here we applied the new concept of capturing the distribution and characteristics of UHP rocks by analyzing inclusions in detrital garnet. Out of 700 inclusion-bearing garnets from seven modern sand samples draining the UHP area around the Saidenbach reservoir, we detected 26 garnets containing 46 mainly monomineralic coesite inclusions and 22 garnets containing 41 diamond inclusions. Combined with geochemical classification of the host garnets, we show that (1) coesite-bearing rocks are common and comprise eclogites as well as felsic gneisses, (2) small inclusion size is a necessary precondition for the preservation of monomineralic coesite, and (3) for the first time, diamond-bearing crustal rocks can be detected by analyzing the detrital record. Our results highlight the potential of this novel application of sedimentary provenance tools to UHP research, and the necessity to look at the μm -scale to find evidence in the form of preserved UHP minerals.

2.1 Introduction

The Gneiss–Eclogite Unit of the Saxonian Erzgebirge, located in the northwestern Bohemian Massif, was subjected to ultrahigh-pressure (UHP) metamorphic conditions during the Variscan Orogeny. This unit is predominantly composed of ortho- and paragneisses with numerous lenses of eclogite and a few lenses of peridotite (e.g., Liati & Gebauer 2009). It is exposed in the central Erzgebirge and has received considerable attention because diamond inclusions have been found in several host minerals in lenses of paragneiss located at the eastern shore of the Saidenbach reservoir (e.g., Nasdala & Massonne 2000; Dobrzhinetskaya et al. 2013; Figure 2.1-1). Besides diamond, coesite occurs mainly as relict in biminerallitic coesite/quartz inclusions of an eclogite at the northern shore (Massonne 2001; O'Brien & Ziemann 2008) and granulite blocks ~4.5 km further east (Marschall et al. 2009). Even though UHP metamorphic conditions are inferred for several eclogites in the area based on geothermobarometry (e.g., Massonne 2011a) and polycrystalline quartz inclusions interpreted as pseudomorphs after coesite (e.g., Schmädicke et al. 1992), mineralogical evidence in the form of preserved coesite and/or diamond is lacking except for the very local occurrences mentioned.

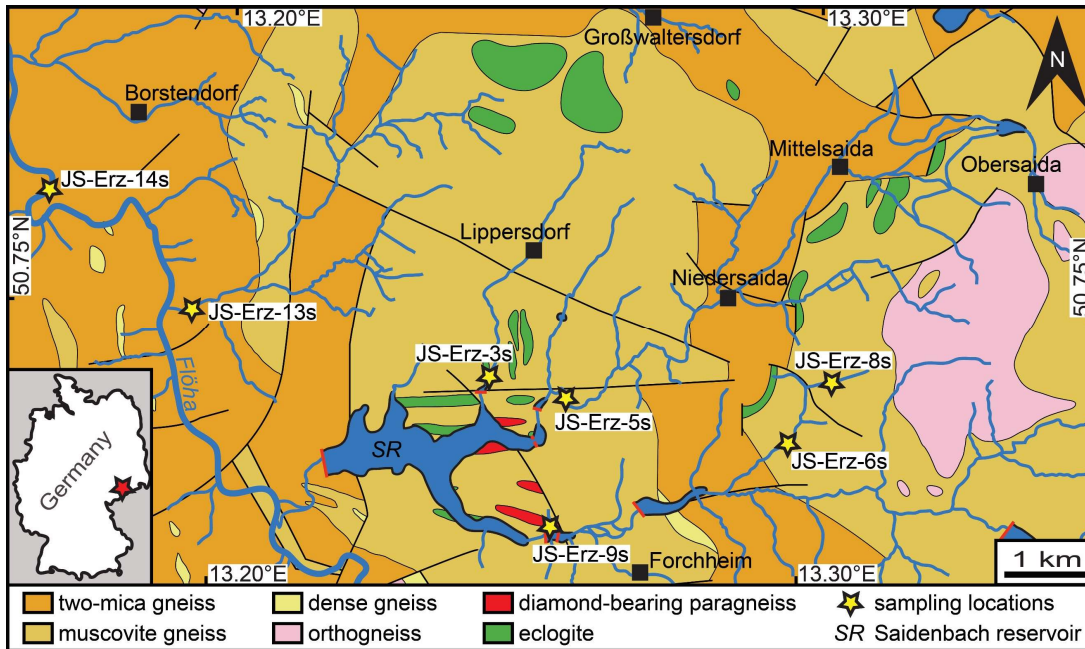


Figure 2.1-1: Geological map of the area around the Saidenbach reservoir in the central Erzgebirge with sampling locations. Inset shows the location marked by the red asterisk. Geological units adopted from the Saxon State Office for Environment, Agriculture and Geology (<http://www.geoportal.sachsen.de>) and supplemented by occurrences of eclogites and diamond-bearing paragneisses after Massonne (2001). Sampling locations are marked by yellow asterisks and coordinates are given in Table Appendix 2-A 1.

The commonly applied approach when searching for evidence of UHP metamorphism, i.e., sampling potential crystalline rocks (mainly eclogites), preparing thin sections, and looking for typical structures resulting from the coesite-to-quartz transformation, suffers in several respects, as outlined by Schönig et al. (2018a). Monomineralic coesite inclusions are prone to be overlooked because they are typically small (<20 µm) and do not show the distinct features of biminerallitic coesite/quartz inclusions (e.g., Parkinson & Katayama 1999). Additionally, the large volumes of felsic lithologies (mainly gneisses) surrounding the eclogitic lenses in most UHP terranes are commonly retrogressed and/or not affected by UHP metamorphism and can be only tested selectively. For the Gneiss–Eclogite Unit south of the Erzgebirge, Kotková et al. (2011) already showed that at least some of the felsic to intermediate metamorphic rocks contain coesite and diamond. Thus, one could expect that mafic as well as felsic UHP rocks are widely distributed in the high-pressure country rocks of the area. In the vicinity of the Saidenbach reservoir, these country rocks yield geothermobarometric results below the coesite stability field (e.g., Massonne 2011a).

Schönig et al. (2018a) introduced a complimentary approach to capture the distribution and characteristics of UHP rocks by identifying monomineralic coesite inclusions in detrital garnet. This allows for screening a mixture of garnets from lithologies exposed in the sampled catchments. Here we applied this concept and present mineral inclusion data of 700 inclusion-bearing detrital garnets in order to determine whether (1) coesite-bearing rocks in the central Erzgebirge can be traced by analyzing the detritus, and if these include felsic lithologies; (2) diamond-bearing rocks supply significant amounts of diamond-bearing garnets to the sedimentary system, and if these rocks are widespread or locally

restricted; (3) the analyzed inclusion size plays a crucial role when searching for UHP minerals; and (4) the technique of tracing UHP metamorphism at the catchment scale can be also applied to larger catchments than tested before.

2.2 Samples and Methods

Seven modern sand samples were taken from tributaries draining the area around the Saidenbach reservoir in the central Erzgebirge (Figure 2.1-1). Samples JS-Erz-3s, -5s, -6s, -8s, and -9s are from creeks draining into the reservoir, whereby sampling spot JS-Erz-3s is located upstream of the coesite-bearing eclogite described by Massonne (2001) and O'Brien & Ziemann (2008), and sampling spot JS-Erz-8s is slightly downstream from the coesite-bearing granulite blocks described by Marschall et al. (2009). Sample JS-Erz-9s is very proximal to the diamond-bearing paragneiss lenses at the eastern shore of the reservoir (Nasdala & Massonne 2000). Sample JS-Erz-13s was derived from a creek north of the reservoir, which drains into the Flöha River and encompasses fewer eclogites in the catchment. Sample JS-Erz-14s was collected from the Flöha River ~3 km further downstream, representing a much larger catchment (>500 km²) than the other samples (Table 2.2-1).

Table 2.2-1:
Omphacite-, coesite-, and diamond-bearing garnets from the Saxonian Erzgebirge, Germany.

Sample	Catchment size (km²)	Screened garnets (n)	Inclusion-bearing garnets (n)	Inclusion-bearing garnets (%)	Omphacite-bearing garnets (n)
JS-Erz-3s	<5	200	100	50	8
JS-Erz-5s	<20	209	100	48	17
JS-Erz-6s	<5	172	100	58	16
JS-Erz-8s	<1	200	100	50	7
JS-Erz-9s	<1	166	100	60	0
JS-Erz-13s	<20	160	100	63	2
JS-Erz-14s	>500	138	100	72	2
total		1245	700	56	52

Sample	Diamond-bearing garnets (n)	Diamond inclusions (n)	Coesite-bearing garnets (n)	Coesite inclusions (n)	UHP garnets (%)*
JS-Erz-3s	0	0	17	33	9
JS-Erz-5s	0	0	1	2	1
JS-Erz-6s	0	0	0	0	0
JS-Erz-8s	0	0	2	3	1
JS-Erz-9s	22	41	0	0	13
JS-Erz-13s	0	0	4	5	3
JS-Erz-14s	0	0	2	3	1
total	22	41	26	46	4

*Percentage of diamond- and coesite-bearing garnets from all screened garnets (UHP – ultrahigh-pressure)

The 125–250 μm heavy mineral fraction was separated and mounted using standard techniques, and polished with Al_2O_3 to eliminate any possibility of contamination with diamond abrasives. Mineral inclusions $\geq 2 \mu\text{m}$ in detrital garnets were identified by Raman spectroscopy and the main band positions of UHP inclusions were determined to estimate remnant inclusion pressures. Only garnets with visible inclusions $\geq 2 \mu\text{m}$ were analyzed, making it necessary to screen 138 to 209 garnets per sample to achieve the target of 100 inclusion-bearing grains per sample (Table 2.2-1). The geochemical composition of all inclusion-bearing garnets was determined by electron microprobe analysis (EMPA). Additional details on samples and methods are given in Appendix 2-A.

2.3 Mineral Inclusions

Forty-six coesite inclusions are present in 26 of the analyzed garnets. Coesite-bearing garnets occur in sample JS-Erz-3s and to a lesser extent in samples JS-Erz-5s, -8s, -13s, and -14s (Table 2.2-1). The inclusions are 1.5–20.0 μm in size (longest axis in plane view), colorless, and typically spheroidal to spherical in shape (Figure 2.2-1A). However, some of the inclusions have an angular shape. The majority of the coesite inclusions (39 out of 46) are monomineralic, $\leq 13.0 \mu\text{m}$ in size, and show no fracturing of the garnet host (coesite 13–15 in Figure 2.2-1A). In contrast, the Raman spectra of seven coesite inclusions, all $>13.0 \mu\text{m}$, show a significant quartz component that increases towards the inclusion/host boundary (coesite 16 in Figure 2.2-1A). A filigree of fine fractures that are partially healed commonly surrounds these inclusions. Coesite inclusions in single garnets co-exist with inclusions of rutile, apatite/monazite, zircon, quartz,

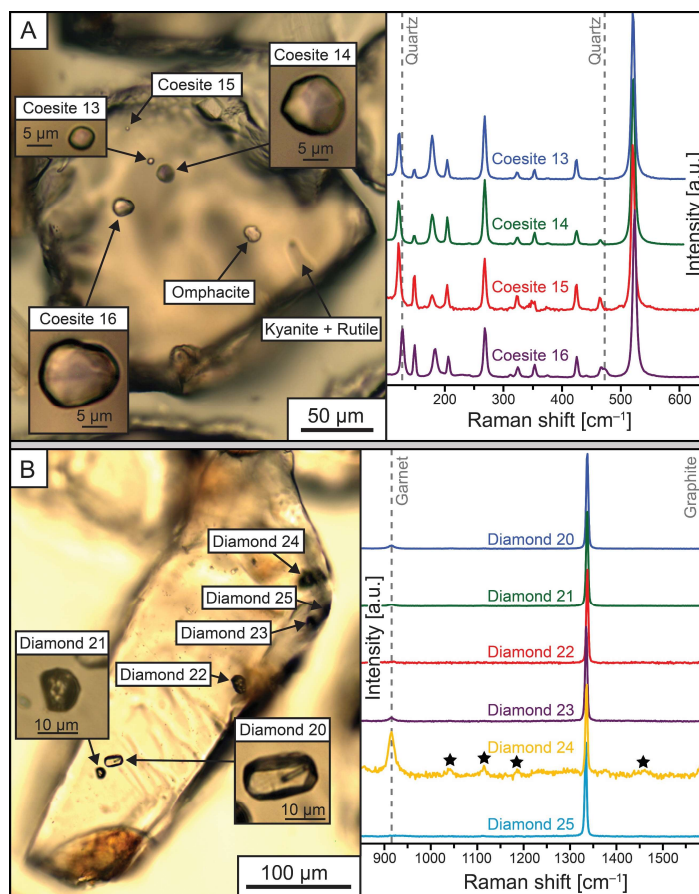


Figure 2.2-1: Coesite and diamond inclusions in detrital garnet. A: Photomicrograph of garnet number 90 from sample JS-Erz-3s with four coesite inclusions, an omphacite + and a kyanite + rutile inclusion, and corresponding Raman spectra of the coesite inclusions. Quartz band positions are given as dashed lines, showing that the larger coesite inclusion 16 ($15.5 \times 13.0 \mu\text{m}$) contains small amounts of quartz. **B:** Photomicrograph of garnet number 88 from sample JS-Erz-9s with six diamond inclusions and corresponding Raman spectra. Diamond 20 shows an exceptional inclusion shape with well-developed crystal faces. It is colorless and contains a rutile needle. In contrast, diamonds 21–25 show the common irregular inclusion shape with a slightly yellow color. Raman main band positions of the garnet host and graphite (only present in diamond 24) are given as dashed lines. Asterisks mark band positions of the embedding medium (epoxy).

omphacite, kyanite, carbonates, graphite, micas, and plagioclase (Electronic Appendix 2e-A). The coesite main band is located at 520–525 cm^{-1} (Electronic Appendix 2e-B), significantly shifted from the position at room pressure (520–521 cm^{-1}), indicating that the inclusions preserve significant stress as a result of entrapment at UHP metamorphic conditions. Band positions which deviate to a lesser extent from those of a free crystal are restricted to inclusions that are exposed at the garnet surface.

Forty-one diamond inclusions were detected in 22 garnets from sample JS-Erz-9s (Table 2.2-1). These diamond inclusions are 2.5–20.0 μm in size, typically slightly yellow to grey in color, and have an irregular shape (e.g., diamond 21 in Figure 2.2-1B). Few diamond inclusions are spheroidal, colorless and occasionally have well-developed crystal faces (e.g., diamond 20 in Figure 2.2-1B). Twenty-two out of 41 diamond inclusions are monomineralic, whereas 19 diamonds occur in polyphase inclusions with phyllosilicates, rutile, graphite, quartz, plagioclase, and apatite/monazite. Diamond inclusions in the single garnets co-exist with inclusions of rutile, graphite, phyllosilicates, quartz, apatite/monazite, cristobalite, and kyanite (Electronic Appendix 2e-A). The diamond main band is located at 1331–1335 cm^{-1} (Electronic Appendix 2e-C), indicating inclusion pressures of up to ~ 1.3 GPa (Tardieu et al. 1990). As a general trend, inclusions that exhibit pressures near atmospheric conditions are restricted to diamonds exposed at the garnet surface or that occur in polyphase inclusions, whereas the highest overpressures are attained from inclusions completely enclosed by garnet. This is in good agreement with theory and has recently been demonstrated by experimental and numerical approaches (e.g., Campomenosi et al. 2018).

Besides the UHP minerals, omphacite inclusions occur in garnet of all samples, except the diamond-bearing one (JS-Erz-9s), with proportions being highest in JS-Erz-5s and -6s, intermediate in JS-Erz-3s and -8s, and low in JS-Erz-13s and -14s (Table 2.2-1).

2.4 Garnet Chemistry

Detrital garnets in sample JS-Erz-14s (largest catchment) show the largest spread in composition, comprising garnets from all local crystalline rocks, with the exception of high-Mg eclogites, as corresponding detrital garnets are absent (Figure 2.4-1A, Figure Appendix 2-A 1). This spread is similar in JS-Erz-13s, but here low-Mg garnet is less frequent and two distinct maxima are present, resembling garnet from local eclogites and diamond-bearing paragneisses. The other samples show even fewer low-Mg garnets and the two maxima are sample-dependent more pronounced. Although several garnets higher in Ca and lower in Mg are present in JS-Erz-9s, the majority shows the characteristics of the diamond-bearing paragneiss, whereas JS-Erz-8s also shows characteristics of eclogitic garnets. The latter are prominent in samples JS-Erz-3s, -5s, and -6s.

The coesite-bearing garnets show the same two maxima with a higher concentration of eclogitic garnets (Figure 2.4-1C, Figure Appendix 2-A 1). Sample JS-Erz-3s only contains coesite-bearing garnets with an eclogitic affinity, whereas samples JS-Erz-5s and -8s only contain coesite-bearing garnets derived from rocks similar to the diamond-bearing paragneisses, and in samples JS-Erz-13s and -14s they occur in both. In contrast, the diamond-bearing garnets resemble the composition of garnets from the diamond-bearing paragneiss (Figure 2.4-1D, Figure Appendix 2-A 1). Omphacite-bearing garnets show

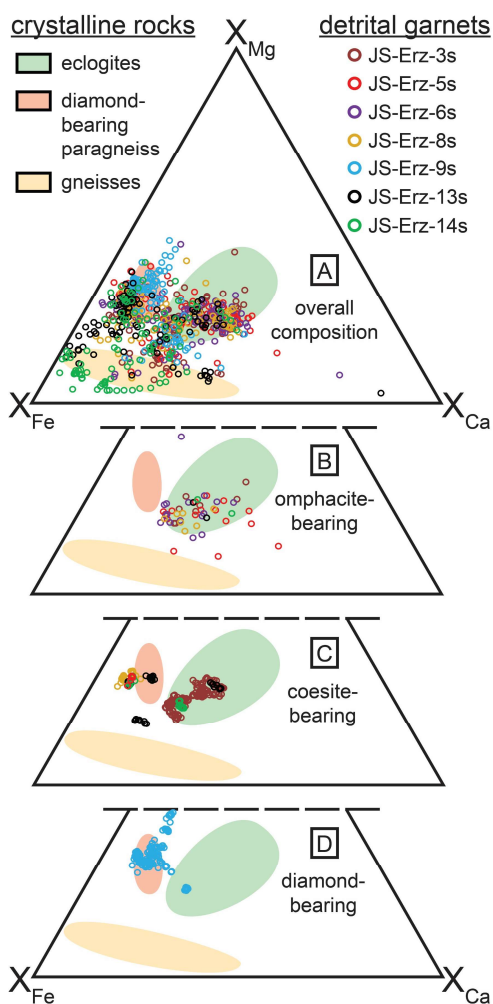


Figure 2.4-1: Chemical composition of detrital garnets in molar proportions of the Mg-, Fe-, and Ca-endmembers. The full dataset is given in Electronic Appendix 2e-D and additional classification using a multivariate discrimination scheme (Tolosana-Delgado et al. 2018) is shown in Figure Appendix 2-A 1. A: All detrital garnets (n = 696; one spot per grain). B: Omphacite-bearing garnets (n = 51; one spot per grain). C: Coesite-bearing garnets (n = 234; 9 spots per grain). D: Diamond-bearing garnets (n = 198; 9 spots per grain). For comparison, garnet data of local crystalline rocks are shown as envelopes (Electronic Appendix 2e-E).

inclusions, and the preferred occurrence in samples from creeks which mainly drain felsic lithologies, i.e., JS-Erz-5s, -8s, and -13s. Thus, coesite inclusions in this rock type are probably more frequent than would be expected from occasional descriptions of pseudomorphs after coesite in the known diamond-bearing paragneisses at the eastern shore of the Saidenbach reservoir (Massonne & Nasdala 2003) and from the absence of coesite inclusions in detrital garnets of sample JS-Erz-9s, which mainly originated from these rocks. One coesite-bearing garnet from JS-Erz-13s shows a lower Mg-content than both

compositions similar to those of garnets from local eclogites (Fig. Figure 2.4-1B, Figure Appendix 2-A 1).

2.5 Discussion

The widespread occurrence of coesite inclusions in detrital garnets of creeks draining the area around the Saidenbach reservoir indicates that UHP metamorphic rocks are distributed over the investigated area. Although these UHP rocks are volumetrically subordinate to the high-pressure country rock gneisses, the detrital fraction is enriched in garnets sourced from the UHP rocks due to (i) their higher modal garnet content, and (ii) the concentration of garnet from the freshest, least retrogressed rocks. This explains the mineralogical evidence for UHP metamorphism recorded in significant proportions of ~4% from all screened garnets and ~7% from the inclusion-bearing garnets, respectively.

Furthermore, the compositional distribution of detrital coesite-bearing garnets points to more than one source lithology. One population (~77%) most likely derives from eclogites, as indicated by similar compositions of garnets from local eclogites, the co-existence of omphacite inclusions in some of the grains (Schönig et al. 2018b), similar composition to other detrital garnets containing omphacite inclusions, and by their highest abundance in sample JS-Erz-3s where eclogites are frequent in the catchment area. The other population (~19%) most likely derives from the more felsic gneisses based on similar composition to garnet from the diamond-bearing paragneiss, the absence of omphacite

eclogites and paragneisses. Although an eclogitic affinity of this garnet is very likely (Tolosana-Delgado et al. 2018; Figure Appendix 2-A 1), it cannot be assigned to a specific source rock.

The observation that coesite inclusions $\leq 13 \mu\text{m}$ are monomineralic and show significant inclusion overpressures without fracturing of the garnet host is in accordance with observations of other monomineralic coesite inclusions in garnet (Schönig et al. 2018a), whereas inclusions $>13 \mu\text{m}$ are biminerally (coesite + quartz) and commonly show a filigree of fine fractures, which is in accordance with similar sized coesite inclusions in garnet (Korsakov et al. 2007). This underlines inclusion size as an important factor for the preservation of coesite.

Diamond-bearing garnets in sample JS-Erz-9s are in all probability sourced from the diamond-bearing paragneiss lenses, based on similar garnet composition, the typical polyphase mineral inclusions (Stöckhert et al. 2009), and the proximal sampling locality. The high abundance of diamond inclusions in detrital garnets shows that diamond-grade UHP rocks effectively transfer UHP signatures to the sedimentary record. However, based on the 138 to 209 garnets analyzed per sample, there is no evidence for the presence of diamond-bearing rocks in the other catchments, suggesting that no other diamond-bearing rocks occur in the vicinity of the Saidenbach reservoir, although similar rocks containing coesite are present. An unusual feature of the enclosed diamonds is the remnant inclusion pressure of up to $\sim 1.3 \text{ GPa}$ and the co-existence with graphite and quartz (no coesite) in some polyphase inclusions, similar to observations by Kotková et al. (2011). Because the thermoelastic properties of diamond entrapped during garnet growth in the diamond stability field should result in remnant inclusion pressures around zero, elastic re-equilibration of at least some of the diamond inclusions in the stability field of quartz and graphite is suggested, confirming pressure reduction at high temperatures (Ferrero & Angel 2018).

2.6 Conclusions

The mineral inclusion data combined with geochemical composition of the detrital host garnets shows that (1) coesite-bearing rocks in the central Erzgebirge are common and include mafic and felsic lithologies, indicating that UHP metamorphic rocks are distributed over the entire study area; (2) high proportions of detrital garnets derived from the diamond-bearing paragneisses contain diamond inclusions, which represents the first report of metamorphic diamond inclusions in detrital mineral grains. The diamond-bearing lithologies appear restricted to the known paragneiss lenses at the eastern shore of the Saidenbach reservoir; (3) analyzing small inclusions $\leq 20 \mu\text{m}$ is crucial for the identification of UHP metamorphic rocks and these may have been often overlooked to date; and (4) overall, the applied method is appropriate to detect UHP metamorphic rocks even in large catchments based on the two most prominent and unequivocal indicator minerals coesite and diamond.

Acknowledgements

We thank Judit E. Dunkl, István Dunkl, and Antje Grebe for their support in sample preparation; Andreas Kronz for advice when using the electron microprobe; and Paul Spry for a pre-submission

review. The comments by Craig Storey and two anonymous reviewers as well as careful editorial handling by Dennis Brown helped improving the manuscript.

Deep subduction of felsic rocks hosting UHP lenses in the central Saxonian Erzgebirge: Implications for UHP terrane exhumation

Jan Schönig¹, Hilmar von Eynatten¹, Guido Meinhold^{1,2}, N. Keno Lünsdorf¹,
Arne P. Willner³, and Bernhard Schulz⁴

¹*Geosciences Center Göttingen, University of Göttingen, Germany*

²*School of Geography, Geology and the Environment, Keele University, United Kingdom*

³*Institute of Geology, Mineralogy and Geophysics, University of Bochum, Germany*

⁴*Institute for Mineralogy, TU Bergakademie Freiberg, Germany*

published 19th August 2020

Gondwana Research 87, 320–329

<https://doi.org/10.1016/j.gr.2020.06.020>

Contrasting metamorphic conditions determined by chemical geothermobarometric investigations of ultrahigh-pressure (UHP) lenses surrounded by high-pressure (HP) and medium-pressure (MP) felsic country rocks are an enigmatic feature of UHP terranes. One of the major questions arising is whether the UHP lenses and the country rocks are a product of different peak metamorphic conditions corresponding to different maximum depth or whether country rocks also experienced UHP conditions but equilibrated and/or re-equilibrated at a different metamorphic stage. Here we address this question to the central Saxonian Erzgebirge in the northwestern Bohemian massif, Germany. In order to screen the variety of garnet from lithologies occurring in the study area, we analyzed the detrital garnet record from seven modern stream sands. In addition to 700 inclusion-bearing garnet grains previously studied from the 125–250 µm grain-size fraction, we analyzed the 63–125 and 250–500 µm fractions and extended the dataset to overall 2100 inclusion-bearing grains. The new findings of coesite and diamond inclusions in several garnet grains, which are in compositional contrast to garnet of the known UHP lenses but match with those of the felsic country rocks, show that considerable parts of the country rocks underwent UHP metamorphism. Melt inclusions containing cristobalite, kokchetavite, and kumdykolite in garnet derived from the country rocks point to partial melting and re-equilibration during exhumation at HP/HT conditions. Although an amalgamation of rocks which reached different maximum depth may be responsible for some of the contrasting peak metamorphic conditions, the mineralogical evidence for UHP conditions in the felsic country rocks surrounding the UHP lenses proves a largely coherent slab subducted to UHP conditions. Furthermore, the presence of coesite in the subducting voluminous felsic crust and its transformation to quartz during exhumation have great implications for buoyancy development during the metamorphic cycle, which may explain the high exhumation rates of UHP terranes.

3.1 Introduction

The occurrence of metamafic and metasedimentary coesite- and/or diamond-bearing lenses within large volumes of high-pressure (HP) and medium-pressure (MP) gneissic and schistose felsic country rocks

is a common feature of ultrahigh-pressure (UHP) terranes (Liou et al. 2009). To understand the geodynamic context of these terranes, it is particularly important to examine whether the country rocks and UHP lenses share a joint pressure–temperature (P – T) path or represent different units amalgamated during exhumation. This is still a matter of debate for many UHP terranes due to the strong ductile deformation obscuring the structural relations and more importantly, the lack of geothermobarometric evidence that the country rocks experienced UHP metamorphism.

In the central Saxonian Erzgebirge of the northwestern Bohemian Massif in Germany, UHP rocks locally occur as lenses within quartzo-feldspathic country rocks (e.g., Nasdala & Massonne 2000; Massonne 2001). The high contrast in peak metamorphic conditions of the adjacent HP/HT (high-temperature) gneisses (HP granulite facies; ~ 2.1 GPa at ~ 830 °C; Willner et al. 1997; Tichomirowa et al. 2018) compared to the coesite- and diamond-bearing UHP lenses has been interpreted as a mixture of rocks which reached different maximum depth and were amalgamated during exhumation (e.g., Massonne 2005, 2011b). Alternatively, both the UHP lenses and the country rocks might have been subducted to UHP conditions as a coherent slab but the felsic country rocks either have not equilibrated at peak conditions or re-equilibrated and re-crystallized during HT decompression (Gose & Schmädicke 2018; Faryad & Cuthbert 2020). In terms of pervasive re-equilibration, rare relictic mineral cores and/or preserved inclusions of coesite and diamond in resistant host minerals may be the only witnesses for a precursor UHP metamorphic event.

Testing this hypothesis is challenging considering the small inclusions to be found within host minerals from huge volumes of country rocks, in particular when outcrops are rather limited like in the Erzgebirge. Nevertheless, by investigating inclusions in the detrital record advantage of natural processes can be taken to systematically sample a mixture of host minerals from various rocks occurring in the sampled catchments (Schönig et al. 2018a). The application of this technique to the 125–250 μm detrital garnet grain-size fraction in the central Saxonian Erzgebirge has already demonstrated that UHP rocks occur frequently and dispersed within the country rocks rather than being restricted to a few localities (Schönig et al. 2019). However, hints for the involvement of the country rocks in the UHP metamorphic cycle are sparse in the analyzed grain-size fraction.

Studies comparing detrital garnet composition and grain size have shown that provenance information may be missed by focusing on a narrow grain-size window (Krippner et al. 2015, 2016). In order to elucidate whether the lack of UHP garnet from the country rocks in the central Erzgebirge can be attributed to contrasting peak metamorphic conditions or whether it is an effect of the narrow grain-size window analyzed so far, we considerably extend the mineral inclusion and chemical data of garnet grains from modern sands previously studied by Schönig et al. (2019) by investigating the 63–125 μm and 250–500 μm grain-size fractions. Based on (i) the compositional contrast of several coesite- and diamond-bearing garnet grains to those from known UHP rocks of the study area and (ii) the occurrence of melt inclusions containing cristobalite, kokchetavite, and kumdykolite in garnet grains derived from felsic rocks, we demonstrate that considerable parts of the felsic country rocks underwent a precursor UHP metamorphic stage but re-equilibrated at HP/HT conditions during exhumation. In addition, we discuss the implications of these findings on conceptual models for the exhumation of UHP terranes.

3.2 Geological framework and samples

The crystalline complex of the Saxonian Erzgebirge formed as part of the European Variscides resulting from the collision of Gondwana (Armorican Terrane Assemblage) and Laurussia (Laurentia, Baltica, Avalonia, Ganderia) during the Variscan orogeny (e.g., Kroner and Romer 2013; Figure 3.2-1A). Its dome structure consists of a stack of composite tectonometamorphic units of contrasting peak metamorphic conditions. The highest P - T conditions are recorded in the “Gneiss–Eclogite Unit” in the central part of the crystalline complex, a heterogeneous nappe in intermediate position of the nappe stack containing MP, HP, and UHP rocks (Willner et al. 1997, 2000; Figure 3.2-1B). Within this nappe,

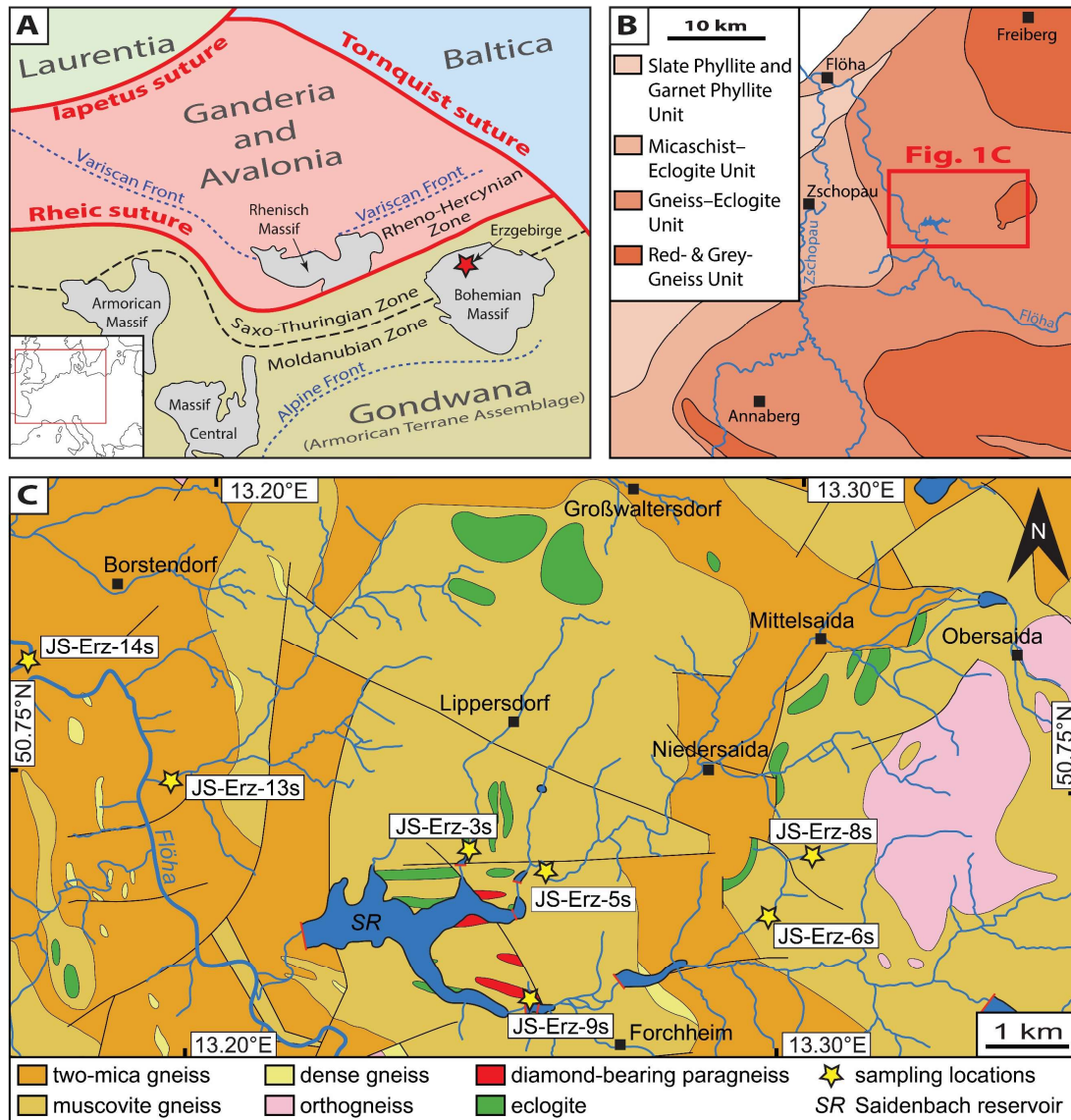


Figure 3.2-1: Maps showing the location and outline of the study area. A: Simplified map of the northern Central European Variscides after Linnemann et al. (2012) with the location of the Erzgebirge marked by a red asterisk. Inset shows Europe with the map section indicated by the red box. B: Tectonometamorphic units subdividing the Saxonian Erzgebirge after Willner et al. (2000). Red box defines the map section of the geological map in (C). C: Geological map of the area around the Saldenbach reservoir in the central Saxonian Erzgebirge with modern sand sampling locations marked by yellow asterisks after Schönig et al. (2019).

two areas containing HP rocks and one area containing UHP rocks can be distinguished (e.g., Schmädicke et al. 1995; Gose & Schmädicke 2018).

Within the HP/UHP nappe, seven modern sand samples were taken from tributaries draining the area around the Saidenbach reservoir (Figure 3.2-1C). Geographic coordinates of sampling localities are given in Schönig et al. (2019). The study area mainly comprises foliated quartzo-feldspathic HP/HT country rock gneisses (e.g., Willner et al. 1997), which host numerous lenses of eclogite (e.g., Liati & Gebauer 2009). Some eclogite lenses contain inclusions of coesite indicating an UHP origin (e.g., Massonne 2001; O'Brien and Ziemann 2008; Gose & Schmädicke 2018). In addition, at the eastern shore of the Saidenbach reservoir diamond-bearing paragneiss lenses occur (e.g., Nasdala & Massonne 2000). These differ from the country rock gneisses by the virtual absence of foliation and the homogenous appearance of mm-sized diamond-bearing garnet (e.g., Massonne 2011b). While most samples represent small catchment areas (<1 to <20 km²; Schönig et al. 2019) the most distal sample from the Flöha River (JS-Erz-14s) represents a relatively large drainage area (>500 km²) comprising not only additional lithologies from the “Gneiss–Eclogite Unit”, i.e., micaschists and ultramafic rocks, but also from the surrounding nappes of lower metamorphic grade (e.g., Willner et al. 2000; Figure 3.2-1B).

3.3 Methods

Mineral separation, sample preparation, and analytical procedures were performed at the Geosciences Center at the University of Göttingen. Sand samples were wet sieved to extract the grain-size fractions. The 63–125 µm and 250–500 µm fractions were treated with acetic acid to remove carbonate contents if present, and the heavy mineral fraction was separated by centrifugation using sodium polytungstate with a density of ~2.85 g×cm⁻³. Heavy mineral concentrates were embedded in synthetic mounts using a bonding epoxy. Mounts were grounded with silicon carbide abrasive paper and polished in five steps with Al₂O₃ abrasives in water suspension up to the finest step with a particle size of 0.05 µm.

Mineral inclusions ≥2 µm in 100 inclusion-bearing detrital garnet grains from both the 63–125 µm and 250–500 µm grain-size fraction were investigated by Raman spectroscopy. Inclusion identification follows the method described in Schönig et al. (2018a, 2018b) by using a Horiba Jobin Yvon XploRA Plus Raman spectrometer. Measurement conditions include a 532 nm laser, a 1800 l×mm⁻¹ grating, confocal hole diameter and slit of 100 µm, and a 100× long working distance objective with a numerical aperture of 0.8. Spectral Raman images of specific inclusion types were prepared by using a WITec alpha300R fiber-coupled ultra-high throughput Raman spectrometer. Conditions include a 532 nm laser, an automatically adjusted laser power of 30 mW, a 300 l×mm⁻¹ grating, a 100× long working distance objective with a numerical aperture of 0.75, a step size of 200 nm, and between 0.5 s and 2.0 s acquisition time per spectrum.

Garnet compositions of all identified coesite- and diamond-bearing garnet grains were determined at nine measurement spots per grain by electron microprobe analysis, except garnet #32 of the 250–500 µm fraction from sample JS-Erz-3s which composition was determined at a single spot. The composition of cristobalite-, kokchetavite-, and kumdykolite-bearing grains was also determined at one measurement spot per grain. Electron microprobe analysis (EMPA) was performed using a JEOL JXA

8900 RL microprobe. Before analysis, all samples were coated with carbon to ensure conductivity. Measurement conditions include an accelerating voltage of 15 kV, a beam current of 20 nA, and counting times of 15 s for silicon, magnesium, calcium, iron, and aluminum, and 30 s for titanium, chromium, and manganese. The multivariate garnet discrimination scheme after Tolosana-Delgado et al. (2018) was applied by using the prior ‘equal-M’.

Results were integrated with data from the previously studied 125–250 μm fraction making up a dataset of 2100 inclusion-bearing garnet grains (7 samples \times 3 grain-size fractions \times 100 garnet grains). Mineral inclusion assemblages and compositions of all coesite-, diamond-, cristobalite-, kokchetavite-, and kumdykolite-bearing garnet grains are given in Electronic Appendix 3e-A. Chemical compositions were compared with literature data of garnet from eclogite, diamond-bearing paragneiss, country rock gneiss, and garnet micaschist, complemented by previously unpublished garnet data from these rock types (Electronic Appendix 3e-B).

3.4 Results

3.4.1 Coesite-bearing detrital garnet

From the studied detrital garnet grains of the central Saxonian Erzgebirge, in total 93 out of 2100 inclusion-bearing grains contain coesite (Table 3.4-1). Compared to the 125–250 μm fraction (Schönig et al. 2019), the larger analyzed grain-size window reveals that coesite inclusions occur in all sampled catchments. Coesite inclusions are mainly monomineralic, whereas larger inclusions >10 μm often show partial transformation to quartz at the inclusion/host boundary. Former coesite inclusions which have been completely transformed to polycrystalline quartz are not considered, as to identify the polycrystalline character of small inclusions a detailed Raman imaging of all quartz inclusions would be required. The amount of coesite-bearing garnet grains varies between individual samples and between the analyzed grain-size fractions of each sample (Table 3.4-1). However, variability with grain size is not systematic, with coesite-bearing garnet being enriched in the 125–250 μm and 250–500 μm fractions of samples JS-Erz-3s, -13s, and -14s, and in the 63–125 μm fraction of samples JS-Erz-5s and -8s, whereas JS-Erz-6s and -9s do not show a clear trend.

Chemical compositions of the detrital coesite-bearing garnet grains show that the majority of these grains derive from rocks similar to the known UHP rocks of the area, i.e., eclogite and paragneiss lenses (Figure 3.4-1). However, the compositions of several grains in the $X_{\text{Fe}}\text{--}X_{\text{Ca}}\text{--}X_{\text{Mg}}$ ternary diagram plot outside the 95% confidence ellipsoids of the known UHP rocks. For the purpose of this study, we will focus on those garnet grains which show the highest compositional contrast to those of the UHP eclogite and paragneiss lenses.

From the coesite-bearing garnet grains of the 63–125 μm fraction, garnet grains #35 and #44 of sample JS-Erz-3s, garnet #53 of JS-Erz-8s, and garnet #92 and #151 from JS-Erz-6s show the highest compositional contrast. In the 125–250 μm fraction, this is garnet #153 from JS-Erz-13s, and in the

Table 3.4-1:
Summary of detrital UHP garnet grains from the central Saxonian Erzgebirge.

Sample number	Grain-size fraction	Screened garnets (n)	Inclusion-bearing garnets (%)	Coesite-bearing garnets (n)	Diamond-bearing garnets (n)
JS-Erz-3s	63-125 μm	318	31	5	0
JS-Erz-3s	125-250 μm	200	50	17	0
JS-Erz-3s	250-500 μm	154	65	17	0
JS-Erz-5s	63-125 μm	330	30	4	0
JS-Erz-5s	125-250 μm	209	48	1	0
JS-Erz-5s	250-500 μm	117	85	2	0
JS-Erz-6s	63-125 μm	313	32	4	0
JS-Erz-6s	125-250 μm	172	58	0	0
JS-Erz-6s	250-500 μm	118	85	3	0
JS-Erz-8s	63-125 μm	320	31	16	0
JS-Erz-8s	125-250 μm	200	50	2	0
JS-Erz-8s	250-500 μm	112	89	5	0
JS-Erz-9s	63-125 μm	419	24	1	4
JS-Erz-9s	125-250 μm	166	60	0	22
JS-Erz-9s	250-500 μm	120	83	0	27
JS-Erz-13s	63-125 μm	292	34	0	0
JS-Erz-13s	125-250 μm	160	63	4	0
JS-Erz-13s	250-500 μm	126	79	6	0
JS-Erz-14s	63-125 μm	206	49	0	0
JS-Erz-14s	125-250 μm	138	72	2	0
JS-Erz-14s	250-500 μm	108	93	4	1
Total	63-500 μm	4298	58	93	54
<i>Average</i>	<i>63-125 μm</i>	<i>314</i>	<i>33</i>	<i>4</i>	<i>1</i>
<i>Average</i>	<i>125-250 μm</i>	<i>178</i>	<i>57</i>	<i>4</i>	<i>3</i>
<i>Average</i>	<i>250-500 μm</i>	<i>122</i>	<i>83</i>	<i>5</i>	<i>4</i>

250–500 μm fraction, these are garnet grains #46 and #59 from JS-Erz-13s and garnet #30 from JS-Erz-14s (Figure 3.4-1, $X_{\text{Fe}}-X_{\text{Ca}}-X_{\text{Mg}}$ diagrams). Their compositional difference is only insufficiently displayed in the classical $X_{\text{Fe}}-X_{\text{Ca}}-X_{\text{Mn}}$ and $X_{\text{Mn}}-X_{\text{Ca}}-X_{\text{Mg}}$ ternary diagrams due to the low manganese content of all garnet grains. This, however, becomes more obvious after perturbation (i.e., centering) of the data after von Eynatten et al. (2002) where several garnet grains (#151 from sample JS-Erz-6s, 63–125 μm ; #53 from sample JS-Erz-8s, 63–125 μm ; #46 and #59 from sample JS-Erz-13s, 250–500 μm ; #30 from sample JS-Erz-14s, 250–500 μm) show clear contrast to the local eclogite and diamond-bearing paragneiss lenses (Figure Appendix 3-A 1).

To use all chemical variables determined by EMPA, the multivariate garnet discrimination scheme after Tolosana-Delgado et al. (2018) was applied. This scheme is based on a large compositional dataset of a variety of garnet-bearing rocks. It is designed for sedimentary provenance studies where the host-rock composition is not available. Solely based on garnet composition, the algorithm assigns garnet grains with a certain probability to major host-rock types. The results show that all garnet grains derive from metamorphic rocks with a probability of >99 %. Furthermore, for metamorphic garnet the algorithm

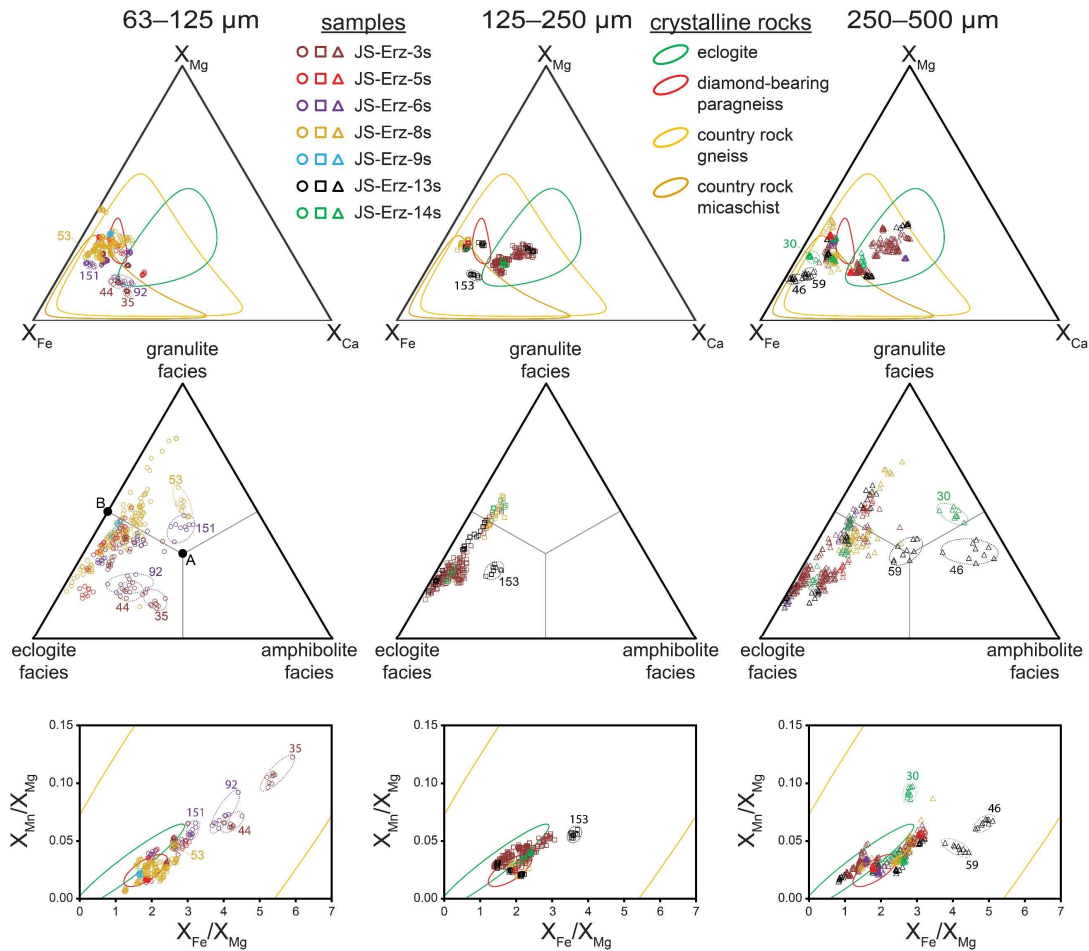


Figure 3.4-1: Chemistry of coesite-bearing detrital garnet grains. Compositions were determined at nine spots per garnet grain, except garnet #32 of the 250–500 μm fraction from sample JS-Erz-3s, and are given in molar proportions for the upper ternary plots ($X_{\text{Fe}}-X_{\text{Ca}}-X_{\text{Mg}}$) and the lower scatter plots ($X_{\text{Fe}}/X_{\text{Mg}}$ versus $X_{\text{Mn}}/X_{\text{Mg}}$). Garnet grains of the 63–125 μm fraction are labelled by a circle, those of the 125–250 μm fraction by a square, and those of the 250–500 μm fraction by a triangle. For comparison, 95 % confidence ellipsoids and ellipses of garnet compositions from local crystalline rocks are shown, whereas the confidence ellipse of micaschist covers the entire scatter plot. Location and garnet composition of local crystalline rocks are given in Electronic Appendix 3e-B. Ternary plots in the central part illustrate the probabilities of individual garnet compositions of belonging to three major metamorphic source rock groups (eclogite, amphibolite, or granulite facies) based on the multivariate discrimination scheme after Tolosana-Delgado et al. (2018). As an example, point ‘A’ and ‘B’ are given in the left diagram: ‘A’ means similar probabilities for all three major metamorphic source rock groups and ‘B’ means similar probabilities for being derived from eclogite and granulite facies sources but zero probability for an amphibolite facies source. Garnet compositions belonging to grains which show compositional contrast to diamond-bearing paragneisses and eclogites are numbered and marked by dashed envelopes. Additional ternary plots considering the X_{Mn} component (perturbed after von Eynatten et al. 2002) are shown in Figure Appendix 3-A 1.

provides probabilities of belonging to rocks of different metamorphic grade, simplified as amphibolite-, granulite-, and eclogite-facies rocks, independent from their composition. These probabilities for the single coesite-bearing garnet grains are visualized in ternary diagrams for the analyzed grain-size fractions (Figure 3.4-1). All aforementioned garnet grains showing chemical contrast to the known UHP rocks in one or more of the ternary major element diagrams yield distinctly higher probabilities of being derived from lower-pressure (i.e., amphibolite-facies) metamorphic rocks.

Resulting from these observations, and considering the elements having strong effects on the multivariate discrimination approach, the chemical contrast of the nine coesite-bearing detrital garnet grains to garnet from the known UHP rocks of the area can be more easily expressed by their higher iron to magnesium and/or manganese to magnesium ratios in a simple scatter plot (Figure 3.4-1). These garnet grains compositionally overlap with those from the country rock gneiss. As micaschist occurs in the large catchment of sample JS-Erz-14s, and garnet from this rock type show a huge compositional spread with the 95 % confidence ellipse covering the entire scatter plot, the micaschist can be also taken into consideration as a possible source for garnet #30 from the 250–500 μm fraction of this sample.

3.4.2 *Diamond-bearing detrital garnet*

Diamond-bearing detrital garnet is dominantly concentrated in sample JS-Erz-9s where 53 garnet grains containing diamond have been identified out of the 300 inclusion-bearing grains analyzed from this sample (Table 3.4-1). Their amount increases with increasing grain size. In addition, diamond-bearing garnet is not restricted to this sample taken proximal to the known diamond-bearing paragneiss lenses. Sample JS-Erz-14s, which represents the largest catchment investigated, contains also diamond-bearing garnet in the 250–500 μm fraction. It should, however, be noted that the catchment of sample JS-Erz-14s encompasses that of sample JS-Erz-9s and thus, diamond-bearing garnet in sample JS-Erz-14s not necessarily point to another diamond-bearing source. Many of the diamond inclusions are monomineralic, but often they occur in polyphase inclusions together with phyllosilicates (mainly phlogopite–biotite), rutile, graphite, and quartz. More rarely, plagioclase, apatite, and carbonates are present in these polyphase inclusions (Electronic Appendix 3e-A).

The majority of diamond-bearing detrital garnet grains shows compositional overlap with garnet from the diamond-bearing paragneiss (Figure 3.4-2). Several of them, however, are clearly distinct like garnet #66 and #123 of the 125–250 μm fraction from sample JS-Erz-9s, garnet #16 and #87 of the 250–500 μm fraction from JS-Erz-9s, and garnet #29 from sample JS-Erz-14s. These garnet grains overlap compositionally with garnet from local eclogite, except for garnet #66 of the 125–250 μm fraction from JS-Erz-9s. This is supported by comparing the manganese contents relative to iron, calcium, and magnesium in the perturbed ternary plots (Figure Appendix 3-A 2). Similar to the coesite-bearing garnet, some of the exceptional diamond-bearing garnet grains show a slightly higher probability of belonging to lower-pressure metamorphic sources (garnet grains #16 and #87 of the 250–500 μm fraction from JS-Erz-9s; Figure 3.4-2). This trend is even more pronounced for garnet #29 from JS-Erz-14s.

As for the coesite-bearing garnet, the chemical contrast of several diamond-bearing garnet grains to the known UHP rocks can be well-observed in the scatter plots (Figure 3.4-2). Garnet #66 from the 125–250 μm fraction as well as #16 and #87 of the 250–500 μm fraction from sample JS-Erz-9s, and garnet #29 from the 250–500 μm fraction of JS-Erz-14s show higher manganese to magnesium and/or iron to magnesium ratios than garnet from eclogite and diamond-bearing paragneiss lenses. In contrast, the composition of garnet #123 of the 125–250 μm fraction from JS-Erz-9s is similar to eclogitic garnet. Consequently, this garnet may be derived from an eclogite intercalated with the diamond-bearing paragneiss and cannot be assigned to the country rock gneisses.

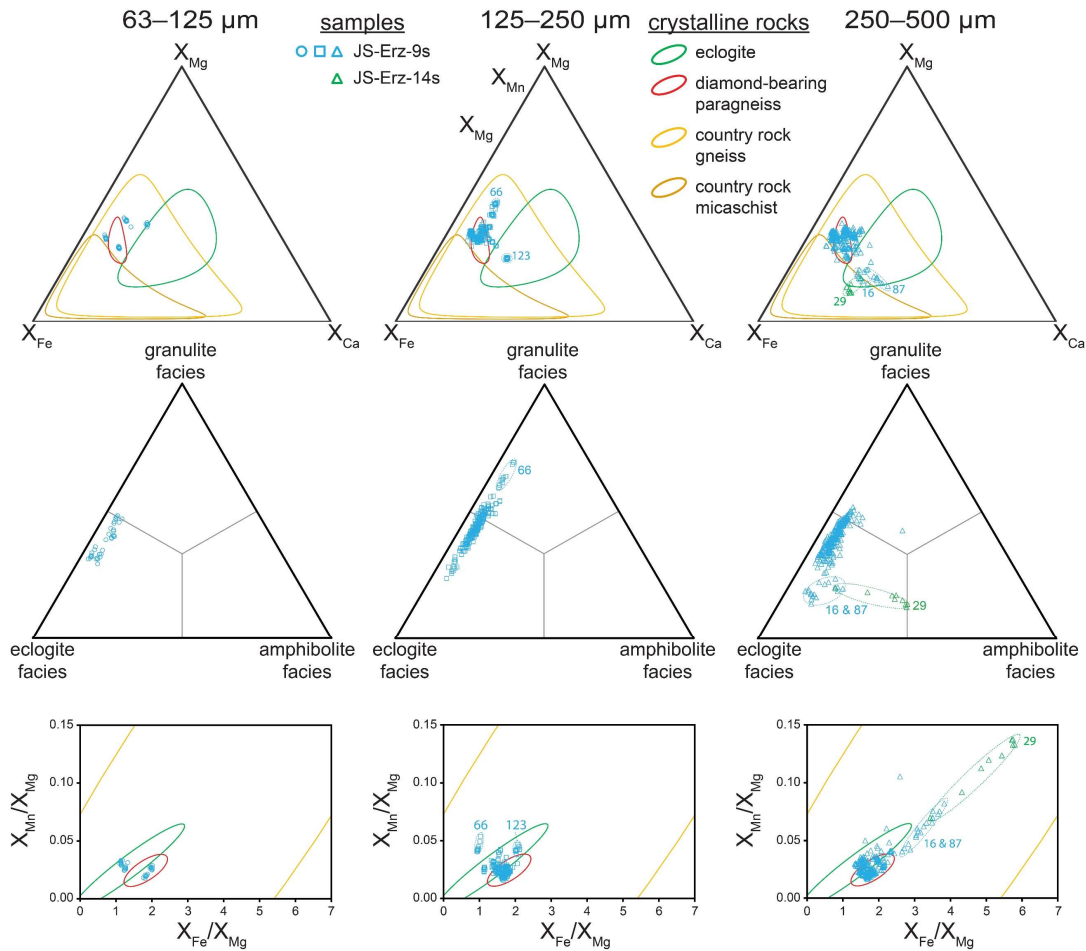


Figure 3.4-2: Chemistry of diamond-bearing detrital garnet grains. Compositions were determined at nine spots per garnet grain and are given in molar proportions for the upper ternary plots (X_{Fe} – X_{Ca} – X_{Mg}) and the lower scatter plots (X_{Fe}/X_{Mg} versus X_{Mn}/X_{Mg}). Garnet grains of the 63–125 μm fraction are labelled by a circle, those of the 125–250 μm fraction by a square, and those of the 250–500 μm fraction by a triangle. For comparison, 95 % confidence ellipsoids and ellipses of garnet compositions from local crystalline rocks are shown, whereas the confidence ellipse of micaschist covers the entire scatter plot. Location and garnet composition of local crystalline rocks are given in Electronic Appendix 3e-B. Ternary plots in the central part illustrate the probabilities of individual garnet compositions of belonging to three major metamorphic source rock groups (eclogite, amphibolite, or granulite facies) based on the multivariate discrimination scheme after Tolosana-Delgado et al. (2018). Garnet compositions belonging to grains which show compositional contrast to diamond-bearing paragneisses and eclogites are numbered and marked by dashed envelopes. Additional ternary plots considering the X_{Mn} component (perturbed after von Eynatten et al. 2002) are shown in Figure Appendix 3-A 2.

3.4.3 *Cristobalite-, kokchetavite-, and kumdykolite-bearing detrital garnet*

Apart from UHP mineral inclusions, particular attention was paid to inclusion types which have been rarely reported from UHP terranes namely cristobalite, the tetragonal SiO_2 polymorph, kokchetavite, the hexagonal KAlSi_3O_8 polymorph, and kumdykolite, the orthorhombic $\text{NaAlSi}_3\text{O}_8$ polymorph (Hwang et al. 2004, 2009).

Inclusions containing cristobalite were identified in 26 out of the 2100 inclusion-bearing detrital garnet grains (Electronic Appendix 3e-A). They occur in all analyzed samples. Although several cristobalite

inclusions primarily seem to be monomineralic, all cristobalite inclusions that were mapped by high-resolution Raman imaging show a polymineralic character. In the polyphase inclusions cristobalite occurs together with hydrous phases, mainly white mica and phlogopite–biotite but also amphibole. Besides the hydrous phases, the polyphase inclusions often contain carbonates and rarely rutile, graphite, and kokchetavite (see below). In two of the garnet grains, cristobalite inclusions co-exist with inclusions of coesite and quartz, thus, presenting three SiO₂ polymorphs in the same grain (e.g., Figure 3.4-3A). In addition, two of the diamond-bearing garnet grains contain inclusions of cristobalite (e.g., Figure 3.4-3B).

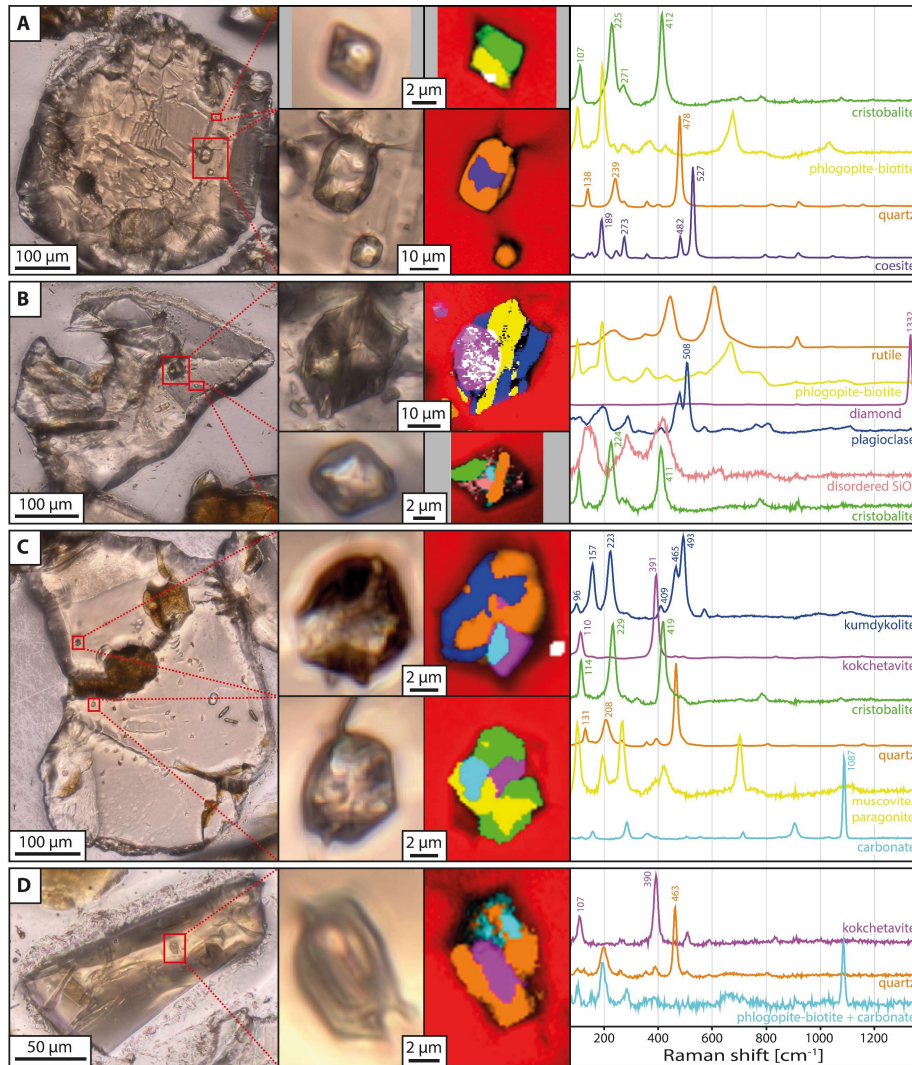


Figure 3.4-3: Photomicrographs and Raman images of cristobalite-, kokchetavite-, and kumdykolite-bearing garnet grains. A: Three SiO₂ polymorphs in garnet #123 of the 250–500 μm fraction from sample JS-Erz-3s. White pixels in Raman image correspond to an unidentified phase. B: Diamond-bearing polyphase inclusion co-existing with cristobalite- and disordered SiO₂-bearing polyphase inclusion in garnet #110 of the 125–250 μm fraction from sample JS-Erz-9s. White pixels correspond to inhomogeneity in the diamond spectra and interference with the phlogopite–biotite spectrum. Pale blue pixels belong to apatite. C: Cristobalite-, kokchetavite-, and kumdykolite-bearing polyphase inclusions in garnet #92 of the 250–500 μm fraction of sample JS-Erz-9s. White pixels in Raman image correspond to a not identified phase. D: Kokchetavite-bearing polyphase inclusion in garnet #66 of the 125–250 μm fraction from sample JS-Erz-3s.

Kokchetavite was identified in four grains, whereas three of them are from sample JS-Erz-9s and one from JS-Erz-3s. It mainly occurs in polyphase inclusions together with white mica, quartz, cristobalite, carbonates, and apatite (Figure 3.4-3C and D). In two garnet grains, kokchetavite co-exists with kumdykolite in the same inclusion (e.g., Figure 3.4-3C). Kumdykolite was also observed in another polyphase inclusion in garnet from sample JS-Erz-9s together with phlogopite–biotite, rutile, and cristobalite (Electronic Appendix 3e-A).

Although some of the cristobalite-, kokchetavite-, and kumdykolite-bearing garnet grains are within the compositional range of eclogitic garnet, the major proportion of them compositionally clearly overlap with garnet of the UHP paragneiss lenses, and all of them match with the quartzo-feldspathic country rock gneiss (Figure 3.4-4). As for the coesite- and diamond-bearing garnet, the manganese to magnesium versus iron to magnesium plot further supports this observation and shows that several cristobalite-, kokchetavite-, and kumdykolite-bearing garnet grains match only with garnet compositions of the quartzo-feldspathic country rocks.

3.5 Discussion

The newly identified sediment samples containing coesite- and diamond-bearing garnet, the heterogeneous distribution of coesite-bearing garnet regarding grain size, and the identified UHP garnet grains which compositionally differ from those of the known UHP rocks of the study area show that it is important to consider a larger detrital grain-size window to achieve thorough provenance information from mineral inclusions, especially in terms of UHP source rocks.

Most valuably, garnet compositions of at least nine coesite-bearing garnet grains from five samples (JS-Erz-3s, -6s, -8s, -13s, -14s) as well as at least four diamond-bearing garnet grains from two samples (JS-Erz-9s, -14s) are in clear contrast to garnet compositions of the known UHP rocks in the study area. Instead, they are compositionally similar to garnet from the quartzo-feldspathic country rocks. This is

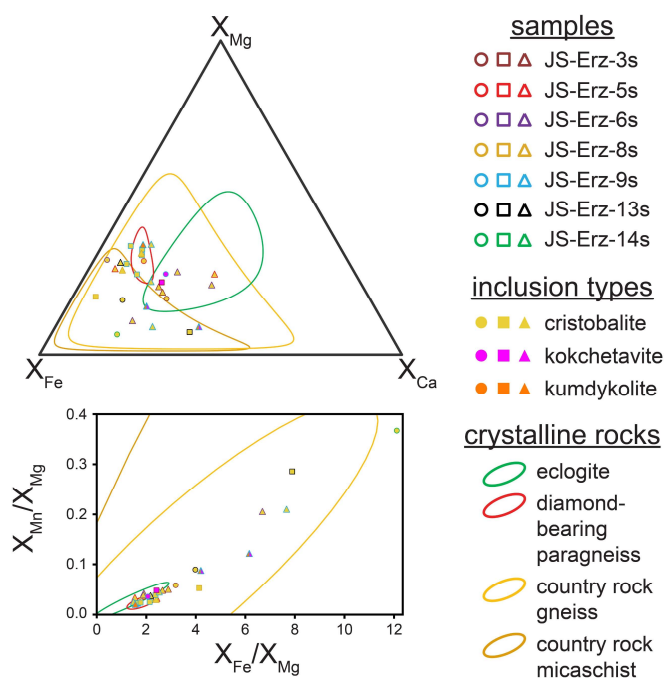


Figure 3.4-4: Chemistry of cristobalite-, kokchetavite-, and kumdykolite-bearing detrital garnet grains. Compositions were determined at one spot per garnet grain and are given in molar proportions. Garnet grains of the 63–125 μm fraction are labelled by a circle, those of the 125–250 μm fraction by a square, and those of the 250–500 μm fraction by a triangle. For comparison, 95 % confidence ellipsoids and ellipses of garnet compositions from local crystalline rocks are given. Datasets of detrital and crystalline garnet grains are given in Electronic Appendix 3e-A and Electronic Appendix 3e-B.

the most reasonable source of these garnet grains, because quartzo-feldspathic gneiss is the dominant rock type in the studied catchments. For the coesite-bearing garnet #29 and the diamond-bearing garnet #30 of the 250–500 μm fraction from sample JS-Erz-14s also micaschist may be considered as a source rock but the major element chemical composition of these garnet grains does not allow to discriminate between the country rock gneiss and micaschist.

The chemical contrast of the coesite- and diamond-bearing garnet grains derived from the country rocks is best expressed by their higher iron and/or manganese content compared to magnesium. This is typical for equilibration at lower-grade metamorphic conditions (e.g., Spear 1993; Cutts et al. 2010), though an UHP stage is confirmed by the inclusions of coesite and/or diamond. Because compositions were determined at nine spots per garnet covering large parts of the entire grain and the chemical contrast is observed for each measurement, a potential bias by zonation is ruled out.

Thus, garnet growth in both the UHP rock lenses and considerable parts of the surrounding country rocks took place at UHP metamorphic conditions during the Variscan orogeny. Furthermore, the occurrence of UHP garnet from the country rocks in six of the seven studied catchments indicates that UHP metamorphism of the country rocks is not locally restricted. Instead, rather large parts of the central Saxonian Erzgebirge appear to be affected by UHP metamorphism. The lower abundance of UHP garnet grains derived from the country rocks compared to those from the known UHP lenses is caused by the much lower modal garnet content in the country rock gneiss compared to high contents in eclogite (15–45 vol%, Gose & Schmädicke 2018) and diamond-bearing paragneiss (15–20 vol%, Nasdala & Massonne, 2001; Massonne 2003).

The UHP event in the quartzo-feldspathic country rocks was likely not recorded by geothermobarometric approaches due to major element re-equilibration of garnet by rapid diffusion during HT exhumation. Even when considering the short period available for diffusional homogenization at HP/HT conditions due to the high exhumation rates (e.g., Kröner & Willner 1998), the fast diffusion rates at temperature conditions >800 °C (as determined for the HP granulite-facies quartzo-feldspathic country rocks; Willner et al. 1997; Tichomirowa et al. 2018) facilitate garnet major element re-equilibration (e.g., Caddick et al. 2010). This agrees with relict garnet zonation patterns reported from the country rocks, which roughly follow the shape of corrosion embayments and cannot be regarded as a prograde feature. However, a precursor prograde stage is recorded by inclusions of white mica and rarely omphacite in garnet (Willner et al. 1997).

The findings of polyphase inclusions containing cristobalite, kokchetavite, and kumdykolite in garnet being mainly derived from felsic lithologies further support the subjection of country rocks to HT conditions. Such inclusions are also called “nanogranitoids” and likely represent melt droplets entrapped during garnet growth at HP/HT conditions (e.g., Cesare et al. 2009; Ferrero et al. 2016; Ferrero et al. 2019). Similar melt inclusions containing kumdykolite and/or kokchetavite have been found in the “Gneiss–Eclogite Unit” drilled in the Eger Crystalline Complex farther south (Kotková et al. 2014) and in the Granulitgebirge farther north (Borghini et al. 2020). The reason for crystal structures other than usual at HP/HT conditions, i.e., quartz, alkali feldspar, and plagioclase, is not yet fully understood. Nevertheless, it is likely related to a combination of (i) the P – T conditions within the inclusions that diverge from the external metamorphic conditions due to the different thermoelastic

properties of the melt and the garnet host, (ii) rapid crystallization and accompanied abrupt pressure changes within the inclusions, and (iii) predetermined nucleation sites given by the host garnet and the first phases crystallizing from the melt (Ferrero & Angel 2018).

In summary, garnet growth in a considerable part of the felsic country rocks took place at UHP conditions and thus precludes that contrasting geothermobarometric conditions determined for the country rocks and the UHP lenses solely result from different maximum subduction depth. Instead, we interpret the UHP terrane exposed in the central Saxonian Erzgebirge as a largely coherent slab that has been subducted to UHP conditions. However, partial amalgamation with lower-pressure metamorphic rocks during exhumation cannot be precluded; the spatial boundary to rocks unaffected by UHP metamorphism remains elusive.

During deep subduction, the mafic lithologies comprehensively equilibrated under UHP conditions and often preserve this information due to the virtual absence of hydration at HP/HT conditions during exhumation. In contrast, the presence of fluid/melt at HP/HT conditions in the felsic lithologies, as shown by the polyphase cristobalite, kokchetavite, and kumdykolite inclusions containing hydrous phases, caused a strong re-equilibration of the country rocks obscuring their precursor subjection to UHP metamorphic conditions. Based on these observations, the search for relicts of the UHP event in crystalline rock samples of the felsic country rocks in future studies may reveal important new insights regarding the structure and history of the Erzgebirge UHP terrane, given by the ability to perform pseudosection modelling. In addition, extending the search for UHP metamorphism to a wider area is crucial to reveal whether the UHP unit is even much larger in size than formerly expected, as one may speculate based on the findings of coesite and diamond inclusions in the same unit ~45 km farther south (Kotková et al. 2011).

3.6 Geodynamic implications

Felsic country rocks surrounding UHP lenses that were subducted to UHP conditions, equilibrated at these conditions, and re-equilibrated at HP/HT conditions is not a unique feature of the Erzgebirge. Instead, based on findings of UHP inclusions in re-equilibrated felsic rocks, this issue has been suggested for several UHP terranes worldwide like the Dabie Shan and Sulu in China (Okay 1993; Ye et al. 2000), the Greenland Caledonides (Gilotti & Ravná 2002), and the Scandinavian Caledonides (Klonowska et al. 2017). Due to the presence of coesite inclusions in country rock garnet, it can be expected that coesite was also present as a matrix phase at UHP conditions. Despite the increasing solubility of OH in coesite with increasing pressure (Mosenfelder 2000), the preservation of coesite as monomineralic inclusions call for low OH contents, agreeing with the typical dry nature of UHP terranes (Hermann & Rubatto 2014). Thus, reaction kinetics of the coesite-to-quartz transformation are strongly reduced during exhumation (Lathe et al. 2005) and under extremely dry conditions, coesite may even survive as a matrix phase (Liou & Zhang 1996; Liu et al. 2017). Whatever process triggers the initial exhumation, the presence of fluid/melt during re-equilibration at HP/HT conditions, most likely being related to phengite breakdown (e.g., Lang & Gilotti 2015), facilitates the coesite-to-quartz transformation within the large volumes of felsic country rocks (Mosenfelder et al. 2005). This transformation is accompanied by a strong density decrease of the SiO₂ component of ~10 %. Thus, the

resulting highly buoyant felsic country rocks can passively transport the unaffected or minor re-equilibrated UHP lenses to lower crustal levels. The high buoyancy may also explain the high exhumation rates reported from UHP terranes like the Erzgebirge (Kröner & Willner 1998; Massonne et al. 2007; Stöckhert et al. 2009).

3.7 Conclusions

The widespread occurrence of coesite and diamond inclusions in detrital garnet from the central Saxonian Erzgebirge as well as coesite- and diamond-bearing garnet grains resembling the chemical composition of garnet from the country rocks demonstrate that UHP metamorphism has not only affected the known metamafic and metasedimentary lenses but also the felsic country rocks. Thus, the HP/UHP terrane of the central Erzgebirge is interpreted as a largely coherent slab subducted to UHP metamorphic conditions during the Variscan orogeny. In contrast to the UHP lenses, the country rocks strongly re-equilibrated at HP/HT conditions during exhumation. This re-equilibration is supported by nanogranitoid inclusions in garnet containing cristobalite, kokchetavite, and kumdykolite. These findings contradict the earlier view of solely different maximum subduction depth to explain contrasting geothermobarometric conditions between very closely related HP country rocks and UHP lenses. Additionally, coesite was present as a matrix phase within the country rocks prior to re-equilibration at HP/HT conditions. This has considerable implications for the understanding of buoyancy development during the subduction and exhumation of UHP terranes and consequently, the rate of exhumation.

Acknowledgements

This work was supported by the German Research Foundation by DFG grant EY 23/27-1 to H. von Eynatten and G. Meinhold. We thank J.E. Dunkl, I. Dunkl, and A. Grebe for their support in sample preparation, and A. Kronz for giving access to the electron microprobe. Careful editorial handling by Tim Johnson is gratefully acknowledged.

Reply to comment on “Deep subduction of felsic rocks hosting UHP lenses in the central Saxonian Erzgebirge: Implications for UHP terrane exhumation”

Jan Schönig¹, Hilmar von Eynatten¹, Guido Meinhold^{1,2}, N. Keno Lünsdorf¹,
Arne P. Willner³, and Bernhard Schulz⁴

¹*Geosciences Center Göttingen, University of Göttingen, Germany*

²*School of Geography, Geology and the Environment, Keele University, United Kingdom*

³*Institute of Geology, Mineralogy and Geophysics, University of Bochum, Germany*

⁴*Institute for Mineralogy, TU Bergakademie Freiberg, Germany*

published 22nd January 2021

Gondwana Research 98, 320–323

<https://doi.org/10.1016/j.gr.2020.12.029>

3.8 Reply to comment by Massonne (2021)

We thank H.-J. Massonne (2021) for his comment on our paper published in *Gondwana Research* (Schönig et al. 2020). Our conclusion that a substantial part of felsic country rocks surrounding the well-known lenses of ultrahigh-pressure (UHP) rocks in the Saxonian Erzgebirge also underwent UHP metamorphism justifies a critical examination, in particular when taking the controversial views on this topic into account. Notably, H.-J. Massonne argues from a single perspective considering the references cited in his comment; only three out of 18 (including the paper commented on and a geological map) are not authored or co-authored by himself. We appreciate the opportunity to underline the robustness of our results and conclusions.

Before replying to the individual points of criticism, we think some rock terminology should be clarified for the readership. We termed the diamond-bearing lenses at the eastern shore of the Saidenbach reservoir (fig. 1 in Schönig et al. 2020, here Figure 3.2-1) ‘diamond-bearing paragneiss’ due to the origination from a sedimentary protolith (e.g., Massonne & Tu 2007) and because it is frequently used in the literature. The term ‘diamondiferous gneiss’ was also used by H.-J. Massonne (e.g., fig. 1 in Massonne & Czambor 2007), even after his interpretation that this rock type is of magmatic origin (Massonne 2003). Anyway, the terms ‘diamondiferous quartzofeldspathic rock’ and ‘saidenbachite’ used by H.-J. Massonne designate the same rock type we called ‘diamond-bearing paragneiss’; in the following called ‘diamond-bearing rock’. The diamond-bearing rock lenses and coesite-bearing eclogite lenses (the known UHP rocks) are surrounded by various felsic gneisses. Depending on the classification used, one may subdivide them into different assemblages (Willner et al. 1997) or use different names as applied by H.-J. Massonne. All these subtypes have previously been interpreted as high-pressure (HP) to medium-pressure (MP) rocks hosting the UHP lenses (Willner et al. 1997), and thus we call them ‘country rock gneiss’.

The first major point of criticism by H.-J. Massonne relates to the source of the detrital UHP garnet grains. He quotes that most coesite- and diamond-bearing garnet grains derive from known UHP rocks and those which do fit to the reported garnet compositions of country rock gneiss, may also be derived from other UHP lenses.

Indeed, the chemical composition of most UHP detrital garnet grains matches or is close to the composition of garnet from previously reported coesite-bearing eclogite and diamond-bearing rock. However, our paper focuses on the nine coesite- and four diamond-bearing grains with compositions clearly deviating from garnet reported from the known UHP rocks of the investigated area (Figure 3.8-1).

H.-J. Massonne suggests that the four diamond-bearing grains may derive from the known diamond-bearing rock and not from the surrounding country rock gneiss, because our study (i) did not consider garnet zoning, (ii) did not consider some extreme garnet compositions which have not been published, and (iii) did not consider unpublished data of a finer grained diamond-bearing rock type (it remains unclear in the comment if such data exist or not).

With regard to zoning, fig. 16 in the field trip guide of Massonne (2011b) is cited to exemplify the compositional range of garnet in the diamond-bearing rock which was claimed to not be considered in our study. We already considered the corresponding data (table 6 in Massonne 2011b) for compositions of garnet core, mantle, and rim (Electronic Appendix 3e-B). Accordingly, the data matches with the 95 % confidence regions shown in figs. 2, 3, and 5 of Schönig et al. (2020, here Figure 3.4-1, Figure 3.4-2, and Figure 3.4-4). This is highlighted in Figure 3.8-1A where the zoned garnet composition of Massonne (2011b) is marked. Note that 95 % confidence is a conservative approach, which already takes considerable variation into account. Neither we nor the readership can evaluate unpublished data which may or may not point in another direction.

In addition to the considered zoning for the diamond-bearing rock garnet, the composition of each of the detrital garnet grains has been determined at nine spots

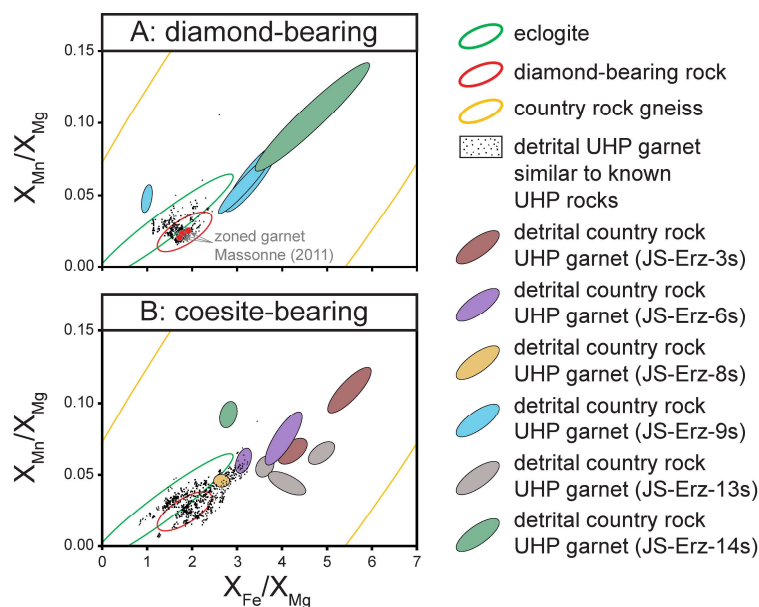


Figure 3.8-1: Composition of (A) diamond- and (B) coesite-bearing detrital garnet summarized after Schönig et al. (2020). Compositions similar to the known eclogite and diamond-bearing rock lenses are shown as small black dots and compositions solely matching with country rock gneiss as colored envelopes (nine spots per grain analyzed). See also figures 2 and 3 in Schönig et al. (2020).

per grain (one at the center, four at the mantle, and four at the rim) to avoid any zonation bias. Although we considered all data available for the compositional range, all nine spots analyzed for each of the four diamond-bearing detrital grains do not match with garnet from the known diamond-bearing rock. In contrast, their composition matches well with garnet of the country rock gneiss.

Without presenting any further reasons than discussed above, H.-J. Massonne mentioned that coesite-bearing grains in samples JS-Erz-3s, -5s, -6s, and -8s may also be derived from other diamond-bearing rock lenses or coesite-bearing eclogite. We agree on this point for most of the coesite-bearing grains but some clearly differ and solely match with country rocks (Figure 3.8-1B). Additionally, samples JS-Erz-13s and -14s also contain coesite-bearing garnet with compositions solely matching with the country rock gneiss.

The second major point of criticism encompasses that (i) the garnet content of country rock gneiss is much lower compared to the known UHP rocks, (ii) the garnet size is much smaller at $\sim 100\ \mu\text{m}$, and (iii) country rock garnet should thus be under-represented in our dataset by considering a grain-size range of $63\text{--}500\ \mu\text{m}$.

First of all, the garnet size in the country rock gneiss is often larger than the $\sim 100\ \mu\text{m}$ mentioned. For the country rock gneiss surrounding the diamond-bearing lenses this is evidenced by fig. 3 in Willner et al. (1997) and sample JS-Erz-11h taken close to this locality (Figure 3.8-2, N 50.72694° , E 13.24681°). Generally, for country rock gneiss of the investigated area garnet crystal sizes up to several millimeters are reported (Willner et al. 1997). Secondly, although the garnet content of the country rock gneiss is much lower, the volume is much larger (fig. 1 in Schönig et al. 2020, here Figure 3.2-1), and therefore the proportional contribution of country rock garnet is expected to be higher than the ratio of the modal contents (i.e., country rock vs. UHP lenses), for most of the catchments.

We agree, however, that detrital country rock garnet is depleted relative to garnet from eclogite and diamond-bearing rock lenses when compared to the bedrock proportions in the catchments. Nevertheless, our samples contain detrital garnet from the country rock gneiss and garnet composition implies that nine coesite-bearing grains as well as four diamond-bearing grains derive from those country rocks. Considering the depletion, this means that UHP metamorphism of the country rocks might be even more frequent than expected from the amount of detrital UHP garnet from the country rocks.

The third major point of criticism relates to the geodynamic models of exhumation. First of all, we do not propose a specific exhumation model in our paper. Many different exhumation mechanisms and models for continental UHP terranes have been

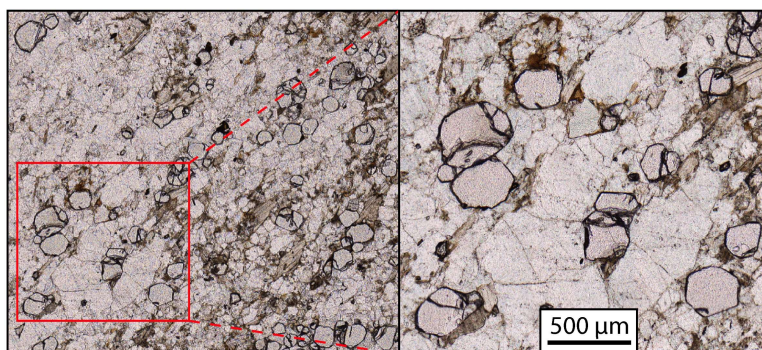


Figure 3.8-2: Photomicrograph of banded country rock gneiss sample JS-Erz-11h taken close to a diamond-bearing rock lens (N 50.72694° , E 13.24681°).

proposed (e.g., Zhang & Wang 2020). Favoring a specific scenario for the Saxonian Erzgebirge is beyond the scope of our paper. Instead, we place well-considered constraints regarding, e.g., the size of the rock body affected by UHP metamorphism and the lithologies involved, although we cannot exactly delimit it. We thus vehemently refuse the implied interpretation of our results by Massonne (2021), as illustrated in his figure 2C along with the insinuation that it is done “*on the basis of the description by Schönig et al. (2020)*”. Such a statement is incorrect and misleading.

Based on our results, we state that (i) the known UHP lenses, as well as substantial parts of the country rocks, experienced UHP metamorphism, (ii) this points to subduction to UHP conditions as a largely coherent slab, and (iii) consequently coesite can be expected to have been present as a matrix phase in the voluminous felsic country rocks. This in turn has significant implications for the buoyancy development during exhumation when coesite transforms to quartz. Many factors contribute to the exhumation velocity, some may be more important than buoyancy, but whatever exhumation mechanism is considered, the effective pressure gradient in the subduction/exhumation channel ($\partial P/\partial x$) is among the controlling factors (Zhang & Wang 2020):

$$\frac{\partial P}{\partial x} = (\rho_{Mantle} - \rho_{Channel})g \sin\theta$$

where ρ_{Mantle} is the density of the surrounding mantle, $\rho_{Channel}$ is the density of rocks in the subduction/exhumation channel, g is the gravitational acceleration, and θ is the subduction angle. Thus, decreasing the density of the voluminous felsic rocks in the subduction channel at the coesite-to-quartz transition increases the effective pressure gradient and consequently exhumation velocities in all models.

H.-J. Massonne defends his model of a magmatic ascent of the diamond-bearing rock lenses through the mantle wedge by referring to the extreme exhumation rates suggested by Stöckhert et al. (2009). Based on this, H.-J. Massonne rules out any other exhumation model. Stöckhert et al. (2009) observed partially healed fractures originating from polyphase inclusions in garnet of the diamond-bearing rock. The inclusions contain diamond/graphite, phlogopite, quartz, phengite, and minor amounts of other minerals. The authors suggest that carbonaceous fluids were entrapped in the stability field of diamond and that brittle failure (decrepitation) occurred at UHP conditions leading to a drop in inclusion pressure and crystallization of silicates at 750 °C and <2.5 GPa. Based on this assumption, exhumation rates must have been fast enough to overcome the garnet dislocation creep at the high temperatures and build up the inclusion overpressures required for decrepitation. Because many factors are unknown like the equation of state parameters of the supercritical fluid, the evolution of fluid composition, density, and solubility, the inclusion shape, the variability of inclusion assemblages, and the possibility of accidental trapping of fluid plus crystals, Stöckhert et al. (2009) use a conservative lower bound for the strain rates at decrepitation. By this inspiring approach, the authors conclude that exhumation rates of 100 m/a are necessary.

Such extreme rates require that the assumptions of decrepitation conditions of ~750 °C at UHP as well as silicate crystallization after decrepitation are fulfilled. This is highly speculative: (i) the inclusion assemblages are not indicative for a specific temperature. Considering 200 °C less at decrepitation results in a change of the strain rate and thus the estimated exhumation rate of approximately four orders

of magnitude (fig. 6 in Stöckhert et al. 2009); (ii) it is unclear whether the silicates crystallized after or prior to decrepitation. It cannot be ruled out that changes of the fluid properties and inclusion pressure due to the early precipitation of carbonaceous phases enabled also silicate crystallization at an early stage without decrepitation; (iii) there is no evidence that decrepitation occurred at UHP conditions. Alternatively, the inclusion strains may elastically re-equilibrated during decompression and decrepitation resulted from later cooling at lower pressure, which agrees with Raman shifts of the diamond main band to higher frequencies observed by Schönig et al. (2019). Based on the high uncertainties, the extreme exhumation rates estimated by Stöckhert et al. (2009) do not prove a magmatic ascent of the diamond-bearing rock lenses.

Massonne et al. (2007) estimated an exhumation velocity >10 cm/a based on SHRIMP U–Pb dating. However, the reported ages of 337.0 ± 2.7 Ma for zircon cores, 336.8 ± 2.8 Ma for the diamond-bearing mantles, and 330.2 ± 5.8 Ma for the rims only allow to estimate minimum exhumation velocities from core-mantle to rim, if at all. The high uncertainty is highlighted by figure 14 in Massonne et al. (2007; note the use of 1σ -errors only). Mean square weighted deviation and probability of concordance are not given. In addition, zircon cores and mantles have later been dated by LASS-ICP-MS at 341.8 ± 2.0 and 340.1 ± 1.8 Ma, respectively (Kylander-Clark et al. 2013).

Considering also earlier works (Kröner & Willner 1998; Werner & Lippolt 2000), Kylander-Clark et al. (2012) concluded that the chronologic data of the Saxonian Erzgebirge does not define a coherent picture and roughly supposed <7 Ma for the exhumation. Hence, the current data referring to exhumation velocities of UHP rocks in the Erzgebirge are insufficient and partly contradictory. Velocities in the order of plate tectonic rates seem more likely than extreme velocities of up to 100 m/a. It should be mentioned that exhumation rates in the order of plate tectonic rates were also considered for HP rocks of the same age (~ 340 Ma) all over the Central European Variscides (e.g., Willner et al. 2002, and references therein).

In conclusion, all points of criticism raised by H.-J. Massonne on our paper do not hold out against objective and detailed examination. Based on the presented data compared to the available literature data, our conclusion that a substantial part of country rocks underwent UHP metamorphism is the most likely interpretation. A depletion of detrital garnet derived from the country rock gneiss in our samples does not affect this conclusion. The model of a magmatic ascent of the diamond-bearing rock lenses favored by H.-J. Massonne is very speculative, in particular when considering the high uncertainties of exhumation rates which the model is based on. Thus, it remains unclear how this should disprove our conclusion of a largely coherent slab subducted to UHP conditions.

Acknowledgements

This work was supported by the German Research Foundation [DFG grant EY 23/27-1].

Garnet sand reveals rock recycling processes in the youngest exhumed high- and ultrahigh-pressure terrane on Earth

Suzanne L. Baldwin¹, Jan Schönig², Joseph P. Gonzalez¹,
Hugh Davies³, and Hilmar von Eynatten²

¹*Department of Earth and Environmental Sciences, Syracuse University, USA*

²*Geosciences Center Göttingen, University of Göttingen, Germany*

³*Geology Department, University of Papua New Guinea, Papua New Guinea*

published 11th January 2021

Proceedings of the National Academy of Sciences 118, e2017231118

<https://doi.org/10.1073/pnas.2017231118>

Rock recycling within the forearcs of subduction zones involves subduction of sediments and hydrated lithosphere into the upper mantle, exhumation of rocks to the surface, and erosion to form new sediment. The compositions of, and inclusions within detrital minerals revealed by electron microprobe analysis and Raman spectroscopy preserve petrogenetic clues that can be related to transit through the rock cycle. We report the discovery of the ultrahigh-pressure (UHP) indicator mineral coesite as inclusions in detrital garnet from a modern placer deposit in the actively exhuming Late Miocene–Recent high- and ultrahigh-pressure ((U)HP) metamorphic terrane of eastern Papua New Guinea. Garnet compositions indicate the coesite-bearing detrital garnets are sourced from felsic protoliths. Carbonate, graphite, and CO₂ inclusions also provide observational constraints for geochemical cycling of carbon and volatiles during subduction. Additional discoveries include polyphase inclusions of metastable polymorphs of SiO₂ (cristobalite) and K-feldspar (kokchetavite) that we interpret as rapidly cooled former melt inclusions. Application of elastic thermobarometry on coexisting quartz and zircon inclusions in six detrital garnets indicates elastic equilibration during exhumation at granulite and amphibolite facies conditions. The garnet placer deposit preserves a record of the complete rock cycle, operative on <10 Ma geologic timescales, including subduction of sedimentary protoliths to UHP conditions, rapid exhumation, surface uplift, and erosion. Detrital garnet geochemistry and inclusion suites from both modern sediments and stratigraphic sections can be used to decipher the petrologic evolution of plate boundary zones and reveal recycling processes throughout Earth's history.

4.1 Introduction

Throughout Earth's history, igneous, metamorphic, and sedimentary rocks have been recycled from the surface to upper mantle depths and subsequently returned as a result of tectonic and sedimentary processes operating within and at the surface of lithospheric plates. In active plate boundary zones, where most igneous and metamorphic rocks form, the rock cycle involves localized lithospheric

deformation, which exhumes rocks to the Earth's surface. When rock exhumation occurs at plate tectonic rates ($\text{cm}\times\text{a}^{-1}$; Rubatto & Hermann 2001; Baldwin et al. 2004), high- and ultrahigh-pressure ((U)HP) metamorphic rocks containing hydrous mineral assemblages, trapped volatiles, and atmospheric gases (Baldwin & Das 2015; Bebout & Penniston-Dorland 2016) may be returned from upper mantle depths to the surface in the forearcs of subduction zones. Mechanically strong host minerals, such as garnet, zircon, and clinopyroxene, and their nondecrepitated mineral inclusions have played a key role in the identification of (U)HP metamorphic rocks and conditions of metamorphism (Ferrero & Angel 2018). After rocks are exposed at the surface, weathering processes erode (U)HP rocks to create sediment that is transported from source to sink, retaining evidence of metamorphic conditions in the compositions, and inclusions trapped within detrital mineral grains (Schönig et al. 2018a, 2019). Garnet is a common mineral in metamorphic and igneous rocks of the upper mantle and crust that can survive transit through the rock cycle (Baxter et al. 2013). Garnet is stable over a large range of pressure–temperature (P – T) conditions in many bulk rock compositions; commonly entraps and preserves (meta-)stable mineral inclusions; and is relatively resistant to chemical alteration during erosion, transport, and deposition. As a result, detrital garnet compositions (Mange & Morton 2007) and their mineral inclusions (Schönig et al. 2018b), identified in the heavy-mineral fractions of sediments and sedimentary rocks, provide constraints on the conditions of garnet growth in source rocks.

The youngest known (U)HP terrane on Earth is actively exhuming in eastern Papua New Guinea within the obliquely convergent Australian (AUS)–Pacific (PAC) plate boundary zone (Baldwin et al. 2012; Figure 4.1-1). The Papuan (U)HP terrane formed when a rifted fragment of the Cretaceous AUS continental margin was subducted at the Aure–Pocklington trough (Zirakparvar et al. 2013; Webb et al. 2014). In the D'Entrecasteaux Islands of the Woodlark Rift, Late Miocene–Recent metamorphic core complexes, composed of (U)HP metamorphic rocks (i.e., lower plate), have been exhumed to the surface at $\text{cm}\times\text{a}^{-1}$ rates from beneath upper plate rocks composed of oceanic lithosphere (Baldwin et al. 1993; Little et al. 2007). Direct evidence for ultrahigh-pressure (UHP) metamorphism has only been identified in one sample at one outcrop in the D'Entrecasteaux Islands (Baldwin et al. 2008). The coesite eclogite at this locality is interpreted to have formed ~ 8 Ma when a partial mantle melt intruded subducted continental lithosphere at UHP conditions (Zirakparvar et al. 2011, 2013; Baldwin & Das 2015). Since the discovery of coesite eclogite, attempts to find additional mineral evidence for UHP metamorphism from outcrop samples, including from felsic lithologies, have been unsuccessful. However, intermediate-depth earthquakes in proximity to exhumed coesite eclogite indicate active seismicity in the tectonic setting where UHP exhumation is ongoing (Abers et al. 2016).

Goodenough Island, the westernmost metamorphic core complex within the subaerial portion of the Woodlark Rift, forms a prominent topographic dome where garnet-bearing eclogite and felsic to intermediate gneisses comprise a core zone and carapace shear zones (Figure 4.1-1). Basement rocks include eclogite, granulite, and amphibolite with abundant evidence for in situ partial melts and granodioritic intrusions (Figure 4.1-1 and Figure 4.1-2). The dome is flanked by seismically active normal faults (Abers et al. 2016). Pliocene–Pleistocene surface uplift (Miller et al. 2012) and emergence of the islands above sea level led to erosion of the (U)HP terrane and deposition of Holocene colluvium and alluvium including the sampled garnet placer deposit, formed from erosion of garnet-bearing

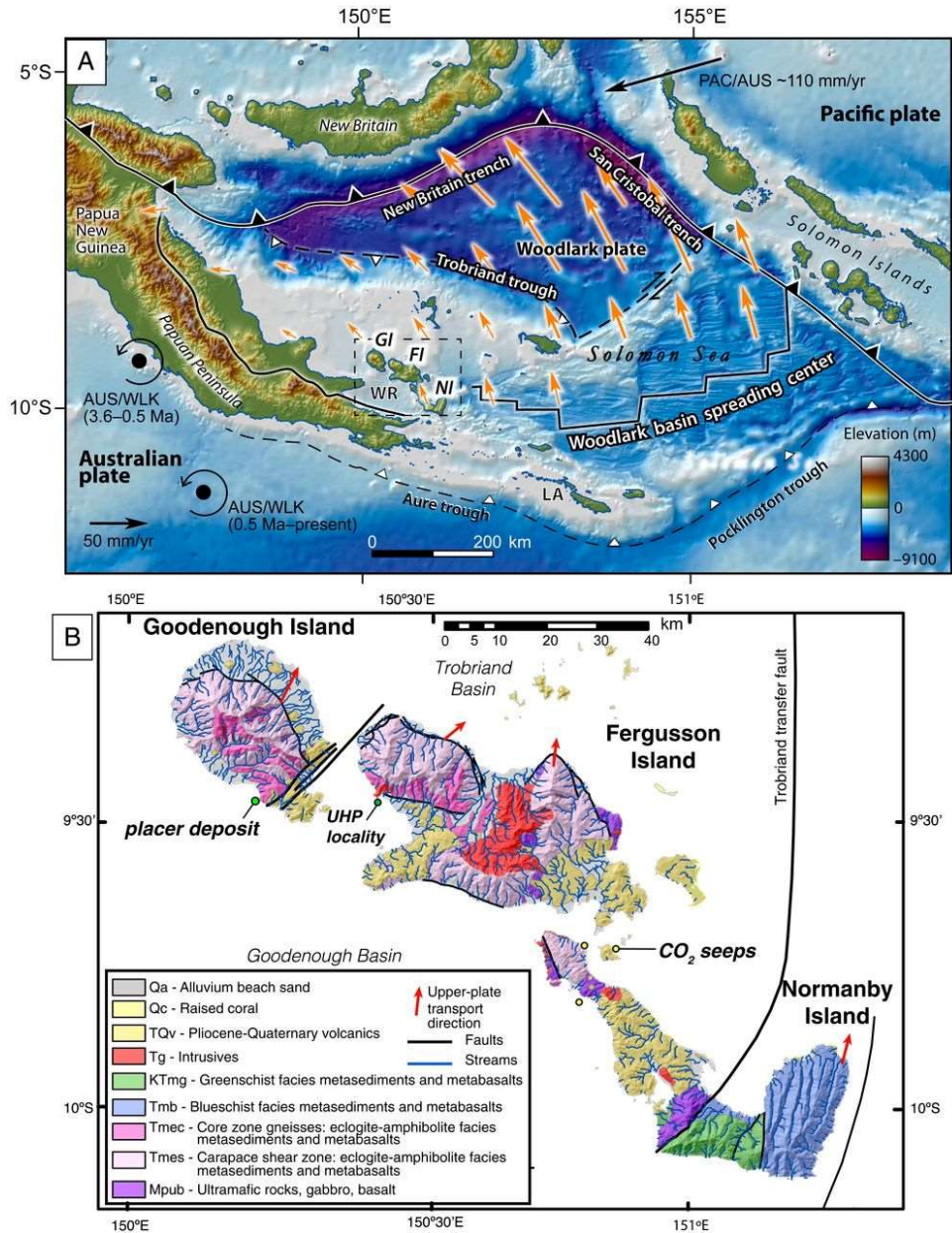


Figure 4.1-1: (A) Tectonic and geologic setting of the (U)HP terrane in the Woodlark Rift of eastern Papua New Guinea. The (U)HP terrane is located within the larger obliquely convergent AUS–PAC plate boundary zone and formed when an AUS-derived continental fragment was subducted northward beneath oceanic lithosphere at the Aure–Pocklington trough. (U)HP rocks are found in the lower plates of metamorphic core complexes in the D’Entrecasteaux Islands (Goodenough Island [GI], Fergusson Island [FI], and Normanby Island [NI]), within the Woodlark Rift (WR). Low-grade metamorphic rocks of the accretionary wedge are exposed in the Louisiade Archipelago (LA). Global Positioning System model vectors (orange arrows) are shown for present-day Woodlark (WLK) plate motion relative to the AUS plate; AUS–WLK rotation poles for 3.6 to 0.5 Ma and 0.5 Ma to present are also indicated (Wallace et al. 2004). Modified from Miller et al. 2012. (B) Geologic map of the D’Entrecasteaux Islands with the garnet placer deposit, coesite eclogite (UHP), and active CO₂ seep localities indicated. Base maps were made with GeoMapApp (Ryan et al. 2009).

protoliths (Figure 4.1-1B and Figure 4.1-2E). Electron microprobe analysis and Raman spectroscopy of detrital garnets revealed evidence for rock recycling processes in the youngest exhumed (U)HP

terrane on Earth where exhumation occurred during the same subduction cycle that produced the (U)HP rocks.

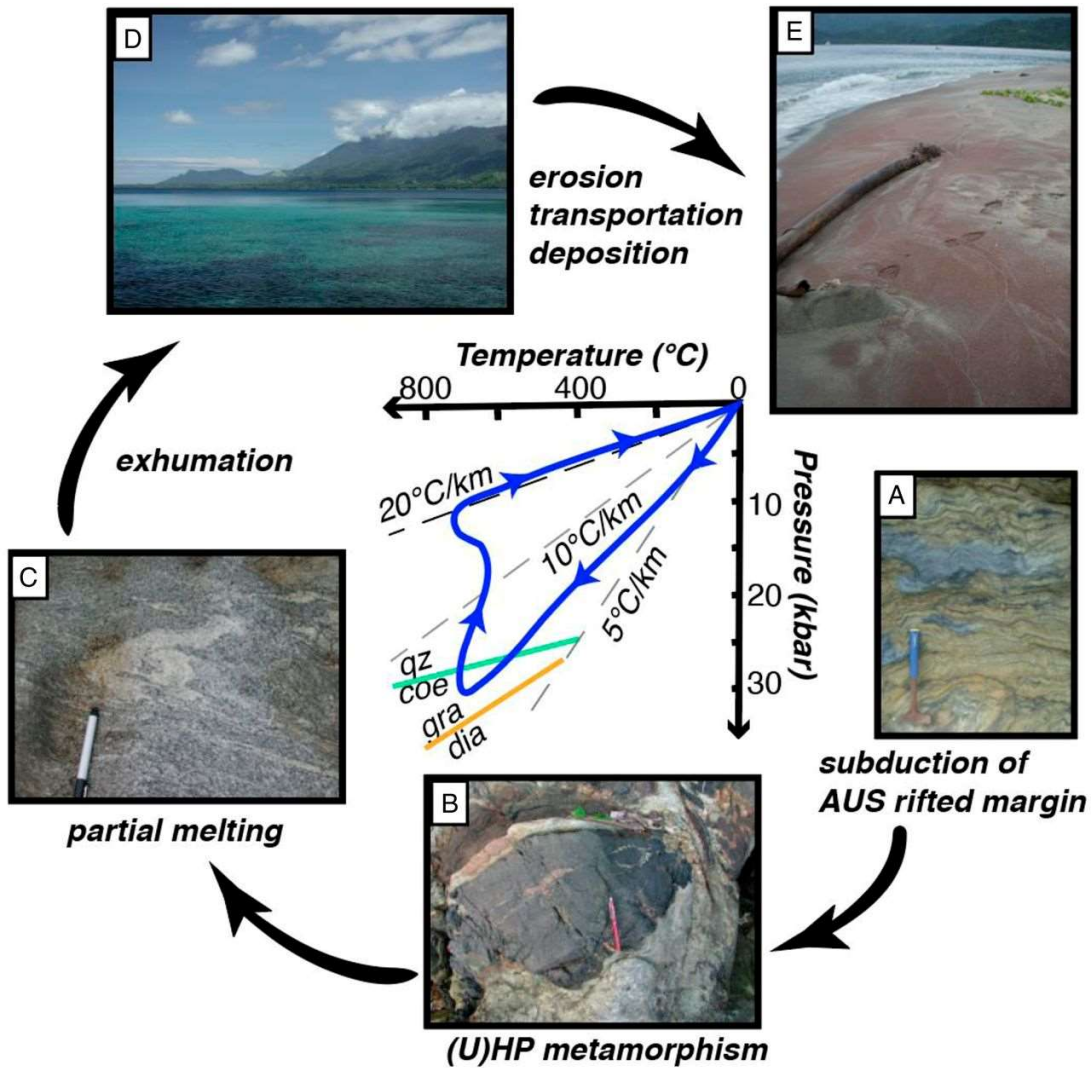


Figure 4.1-2: Schematic figure illustrating rock (re-)cycling in the eastern Papuan (U)HP terrane where rifting of a subduction complex has exhumed (U)HP rocks since ~8 Ma (i.e., negligible petrologic lag times). (A) Early–Middle Miocene northward subduction of an AUS continental fragment formed low-grade metamorphic rocks of the accretionary wedge [Calvados Schist, Louisiade archipelago (Webb et al. 2014)]. (B) (U)HP metamorphism of basalts and felsic protoliths formed eclogite in quartzofeldspathic host gneisses now exposed in the core zone, including in the catchment areas nearby the placer deposit locality. Coesite eclogite (UHP locality in Figure 4.1-1B) formed at ~8 Ma, whereas eclogite in the catchment area (in the photo) is as young as 2 Ma (Monteleone et al. 2007; Zirakparvar et al. 2014). (C) Partial melting of gneisses in the garnet placer catchment area (in the photo), intrusion of igneous rocks, and volcanism have occurred since ~4 Ma (Baldwin et al. 1993; Gordon et al. 2012). (D) Surface uplift to form the D'Entrecasteaux Islands since the Quaternary (Miller et al. 2012). (E) Rock erosion, transportation, and deposition of sediment to form a garnet-rich placer deposit. Schematic $P-T$ path (details are presented in Figure 4.2-3) illustrates conditions associated with metamorphic, igneous, and sedimentary rock formation and recycling in the Papuan (U)HP terrane. Geothermal gradients and reaction curves indicated (quartz [qz], coesite [coe], graphite [gra], and diamond [dia]).

4.2 Results

The placer deposit contains (sub-)angular detrital garnet grains derived from a proximal source. Electron microprobe analyses of garnet from outcrop samples (compiled from the literature and this study) and detrital garnet (this study) allow a comparison of garnet compositions to assess potential sediment sources (Figure 4.2-1, Electronic Appendix 4e-A, and Electronic Appendix 4e-C). Ternary plots of garnet compositions (Fe+Mn, Ca, and Mg end-members) for crystalline rocks (n = 881) compared with detrital garnet compositions (n = 716) indicate that the detrital garnet grains cover the entire compositional range of potential crystalline source rocks.

Sixty-two percent of the detrital garnet grains investigated contained mineral inclusions. These include 83 garnets from the 63- to 125- μm -sized fraction, 117 garnets from the 125- to 200- μm -sized fraction, and 154 garnets from the >200- μm -sized fraction, with the largest grain having a long axis of $\sim 600\ \mu\text{m}$ (Electronic Appendix 4e-A). Detrital garnet mineral inclusions ($\geq 2\ \mu\text{m}$) identified using Raman spectrometry include omphacite, kyanite, epidote, oxides (SiO_2 polymorphs, rutile), feldspars (alkali feldspar, plagioclase feldspar, kokchetavite), phyllosilicates (paragonite–muscovite series, phlogopite–biotite, chamosite–clinochlore, and pyrophyllite), and accessory phases (apatite, zircon, titanite) (Figure 4.2-2 and Electronic Appendix 4e-A). Rutile is the most abundant mineral inclusion, occurring in 73 % of the inclusion-bearing detrital garnet grains studied. At least 2 % of inclusion-bearing detrital garnets are inferred to be sourced from mafic eclogite as indicated by omphacite inclusions in high-Mg garnets (Figure 4.2-1).

Three SiO_2 polymorphs (coesite, cristobalite, and quartz) were identified as inclusions in detrital garnets (Figure 4.2-2). Quartz is the most abundant SiO_2 inclusion, occurring in 30 % of the inclusion-bearing

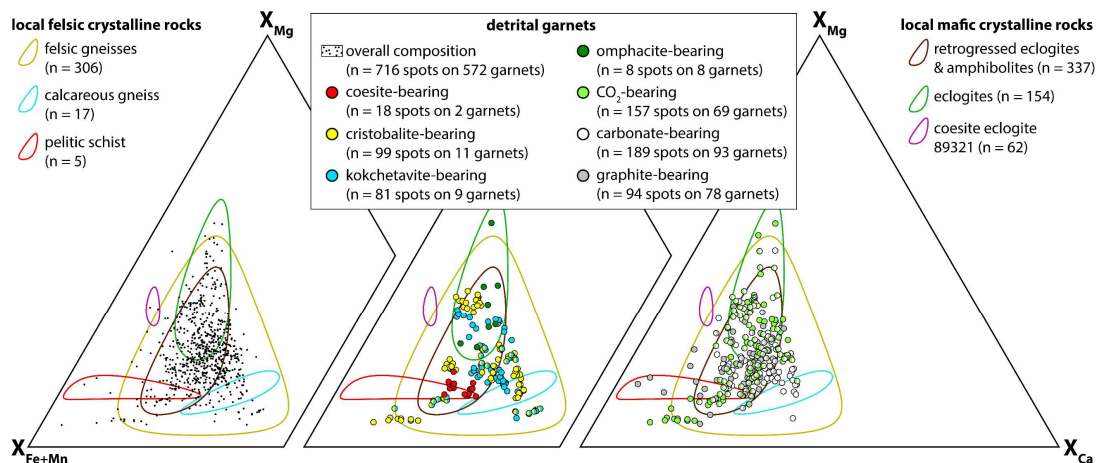


Figure 4.2-1: Ternary plots of garnet compositions (molar proportions of Fe+Mn, Ca, and Mg) for metamorphic rocks of the lower plates of the D'Entrecasteaux Islands core complexes, as compared with detrital garnet compositions from the placer deposit. Garnet compositions from metamorphic rocks are color coded according to their bulk composition and plotted with 90% confidence ellipsoids; data were compiled from Davies & Warren (1992), Monteleone et al. (2007), Baldwin et al. (2008), DesOrmeau et al. (2017), Faryad et al. (2019), Gonzalez et al. (2019) and this study (Electronic Appendix 4e-C). The field-labeled felsic gneisses (n = 306) include aluminous gneisses, silicic gneisses, and quartzofeldspathic gneisses (including 03118m and 03115). Superimposed on garnet compositional fields are detrital garnet compositions (this study). Compositions of all detrital garnets (n = 716 spots on 572 garnets) are shown in Left. Garnet compositions corresponding to specific inclusion suites are shown in Center (coesite, cristobalite, kokchetavite, omphacite) and Right (CO_2 , carbonate, graphite), as indicated in the legend.

detrital garnets. Two garnets in the >200- μm fraction were sourced by UHP protoliths as indicated by a $4.0 \times 3.0\text{-}\mu\text{m}$ polyphase SiO_2 inclusion, consisting of quartz and coesite (Figure 4.2-2A), and a $6.5 \times 5.5\text{-}\mu\text{m}$ monomineralic coesite inclusion (Figure 4.2-2B). The garnet containing a polyphase coesite/quartz inclusion also contains carbonate, epidote, and CO_2 inclusions (Figure 4.2-2A), whereas the monomineralic coesite inclusion coexists with numerous graphite inclusions in the same garnet grain (Figure 4.2-2B).

Eleven detrital garnets contain cristobalite, the metastable highest-temperature polymorph of SiO_2 . Raman spectra (Figure 4.2-2C) indicate the inclusions are likely α -cristobalite (Swainson et al. 2003). Nine (of 13) cristobalite crystals occur as polyphase inclusions, often together with mica (muscovite–paragonite, pyrophyllite, or chamosite–clinochlore) \pm carbonate \pm kokchetavite (Figure 4.2-2C and Electronic Appendix 4e-A). Kokchetavite, a metastable polymorph of K-feldspar (Hwang et al. 2004), occurs in 4 of the 11 cristobalite-bearing garnets either in the same polyphase inclusion or as an adjacent inclusion. Five additional garnets were found to contain kokchetavite as polyphase inclusions (\pm quartz \pm carbonate \pm muscovite–paragonite \pm rutile) (Electronic Appendix 4e-A). The compositions of cristobalite- and kokchetavite-bearing garnet grains span the entire compositional range of the measured detrital garnets (Figure 4.2-1).

Carbon-bearing inclusions consist of carbonate minerals (26 % of inclusion-bearing garnets), graphite (22 %), and CO_2 (19 %) (Figure 4.2-2 and Electronic

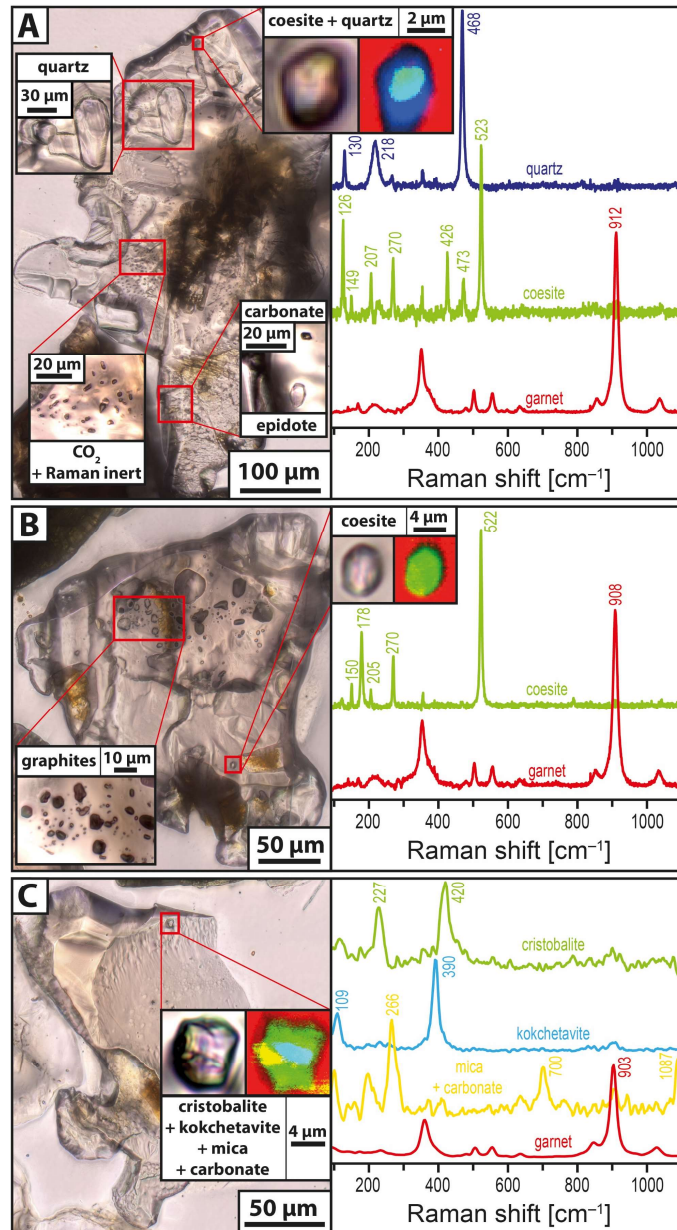


Figure 4.2-2: Representative detrital garnets and inclusion suites and associated Raman spectra. (A) Detrital garnet containing polyphase quartz and coesite, carbonate, epidote, and CO_2 inclusions. (B) Detrital garnet containing monomineralic coesite and graphite inclusions. (C) Detrital garnet containing a polyphase inclusion of cristobalite + kokchetavite + mica + carbonate.

Appendix 4e-A). The compositions of carbon-bearing garnet grains also span the entire compositional range of the measured detrital garnets. However, graphite inclusions do not occur in high-Mg garnets. Therefore, we infer that carbon-bearing detrital garnets were derived from felsic sources (Figure 4.2-1).

Six detrital garnets contained monomineralic elastically isolated quartz and zircon inclusions (i.e., away from grain boundaries, cracks, or other inclusions). The remnant strains of elastically isolated monomineralic quartz and zircon inclusions were used to constrain the P - T conditions of elastic equilibration within garnet hosts (Figure 4.2-3). Application of elastic geothermobarometry requires that the inclusions remained isolated and fully contained within the host mineral after entrapment in order to preserve elastic strains from inclusion entrapment (Angel et al. 2015). However, inclusion strains can be modified through elastic, brittle, or ductile deformation (Campomenosi et al. 2018; Alvaro et al. 2020; Zhong et al. 2020), leading to modification of the calculated P - T conditions of elastic equilibration. Small (<10- μ m-diameter) monomineralic inclusions contained within six detrital garnets from the >200- μ m-size fraction were analyzed using Raman spectroscopy, ensuring that there is sufficient garnet volume to elastically isolate the inclusions (Mazzucchelli et al. 2018; Campomenosi et al. 2020; Zhong et al. 2020) (Electronic Appendix 4e-D). Each inclusion was verified to be more than three times the inclusion radii beneath the surface of the garnet and away from any visible

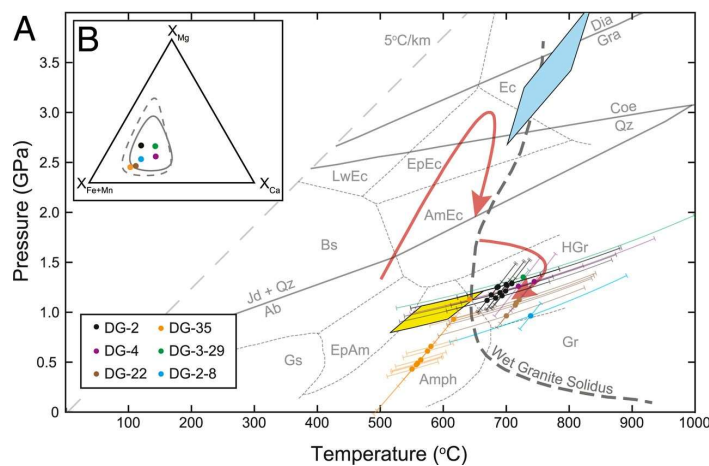


Figure 4.2-3: P - T diagram showing (A) quartz-in-garnet and zircon-in-garnet elastic thermobarometric data for detrital garnets (DGs; this study). Also shown are P - T constraints for outcrop samples, including quartzofeldspathic gneiss in the catchment area [sample 03115; yellow field (Gonzalez et al. 2019)]. P - T path (red arrows) was derived from garnet compositions from coesite eclogite (Faryad et al. 2019). Blue field indicates Ti-in-coesite trace element thermobarometry, combined with zirconium-in-rutile thermometry for coesite eclogite (Osborne et al. 2019, Kohn 2020). (B) Ternary plot of detrital garnet compositions (molar proportions of Fe+Mn, Ca, and Mg) corresponding to the quartz-in-garnet and zircon-in-garnet elastic thermobarometric data plotted in A. The solid line indicates the 90% confidence ellipsoids for all detrital garnet grains, and the dashed line is the 90% confidence ellipsoid for all garnet compositions from basement rocks. Coe, coesite; Dia, diamond; Gra, graphite; Qz, quartz; Jd, jadeite; Ab, albite. Metamorphic facies indicated: Ec, eclogite; EpEc, epidote eclogite; AmEc, amphibole eclogite; LwEc, lawsonite eclogite; Bs, blueschist; Gs, greenschist; EpAm, epidote amphibolite; Amph, amphibolite; Gr, granulite; HGr, high-pressure granulite.

inhomogeneities in the garnet host (i.e., other inclusions, fractures, or grain boundaries). The 1,008- cm^{-1} peak width, in terms of full width at half-maximum intensity, of less than 5 cm^{-1} was used as a criterion in the selection of nonmetamict zircon inclusions for Raman thermobarometry (Campomenosi et al. 2020) (Electronic Appendix 4e-D). Remnant strains were determined for quartz and zircon inclusions from measured Raman shifts using their respective Grüneisen tensor (Angel et al. 2019). No evidence of microfractures around inclusions was observed from visual inspection of each measured inclusion. Therefore, the remnant strains of the isolated inclusions within the garnet hosts are interpreted as the P - T conditions of elastic equilibration. Strains were used in conjunction with the

elastic stiffness tensors of quartz and zircon to calculate the average remnant stress within the inclusions for use in an isotropic elastic model to constrain the range of possible elastic equilibration conditions [i.e., isomekes (Angel et al. 2017a)]. P - T conditions of elastic equilibration between the host and inclusions were determined from the intersection points of isomekes calculated for coexisting quartz and zircon inclusions in six detrital garnets that met the criteria as stated above. Results indicate P - T conditions of elastic equilibration ranging from 0.5 to \sim 1.3 GPa and from 550 °C to 750 °C. Despite the large uncertainties, the data suggest elastic equilibration under primarily granulite facies conditions and subordinate amphibolite facies conditions (Figure 4.2-3).

4.3 Discussion

In the eastern Papuan (U)HP terrane outcrop samples of felsic gneisses that preserve UHP indicator minerals have yet to be found. Only one sample of mafic eclogite enclosed within retrogressed felsic gneiss has been found to preserve coesite as a partially transformed inclusion in omphacite (Baldwin et al. 2008). The coesite crystallized at 763 °C (+72 °C to -61 °C) and 3.3 GPa (+0.77 to -0.60 GPa) (Osborne et al. 2019) during UHP metamorphism at \sim 8 Ma (Monteleone et al. 2007; Zirakparvar et al. 2011; Baldwin & Das 2015; Figure 4.2-3). Garnet growth in coesite eclogite occurred in two stages (Faryad et al. 2019): (1) core garnet growth at \sim 650 °C and $>$ 2.7 GPa within the coesite stability field and (2) garnet rim growth following partial exhumation from UHP conditions at $<$ 7.1 Ma during a transient (0.3-Ma) heating event at 1.5 GPa (Figure 4.2-3).

Although it is not possible to extract the detailed P - T paths followed by individual detrital garnet grains, their compositions and inclusion suites can be compared with those from outcrop samples to assess the P - T paths followed by protoliths with a range of bulk compositions, during transit through the rock cycle (Figure 4.2-1, Figure 4.2-3, Electronic Appendix 4e-A, Electronic Appendix 4e-B, and Electronic Appendix 4e-C). The discovery of coesite inclusions in detrital garnets provides direct mineral evidence that UHP metamorphism also affected felsic lithologies in the eastern Papuan (U)HP terrane (Figure 4.1-2, Figure 4.2-1, and Figure 4.2-2). Compared with garnet from the coesite eclogite outcrop, the two coesite-bearing detrital garnets have lower Mg contents and contain carbon-bearing inclusions (i.e., graphite, carbonate minerals, CO₂). These detrital garnets are inferred to have formed from metamorphism of organic-rich sedimentary rocks (Figure 4.2-1 and Electronic Appendix 4e-A), providing petrologic evidence for subduction of protoliths originating at the Earth's surface. No microdiamonds were found as inclusions in detrital garnet. Therefore, protolith conditions are inferred to have reached the coesite stability field but not the stability field for diamond (Figure 4.1-2 and Figure 4.2-3). Our findings expand the range of bulk compositions, notably low-density bulk compositions (felsic gneiss and metasedimentary rocks), that preserve evidence for UHP conditions in eastern Papua New Guinea.

Many mineral inclusions in the placer deposit garnets are commonly found as matrix minerals in basement rocks of the D'Entrecasteaux Islands (e.g., eclogite, felsic host gneiss, and amphibolite). However, cristobalite and kokchetavite are discoveries that have not yet been documented in basement rocks. Preservation of hydrous phases in the gneisses and shear zones on Goodenough Island (i.e., peak phengite, retrograde muscovite, biotite and chlorite, serpentinite) and mica and fluid inclusions

preserved in detrital garnet span the entire compositional range (Figure 4.2-1, Electronic Appendix 4e-A, and Electronic Appendix 4e-C). We infer that fluids affected all lithologies during transit through the rock cycle. In order to be preserved, metastable mineral inclusions (i.e., coesite, cristobalite, kokchetavite) must have remained isolated systems, trapped within mechanically strong garnet hosts during rapid exhumation. These metastable inclusions also remained insulated from fluids during erosion and transport of sediment from limited catchment areas and deposition to form the placer deposit.

Detrital garnet mineral inclusions sourced by subducted carbonates and organic materials include graphite, carbonate minerals, and CO₂. We infer that subducted carbonaceous material converted to graphite via rapid recrystallization and devolatilization (Nakamura et al. 2020). However, subducted carbonaceous material apparently did not reach sufficient depths to form diamond. The abundance of graphite and CO₂ inclusions (22 and 19 % of inclusion-bearing garnets, respectively) provides evidence for deep carbon recycling in the subduction channel (Galvez & Pubellier 2019). At present, shallow seeps offshore Normanby and Dobu Islands are releasing CO₂ (>98 %) and CH₄ (87 to 4,360 ppm) (Fabricius et al. 2011; Figure 4.1-1B), providing evidence for the return of recycled carbon to the oceans and atmosphere.

Evidence for high-temperature conditions occurs in detrital garnets of all compositions. Polyphase inclusions of cristobalite + kokchetavite + mica (Figure 4.2-2C) are interpreted as trapped partial melt crystallized during rapid decompression (i.e., “nanogranitoids”) (Ferrero et al. 2016; Schönig et al. 2020; Electronic Appendix 4e-A). Elastic thermobarometry of individual detrital garnet grains also suggests elastic equilibration of quartz and zircon inclusions under granulite facies conditions and for one grain in the amphibolite facies (Figure 4.2-3). Such high thermobaric ratios (T/P) are not compatible with equilibration along a prograde path associated with low- T/P subduction gradients but instead, provide additional evidence for heating during exhumation.

Although we are unable to ascertain the potential effects of chemical variations in quartz and zircon inclusions in the detrital garnets used for elastic thermobarometry, we found no evidence for elastic equilibration of quartz and zircon inclusions in detrital garnet corresponding to eclogite facies conditions. Instead, consistent P – T conditions in the high-temperature, lower-pressure metamorphic facies are obtained and cannot be attributed to processes that would variably affect individual inclusions, such as changes in the degree of elastic isolation or brittle deformation of inclusions. Therefore, we infer that the elastically isolated quartz and zircon inclusions in detrital garnets reequilibrated by viscous creep in their garnet hosts at temperatures >600 °C (Zhong et al. 2020). Amphibolite facies conditions determined for one detrital garnet (DG-35) provide additional evidence for retrograde garnet growth, in agreement with quartz-in-garnet and Ti-in-quartz thermobarometry for a quartzofeldspathic gneiss in the catchment area (Gonzalez et al. 2019; Figure 4.2-3).

The formation and preservation of both coesite and cristobalite as inclusions in garnet require extreme metamorphic conditions indicative of transient geothermal gradients (i.e., from low T/P to higher T/P). The rock record in eastern Papua New Guinea preserves evidence for Late Miocene low- T/P metamorphism reaching UHP conditions and higher- T/P metamorphism during exhumation, as well as highest- T/P gradients associated with decompression melting of asthenospheric mantle to form basalts

in the Woodlark Basin (Figure 4.1-1 and Figure 4.1-2). The UHP locality occurs along strike of a sinistral strike-slip transfer fault system from the placer deposit (Hill 1994); the faults displace Pliocene–Quaternary basaltic lavas (Figure 4.1-1B). Such petrologic variation preserved in the geologic record over short spatial and temporal scales indicates that steady-state processes are not operative within this part of the obliquely convergent AUS–PAC plate boundary zone (Baldwin et al. 2012).

The detrital garnet data support models for the transport and transformation pathways of heterogeneous lithologies, including organic and inorganic carbon, in the forearcs of subduction zones (Galvez & Pubellier 2019). Results reinforce the observation that subducted rocks do not have to remain dry during transport through the rock cycle in order to preserve evidence for UHP metamorphism, as long as mineral inclusions (such as coesite) in strong host minerals, like garnet, remain isolated from metamorphic fluids (Ferrero & Angel 2018). In addition, detrital garnet data provide observational evidence for H₂O and CO₂ storage in the forearc and volatile and melt migration within the forearc during rifting. We infer that the detrital garnet SiO₂ inclusions (coesite, quartz, and cristobalite) capture processes including subduction to upper mantle depths along low-*T/P* gradients and exhumation associated with an increase in geothermal gradients (i.e., to higher *T/P*) as the Woodlark Rift formed ahead of the westward-propagating Woodlark Basin seafloor-spreading system (Figure 4.1-1A).

The Papuan (U)HP terrane preserves evidence for geochemical cycling between the surface and the upper mantle, including UHP rock formation and exhumation, that can be directly linked to the rapid spatial and temporal evolution of the obliquely convergent PAC–AUS plate boundary zone. Microplate rotation of the Woodlark plate relative to the AUS plate (Webb et al. 2008), upper plate divergence (Malusà et al. 2015), and buoyancy forces (Ellis et al. 2011) contributed to rapid (U)HP exhumation during the transition from subduction to rifting in eastern Papua New Guinea (Figure 4.1-1). Following the onset of upper plate divergent motion, the oceanic upper plate and subducted continental lower plate will decouple, providing accommodation space (Malusà et al. 2015) for subducted metasediments, felsic gneisses, and their partial melts to rapidly exhume within the subduction channel. Numerical models that use constraints provided by the geologic record in eastern Papua New Guinea (Petersen & Buck 2015; Liao et al. 2018) predict that asthenospheric mantle will flow upward toward the subduction channel to fill the accommodation space left by the buoyantly exhuming felsic (U)HP rocks, resulting in isotherm advection, an increase in geothermal gradients, and heating of the (U)HP terrane during exhumation.

The investigation of erosional products at the catchment scale expands the potential for finding additional evidence of UHP metamorphism in the eastern Papuan (U)HP terrane where pervasively overprinted felsic rocks and their partial melts have yet to yield additional evidence in outcrop since coesite was discovered in a mafic eclogite. Results demonstrate that inclusions in detrital garnets from modern sediments preserve evidence for UHP metamorphism. Such geologically short timescales (i.e., since the Late Miocene) for rock recycling within this active plate boundary zone imply <10-Ma petrologic lag times for metamorphic rocks exhumed from approximately ≤120-km depths, eroded, and deposited as sediment. High-spatial resolution spectroscopic imaging of heavy mineral fractions of sediment derived from the erosion of the Papuan (U)HP terrane provides a means to efficiently search for evidence of UHP metamorphism and to further constrain the thermal evolution and geodynamics of continental subduction. A better understanding of subduction and exhumation processes in active plate

boundaries is needed before modern processes can be accurately extrapolated and applied to the geologic record. Raman spectroscopy of mineral inclusions in detrital garnet in both modern sediments and stratigraphic sections, especially when integrated with single-grain Sm–Nd detrital garnet ages (Maneiro et al. 2019), has the potential to provide insight into the tempo of rock recycling processes throughout Earth's history, including on early Earth when plate velocities and transport through the rock cycle were at least as fast as present day.

4.4 Materials and Methods

The beach placer sample (PNG08002c) was dry sieved into sized fractions (63 to 125, 125 to 200, and >200 μm), split by coning and quartering, mounted in epoxy, ground with SiC, and polished with Al_2O_3 to expose grain surfaces. The compositions of 572 detrital garnet grains were obtained by electron microprobe analysis at the Geosciences Center of the University of Göttingen using a JEOL JXA 8900 RL equipped with five wavelength dispersive spectrometers. Measurements were performed with an accelerating voltage 15 kV and a beam current of 20 nA. Counting times were 15 s for Si, Mg, Ca, Fe, and Al and 30 s for Ti, Cr, and Mn. Measurement spots were preferentially set to the garnet centers but shifted toward the rim when inclusions or fractures are located in the center. For the coesite-, cristobalite-, and kokchetavite-bearing garnet grains, nine spots per garnet were set: one at the center, four at the mantle, and four at the rim.

From the investigated 572 garnet grains, 354 contain inclusions $\geq 2 \mu\text{m}$, which were identified using a Horiba Jobin Yvon XploRA Plus spectrometer equipped with an Olympus BX41 microscope at the Geosciences Center of the University of Göttingen (Schönig et al. 2018b). Analytical conditions include a 532 nm excitation laser, a $1,800 \text{ l}\times\text{mm}^{-1}$ grating, a $100\times$ long working distance objective with a numerical aperture of 0.8, a confocal hole diameter of 100 μm , and a slit of 100 μm . Two-dimensional Raman images of monomineralic coesite, bimineralic coesite/quartz, and polyphase inclusions containing cristobalite and kokchetavite were collected with a WITec alpha300R ultrahigh-throughput Raman spectrometer at the Geosciences Center of the University of Göttingen. The spectral images were acquired with a 532 nm excitation laser, an automatically controlled laser power of 20 mW, a $1,200 \text{ l}\times\text{mm}^{-1}$ grating, and a $100\times$ long working distance objective with a numerical aperture of 0.75. Spectra were collected at a step size of between 50 and 200 nm using an acquisition time of between 1 and 2 s per spectrum, depending on the specific inclusion. Automated cosmic ray correction, background subtraction, spectral averaging/smoothing, and supervised component analysis were performed using the WITec Project software.

A Renishaw inVia Raman spectrometer with a confocal optical microscope at Syracuse University was used to measure the Raman shifts of quartz and zircon inclusions in detrital garnet for elastic thermobarometric calculations following procedures for quartz-in-garnet inclusions (Bonazzi et al. 2019; Gonzalez et al. 2019) and zircon-in-garnet inclusions (Campomenosi et al. 2020). All measured inclusions were elastically isolated and located more than three inclusion radii from other inclusions, grain boundaries, and visible defects in the host garnet. Because metamictization of zircon modifies the zircon bulk elastic properties (Campomenosi et al. 2020), only nonmetamict zircon inclusions were selected for analysis as determined using the $1,008\text{-cm}^{-1}$ peak width, in terms of full width at half-

maximum (FWHM) intensity, of less than 5 cm^{-1} (Electronic Appendix 4e-D). A 532 nm laser was focused onto specimens with a $100\times$ microscope objective with a numerical aperture of 0.9. The Raman scattered light was statically dispersed with a $1,800 \text{ l}\times\text{mm}^{-1}$ grating onto a charged couple device, resulting in a spectral resolution of 0.5 cm^{-1} . The spectrometer was calibrated against neon lines and a silicon standard. Spectral accuracy and linearity were checked throughout each analytical session by measuring the Rayleigh scattered light from the 532 nm laser, the 520.5-cm^{-1} Raman band of a silicon standard, the Raman bands of a synthetic quartz reference material from the Westinghouse Corporation, and the Raman bands of a synthetic zircon reference material. All Raman spectra were acquired for 20 s and measured at room conditions of $23 \text{ }^\circ\text{C}$ and 1 bar. Spectra were not processed or corrected prior to peak fitting using a pseudo-Voigt function in the Renishaw software. Errors on fitted band positions are ~ 0.2 to 0.3 cm^{-1} .

For strain calculations, Raman band frequencies of quartz were measured at ~ 127.5 , 205.9 , and 464.8 cm^{-1} , and the Raman band frequencies of zircon were measured at 213.4 , 224.0 , 356.0 , 438.8 , 974.8 , and $1,008.7 \text{ cm}^{-1}$. Synthetic quartz and zircon reference materials were measured between sample measurements to derive calibration curves in the case of any spectral drift. Measurements were performed near the centers of the inclusions, where the effects of inclusion geometry and elastic anisotropy have the least effect (Mazzucchelli et al. 2018). Furthermore, it has recently been demonstrated that when elastically anisotropic inclusions, such as quartz and zircon, are contained within nearly isotropic host minerals such as garnet, the effect of elastic anisotropy on calculated entrapment conditions is $<2 \%$ and therefore, negligible as compared with the errors on Raman measurements (Mazzucchelli et al. 2019). The remnant strains ($\epsilon_1 + \epsilon_2, \epsilon_3$) in inclusions were calculated using the fitted Raman band positions using the stRAinMAN software and the respective Grüneisen tensors of quartz and zircon (Angel et al. 2019). Errors on fitted band positions of 0.3 cm^{-1} were used in stRAinMAN to calculate the estimated standard deviation (esd) and covariance matrix needed for error calculation of the remnant inclusion pressure (Angel et al. 2017b). Remnant strains of quartz and zircon inclusions were used in conjunction with the respective elastic tensor to calculate the pressure within the inclusion. Elastic modeling of inclusion pressures and entrapment isomekes was performed for quartz and zircon inclusions in an almandine host using an isotropic elastic model implemented in the EntraPT program (Mazzucchelli et al. 2021). Errors on remnant strains were propagated to entrapment isomekes using the covariance matrix and esd on inclusion strains according to the method described in Mazzucchelli et al. 2021. Errors on calculated entrapment isomekes, especially for zircon inclusions in garnet, varied over a large temperature range. Inclusions with the largest errors were those that had the least number of fitted Raman bands and were subsequently excluded from P - T calculations and interpretation.

Acknowledgements

Suzanne L Baldwin acknowledges support from NSF Division of Earth Sciences Grant 0709054, NSF Major Research Instrumentation Program Grant 1625835, and the Thonis Endowment at Syracuse University. Jan Schönig and Hilmar von Eynatten acknowledge support from German Research Foundation Grant EY 23/27-1. Joseph P Gonzalez acknowledges support from a Syracuse University Science Technology Engineering Math fellowship and a European Research Council Postdoctoral

Fellowship (Grant 714936 to M Alvaro). We thank RM Davies for garnet electron microprobe analyses and PG Fitzgerald for providing comments on an earlier version of the manuscript. We acknowledge the constructive reviews of Editor P Kelemen and two anonymous reviewers, which helped us improve our manuscript. Collaborative discussions on detrital analysis with S Andò, MG Malusà, E Garzanti, and PG Fitzgerald are greatly appreciated.

Life-cycle analysis of coesite-bearing garnet

Jan Schönig¹, Hilmar von Eynatten¹, Guido Meinhold^{1,2}, and N. Keno Lünsdorf¹

¹*Geosciences Center Göttingen, University of Göttingen, Germany*

²*School of Geography, Geology and the Environment, Keele University, United Kingdom*

published 22nd February 2021

Geological Magazine 158, 1421–1440

<https://doi.org/10.1017/S0016756821000017>

Detrital coesite-bearing garnet is the final product of a complex geological cycle including coesite entrapment at ultra-high-pressure conditions, exhumation to Earth's surface, erosion and sedimentary transport. In contrast to the usual enrichment of high-grade metamorphic garnet in medium- to coarse-sand fractions, coesite-bearing grains are often enriched in the very-fine-sand fraction. To understand this imbalance, we analyze the role of source-rock lithology, inclusion size, inclusion frequency and fluid infiltration on the grain-size heterogeneity of coesite-bearing garnet based on a dataset of 2100 inclusion-bearing grains, of which 93 contain coesite, from the Saxonian Erzgebirge, Germany. By combining inclusion assemblages and garnet chemistry, we show that (1) mafic garnet contains a low number of coesite inclusions per grain and is enriched in the coarse fraction, and (2) felsic garnet contains variable amounts of coesite inclusions per grain, whereby coesite-poor grains are enriched in the coarse fraction and coesite-rich grains extensively disintegrated into smaller fragments resulting in an enrichment in the fine fraction. Raman images reveal that: small coesite inclusions of dimension <9 μm are primarily monomineralic, whereas larger inclusions partially transformed to quartz; and garnet fracturing, fluid infiltration and the coesite-to-quartz transformation is a late process during exhumation taking place at ~330 °C. A model for the disintegration of coesite-bearing garnet enables the heterogeneous grain-size distribution to be explained by inclusion frequency. High abundances of coesite inclusions cause a high degree of fracturing and fracture connections to smaller inclusions, allowing fluid infiltration and the transformation to quartz, which in turn further promotes garnet disintegration.

5.1 Introduction

Since the first application of detrital garnet chemistry to discriminate sediment source regions (Morton 1985), garnet major-element composition has become a valuable information resource in provenance studies (Mange & Morton 2007; Krippner et al. 2014; Hardman et al. 2018; Tolosana-Delgado et al. 2018) and first approaches of considering trace elements seem to be promising for future investigations (Čopjaková et al. 2005; Hong et al. 2020). Beyond garnet chemistry, the identification of mineral inclusions in detrital garnet by Raman spectroscopy allows for the determination of mineral assemblages, a piece of information that is otherwise not available because detrital mineral grains mostly lose their paragenetic context (Schönig et al. 2018b). This becomes particularly important for sediments being derived from high-pressure (HP) to ultra-high-pressure (UHP) source rocks, as state-of-the-art discrimination schemes based on garnet composition do not enable their distinction. In

contrast, detrital UHP garnet grains often contain inclusions of coesite and diamond, which enables the systematic screening of entire catchments for the presence of UHP rocks as demonstrated in the Western Gneiss Region of Norway (Schönig et al. 2018a), the central Saxonian Erzgebirge of Germany (Schönig et al. 2019, 2020) and the D'Entrecasteaux Islands of Papua New Guinea (Baldwin et al. 2021).

By considering a single mineral species in provenance studies, one of the major advantages is the minimization of hydrodynamic fractionation processes (Morton 1991). However, strong grain-size control on U–Pb ages of zircon (e.g., Lawrence et al. 2011; Ibañez-Mejia et al. 2018), tourmaline chemistry (Viator 2003) and garnet chemistry (e.g., Krippner et al. 2015, 2016) has been demonstrated, and should also be considered for other mineral phases (von Eynatten & Dunkl 2012). For garnet, grain-size effects do not solely result from density contrasts due to compositional variation (Schuiling et al. 1985), but are also related to inherited grain size from source to sink (Krippner et al. 2015, 2016). From the western Hohe Tauern of Austria, Krippner et al. (2015) observed an increase in the magnesium content with increasing garnet grain size, pointing to enrichment of garnet grains derived from HP metamorphic rocks with increasing grain size (Figure 5.1-1; green arrows), in accordance with the typical large garnet crystal size in these rock types. This trend of increasing metamorphic grade with increasing grain size can be also observed from the detrital garnet major-element chemistry of Krippner et al. (2016) and Schönig et al. (2018b) from the Western Gneiss Region of Norway (Figure 5.1-1; red arrows). In addition, detrital garnet data of several samples from the Northern Alps, Black Forest, Rhine Graben and Neckar River investigated by Hülscher et al. (2018) imply a similar pattern, although some do not show a clear trend (Figure 5.1-1; yellow, purple, black, and blue arrows, respectively). Notably, Hülscher et al. (2018) solely studied garnet rims, an approach that may bias the composition versus grain-size distribution.

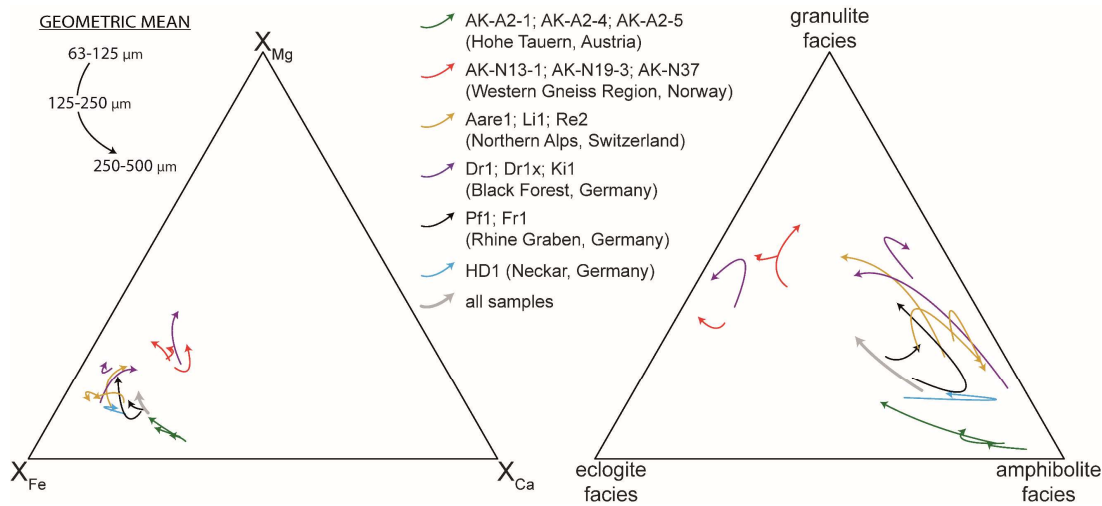


Figure 5.1-1: Trends of geometric means of detrital garnet composition from the 63–125 μm fraction (origin of arrow), via the 125–250 μm fraction to the 250–500 μm fraction (head of arrow). Compositions are shown in the X_{Fe} – X_{Mg} – X_{Ca} ternary plot (molar proportions) (left side) and in a ternary plot giving probabilities for metamorphic garnet of belonging to eclogite facies, granulite facies, and amphibolite facies host rocks using multivariate discrimination (Tolosana-Delgado et al. 2018, prior probability ‘equal-M’) (right side). Compositional garnet data were taken from Krippner et al. (2015): AK-A2-1 (n = 287), AK-A2-4 (n = 293), AK-A2-5 (n = 294); Krippner et al. (2016): AK-N19-3 (n = 294); Schönig et al. (2018b): AK-N13-1 (n = 148), AK-N37 (n = 148); and Hülscher et al. (2018): Aare1 (n = 91), Li1 (n = 98), Re2 (n = 90), Dr1 (n = 74), Dr1x (n = 76), Ki1 (n = 93), Pf1 (n = 66), Fr1 (n = 77), HD1 (n = 87).

Based on the general trend of increasing metamorphic grade with increasing detrital garnet grain size (Figure 5.1-1, grey arrows), in particular in samples from HP regions such as the Hohe Tauern and Western Gneiss Region, it would be expected that the proportion of detrital garnet grains sourced from UHP rocks progressively increases with grain size. However, the few studies carried out so far convey a contrasting and non-uniform picture. Coesite-bearing garnet grains of a modern sand sample from the Western Gneiss Region of Norway only occur in the 63–250 μm fraction and are absent from the 250–500 μm fraction (Schönig et al. 2018a). In contrast, in a beach placer of the D’Entrecasteaux Islands of Papua New Guinea, coesite-bearing garnet has solely been found in the >200 μm fraction (Baldwin et al. 2021). In modern sands from the central Saxonian Erzgebirge of Germany, coesite-bearing garnet grains show an even more complex distribution (Schönig et al. 2019, 2020). In some samples they are enriched in the 250–500 μm fraction and in others in the 63–125 μm fraction, while some do not show a clear trend.

In order to understand the grain-size distribution of detrital coesite-bearing garnet, the previously investigated modern sand samples from tributaries draining the UHP nappe in the central Saxonian Erzgebirge represent an ideal study object. Compared with the Western Gneiss Region and the D’Entrecasteaux Islands, detrital UHP garnet grains of the Erzgebirge show higher variability in terms of grain size, the sampled catchment areas are better constrained, the chemical garnet database of local UHP lithologies is more substantiated and the geological framework is less complex.

In addition to mineral inclusion and chemical data of the coesite- and diamond-bearing detrital garnet of the central Saxonian Erzgebirge presented by Schönig et al. (2019, 2020), we here present and comprehensively evaluate the entire dataset of 2100 inclusion-bearing garnet grains with the aim of unravelling the distribution systematics of detrital coesite-bearing garnet regarding grain size and source-rock composition. In addition, the substantial quantity of 93 coesite-bearing grains, which contain a total of 193 coesite inclusions, enables the evaluation of the role of inclusion size, inclusion frequency and fluid availability for coesite preservation. We show that the disintegration of the initially large coesite-bearing garnet crystals during exhumation and processes of the sedimentary cycle is strongly controlled by inclusion size and frequency, leading to a heterogeneous detrital grain-size distribution.

5.2 Geological framework and sampling locations

The Saxonian Erzgebirge in the northwestern Bohemian Massif represents a dome-structure crystalline complex formed during the Variscan Orogeny resulting from the collision of Gondwana and Laurussia (e.g., Kroner & Romer 2013). The study area is located in the central part of the complex within the previously defined Gneiss–Eclogite Unit (Kröner et al. 1995), a heterogeneous nappe in the intermediate position of the nappe stack, which records the highest peak metamorphic conditions in the Erzgebirge (e.g., Willner et al. 2000; Figure 5.2-1a).

Six modern sand samples are from catchments of tributaries draining the area around the Saidenbach reservoir (JS-Erz-3s, -5s, -6s, -8s, -9s, -13s). These catchments mainly consist of foliated felsic HP country-rock gneiss (Willner et al. 1997) hosting lenses of eclogite and non-foliated diamond-bearing paragneiss (Figure 5.2-1b; for sampling coordinates see Schönig et al. 2019, here Table Appendix 2-A

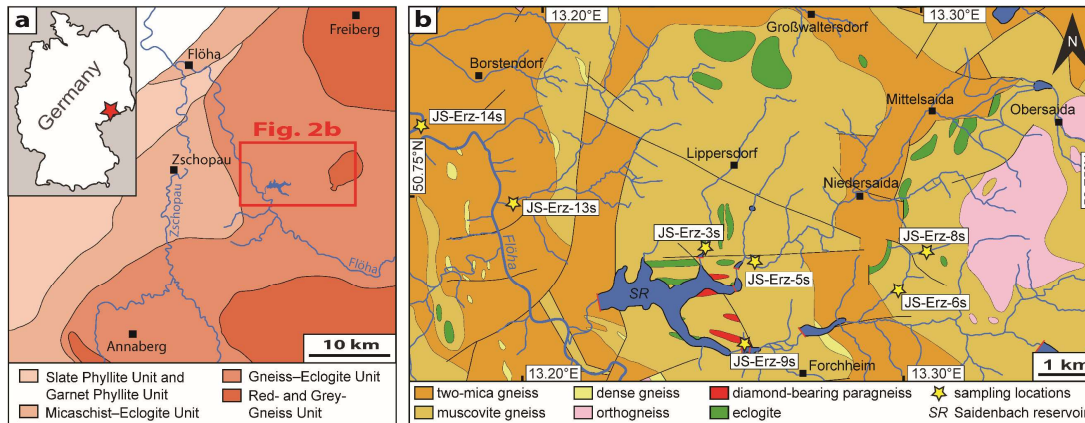


Figure 5.2-1: Maps showing the location and outline of the study area, modified after Schönig et al. (2019, 2020). (a) Tectonometamorphic units subdividing the Saxonian Erzgebirge after Willner et al. (2000) with an inset showing the location in Germany marked by red asterisk. Red box defines the map section of the geological map in (b). (b) Geological map of the area around the Saidenbach reservoir in the central Saxonian Erzgebirge with modern sand sampling locations marked by yellow asterisks. Compared to the map of Schönig et al. (2019, 2020), an eclogite lens was added in the catchment of sample JS-Erz-8s according to Kossmat & Reinisch (1931).

1). As well as diamond inclusions in the paragneiss lenses at the eastern shore of the Saidenbach reservoir (e.g., Nasdala & Massonne 2000), a UHP stage is also confirmed for some locally occurring eclogite lenses by the presence of coesite or pseudomorphs after coesite (Schmädicke et al. 1992; Massonne 2001; O'Brien & Ziemann 2008; Gose & Schmädicke 2018). However, previous investigations of mineral inclusions in detrital garnet of the sampled catchments revealed that coesite-bearing UHP rocks occur in all studied catchments; they are not solely confined to eclogite and paragneiss lenses, but also include country-rock gneiss which re-equilibrated during high-temperature (HT) exhumation at HP conditions (Schönig et al. 2019, 2020). All lithologies occurring in the six catchments therefore represent a potential source for coesite-bearing garnet grains and can be roughly subdivided into mafic sources, that is, eclogite and felsic sources (i.e., preserved paragneiss lenses), re-equilibrated country-rock gneiss and their partially re-equilibrated intermediate representatives.

The proportion of mafic and felsic sources differs between the investigated catchments. In the small catchment of sample JS-Erz-9s, almost exclusively felsic rocks occur including high proportions of diamond-bearing paragneiss lenses (Figure 5.2-1b). The catchments of samples JS-Erz-8s and JS-Erz-13s also mainly consist of felsic rocks with few eclogite lenses. Eclogites are more prominent in the catchments of samples JS-Erz-3s, JS-Erz-5s and JS-Erz-6s. In contrast to the six samples described above, the seventh modern sand sample JS-Erz-14s was taken from the Flöha main river and comprises a much larger catchment draining an area of >500 km². Within the catchment, larger parts of the Gneiss–Eclogite Unit and the surrounding nappes of lower metamorphic grade are drained, that is, the Micaschist–Eclogite Unit and Red- and Grey-Gneiss Unit (Figure 5.2-1a).

5.3 Methods

The seven modern sand samples were wet sieved to separate grainsize fractions. Heavy minerals from the 63–125, 125–250 and 250–500 µm fractions were separated by centrifugation in sodium-

polytungstate with a density of $\sim 2.85 \text{ g}\cdot\text{cm}^{-3}$. Heavy mineral concentrates were split by coning and quartering, embedded in one-inch epoxy ring mounts, then grounded and polished over several steps using SiC abrasive paper and Al_2O_3 abrasive in water suspension, with a final particle size of $0.05 \mu\text{m}$.

All analytical methods were performed at the Geosciences Center of the University of Göttingen. Mineral inclusions $\geq 2 \mu\text{m}$ in garnet of the embedded heavy mineral concentrates were identified by Raman spectroscopy using a Horiba Jobin Yvon XPlora Plus spectrometer equipped with an Olympus BX41 microscope. Analytical conditions include a 532 nm excitation laser, a $1800 \text{ l}\cdot\text{mm}^{-1}$ grating, a $100\times$ long working distance objective with a numerical aperture of 0.8, a confocal hole diameter of $100 \mu\text{m}$ and a slit of $100 \mu\text{m}$. The aim was to obtain 100 inclusion-bearing garnet grains for each grain-size fraction for each sample, resulting in a range of 108 to 419 screened garnet grains per grain-size fraction of each sample. For a detailed description of the inclusion identification procedure the reader is referred to Schönig et al. (2018b).

Two-dimensional Raman images of monomineralic coesite and bimineralic coesite/quartz inclusions were collected with a WITec alpha300R ultra-high-throughput Raman spectrometer. The spectral images were acquired with a 532 nm excitation laser, an automatically controlled laser power of 20 mW, a $300 \text{ l}\cdot\text{mm}^{-1}$ grating, and a $100\times$ long working distance objective with a numerical aperture of 0.75. Spectra were collected at a step size of 100–200 nm by an acquisition time of 250 ms. Automated cosmic ray correction, background subtraction, spectral averaging/smoothing and supervised component analysis were performed using the WITec Project software.

Raman spectra of carbonaceous material detected in coesite/quartz inclusions were used to estimate peak temperatures of fluid infiltration. Spectral parameters were determined by applying the automated iterative curve-fitting approach of Lünsdorf & Lünsdorf (2016), whereby the script was slightly modified following the instructions. Based on the determined parameters, peak temperatures were estimated using the reference data series for the 532 nm laser and the geothermometer of Lünsdorf et al. (2017).

The chemical composition of all inclusion-bearing garnet grains was determined with a JEOL JXA 8900 RL electron microprobe equipped with five wavelength-dispersive spectrometers. Samples were coated with carbon to ensure conductivity. Measurement conditions include an accelerating voltage of 15 kV and a beam current of 20 nA. Counting times were 15 s for Si, Mg, Ca, Fe and Al, and 30 s for Ti, Cr and Mn. Measurement spots were preferentially set to the garnet centers but shifted towards the rim when inclusions or fractures were located in the centre. For the coesite- and diamond-bearing garnet grains, nine spots per garnet were set: one at the center, four at the mantle and four at the rim. As coesite- and diamond-bearing garnet grains do not show strong zonation, their compositions were averaged by the arithmetic mean. In addition to compositional evaluation directly based on measured and calculated major-element contents, the multivariate discrimination scheme of Tolosana-Delgado et al. (2018) was used. Due to the metamorphic character of the study area, the prior probability ‘equal-M’ was applied throughout.

5.4 Results and discussion

5.4.1 Garnet chemistry compared with grain size

Compositions of the detrital inclusion-bearing garnet grains are dominated by the iron component with a geometric mean of the molar proportion (X_{Fe}) of ~60 %. This is followed by the magnesium component with X_{Mg} ~21 % and the calcium component with X_{Ca} ~17 %. The proportion of the manganese component is significantly lower with X_{Mn} ~1 % and titanium, as well as the chromium component, is subordinate.

As shown in the ternary kernel density plots of the main components X_{Fe} – X_{Mg} – X_{Ca} and after multivariate discrimination, the majority of detrital inclusion-bearing garnet grains are similar in composition to high-grade metamorphic sources of the area, that is, eclogite and diamond-bearing paragneiss (Figure 5.4-1). By considering the individual grain-size fractions, high-grade metamorphic sources are prominent in all fractions but less pronounced in the 63–125 μ m fraction, in particular in terms of an eclogitic affinity.

The increasing proportion of garnet grains from high-grade sources with increasing grain size is further reflected by the geometric mean compositions (Figure 5.4-1, grey arrow) with slightly decreasing X_{Fe} component and increasing X_{Mg} component. This is supported by the multivariate discrimination showing a progressive increase of probabilities for granulite and eclogite facies sources and a pronounced decrease for amphibolite facies sources (Figure 5.4-1). Counter-intuitively, although eclogitic garnet is high in calcium, the geometric mean of the X_{Ca} component slightly decreases with increasing grain size. This is caused by two effects. First, from the 63–125 μ m fraction to the 125–

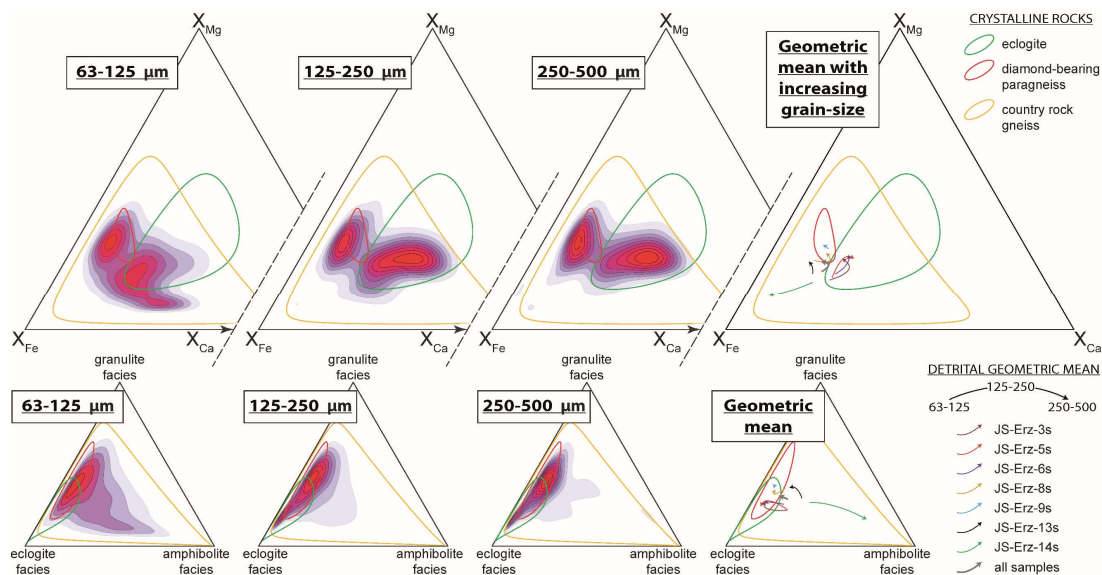


Figure 5.4-1: Composition of inclusion-bearing detrital garnet. Distributions are shown for the three grain-size fractions as kernel density estimate heatmaps in the X_{Fe} – X_{Mg} – X_{Ca} ternary plot and in the probability ternary plot of metamorphic garnet after multivariate discrimination (Tolosana-Delgado et al. 2018). See Electronic Appendix 5e-A for the dataset. In addition, the trends of the geometric means for the individual samples are shown from the 63–125 μ m fraction (origin of arrow) via the 125–250 μ m fraction to the 250–500 μ m fraction (head of arrow). For comparison, garnet composition of local crystalline rocks compiled by Schönig et al. (2020) are shown as 95 % confidence ellipsoids.

250 μm fraction, the amount of garnet grains with an eclogitic affinity increases at the expense of grains from the lower-grade (e.g., amphibolite facies) country-rock gneiss. The grains of both eclogitic and country-rock gneiss affinity are rich in X_{Ca} , leading to an almost constant geometric mean of X_{Ca} from the 63–125 μm to the 125–250 μm fraction. Second, although the amount of garnet grains sourced from the high-grade metamorphic rocks further increases from the 125–250 μm to the 250–500 μm fraction, the amount of garnet sourced from felsic rocks similar to the diamond-bearing paragneiss, which is lower in X_{Ca} , exceeds the amount of eclogitic garnet grains, resulting in a slight decrease of the geometric mean of X_{Ca} .

In addition to the observations from the entire dataset, the trends of the geometric means for the individual samples with increasing garnet grain size reveal significant contrasts between the samples (Figure 5.4-1, coloured arrows). Most obviously, sample JS-Erz-14s shows an inverse trend to the six other samples with an increase of X_{Fe} , and a decrease of X_{Mg} and X_{Ca} with increasing grain size, characteristic of an increasing amount of garnet grains from lower-grade metamorphic sources. This is well reflected by the multivariate discrimination showing a strong increase in the probability of amphibolite facies sources with increasing grain size. These observations cannot be explained by hydraulic sorting as almandine is the densest garnet end-member (e.g., Babuška et al. 1978); consequently, it has to be an effect of inherited grain size from source to sink. In contrast to the other samples, the much larger catchment of sample JS-Erz-14s comprises not only rocks from the Gneiss–Eclogite Unit but also from the surrounding lower-grade units (see Section 5.2). These include micaschist from the Micaschist–Eclogite Unit, which contains abundant iron-rich and magnesium-poor garnet with crystal sizes larger than the analyzed grain-size window (Rötzler et al. 1998; Schumacher et al. 1999). It is therefore likely that the inherited garnet grain size from micaschist sources lead to the enrichment of garnet grains from lower-grade metamorphic sources with increasing grain size in sample JS-Erz-14s. This is in contrast to most of the previous studies and shows that grain-size inheritance effects are variable and strongly control garnet grain-size distributions.

Compared with sample JS-Erz-14s, the garnet composition of sample JS-Erz-13s starts from a similar geometric mean in the 63–125 μm fraction, although slightly higher in X_{Mg} and the probability of high-grade sources (i.e., granulite and eclogite facies, Figure 5.4-1), but evolves to higher X_{Mg} and higher probabilities of high-grade sources with increasing grain size, agreeing with the absence of micaschists in this catchment (Figure 5.2-1b) and previous studies from HP regions (Figure 5.1-1). Eclogite lenses within the catchment area are minor and, although the number of garnet grains with an eclogitic affinity increases from the 63–125 μm to the 125–250 and 250–500 μm fraction, their low amount compared with garnet grains from high-grade felsic sources leads to a decrease in X_{Ca} . The almost complete absence of eclogitic sources and the dominance of high-grade felsic sources is emphasized in sample JS-Erz-9s. Here, garnet mean compositions are exclusively within the 95 % confidence ellipsoid of the diamond-bearing paragneiss lenses, and only a very minor increase in X_{Mg} and decrease in X_{Ca} with increasing grain size is observed (Figure 5.4-1). As well as JS-Erz-9s, JS-Erz-8s also shows compositional geometric means similar to the diamond-bearing paragneiss. However, due to the increase of eclogitic garnet grains from the 63–125 μm to the 125–250 μm grain-size fraction, the geometric mean first increases in X_{Mg} and X_{Ca} along with the probability of an eclogite facies source; subsequently, X_{Ca} and the probability of an eclogite facies source decrease from the 125–250 μm to the

250–500 μm fraction due to the dominance of garnet from high-grade felsic sources. A similar trend can be observed for sample JS-Erz-3s, but X_{Ca} and the probability of an eclogite facies source are significantly higher because of the more abundant occurrence of eclogites in the catchment of this sample. As for JS-Erz-3s, samples JS-Erz-5s and JS-Erz-6s show a high X_{Ca} component and a high probability of an eclogite facies source that are lower in the 63–125 μm fraction because of garnet from the country-rock gneiss, but continually increase with increasing grain size together with X_{Mg} caused by the dominance of eclogitic source rocks.

In summary, the compositions of garnet grains from all catchments solely draining the UHP area reflect an increasing amount of high-grade metamorphic garnet grains with increasing grain size. These garnet grains are dominantly sourced from eclogitic sources in samples JS-Erz-3s, JS-Erz-5s and JS-Erz-6s. In contrast, eclogitic grains are less frequent in JS-Erz-8s and JS-Erz-13s, and even absent from JS-Erz-9s. Garnet compositions of sample JS-Erz-14s show an inverse trend to all other samples, most likely related to the involvement of lower-grade metamorphic source rocks such as micaschist, which shed large garnet crystals. These main observations agree with the geological framework of the area (see Section 5.2).

5.4.2 Frequent mineral inclusion types compared with garnet chemistry and grain size

As well as many different inclusion types occurring in minor proportions of the detrital garnet grains (see Electronic Appendix 5e-A), the most frequent inclusion types are rutile (in ~62 % of the garnet grains, $n = 1,292$), zircon (~37 %, $n = 778$), apatite (~29 %, $n = 615$), quartz (~23 %, $n = 489$) and graphite (~18 %, $n = 372$). In addition, substantial amounts of garnet grains contain kyanite (~11 %, $n = 230$) and omphacite (~7 %, $n = 156$). As zircon and apatite inclusions yield very limited information (Schönig et al. 2018b), we focus here on the main features of rutile-, omphacite-, graphite-, quartz- and kyanite-bearing garnet grains with regard to grain size. A detailed description for each inclusion type is given in Appendix 5-A.

The proportion of inclusion-bearing garnet increases with grain size: on average ~33 % in the 63–125 μm fraction, ~57 % in the 125–250 μm fraction and ~83 % in the 250–500 μm fraction. Similarly, rutile-bearing garnet, which resamples the entire compositional range and the distribution which is independent of source-rock composition, shows enrichment in the coarser grain-size fractions (Figure 5.4-2, Figure Appendix 5-A 1). It can therefore be concluded that the amount of garnet containing a specific inclusion type generally increases with increasing grain size, in accordance with the higher analyzed garnet volume per grain, making it more likely that the garnet fragment contains a specific inclusion assuming a similar inclusion frequency per volume.

Omphacite co-existing with garnet is the diagnostic mineral assemblage of eclogite-facies metamorphism. Potentially, omphacite-bearing garnet could derive from felsic eclogite-facies rocks but, in the investigated area, omphacite inclusions in garnet as well as symplectites after omphacite in felsic rocks only occur occasionally (Willner et al. 1997). Omphacite-bearing garnet is therefore an appropriate indicator for the mafic high-grade source rocks (i.e., eclogites), which is supported by their composition almost exclusively matching the 95 % confidence ellipsoid for garnet from local eclogite

(Figure 5.4-2). In the grain-size distribution plot, it is clearly indicated that garnet-containing omphacite is enriched in the coarse fraction independently of the proportion of eclogite occurring in the catchment. This agrees with previous observations of an increasing metamorphic grade with increasing garnet grain size (Figure 5.1-1), and the typical large garnet crystal size in eclogite leading to a grain-size inheritance effect.

Contrary to omphacite-bearing garnet, garnet containing inclusions of graphite compositionally cover the entire range of local felsic rocks and only marginally overlap with that of eclogite, reflecting the general compositional overlap of felsic and eclogitic rocks (Figure 5.4-2). Graphite inclusions are therefore a characteristic feature of felsic parametamorphic source rocks. Compared with the grain-size distributions of rutile- and omphacite-bearing garnet, which internally have a similar pattern for almost all samples, graphite-bearing garnet in the individual samples show strong variations regarding grain size. Samples JS-Erz-9s, JS-Erz-13s and JS-Erz-14s show an increase of graphite-bearing garnet with increasing grain size. In contrast, sample JS-Erz-6s in particular but also JS-Erz-3s, JS-Erz-5s and JS-Erz-8s show enrichment of graphite-bearing garnet in the 63–125 μm fraction. Samples containing minor amounts of omphacite-bearing garnet due to the low proportion of eclogitic sources (i.e., JS-Erz-9s, JS-Erz-13s and JS-Erz-14s) show an increase of graphite-bearing garnet with increasing grain size as a result of the larger garnet volume analyzed. In contrast, samples containing higher amounts of omphacite-bearing garnet (e.g., JS-Erz-5s and JS-Erz-6s, but also JS-Erz-3s and JS-Erz-8s) show enrichment of graphite-bearing garnet in the 63–125 μm fraction. This dilution effect

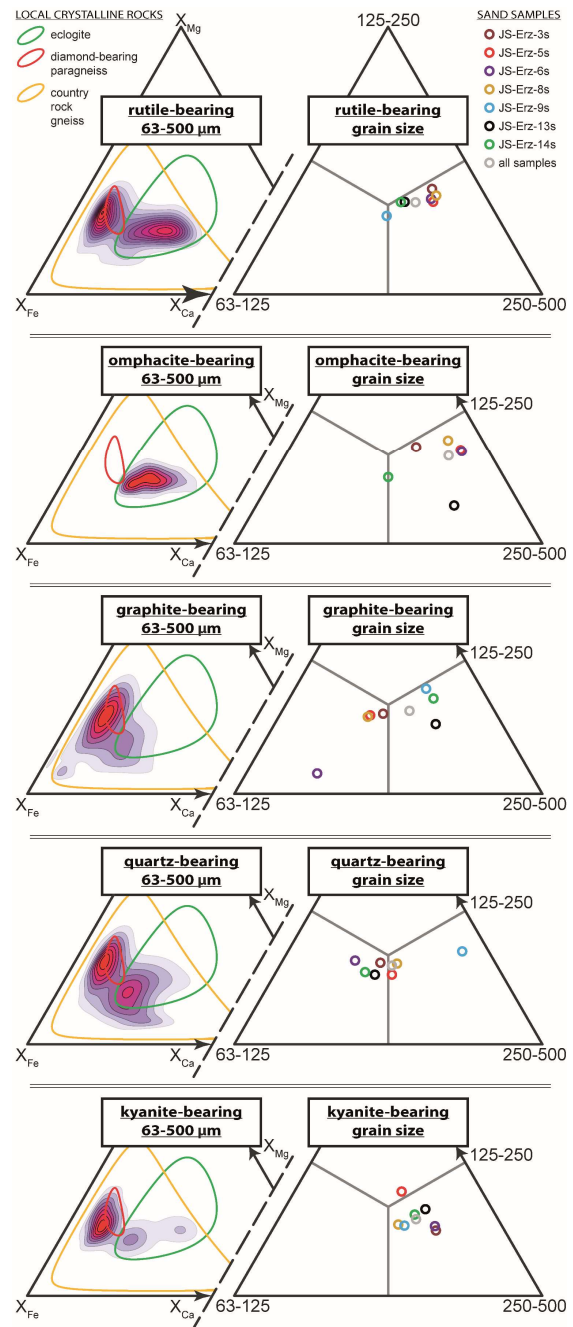


Figure 5.4-2: Composition and grain-size distribution of detrital garnet containing specific mineral inclusion types. Composition is shown for the entire grain-size range from 63–500 μm as kernel density estimate heatmaps in the $X_{\text{Fe}}-X_{\text{Mg}}-X_{\text{Ca}}$ ternary plots. See Electronic Appendix 5e-A for the dataset and Appendix 5-A for inclusion frequency and individual plots for each grain-size fraction. For comparison, garnet composition of local crystalline rocks compiled by Schönig et al. (2020) are shown as 95 % confidence ellipsoids. Grain-size distributions for the individual samples are illustrated in a ternary plot showing relative proportions for the number of grains in each analyzed grain-size fraction.

can be best observed by following the development of omphacite- and graphite-bearing garnet from sample JS-Erz-8s (upstream) to sample JS-Erz-6s (downstream, Figure 5.2-1b). Compared with the other samples, JS-Erz-8s shows an intermediate amount of omphacite-bearing garnet enriched in the coarse fractions and an intermediate amount of graphite-bearing garnet slightly enriched in the fine fraction (Figure 5.4-2). Further downstream the catchment of the sampled creek drains a large eclogite body at its western site, leading to a significant increase of omphacite-bearing garnet in JS-Erz-6s that is strongly enriched in the coarse fraction, and a decrease of graphite-bearing garnet that is highly enriched in the fine fraction.

As graphite-bearing garnet represents the entire range of exclusively felsic sources and its grain-size distribution is highly affected by the proportion of eclogitic source rocks (see above), graphite-bearing garnet is not suitable for evaluating the grain-size distribution of garnet from lower-grade felsic sources, that is, country-rock gneiss, compared with high-grade felsic sources similar to the diamond-bearing paragneiss. For that, the distribution of garnet containing inclusions of quartz and kyanite are more suitable. Both inclusion types are mainly a feature of the felsic sources (e.g., Willner et al. 1997; Nasdala & Massonne 2000), which is supported by garnet chemistry from all grain-size fractions (Figure 5.4-2). However, both types also occur subordinately in eclogite (e.g., Schmädicke et al. 1992; Gose & Schmädicke 2018), as supported by smaller populations matching the composition of garnet from local eclogite (Figure 5.4-2). Quartz- and kyanite-bearing garnet therefore mainly represent felsic sources and their grain-size distribution is less affected by varying proportions of eclogitic sources. In addition, detrital garnet composition reveals that the amount of quartz-bearing garnet is more pronounced for lower-grade felsic sources (i.e., country-rock gneisses), whereas the amount of kyanite-bearing garnet is more pronounced for high-grade felsic sources.

The grain-size distribution plots show enrichment of quartz-bearing garnet in the 63–125 μm fraction overcoming the effect of the increasing garnet volume analyzed with increasing grain size, except for garnet of sample JS-Erz-9s, which is exclusively shed from homogeneous felsic rocks (Figure 5.4-2). In contrast, kyanite-bearing garnet is clearly enriched in the coarsest fraction. It can therefore be concluded that high-grade metamorphic rocks of both mafic and felsic composition primarily supply large garnet crystals to the sedimentary system, leading to enrichment in the coarser detrital garnet fractions as a result of the inherited grain size from source to sink.

The conclusions drawn so far for the grain-size distribution can be summarized by considering ratios of garnet grains containing the above-discussed inclusion types. First, sample JS-Erz-14s shows the highest value of graphite-/omphacite-bearing garnet in the 125–250 and 250–500 μm fractions, indicating minor amounts of eclogitic garnet and high amounts of felsic garnet (Figure 5.4-3). This ratio is slightly shifted to the finer fractions for JS-Erz-13s as a result of slightly higher amounts of eclogitic garnet (strongly enriched in the 250–500 μm , Figure 5.4-2). The increasing amount of eclogitic sources is indicated by the increasing proportion of the 63–125 μm fraction from sample JS-Erz-3s via JS-Erz-8s and -5s to JS-Erz-6s (Figure 5.4-3). Second, the increasing amount of high-grade felsic sources with increasing garnet grain size, independent of the geological framework of the catchment, is shown by a higher ratio of kyanite-/omphacite-bearing garnet in the coarser fractions compared with quartz-/omphacite-bearing garnet (Figure 5.4-3). This holds for all samples except JS-Erz-8s, which contains less omphacite-bearing garnet than JS-Erz-5s, and the value of kyanite-/omphacite-bearing garnet

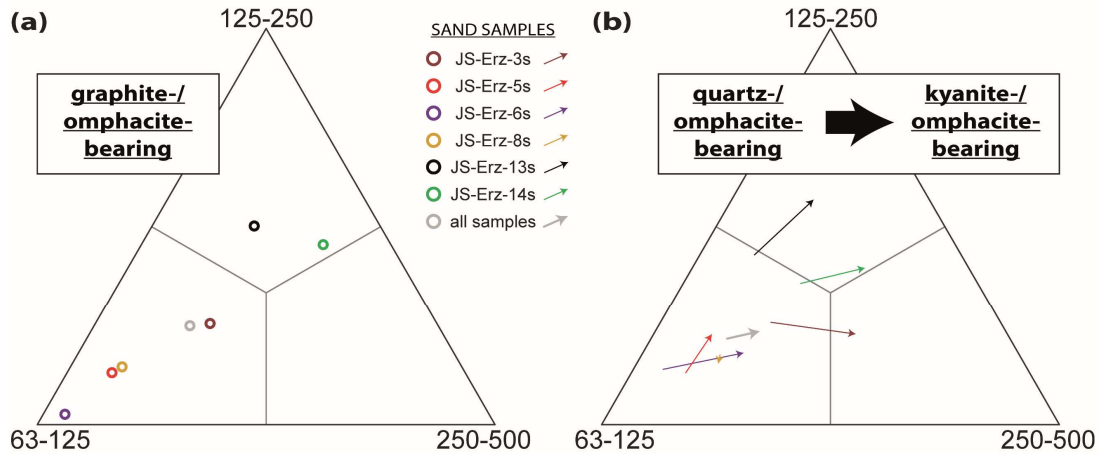


Figure 5.4-3: Ratios of garnet grains containing specific mineral inclusion types, displayed in ternary diagrams reflecting the three grain size fractions. (a) Ratio of graphite- versus omphacite-bearing garnet. (b) Ratio of quartz- versus omphacite-bearing garnet (origin of arrow) compared to kyanite- versus omphacite-bearing garnet (head of arrow).

compared with quartz-/omphacite-bearing garnet does not significantly change with grain size. This implies that JS-Erz-8s is enriched in high-grade felsic garnet in the 63–125 μm fraction.

5.4.3 UHP mineral inclusions compared with garnet chemistry and grain size

Apart from the frequent mineral inclusion types, the distribution of garnet grains containing diamond and coesite is of major interest because of their direct relation to the erosion of UHP rocks in the sampled catchments. Garnet containing diamond inclusions is concentrated in sample JS-Erz-9s, while sample JS-Erz-14s contains a single diamond-bearing garnet grain; all other samples lack evidence of the erosion of diamond-bearing lithologies. The composition and mineral inclusion assemblage of inclusion-bearing garnet grains in JS-Erz-9s clearly point to a dominantly felsic origin (see Sections 5.4.1 and 5.4.2). This agrees with the compositional kernel density distribution of diamond-bearing garnet in all grain-size fractions (Figure 5.4-4a). Although minor amounts of diamond-bearing garnet grains are shed from felsic country rocks and a single diamond-bearing garnet may be derived from an eclogite (Schönig et al. 2020), most of the diamond-bearing garnet grains are derived from the high-grade felsic rocks, that is, diamond-bearing paragneiss lenses. The strong increase in diamond-bearing garnet grains with increasing grain size (Figure 5.4-4a, grain-size plot) can be explained by the increase of high-grade felsic garnet with increasing grain size, being related to inherited grain size, and the larger garnet volume analyzed (see Section 5.4.2).

For coesite-bearing garnet, the pattern is more complex. Coesite inclusions occur in garnet grains of all analyzed samples but the garnet grains show high variation regarding chemistry and grain-size distribution (Figure 5.4-4b). Coesite-bearing garnet composition mostly matches that of felsic sources in the 63–125 μm fraction, while they mostly match that of mafic (i.e., eclogitic) sources in the 125–250 μm fraction. In the 250–500 μm fraction, the composition of coesite-bearing garnet grains shows dense populations for both felsic and mafic sources. In addition, the frequency and especially the grain-size distribution of coesite-bearing garnet is very heterogeneous (Figure 5.4-4b, bar plot and grain-size plot). Conspicuously, some of the samples show enrichment of coesite-bearing garnet in the 63–125 μm

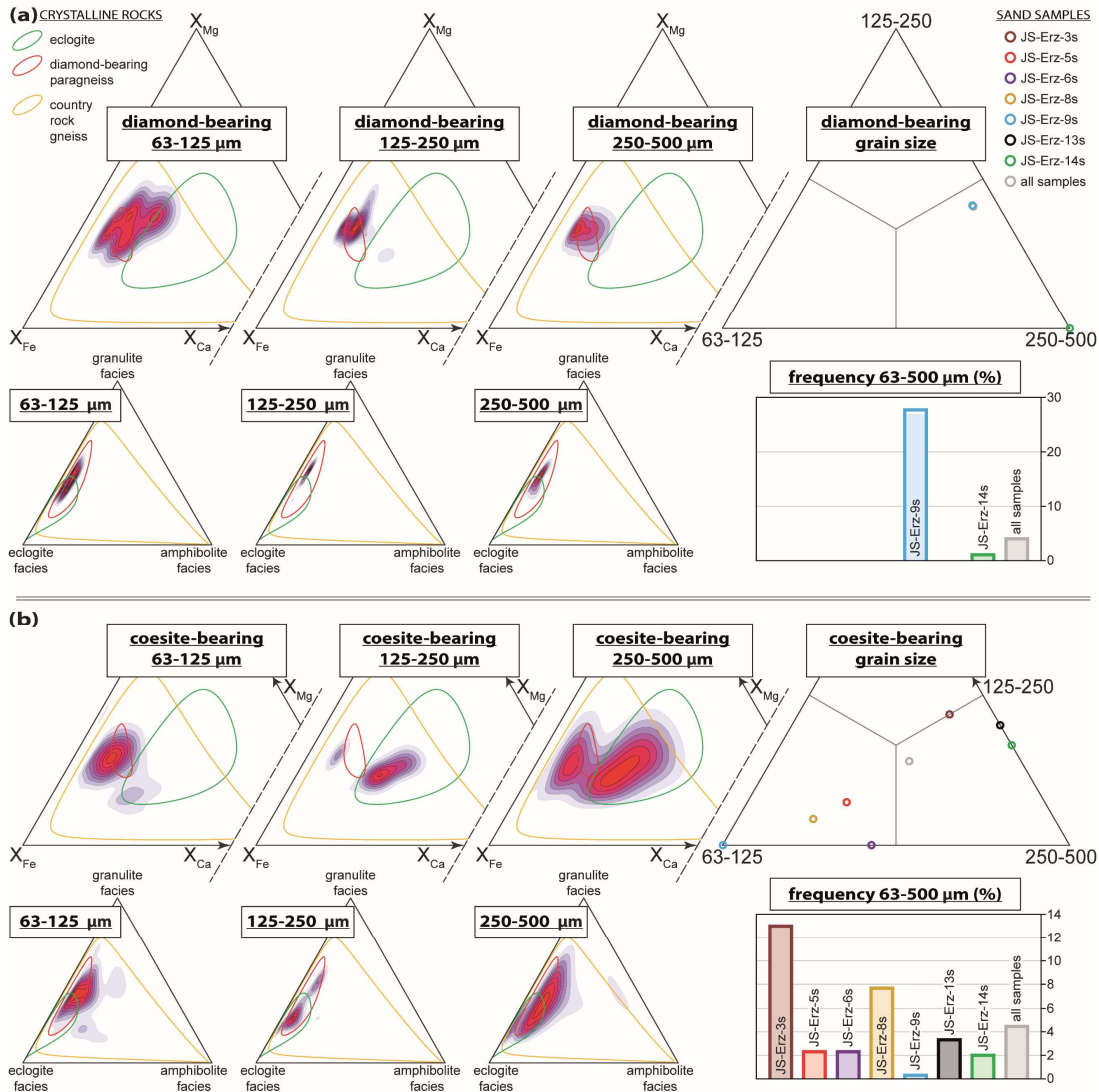


Figure 5.4-4: Composition, grain-size distribution, and frequency of (a) diamond- and (b) coesite-bearing detrital garnet. Compositional distributions are shown for the three grain-size fractions as kernel density estimate heatmaps in the X_{Fe} – X_{Mg} – X_{Ca} ternary plots and in the probability ternary plots of metamorphic garnet after multivariate discrimination (Tolosana-Delgado et al. 2018). See Electronic Appendix 5e-A for the dataset. For comparison, garnet composition of local crystalline rocks compiled by Schönig et al. (2020) are shown as 95 % confidence ellipsoids. Grain-size distributions of diamond- and coesite-bearing garnet for the individual samples are illustrated in ternary plots showing relative proportions for the number grains in each analyzed grain-size fraction. The frequencies of diamond- and coesite-bearing garnet for the individual samples of the analyzed grain-size window of 63–500 μm are shown in bar plots.

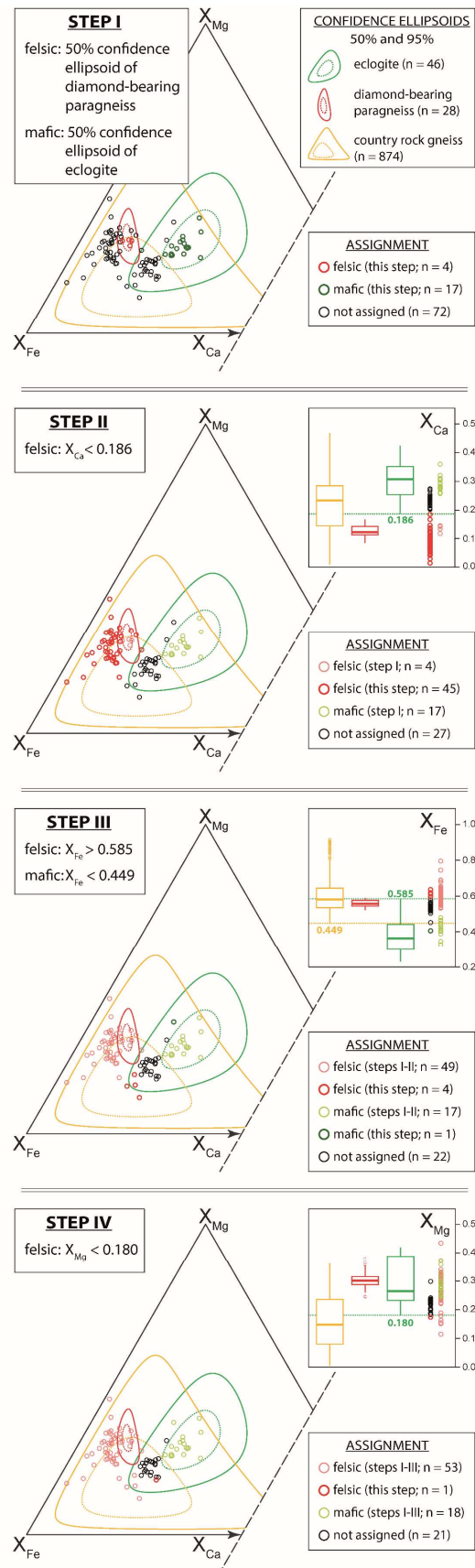
fraction (JS-Erz-5s, JS-Erz-6s and JS-Erz-8s), contrast to the small analyzed garnet volume and the typical increase of high-grade metamorphic garnet grains with increasing grain size (see Sections 5.4.1 and 5.4.2). These observations imply a strong control of source-rock composition and initial garnet crystal size. To understand the grain-size distribution of coesite-bearing garnet, a separate evaluation of felsic and mafic grains is therefore necessary.

To assign the individual coesite-bearing garnet grains to their most likely source, that is, felsic or mafic, a step-wise classification is performed by comparing their chemistry and mineral inclusion assemblage

with that of garnet from crystalline rocks in the catchment areas (for details, see Appendix 5-B). In the first four steps, the molar proportions of X_{Ca} , X_{Fe} and X_{Mg} are considered (Figure 5.4-5). For step I, it is reasonable to assume that garnet grains matching the 50 % confidence ellipsoid of diamond-bearing paragneiss are of felsic origin, whereas those matching the 50 % confidence ellipsoid of eclogite are derived from mafic rocks. For steps II to IV, the boxplots indicate that garnet from local eclogites contains $X_{Ca} \geq 0.186$, $X_{Fe} \leq 0.585$ and $X_{Mg} \geq 0.180$. In contrast, garnet of felsic rocks partially shows lower values for X_{Ca} and X_{Mg} , and are restricted to $X_{Fe} \geq 0.449$, but partially exceed the upper limit of eclogitic garnet. Based on these limits, 72 out of the 93 coesite-bearing garnet grains (~77 %) are assigned to their most likely source.

The 21 remaining coesite-bearing garnet grains after step IV are more difficult to assign as they show a strong overlap with compositions of garnet from both country-rock gneiss and eclogite. To tackle this issue, a principal component analysis was first performed on the unassigned grains. All measured oxide weight percentages were used, except Cr_2O_3 because of amounts that are exclusively below the detection limit. Prior to analysis, the data were centered log-ratio transformed. Based on the biplot, the

Figure 5.4-5: Steps I to IV of the step-wise assignment of coesite-bearing garnet to their most likely source based on garnet composition in molar proportions. Compositions of coesite-bearing grains are shown in the X_{Fe} - X_{Mg} - X_{Ca} ternary plot. For comparison, garnet composition of local crystalline rocks compiled by Schönig et al. (2020) are shown as 50 % (dashed line) and 95 % (solid line) confidence ellipsoids. Boxplots show molar proportions of the element considered in the corresponding step.



log ratios of the variables $\text{FeO}/(\text{CaO}+\text{MgO})$ and CaO/MgO are most suitable for further analysis (Figure Appendix 5-B 1), and are shown in a scatter plot in comparison to mineral inclusion assemblages co-existing with coesite (Figure 5.4-6). Ten of the unclassified grains can be assigned in step V based on: (1) omphacite inclusions indicating a mafic source; (2) graphite inclusions indicating a felsic source; and (3) inclusion assemblages of alkali feldspar, phlogopite–biotite, quartz and cristobalite (see the discussion in Schönig et al. 2020) dominantly occurring in coesite-bearing garnet assigned to a felsic source.

From the remaining 11 unassigned coesite-bearing grains, five show a compositional contrast to local eclogite and compositions similar to garnet previously assigned to a felsic source (Figure 5.4-6). These five grains are assigned to a felsic source in step VI, leading to a total of 87 out of the 93 coesite-bearing garnet grains (~94 %) assigned to their most likely source. From these 87 grains, 66 (~76 %) were assigned to a felsic and 21 (~24 %) to a mafic source. For the six unassigned coesite-bearing grains, there are only subordinate indications with regard to source-rock composition; whether the six remaining garnet grains are assigned to a felsic or a mafic source yields only negligible differences in the grain-size pattern of coesite-bearing garnet (Figure Appendix 5-B 3). We therefore use the ~94 % of coesite-bearing garnet grains confidently assigned. Their frequency and grain-size relations for the seven sediment samples are shown in Figure 5.4-7.

Figure 5.4-7b shows that mafic coesite-bearing garnet is only present in JS-Erz-3s, JS-Erz-6s and JS-Erz-13s. Because the other samples also show a contribution from eclogitic source rocks as expressed by omphacite-bearing garnet (Figure 5.4-2), this implies that eclogite lenses of the area contain coesite less frequently than the felsic lithologies. Compared with the low amounts in JS-Erz-6s in the eastern part of the studied area, mafic coesite-bearing garnet frequently occurs in samples north of the Saidenbach reservoir (JS-Erz-13s and especially JS-Erz-3s), although JS-Erz-6s show a significantly higher input of garnet from eclogite (Figure 5.4-2). However, because of the presence of mafic coesite-bearing garnet in JS-Erz-6s and the frequent occurrence of felsic coesite-bearing garnet, the generally

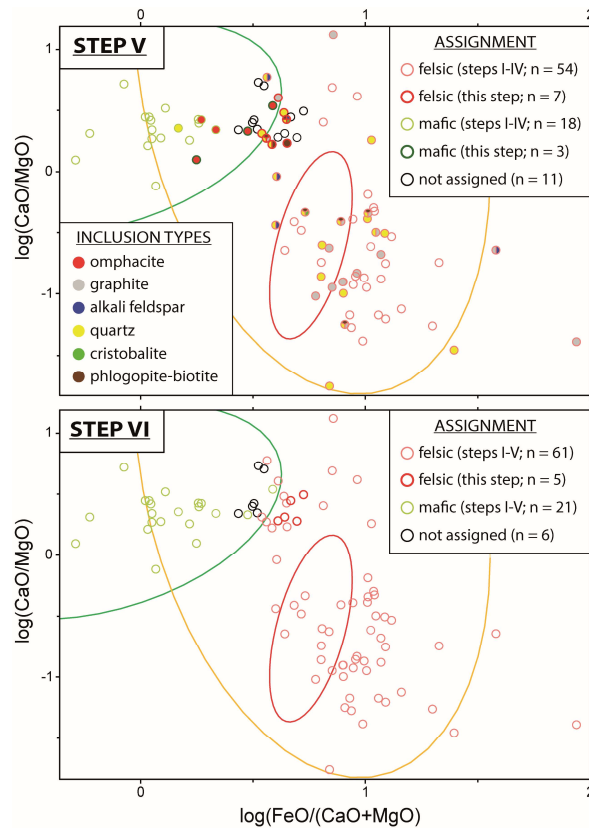


Figure 5.4-6: Steps V and VI of the step-wise assignment of coesite-bearing garnet to their most likely source based on log-ratio plots in comparison with mineral inclusion assemblages. Log-ratios are chosen based on the principal component analysis biplot shown in Figure Appendix 5-B 1. For comparison, garnet composition of local crystalline rocks compiled by Schönig et al. (2020) are shown as 95 % confidence ellipsoids with colors similar to Figure 5.4-5.

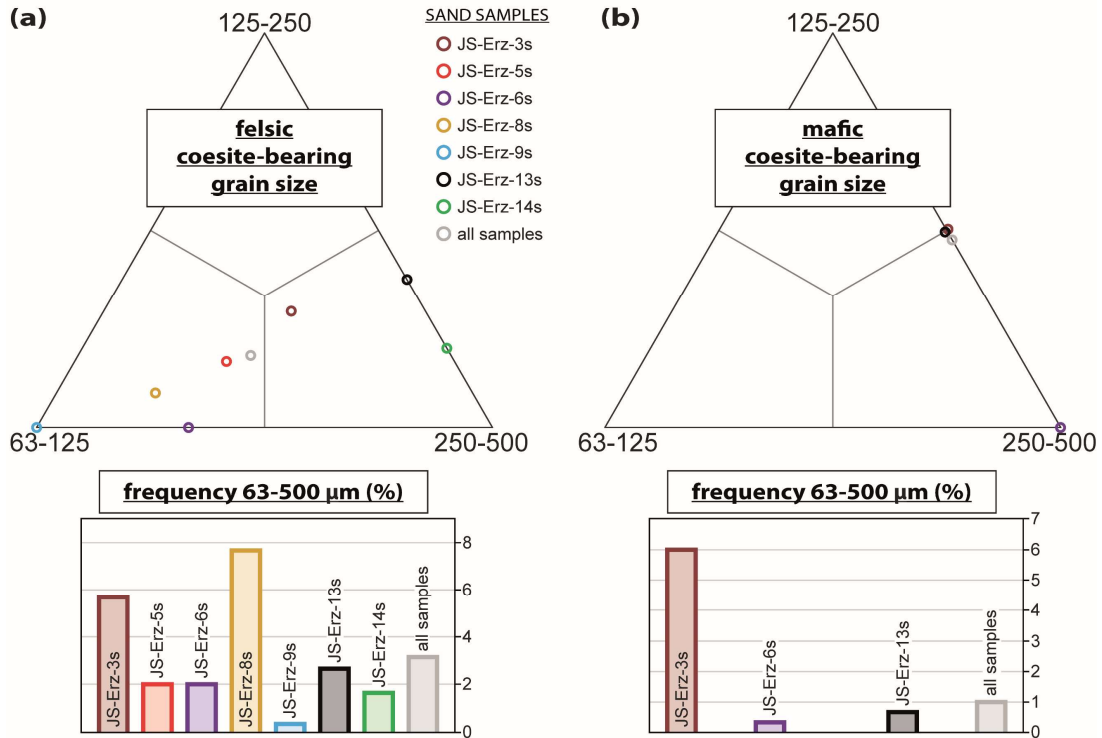


Figure 5.4-7: Grain-size relations and frequency of (a) felsic and (b) mafic coesite-bearing garnet for the individual samples based on the step-wise assignment performed in Figure 5.4-5 and Figure 5.4-6.

lower amount of mafic coesite-bearing garnet in the eastern part of the study area is probably related to a lack of free silica in the eastern eclogites at UHP metamorphic conditions, as proposed for many UHP eclogites (e.g., Carswell & Zhang 1999; Tsai & Liou 2000), rather than lower-pressure, peak metamorphic conditions below the coesite stability field. Regarding grain size, all grains of mafic affinity are strongly enriched in the coarse fractions and none of them occurs in the 63–125 μm fraction (Figure 5.4-7b). This agrees with the increase of high-grade mafic garnet with increasing grain size due to grain-size inheritance from source to sink (see Section 5.4.2).

Felsic coesite-bearing garnet occurs in all samples (Figure 5.4-7a). Notably, although diamond inclusions frequently occur in garnet of sample JS-Erz-9s, only one garnet of the sample contains coesite in a polyphase inclusion together with quartz, graphite and rutile. Discussing the virtual absence of coesite in the diamond-bearing paragneiss is beyond the scope of this paper, but probably relates to: diamond crystallization from an entrapped fluid/melt (as implied from the frequent polyphase inclusions); the pressure conditions after diamond crystallization within the melt inclusions, which strongly differ from external metamorphic conditions; no further garnet growth during exhumation through the coesite stability field; and/or coesite replacement by quartz during exhumation.

The felsic coesite-bearing garnet grains show a much more complex and heterogeneous grain-size distribution compared with mafic garnet (Figure 5.4-7). First of all, felsic coesite-bearing garnet occurs in the 250–500 μm fraction of all samples, suggesting an initially large garnet crystal size (Figure 5.4-7a). Nevertheless, an increase of coesite-bearing garnet with increasing grain size is only observed in the northern samples (JS-Erz-3s, JS-Erz-13s) and sample JS-Erz-14s from the largest catchment, the

Flöha River. Notably, in JS-Erz-14s, the increase with increasing grain size even overcomes the strong dilution by lower-grade metamorphic garnet in the coarse fraction of this sample (see Sections 5.4.1 and 5.4.2). In contrast, the eastern samples JS-Erz-5s, JS-Erz-6s and JS-Erz-8s show an increase of felsic coesite-bearing garnet with decreasing grain size. This enrichment in the fine fraction even overcomes that of graphite- and quartz-bearing garnet (Figure 5.4-2), and calls for an additional process apart from the dilution effect of felsic garnet in the coarse fraction due to the increasing contribution of mafic garnet. The increase with decreasing grain size is most prominent in JS-Erz-8s, the only sample where the ratios of quartz-/omphacite-bearing and kyanite-/omphacite-bearing garnet do not significantly differ with grain size (Figure 5.4-3b). All these observations imply that high-grade felsic garnet grains in JS-Erz-8s started with an initially large garnet size, in particular those containing coesite, but strongly disintegrated into smaller fragments during exhumation, weathering and/or sedimentary transport. This also affected, to a smaller extent, the garnet of sample JS-Erz-5s. The grain size of felsic coesite-bearing garnet in JS-Erz-6s (downstream) mainly resembles that of JS-Erz-8s (upstream) which becomes further diluted by the high proportion of eclogitic garnet (see Section 5.4.2).

In summary, diamond-bearing garnet grains are of felsic affinity, occur only locally and show a strong increase in abundance with increasing grain size. Garnet grains containing coesite are sourced from both mafic and felsic rocks, but felsic coesite-bearing grains are more frequent than mafic (ratio ~3:1). Both felsic and mafic coesite-bearing garnet grains were initially large. While this leads to a strong increase of mafic coesite-bearing garnet with increasing grain size, this trend is observed only for felsic coesite-bearing garnet grains from catchments north of the Saidenbach reservoir. East of the reservoir, in particular for sample JS-Erz-8s, felsic coesite-bearing garnet also shows an initial large crystal size, but the grains strongly disintegrated from source to sink, leading to increasing abundance with decreasing grain size.

5.4.4 Coesite preservation: the role of inclusion size and fluid availability

As well as metamorphic conditions below the coesite stability field, reaction kinetics primarily control whether coesite will be preserved or replaced by quartz (e.g., Mosenfelder et al. 2005). Fluid availability is a necessary pre-condition to enable the coesite-to-quartz transformation as shown by the occasional preservation of matrix coesite under completely dry conditions (Liou & Zhang 1996; Liu et al. 2017). In the presence of moderate amounts of fluid (~0.04 wt%) and temperatures ≥ 375 °C, coesite crystals of ~100 μm will be completely replaced by quartz within <1 Ma (Mosenfelder & Bohlen 1997). Numerous studies of a wide compositional range of crystalline UHP rocks have reported coesite relicts in the center of bimineralic coesite/quartz inclusions, resulting from the partial coesite-to-quartz transformation during exhumation. These bimineralic inclusions typically show radial fractures originating from the host/inclusion boundary and spreading out into their host mineral. For relatively ‘stiff’ host minerals such as garnet (compared with relatively ‘soft’ coesite, e.g., Ferrero & Angel 2018), the fracturing results from the development of non-lithostatic strains and stresses during exhumation due to the different thermoelastic properties of garnet and coesite. The fractures enable metamorphic fluids to infiltrate the coesite inclusions, which were previously shielded from the external conditions by their nominally anhydrous host minerals such as garnet, facilitating the coesite-to-quartz transformation. Considering the fast reaction kinetics, although exhumation rates of UHP terranes such

as the central Erzgebirge are extremely high, the partial preservation of coesite within the inclusions calls for a rather late fracturing, that is, at low temperatures, where reaction kinetics are becoming slow and inhibited shortly thereafter (Mosenfelder 2000).

Fractures in garnet originating from coesite inclusions represent weakness zones and the higher the amount of coesite being transformed to quartz, the more fractures will develop and the wider the fractures will be due to the volume increase during transformation. For the disintegration process of coesite-bearing garnet, it is therefore of major importance (1) whether coesite inclusions fractured their host garnet; (2) whether fluids were present, enabling their transformation to quartz; and (3) at which temperatures fracturing occurred, controlling the reaction kinetics and available time span. Based on the findings of monomineralic coesite inclusions <12 μm in detrital garnet, Schönig et al. (2018a) supposed that inclusion size may be an important factor for coesite preservation.

To evaluate the role of inclusion size with regard to coesite preservation on a significantly larger number of observations, 192 of the 193 detected coesite inclusions were analyzed regarding their size and the presence of quartz (one coesite inclusion in JS-Erz-9s was excluded because of its polyphase inclusion character). For the vast majority, the results were confirmed by high-resolution two-dimensional Raman imaging. Figure 5.4-8 shows the relation between monomineralic coesite inclusions and bimineralic coesite/quartz inclusions in terms of inclusion size. Results are shown in form of a histogram (bars) with logarithmic kernel density estimates (lines), and selected Raman images of the inclusions ordered as a function of their size (all at the same scale; for further examples see Figure Appendix 5-C 1). Monomineralic coesite inclusions are dominant (~82 %). As shown by the kernel density estimate, inclusions with their long axis <9 μm are primarily monomineralic coesite, whereas larger inclusions are primarily bimineralic coesite/quartz. However, the transition from a primarily monomineralic to a primarily bimineralic character is rather smooth and both types occur in the range of 5.5–21.0 μm . This transition range may be narrowed to 7.5–15.0 μm by excluding the two largest monomineralic inclusions and the smallest bimineralic inclusion, as they seem exceptional compared with the general distribution (Figure 5.4-8, histogram). In addition, under the microscope, the smallest

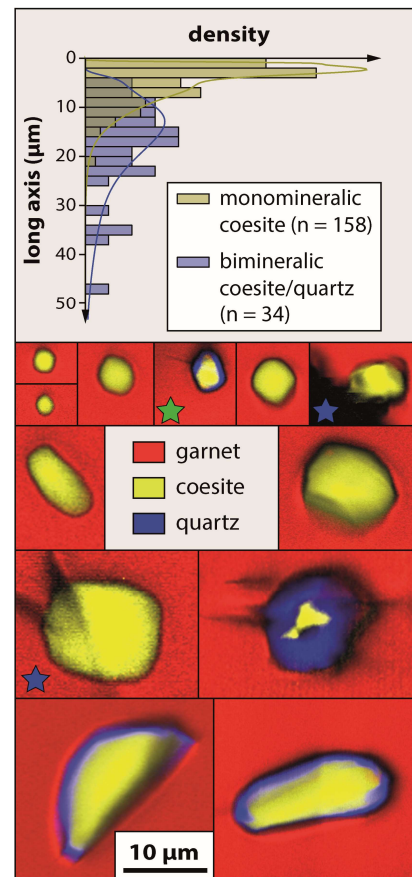


Figure 5.4-8: Monomineralic coesite and bimineralic coesite/quartz inclusions compared to inclusion size. The upper diagram shows a histogram and kernel density estimates of all coesite inclusions, except one inclusion of sample JS-Erz-9s due to its polyphase character. Two-dimensional Raman images show a selection of coesite inclusions at the same scale ordered with regard to inclusion size. Colors correspond to Raman mode intensities of the garnet (red), coesite (yellow), and quartz (blue) components. Colored asterisks mark specific inclusions used as examples in the main text, which are referenced at the corresponding section.

bimineralic inclusion (Figure 5.4-8, green asterisk) seems to be connected to a larger bimineralic inclusion by a fine fracture. Its bimineralic character may therefore originate from a connection to external fluids by the fracture developed from the larger inclusion next to it.

Although monomineralic and bimineralic inclusions occur in a rather large size range, the size seems to be related to the specific garnet where they are entrapped. From the 93 coesite-bearing garnet grains, 10 contain monomineralic as well as bimineralic inclusions, and in each of these grains the bimineralic inclusions are always larger than the monomineralic inclusions. As an example, garnet grains number 55 and number 75 from the coarse fractions of samples JS-Erz-14s and JS-Erz-6s are shown in Figure 5.4-9a and b, respectively (for another example see fig. 2 in Schönig et al. 2019, here Figure 2.2-1). Reasons for the varying inclusion size where the coesite inclusions start to fracture their host garnet and (partially) transform into quartz can be diverse. These may be related to various combinations of: (1) slightly diverging thermoelastic properties of the host garnet grains due to compositional differences (e.g., Milani et al. 2015, 2017); (2) different pressure–temperature conditions during entrapment, predefining the highest attainable strain within the inclusion (e.g., Rosenfeld & Chase 1961; Angel et al. 2015); (3) anisotropic strains, in particular, due to the monoclinic symmetry of coesite and/or varying inclusion shape (Campomenosi et al. 2018; Mazzucchelli et al. 2018; Murri et al. 2018); (4) inclusion strain reduction due to viscous relaxation (e.g., Zhong et al. 2020); and (5) fluid availability (Mosenfelder et al. 2005).

The importance of available fluids for enabling the coesite-to-quartz transformation is highlighted by the presence of H₂O in filigree fractures and at the inclusion/host boundary of several bimineralic coesite/quartz inclusions (Figure 5.4-9b and c, pink component). Even more importantly, carbonaceous material was observed in some bimineralic inclusions, indicating the infiltration by a carbonaceous fluid (Figure 5.4-9d, green component). The Raman spectrum allows the peak temperatures of the carbonaceous material precipitated from the infiltrated fluid to be estimated. By applying the thermometer of Lünsdorf et al. (2017), carbonaceous material in two bimineralic coesite/quartz inclusions of Figure 5.4-9d give peak temperatures of 321 °C and 341 ± 36 °C, respectively. In addition, although the signal-to-noise ratio of the Raman spectrum of carbonaceous material in another bimineralic inclusion does not allow temperature calculations, its pattern qualitatively points to similar temperatures. This shows that partially transformed coesite inclusions fractured their host garnet at a late exhumation state. Based on the experiments of Mosenfelder & Bohlen (1997), reaction kinetics slow down by two orders of magnitude from ~375 °C to ~320 °C. For the preservation of coesite, small differences in the timing (i.e., temperature) of garnet fracturing are therefore crucial.

In summary, coesite inclusion size represents a primary factor that controls whether the host garnet will be fractured during exhumation and at which temperatures the fracturing takes place. This in turn controls the temperature at which fluids are able to infiltrate the coesite inclusions, the reaction kinetics and the time left for the coesite-to-quartz transformation. Even small differences in the timing of fracturing and fluid infiltration have significant consequences for the proportion of coesite being transformed into quartz. Although the critical inclusion size for garnet fracturing is well-defined for individual grains, it shows a rather large range considering the entire detrital coesite-bearing garnet record. Considering all the additional factors in detail is beyond the scope of this study; however, all

these factors are related to the composition and metamorphic evolution of the initial coesite-bearing host rock.

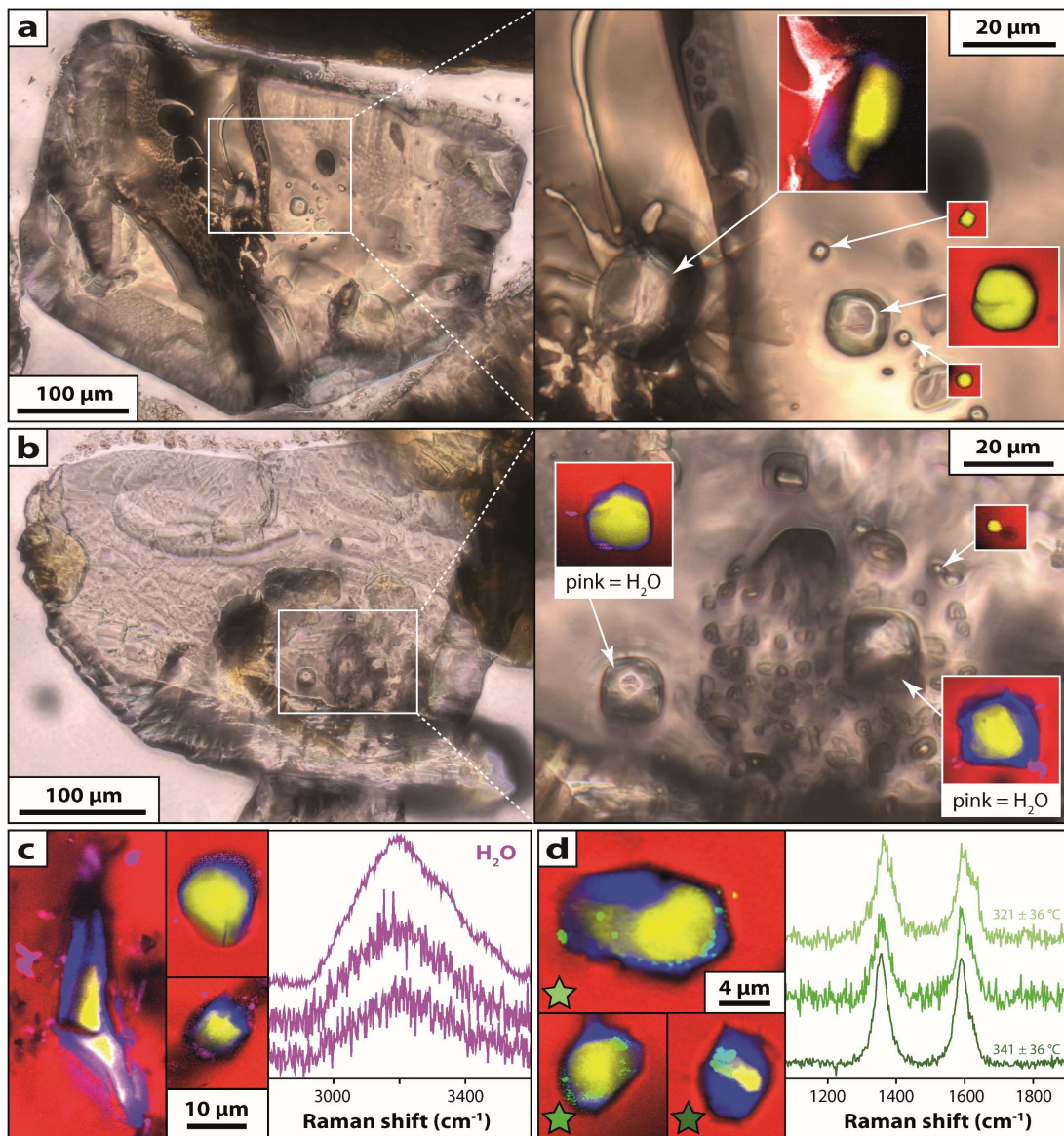


Figure 5.4-9: Photomicrographs and Raman images of selected garnet grains and coesite inclusions. Colors in Raman images correspond to mode intensities of garnet (red), coesite (yellow), quartz (blue), embedding medium (white), H₂O (pink), and carbonaceous material (green). (a) Garnet number 55 from the 250–500 µm fraction of sample JS-Erz-14s showing the inclusion-size dependence on the monomineralic versus bimineralic state. (b) Garnet number 75 from the 250–500 µm fraction of sample JS-Erz-6s again showing the inclusion-size dependence and the presence of H₂O in bimineralic inclusions. (c) Several examples of bimineralic coesite/quartz inclusions containing water at fractures and the inclusion/host boundary and the corresponding H₂O Raman spectra. (d) Bimineralic coesite/quartz inclusions containing carbonaceous material at the inclusion/host boundary and the corresponding Raman spectra with peak temperature estimates after Lünsdorf et al. (2017). Colors of asterisks in the Raman images correspond to colors of the Raman spectra.

5.4.5 Source-rock- and catchment-specific coesite inclusion characteristics

Fractures originating from coesite inclusions lead to a disintegration of the initially large garnet grains from UHP source rocks into smaller fragments. This disintegration process is most intense for bimineralic coesite/quartz inclusions, whereby the fractures often form the detrital garnet surface (e.g., Figure 5.4-9a). However, several monomineralic coesite inclusions also show fractures promoting the disintegration of garnet (e.g., Figure 5.4-8; Figure Appendix 5-C 1, blue asterisks, dark contrasts). Thus, the higher the amount of coesite inclusions per detrital garnet grain and the more of these inclusions transformed to quartz (partially or completely), the higher the degree of garnet disintegration.

To evaluate the disintegration process of coesite-bearing garnet from mafic and felsic sources as well as for the individual catchments, Figure 5.4-10 shows logarithmic kernel density estimates for monomineralic versus bimineralic inclusions with regard to the sample and assigned source. Bar-plots show the accompanying density of coesite inclusions, that is, the average number of coesite inclusions per coesite-bearing garnet grain, for the entire 63–500 μm fraction and for each of the individual three grain-size fractions. For comparison, grey vertical lines indicate the intersection of monomineralic versus bimineralic kernel density estimates for all coesite-bearing garnet grains at $\sim 9 \mu\text{m}$ and the accompanied density of coesite inclusions of ~ 2.1 per coesite-bearing garnet.

In comparison to all coesite-bearing garnet grains, the changeover from a primary monomineralic to a primary bimineralic state occurs at $\sim 3 \mu\text{m}$ larger inclusion size for mafic coesite-bearing garnet (Figure 5.4-10, left side, green line). As samples JS-Erz-6s and JS-Erz-13s contain only very few mafic coesite-bearing grains, this mainly reflects the characteristics from sample JS-Erz-3s, where mafic coesite-bearing garnet is frequent. The bar-plots furthermore show that the mafic grains contain less coesite inclusions per grain compared with all coesite-bearing garnet grains (Figure 5.4-10, right side, green line), and that the number of coesite inclusions per grain increases with increasing grain size. Consequently, the low inclusion density, the late fracturing of the host garnet (i.e., inclusions have to be large and the temperature has to be low) and therefore the lower potential of coesite inclusions to transform into quartz inhibit a strong disintegration of mafic coesite-bearing garnet. This results in enrichment in the coarser detrital fractions compared with the fine fraction as observed in Figure 5.4-7b, and an increasing number of coesite inclusions with increasing grain size due to the higher analyzed garnet volume.

In contrast to mafic garnet, the changeover from the monomineralic to bimineralic state for felsic coesite-bearing garnet occurs at a significantly smaller inclusion size (Figure 5.4-10, left side, red line). In addition, the inclusion density is higher (Figure 5.4-10, right side, red line) and increases with decreasing grain size. However, there are strong differences between the individually sampled catchments.

Samples JS-Erz-6s and JS-Erz-8s from the eastern part of the study area, which are both strongly enriched in coesite-bearing garnet in the fine fraction (Figure 5.4-7a), show a changeover from the monomineralic to the bimineralic state at even smaller inclusion sizes than the average of felsic garnet grains. This is accompanied by the highest number of coesite inclusions per grain observed in these samples (Figure 5.4-10). Moreover, the fact that much more coesite inclusions per grain occur in the finest fraction, although the analyzed volume is the smallest, indicate a felsic source rock with a large

initial garnet crystal size and varying coesite inclusion density, whereby those garnets with the highest coesite inclusion density preferentially disintegrated into smaller fragments. Notably, the proportion of

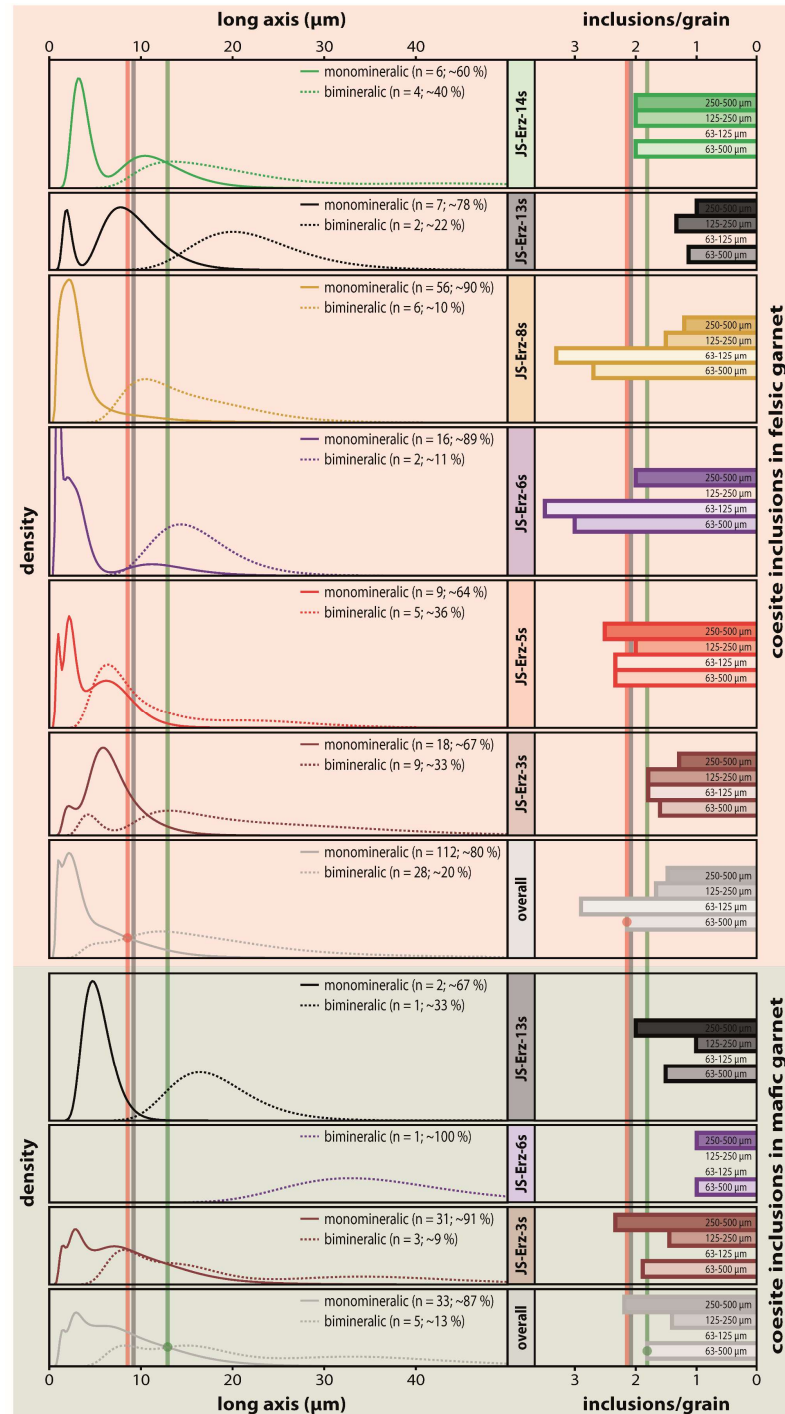


Figure 5.4-10: Distribution of monomineralic coesite versus bimineralic coesite/quartz inclusions and inclusion frequency with regard to the individual sample and assigned source. Left side shows logarithmic kernel density estimates. Right side shows barplots of the accompanied frequency of coesite inclusions, i.e., the average number of coesite inclusions per coesite-bearing garnet grain. For comparison, grey vertical lines indicate the intersection of monomineralic versus bimineralic kernel density estimates for all coesite-bearing garnet grains and the accompanied frequency of coesite inclusions. Vertical lines are also shown for felsic (red) and mafic (green) coesite-bearing garnet.

bimineralic inclusions in garnet of the two samples is rather low at ~10 and ~11 %, respectively. This seems counterintuitive at first instance. However, considering that coesite inclusions fractured their host garnet at higher temperatures, at which reaction kinetics are much faster, and also that small inclusions that fractured their host garnet have much less volume of coesite to be replaced by quartz, most coesite inclusions that were infiltrated by fluids probably completely transformed to quartz. As the coesite-to-quartz transformation is accompanied by a volume increase of ~10 %, this further promotes fracture opening and garnet disintegration.

As well as JS-Erz-6s and JS-Erz-8s, coesite inclusions in garnet of JS-Erz-5s show a changeover from a primary monomineralic to a primary bimineralic state at small inclusion size, even smaller than for JS-Erz-6s and JS-Erz-8s (Figure 5.4-10), accompanied by a high coesite inclusion density. Nevertheless, the coesite density is lower than in JS-Erz-6s and JS-Erz-8s and there is no enrichment of coesite inclusions in a specific grain-size fraction. In addition, the transition zone regarding inclusion size where both monomineralic and bimineralic inclusions occur is very broad. These observations indicate that coesite inclusion density has a strong control on this transition zone. It therefore seems likely that the higher the inclusion density, the higher the potential that fractures originating from large coesite inclusions connect to smaller coesite inclusions, paving the way for fluids to infiltrate the smaller inclusions and enable their transformation to quartz. Moreover, the higher the inclusion density, the more likely that stress fields from adjacent coesite inclusions overlap and may concentrate at specific locations (e.g., Howell et al. 2010), and the more likely that coesite inclusions occur close to the garnet rim so that stress fields extend beyond the garnet host facilitating fracture development (e.g., Campomenosi et al. 2018; Zhong et al. 2020). In conclusion, JS-Erz-5s is similar to JS-Erz-6s and JS-Erz-8s but the lower inclusion density led to a slightly lower disintegration of garnet, which explains that coesite-bearing garnet in JS-Erz-5s is enriched in the fine fraction but less strong than JS-Erz-6s and JS-Erz-8s.

In contrast to the three samples from the eastern study area discussed above, felsic coesite-bearing garnet grains from the northern samples JS-Erz-3s and JS-Erz-13s show a much lower coesite inclusion density and a changeover from monomineralic to bimineralic at a larger inclusion size (Figure 5.4-10). This is best expressed for sample JS-Erz-13s that shows the lowest density and the largest changeover leading to a strong enrichment of coesite-bearing garnet in the coarse fractions (Figure 5.4-7). Felsic coesite-bearing garnet of JS-Erz-3s is also enriched in the coarse fractions but less strongly than for JS-Erz-13s, agreeing with the still low but higher inclusion density. Felsic coesite-bearing garnet of sample JS-Erz-14s is intermediate between JS-Erz-3s and JS-Erz-13s. Although the inclusion density is slightly higher, this is mainly a result of the low number of coesite-bearing grains in this sample (Figure 5.4-4 and Figure 5.4-7) and a single garnet grain containing four coesite inclusions (Figure 5.4-9a), which strongly influence the averaged inclusion density. Regardless, due to the large catchment of JS-Erz-14s comprising lower-grade metamorphic rocks, this sample is less suitable to draw conclusions on the grain-size distribution of coesite-bearing garnet.

In summary, although coesite inclusion size represents a superordinate factor controlling the timing of fracturing during exhumation, the differences in grain-size distribution of coesite-bearing garnet from mafic and felsic sources as well as between the single catchments is highly influenced by coesite inclusion density. Mafic garnet shows the lowest number of coesite inclusions, and the fracturing

therefore mainly depends on inclusion size. This leads to a low disintegration potential and an enrichment of mafic coesite-bearing garnet in the coarse garnet grain-size fraction. Felsic coesite-bearing garnet shows a wide range of inclusion density with higher values in the eastern catchments and lower values in the northern catchments. Coesite-bearing felsic garnet from northern catchments therefore behaves more similar to mafic garnet, that is, fracturing is mainly controlled by inclusion size leading to an enrichment in the coarse garnet fraction. In contrast, the disintegration of coesite-bearing felsic garnet from the eastern catchments is not only controlled by inclusion size but more importantly by inclusion density. The high inclusion density leads to a higher disintegration, and thus to an enrichment in the fine detrital garnet fraction.

5.4.6 A model of coesite-bearing garnet disintegration

Based on all the observations, a model for the disintegration of coesite-bearing garnet during exhumation, weathering and sedimentary transport can be deduced. This model starts with inclusion entrapment, assuming a temperature of ~950 °C, agreeing with estimates for local UHP rocks (e.g., Schmädicke et al. 1992; Nasdala & Massonne 2000; Zack & Luvizotto 2006). The model considers: (1) mafic garnet with inclusions of omphacite, rutile and lesser kyanite that co-exist with less abundant coesite inclusions; (2) felsic garnet poor in coesite inclusions, which co-exists with graphite, rutile, kyanite and apatite; and (3) felsic garnet rich in coesite inclusions (Figure 5.4-11a).

During the pressure and temperature reduction caused by exhumation, a relatively ‘soft’ coesite inclusion will expand more than the cavity in the relatively ‘stiff’ garnet host. If no elastic re-equilibration occurs, an increasing positive strain therefore develops within the inclusion with increasing exhumation state, that is, the coesite inclusion becomes ‘overpressured’ compared with the external metamorphic conditions (Figure 5.4-11b, black arrows). This overpressure is independent of inclusion size. At a specific point along the exhumation path, the inclusion overpressure may become high enough to fracture the host garnet (e.g., van der Molen & van Roermund 1986). As shown in Section 5.4.4, a large coesite inclusion fractures its host garnet at a higher temperature and therefore lower overpressure than a small inclusion. Most likely, this is related to a longer inclusion/host boundary of large inclusions defining a larger initial fracture length that can more easily propagate than a smaller fracture length (Whitney et al. 2000). Based on the temperatures of ~330 °C for fluid infiltration estimated from the Raman spectrum of carbonaceous material in $\leq 14 \mu\text{m}$ bimineralic coesite/quartz inclusions (Figure 5.4-9d), it can be concluded that fracturing is a late process during exhumation. Although the timing of fracturing for larger inclusions is speculative, it must take place earlier, that is, at higher temperatures (Figure 5.4-11b).

Once the fractures of large coesite inclusions reach the garnet surface, the inclusions are no longer isolated from metamorphic fluids in the system, enabling the coesite-to-quartz transformation (Figure 5.4-11c). For garnet grains rich in coesite inclusions, fractures originating from large inclusions have a high probability of connecting small inclusions to the external conditions (Figure 5.4-11c, red arrows). At the same stage, the next smaller coesite inclusions are able to propagate their initial fractures into the garnet host. This process continues to the next time slice and increasingly smaller inclusions fracture the host garnet, resulting in a close-meshed fracture network for felsic garnet that is rich in coesite inclusions, which is less pronounced in inclusion-poor garnet (Figure 5.4-11d). As well as the higher

number of larger coesite inclusions and the higher probability of smaller inclusions to be connected by fractures from larger inclusions, the high inclusion density also makes it more likely that smaller

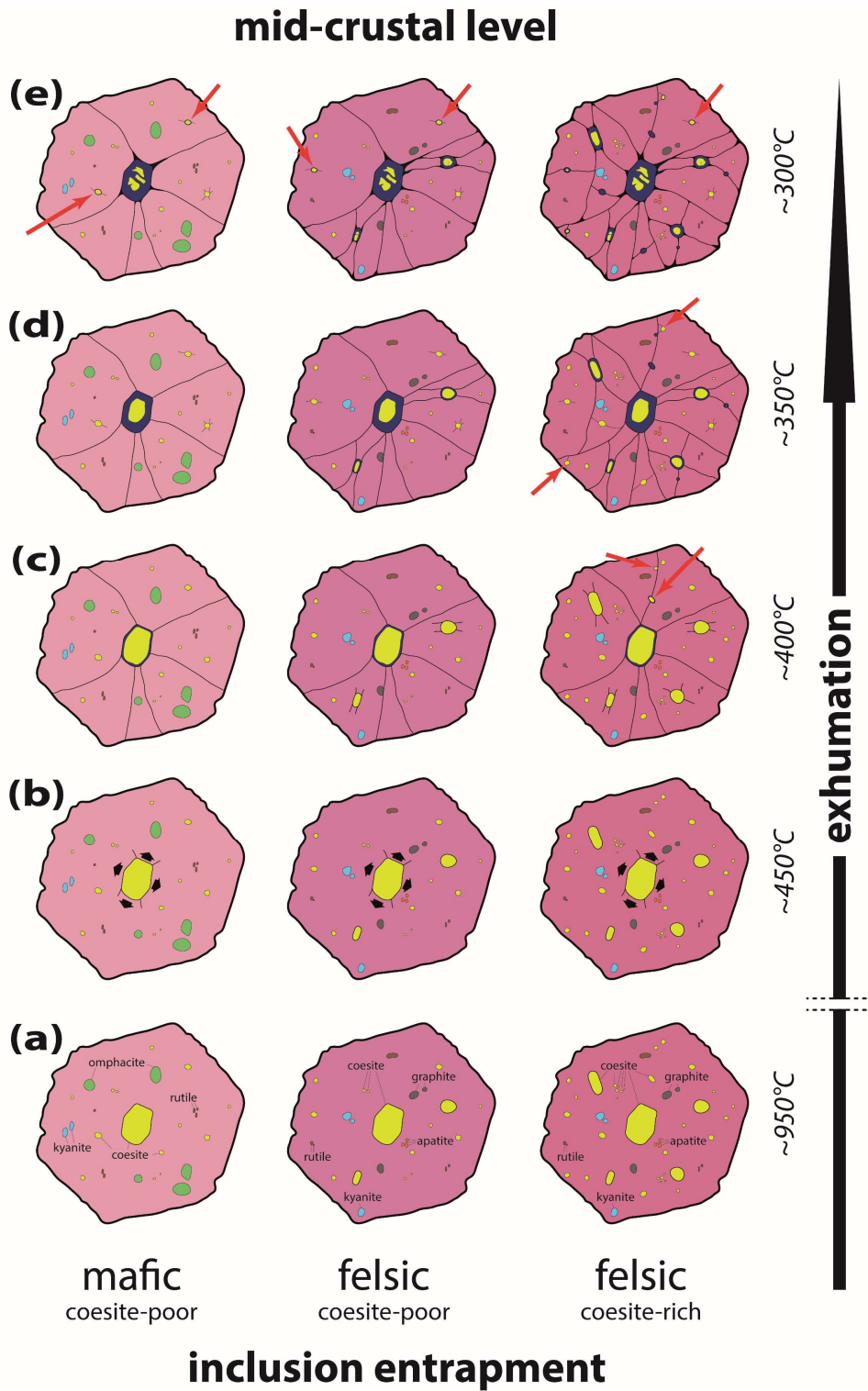


Figure 5.4-11: Disintegration model for coesite-bearing garnet from entrapment to exhumation to mid-crustal levels. (a) – (e) corresponds to different time/temperature slices during exhumation (see explanation in the text).

inclusions are located close to the garnet surface and other fractures. These inclusions are not elastically isolated; their stress fields extend beyond the next fracture or garnet surface (e.g., Campomenosi et al. 2018; Zhong et al. 2020) and they are therefore likely to fracture their host garnet earlier than similar-sized but isolated inclusions (Figure 5.4-11d, red arrows). Because of the still fast reaction kinetics at 400–350 °C, high proportions of the coesite inclusions becoming connected to the external conditions transform into quartz. In particular, small inclusions will completely transform into quartz. As this transformation is accompanied by a volume increase of ~10 %, fractures will not heal and instead become wider as long as coesite is left to be transformed.

Based on reaction kinetics, during the 350–300 °C time slice the coesite-to-quartz transformation dramatically slows down and finally becomes inhibited (Mosenfelder & Bohlen 1997). Inclusions in the critical size range of 7.5–15.0 µm fractured the host garnet shortly before and only a tiny rim was transformed into quartz (Figure 5.4-11e, red arrows). For garnet poor in coesite inclusions, these smallest bimineralic coesite/quartz inclusions show a filigree of fine fractures and are likely to be preserved in garnet fragments. In contrast, for inclusion-rich felsic garnet, the fine fractures are more likely to connect to other fractures, resulting in a higher amount of coesite being transformed into quartz and a primary location at the surface of the individual garnet fragments. Below 300 °C, the coesite inclusion pressure still increases and some inclusions may fracture the host garnet, but the coesite-to-quartz transformation is kinetically inhibited (Mosenfelder 2000).

When the coesite-bearing garnets reach the Earth's surface, they are exposed to weathering processes; at the transition to the sedimentary system, the garnet grains disintegrate along the fracture network created during exhumation (Figure 5.4-12a). In particular, physical weathering has a major influence as surface water can easily infiltrate along the fractures. Because of the more pronounced fracture network of felsic garnet being rich in coesite inclusions, these grains will disintegrate in finer fragments. In contrast, the erosion of inclusion-poor felsic and mafic garnet results in fewer and coarser fragments. Even if some fine fragments exist, they are less likely to contain coesite because of the overall lower number of coesite inclusions.

During sedimentary transport, the erosional material is subjected to further mechanical stress. In this way, the large bimineralic coesite/quartz inclusions will often enter the sedimentary system as individual grains (Figure 5.4-12b). Any palisade quartz rims surrounding the coesite inclusions are unstable against mechanical stress and will be quickly abraded. This is shown, for instance, by bimineralic inclusions located at the garnet surface or along wide fractures where the quartz rim has been partially or completely lost and now the remaining cavity is filled by the embedding medium (Figure Appendix 5-C 1, white component). The produced garnet fragments will be rounded, whereby the loss in volume will be higher for fragments from felsic coesite inclusion-rich garnet because these finer fragments have a much higher surface-to-volume ratio than coarse fragments.

Taken together, sediment derived from felsic UHP rocks with garnet rich in coesite inclusions will have mainly fine-grained garnet fragments often containing coesite inclusions and less coarse-grained fragments, which also contain coesite (Figure 5.4-12b). Bimineralic coesite/quartz inclusions are less likely to be preserved in the fine-grained fragments because of the high probability of connecting their fractures to others; they are therefore often completely transformed or enter the sedimentary system as

individual grains. In contrast, sediment derived from felsic and mafic UHP rocks with garnet being poor in coesite inclusions will have mainly coarse-grained fragments containing coesite and few fine-grained fragments, which often do not contain coesite inclusions.

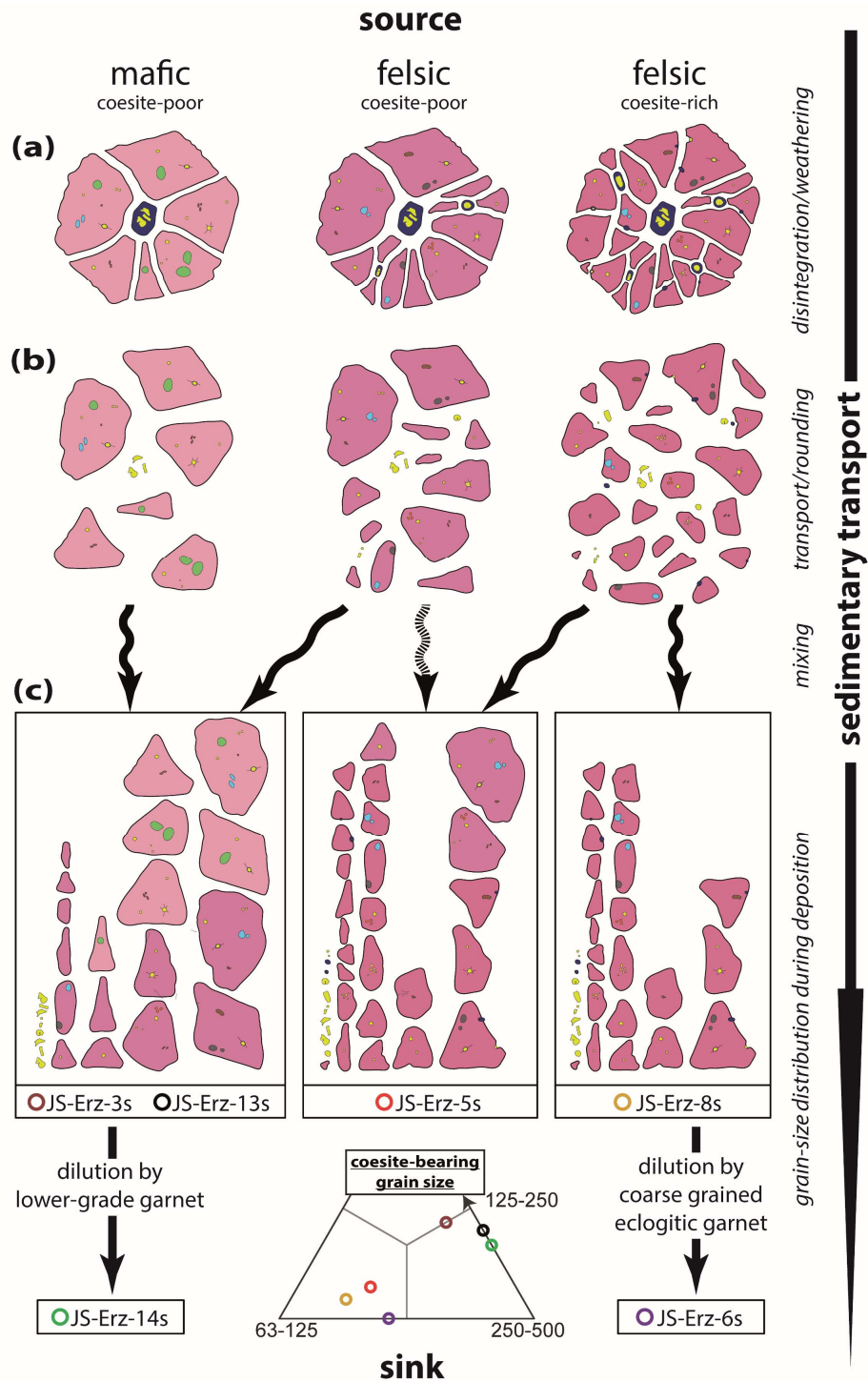


Figure 5.4-12: Disintegration model for coesite-bearing garnet from source to sink. (a) Weathering at surface conditions and transition to the sedimentary system. (b) Rounding and further disintegration during sedimentary transport. (c) Mixing of garnet sourced from different UHP rocks explaining the observed heterogeneous grain-size distribution of coesite-bearing garnet.

Mixing of these source-rock-specific garnet fragments can explain the grain-size distribution of coesite-bearing garnet in the individual samples as observed in Figure 5.4-4 for all garnet grains (also shown in Figure 5.4-12) and in Figure 5.4-7 for garnet separated in felsic and mafic origin. The northern samples JS-Erz-3s and JS-Erz-13s show mixing of coesite-poor mafic and felsic garnet leading to a strong enrichment of coesite-bearing garnet in the coarse fraction (Figure 5.4-12c). Further downstream at sample JS-Erz-14s, this signal becomes diluted by the strong contribution of garnet from lower-grade metamorphic lithologies occurring in the large catchment, leading to an even stronger enrichment in the coarse fraction. In the eastern part of the study area, sample JS-Erz-8s shows the characteristics of felsic UHP rocks shedding garnet grains rich in coesite inclusions, resulting in an enrichment of coesite-bearing garnet in the fine fraction. Further downstream to JS-Erz-6s, this signal becomes diluted in the coarse fraction by the strong input of mafic coarse-grained garnet from the large eclogite lenses that rarely contain coesite. Coesite-bearing garnet in JS-Erz-5s is similar to JS-Erz-8s but slightly less enriched in the fine fraction, which points to minor contributions of felsic garnet poorer in coesite inclusions.

5.4.7 Selecting the most efficient garnet grain-size fraction

Garnet grains from the seven modern sand samples of the central Saxonian Erzgebirge analyzed for their mineral inclusion assemblage provide a good example of increasing provenance information by widening the analyzed grain-size window (e.g., Garzanti et al. 2009). Initially, the 125–250 μm fraction was investigated. As well as the finding of diamond inclusions in one of the seven samples, coesite inclusions in five of the seven samples revealed that UHP metamorphism affected a larger area than previously assumed, and that both mafic and felsic lithologies were involved (Schönig et al. 2019). Additional analyses of the 63–125 μm and 250–500 μm fractions revealed that: (1) diamond also occurs in another sample; (2) all seven catchments drain coesite-bearing lithologies; and (3) most importantly, the felsic country rocks surrounding the UHP lenses also underwent a UHP stage before re-equilibration at HP/HT conditions (Schönig et al. 2020). However, when considering future studies where large regions are screened by many samples from large drainage systems, it becomes inefficient to apply the time-consuming mineral inclusion analysis to a large number of garnet grains from several grain-size fractions from each sample. When applying detrital garnet analysis to a new terrane in order to decipher the metamorphic history, key questions include the following: (1) Did rocks of the region undergo UHP metamorphism? (2) Did they reach the diamond stability field? (3) What kind of lithologies were involved?

To answer the first and second question, the finding of a single garnet grain of crustal origin containing coesite and/or diamond is already sufficient, whereas to answer the third question at least a few grains are necessary. With regard to efficiency, the selection of a specific grain-size fraction with the highest potential to solve the questions in the least amount of time is therefore important. In our case, the screening of the inclusion assemblages of 100 garnet grains in the 125–250 μm and 250–500 μm fractions took on average ~ 1.3 (17 hours) and ~ 1.8 (24 hours) times longer than for the 63–125 μm fraction (13 hours). Although the absolute time needed will vary significantly between different laboratories, the relative ratios will be similar.

To evaluate which fraction is most suitable in terms of UHP garnet, the information value must be compared with the invested analytical time. Because diamond-bearing garnet is restricted to two samples, the most efficient grain-size fraction to detect UHP garnet grains is strongly controlled by the heterogeneous grain-size distribution of coesite-bearing garnet, which in turn is mainly controlled by the grain-size distribution of felsic coesite-bearing garnet. In consequence, although the most efficient grain-size fraction varies for the individual samples (see Figure Appendix 5-D 1), on average none of the fractions is more favorable than any other; the fraction with the highest information value should therefore be selected.

If considering solely the 63–125 μm fraction, the UHP rocks occurring in the catchments of JS-Erz-13s and JS-Erz-14s would not have been detected, including diamond-bearing rocks in JS-Erz-14s. In addition, for detecting mafic coesite-bearing rocks the 63–125 μm fraction is not suitable (JS-Erz-3s and JS-Erz-6s) and also shows the lowest efficiency for detecting diamond-bearing rocks. When considering solely the 125–250 μm fraction, the UHP rocks occurring in the catchment of JS-Erz-6s, the coesite-bearing rocks in the catchment of JS-Erz-9s and the diamond-bearing rocks in the catchment of JS-Erz-14s would not have been detected. Furthermore, the 125–250 μm fraction shows the lowest efficiency for detecting felsic coesite-bearing garnet (see Figure Appendix 5-D 1). In contrast, the 250–500 μm fraction provides overall the highest information value and efficiency. With the exception of the single coesite-bearing garnet in JS-Erz-9s, no information in terms of the erosion of felsic coesite-bearing rocks, mafic coesite-bearing rocks, and diamond-bearing rocks would be missed in any of the samples by considering solely the 250–500 μm fraction. However, this result cannot be generalized as the 250–500 μm garnet fraction from a sample of the Western Gneiss Region of Norway lacked coesite-bearing garnet, whereas coesite-bearing garnet was found in the 63–125 μm and 125–250 μm fractions (Schönig et al. 2018a).

In summary, when exploring a new region with regard to presence of UHP rocks by the detrital approach, it is most efficient to start with the 250–500 μm fraction. In the case that the investigated sediment or sedimentary rock contains fine or very fine sand only, it is recommended to start with the coarsest grain-size fraction available. An absence of UHP garnet grains in the starting fraction does not necessarily rule out the presence of UHP rocks in the sampled catchment, but makes it much less likely. Once UHP garnet is detected, it is highly recommended to screen a wider grain-size window to achieve sufficient information with regard to UHP source rocks.

5.5 Conclusions

The key findings of this sedimentary provenance study of modern sand samples from tributaries draining the UHP nappe in the central Saxonian Erzgebirge, Germany, can be summarized as follows.

1. The geochemical composition of detrital garnet well reflects the geological framework of the sampled catchments, and shows that grain-size inheritance effects are variable and strongly control garnet grain-size distributions. Garnet grains of samples draining exclusively the UHP area typically show an increase in metamorphic grade with increasing grain size, agreeing with the large garnet crystal size in eclogite and high-grade felsic gneiss. However, when mixed with garnet from lower-grade metamorphic units, the grain-size distribution can be completely

reversed; this is most likely related to the large crystal size of garnet from micaschist sources. To attain sufficient garnet provenance information, a wide grain-size window should therefore be considered.

2. A combination of garnet composition and mineral inclusion assemblages is a powerful tool to resolve specific source-rock characteristics with regard to detrital garnet grain-size relations by mineralogical evidence. In particular, the proportions of omphacite- versus graphite-bearing garnet are useful to discriminate eclogitic versus felsic sources, reflecting the proportions of eclogite occurring in the individual catchments and showing that the amount of eclogitic garnet increases with increasing grain size. In addition, the proportions of quartz- versus kyanite-bearing garnet compared with omphacite-bearing garnet also show that the amount of garnet shed from high-grade felsic sources increases with increasing grain size.
3. Diamond-bearing garnet grains are of felsic origin, occur only locally, and their amount increases with increasing grain size.
4. Coesite-bearing garnet grains are mainly sourced from felsic lithologies, but significant amounts are also shed from eclogite, in particular in the northern study area. Although all coesite-bearing garnet grains show an initially large grain size, they disintegrated in varying degrees leading to a heterogeneous grain-size distribution. The amount of mafic coesite-bearing garnet generally increases with increasing grain size. Felsic coesite-bearing garnet grains in the northern samples also show an increase with increasing grain size, but those from the eastern samples show a decrease with increasing grain size.
5. A primary factor for the preservation of coesite inclusions is the inclusion size. Inclusions <math><9\ \mu\text{m}</math> are primarily monomineralic, whereas most larger inclusions partially transformed into quartz. Large inclusions are able to fracture their host garnet at an earlier exhumation stage due to their larger initial fracture length. This in turn controls the temperature conditions at which fluids are able to infiltrate the inclusions, facilitating the coesite-to-quartz transformation. Temperature estimates of carbonaceous material precipitated from fluids in bimineralic coesite/quartz inclusions show that fracturing and transformation are a late process during exhumation occurring at $\sim 330\ ^\circ\text{C}$.
6. As well as inclusion size, the number of coesite inclusions per garnet grain strongly controls garnet disintegration during the exhumation processes of the sedimentary cycle. The higher the number of coesite inclusions, the higher the degree of fracturing, the higher the probability of fracture connections, the earlier the fluids are able to infiltrate and the more likely that even small inclusions will transform into quartz, leading to stronger disintegration into smaller garnet fragments.
7. Coesite-bearing garnet of the northern samples originates from mafic and felsic UHP rocks poor in coesite inclusions, resulting in minor garnet disintegration into coarse fragments; the amount of coesite-bearing garnet therefore increases with increasing grain size. In contrast, coesite-bearing garnet of the eastern samples mainly originates from felsic UHP rocks rich in

coesite inclusions, resulting in strong garnet disintegration; the amount of coesite-bearing garnet therefore decreases with increasing grain size.

8. The 250–500 μm detrital garnet grain-size fraction is most efficient, in terms of invested analytical time, in providing the highest information value in terms of UHP source rocks.

Acknowledgements

This work was supported by the German Research Foundation (DFG grant EY 23/27-1). We thank JE Dunkl, I Nagy, I Dunkl and A Grebe for their support with sample preparation, and A Kronz for providing access to the electron microprobe. The manuscript benefitted from thoughtful reviews by two anonymous reviewers.

Garnet major-element composition as an indicator of host-rock type: a machine learning approach using the random forest classifier

Jan Schönig¹, Hilmar von Eynatten¹,
Raimon Tolosana-Delgado², and Guido Meinhold^{1,3,4}

¹*Geosciences Center Göttingen, University of Göttingen, Germany*

²*Helmholtz-Zentrum Dresden-Rossendorf, Helmholtz Institute Freiberg, Germany*

³*School of Geography, Geology and the Environment, Keele University, United Kingdom*

⁴*Institute for Geology, TU Bergakademie Freiberg, Germany*

accepted 13th October 2021

Contributions to Mineralogy and Petrology

<https://doi.org/10.1007/s00410-021-01854-w>

The major-element chemical composition of garnet provides valuable petrogenetic information, particularly in metamorphic rocks. When facing detrital garnet, information about the bulk-rock composition and mineral paragenesis of the initial garnet-bearing host rock is absent. This prevents the application of chemical thermobarometric techniques and calls for quantitative empirical approaches. Here we present a garnet host-rock discrimination scheme that is based on a random forest machine-learning algorithm trained on a large dataset of 13,615 chemical analyses of garnet that covers a wide variety of garnet-bearing lithologies. Considering the out-of-bag error, the scheme correctly predicts the original garnet host rock in (i) >95 % concerning the setting, that is either mantle, metamorphic, igneous, or metasomatic; (ii) >84 % concerning the metamorphic facies, that is either blueschist/greenschist, amphibolite, granulite, or eclogite/ultrahigh-pressure; and (iii) >93 % concerning the host-rock bulk composition, that is either intermediate–felsic/metasedimentary, mafic, ultramafic, alkaline, or calc–silicate. The wide coverage of potential host rocks, the detailed prediction classes, the high discrimination rates, and the successfully tested real-case applications demonstrate that the introduced scheme overcomes many issues related to previous schemes. This highlights the potential of transferring the applied discrimination strategy to the broad range of detrital minerals beyond garnet. For easy and quick usage, a freely accessible web app is provided that guides the user in five steps from garnet composition to prediction results including data visualization.

6.1 Introduction

Garnet is one of the most useful minerals in Earth Sciences providing key information on mantle, metamorphic, metasomatic, and igneous processes (e.g., Baxter et al. 2013). Due to its widespread occurrence and its wide compositional range that mainly depends on pressure, temperature, and host-rock composition, garnet major-element chemistry became a well-established tool in sedimentary provenance analysis (e.g., Krippner et al. 2014) and economic exploration campaigns (e.g., Hardman et al. 2018). Apart from discriminating different source regions, the potential capability of extracting

petrogenetic host-rock information in terms of geological setting, metamorphic conditions, and composition by solely considering garnet single grains is of particular significance in interdisciplinary research linking sedimentary, metamorphic, tectonic, and geodynamic processes (e.g., Schönig et al. 2018a).

For instance, our knowledge about the evolution of metamorphism and plate tectonic regimes through time is mainly based on the preserved crystalline rock record (e.g., Brown & Johnson 2018; Holder et al. 2019), which is increasingly incomplete with increasing age (e.g., Goodwin 1996). To overcome this issue, detrital zircon is commonly used and has been shown to provide important information on eroded crustal rocks, enabling a more reliable global-scale reconstruction of continental growth and igneous suites throughout Earth history (e.g., Dhuime et al. 2017, and references therein). Similar approaches to reconstruct metamorphic conditions and/or plate tectonic regimes via the detrital record are absent, but garnet major-element chemistry provides a potential tool to tackle this issue. However, to link detrital garnet composition with petrogenetic host-rock information a robust statistical model with reliable prediction success is required.

Since the first application of detrital garnet major-element chemistry to constrain different source regions (Morton 1985), several petrogenetic schemes have been developed to discriminate specific garnet host rocks (Teraoka et al. 1998; Schulze 2003; Mange & Morton 2007; Aubrecht et al. 2009; Suggate & Hall 2014; Hardman et al. 2018; Tolosana-Delgado et al. 2018). Until 2018, all schemes used strict and subjective compositional fields to discriminate garnet source rocks by considering a subset of available variables. Krippner et al. (2014) and Suggate & Hall (2014) demonstrated that this approach leads to high misclassification rates due to large compositional overlaps of garnets from various source rocks. Notably, although garnet growth stages are often preserved by compositional zoning (e.g., Tracy et al. 1976; Tracy 1982), the composition does (i) not always pinpoint unique growth conditions (e.g., Lanari et al. 2017), (ii) may be influenced by progressive fractionation of the reactive bulk-rock composition (e.g., Lanari & Engi 2017), and (iii) may be modified by post-growth diffusion at high temperatures (e.g., Caddick et al. 2010).

Recently, the usage of robust multivariate statistics has been shown to significantly improve classification results (Hardman et al. 2018; Tolosana-Delgado et al. 2018). While Hardman et al. (2018) focus on the discrimination of mantle versus crustal garnet, Tolosana-Delgado et al. (2018) consider five major garnet host-rock types including amphibolite-, granulite-, and eclogite-facies metamorphic rocks, igneous rocks, and ultramafic rocks. The capabilities of extracting petrogenetic information from the detrital garnet record have further been improved by considering trace elements (Čopjaková et al. 2005; Hong et al. 2020), mineral inclusions (e.g., Schönig et al. 2019, 2020; Baldwin et al. 2021), U–Pb geochronology (e.g., Seman et al. 2017; Millonig et al. 2020), as well as Sm–Nd geochronology (Maneiro et al. 2019). However, all these novel techniques require a wealth of experience, caution, equipment, and effort. In contrast, major-element chemistry is routinely applied and enables to efficiently screen a statistically significant number of grains. Although multivariate schemes are already highly advanced, these may be improved by (i) enlarging the database, (ii) including previously unconsidered host-rock types, (iii) considering host-rock composition, (iv) refining prediction classes, and (v) applying statistical classification methods with enough flexibility to disentangle the strongly overlapping compositional signatures of garnet types. Particularly machine-learning algorithms are

suitable to tackle multivariate discrimination tasks as demonstrated by prediction models that are based on bulk-rock chemistry (Petrelli & Perugini 2016; Petrelli et al. 2017, Ren et al. 2019), glass composition (Bolton et al. 2020), as well as single-grain chemistry (Han et al. 2019; Itano et al. 2020). In addition, random forest regression lead to an improvement of barometric predictions for majoritic garnet inclusions in diamond that crystallized at $P > 5$ GPa (Thomson et al. 2021), implying that the algorithm may prove suitable for developing a model to discriminate detrital garnet sourced from a potentially broad range of host rocks.

Here we present a new garnet major-element discrimination scheme for host-rock prediction developed by a machine learning approach using the random forest algorithm in classification mode (Breiman 2001). It is based on a large database compiled from the literature ($n = 13,615$), which was used to train and test the discrimination model simultaneously. The new scheme enables garnet discrimination into host-rock setting (mantle versus metamorphic versus igneous versus metasomatic), metamorphic facies (blueschist/greenschist versus amphibolite versus granulite versus eclogite/ultrahigh-pressure), and composition (intermediate–felsic/metasedimentary versus mafic versus ultramafic versus alkaline versus calc–silicates). Besides providing a more detailed classification than any previous scheme, we highlight the usefulness of our scheme by demonstrating the much higher discrimination success and interpretability of results compared to others. We introduce a freely accessible web application, allowing users to easily apply the discrimination scheme to their own data without the need for programming expertise. Finally, application examples emphasize the potential to reflect (i) varying pressure–temperature conditions during garnet growth, (ii) the geological framework of catchments, and (iii) provenance shifts through time.

6.2 Database

The compiled chemical garnet database (Electronic Appendix 6e-A, <https://rodare.hzdr.de/record/1220>) includes 13,615 observations of eight oxides commonly analyzed in lab routines: SiO₂, TiO₂, Al₂O₃, Cr₂O₃, FeO_{total}, MnO, MgO, and CaO (in wt%). Data compilation results from a comprehensive literature survey and benefitted from several published databases, most importantly to mention are Grütter et al. (2004), Krippner et al. (2014), Suggate & Hall (2014), and Hardman et al. (2018). Original references have been cross-checked to promote database quality. If any of the eight oxides is not included on any particular observation, that value is handled as not available (NA). As most standard routines use a detection limit between 0.02 and 0.03 wt%, we chose 0.03 wt% as the threshold and all values below are handled as below detection limit (BDL).

Garnets have been subdivided according to host-rock type (main group), metamorphic facies (group), and composition (subgroup, Table 6.2-1). Host-rock types include mantle (MA), metamorphic (MM), igneous (IG), and metasomatic rocks (MS). For metamorphic facies, estimated pressure–temperature (P – T) conditions in the original references have been used instead of facies-specific mineral assemblages. The assignment follows the facies scheme after Bucher & Frey (2002) for protoliths of

Table 6.2-1:
Number of observations for individual garnet host-rock types (main group), metamorphic facies (group), and composition (subgroup) included in the database.

main group	observations (main group)
group	observations (group)
subgroup	<i>Observations (subgroup)</i>
MA: mantle rocks	3,439
<i>M: mafic</i>	1,662
<i>UM: ultramafic</i>	1,777
MM: metamorphic rocks	8,276
GS: greenschist facies	786
<i>M: mafic</i>	352
<i>IF/S: intermediate–felsic/metasedimentary</i>	434
BS: blueschist facies	418
<i>M: mafic</i>	200
<i>IF/S: intermediate–felsic/metasedimentary</i>	213
<i>CS: calc–silicate</i>	5
AM: amphibolite facies	2,605
<i>M: mafic</i>	824
<i>IF/S: intermediate–felsic/metasedimentary</i>	1,767
<i>CS: calc–silicate</i>	14
GR: granulite facies	1,011
<i>M: mafic</i>	180
<i>IF/S: intermediate–felsic/metasedimentary</i>	672
<i>CS: calc–silicate</i>	159
EC: eclogite facies	2,095
<i>M: mafic</i>	1,813
<i>IF/S: intermediate–felsic/metasedimentary</i>	274
<i>CS: calc–silicate</i>	8
UHP: ultrahigh-pressure metamorphism	1,361
<i>M: mafic</i>	882
<i>IF/S: intermediate–felsic/metasedimentary</i>	295
<i>CS: calc–silicate</i>	184
IG: igneous rocks	1,074
<i>M: mafic</i>	66
<i>IF: intermediate–felsic</i>	919
<i>A: alkaline</i>	89
MS: metasomatic rocks	826
<i>CS: calc–silicate</i>	826

mid-oceanic ridge basalt composition. This comprises greenschist facies (GS), blueschist facies (BS), amphibolite facies (AM), granulite facies (GR), eclogite facies (EC), and ultrahigh-pressure metamorphism (UHP). In case geothermobarometry was not applied in the original literature, datasets were only used when rock descriptions and reported facies are conclusive. Host-rock compositions were simplified into ultramafic (UM), mafic (M), intermediate–felsic/metasedimentary (IF/S, mafic metasediments omitted), calc–silicate (CS), and alkaline (A).

6.3 Model development

For developing the garnet discrimination scheme, the random forest machine-learning algorithm (Breiman 2001) is applied in classification mode. A description of the principle of creating a random forest classification model is given in Appendix 6-A. For a more detailed and mathematically based explanation, the reader is referred to the original work of Breiman (2001) and reviews treating this topic (Boulesteix et al. 2012; Ziegler & König 2014; Belgiu & Drăgut 2016; Biau & Scornet 2016).

Data processing, calculations, and plotting were performed using the statistic software R (R Core Team 2019). Used packages include 'compositions' (van den Boogart & Tolosana-Delgado 2008) for compositional data analysis, 'dplyr' (Wickham et al. 2019) for data wrangling, 'ggtern' (Hamilton & Ferry 2018) for display, 'magittr' (Bache & Wickham 2014) for readability of complex code, and 'randomForest' (Liaw & Wiener 2002) for the calculations of the forest itself.

Two models are developed called 'setting and metamorphic facies' and 'composition'. For the 'setting and metamorphic facies' model, main groups and groups of Table 6.2-1 have partially been merged into seven classes, namely garnet of (i) mantle rocks (class MA, includes main group MA), (ii) blueschist-/greenschist-facies metamorphic rocks (class BS/GS, includes groups BS and GS), (iii) amphibolite-facies metamorphic rocks (class AM, includes group AM), (iv) granulite-facies metamorphic rocks (class GR, includes group GR), (v) eclogite-/ultrahigh-pressure-facies metamorphic rocks (class EC/UHP, includes groups EC and UHP), (vi) igneous rocks (class IG, includes main group IG), and (vii) metasomatic rocks (class MS, includes main group MS) (Table 6.3-1). For the 'composition' model, subgroups of Table 6.2-1 have partially been merged into five classes, namely garnet of (i) ultramafic rocks (class UM, includes subgroup MA-UM), (ii) mafic rocks (class M, includes subgroups MA-M, GS-M, BS-M, AM-M, GR-M, EC-M, UHP-M, and IG-M), (iii) intermediate-felsic/metasedimentary rocks (class IF/S, includes subgroups GS-IF/S, BS-IF/S, AM-IF/S, GR-IF/S, EC-IF/S, UHP-IF/S, and IG-IF), (iv) alkaline rocks (class A, includes subgroup IG-A), and (v) calc-silicates (class CS, includes subgroups BS-CS, AM-CS, GR-CS, EC-CS, UHP-CS, and MS-CS) (Table 6.3-1).

Table 6.3-1:
Classes and parameters of the random forest garnet discrimination models.

'setting and metamorphic facies' (ntree = 3,400; mtry = 5; nodesize = 1)							
classes	MA	BS/GS	AM	GR	EC/UHP	IG	MS
observations	3,439	1,204	2,605	1,011	3,456	1,074	826
sampsize	1,011	1,011	1,200	1,011	1,100	1,011	826
'composition' (ntree = 3,200; mtry = 6; nodesize = 1)							
classes	UM	M	IF/S	A	CS		
observations	1,777	5,979	4,574	89	1,196		
sampsize	1,777	2,600	2,100	89	1,196		

Each observation in the database includes eight variables in form of oxide wt% (see Section 6.2). These observations have been acquired by many operators since major-element analysis has become a standard analytical tool. Thus, observations in the database include a wide range of used systems, analyzed oxides, calibrations, operating conditions, and data processing techniques. This mainly results in discrepancies in the total wt% of the eight oxides considered for discrimination, making the amount of the whole (or total sum by sample) a non-informative quantity. In addition, all chemical components are rarely analyzed, but rather the amount of each component is limited to that whole. Thus, only relative changes are relevant (e.g., van den Boogart & Tolosana-Delgado 2008). In order to tackle this issue and to get rid of spurious anti-correlations (Chayes 1960), the natural logarithms of ratios between all pairs of oxides are used as variables instead of the single values (Aitchison 1986). The usage of log-ratios is a mathematically elegant transformation that enables the use of standard unconstrained multivariate statistics (Aitchison & Egozcue 2005). This approach increases the total number of variables from eight oxides measured to 28 pairwise log-ratios. Besides the advantages, this introduces a difficulty when handling values BDL, that is <0.03 wt%. The log-ratios with values BDL in the numerator and/or denominator can potentially span a wide range of values. Considering a log-ratio that contains a value BDL in the numerator with a detection limit DL, the log-ratio of numerator and a denominator with value x is always $<\ln(DL \times x^{-1})$. Conversely, a value BDL in the denominator with a detection limit DL leads to a log-ratio $>\ln(x \times DL^{-1})$ with x the value of the numerator. Thus, log-ratios with a value BDL in the numerator or denominator have been replaced by the minimum of that log-ratio in the database minus one or the maximum plus one, respectively (see pair-wise log-ratio function in Appendix 6-B). This approach ensures that values BDL are treated in the same way than fully observed values, while maintaining and making use of this information. Those log-ratios with values BDL both in the numerator and denominator are replaced by NA. All missing values (those that involve an NA and those that involve two BDLs) are treated by the ‘na.roughfix’ function, which first replaces missing values by the median of not-missing values, trains a random forest model, computes the proximity matrix between samples, and refines the missing values by replacing it with the weighted median of non-missing values (using the proximity values as weights).

The method parameters of the random forest were chosen in a double procedure. The ‘sampsiz’e parameter was set by a discretionary approach. This parameter controls the number of observations taken from each class for each tree by random sampling. As random forest is optimized for creating discrimination models that have the highest overall classification success, classes that include more observations are often better classified compared to those where fewer observations are available (Appendix 6-A). The aim of the garnet discrimination model was to balance the classification success rates for the individual classes as well as possible. Therefore, the ‘sampsiz’e for classes containing a higher number of observations was reduced (Table 6.3-1). This results in a slightly lower classification success for the entire database, but more balanced success rates for the individual classes (Chen et al. 2004). The other parameters were set by formal exhaustive cross-validation. Both models have been computed by five iterations with all combinations of ‘ntree’ between 200 and 6,000 (step size = 200), ‘mtry’ between 1 and 12 (step size = 1), and ‘nodesize’ between 1 and 3 (step size = 1). Those parameter values giving on average the lowest OOB (out-of-bag) error have been chosen for the final models (Table 6.3-1).

6.4 Model performance

6.4.1 Performance of the ‘setting and metamorphic facies’ model

The ‘setting and metamorphic facies’ model predicts the correct class out of seven classes for >88 % of all observations included in the database based on the OOB error (Table 6.4-1). Notably, the predicted classes are more detailed and useful in terms of petrogenetic information compared to the most frequently used scheme after Mange & Morton (2007), which includes prediction classes that do not point to a specific host-rock type (Appendix 6-C).

To take full and quick advantage of the classification regarding provenance, the voting results are shown in two separate graphical schemes for ‘setting’ and ‘metamorphic facies’, each representing the four ternary sides of a tetrahedron (Figure 6.4-1). The ‘setting’ scheme discriminates garnet sourced from MA, IG, MS, and metamorphic rocks (MM) based on the votes for each class. MM is represented by the maximum vote of the four metamorphic classes, that is BS/GS, AM, GR, and EC/UHP. The decision of taking the maximum vote instead of the sum of votes is based on two major points. First, taking the sum of votes artificially introduces classification results that are based on a much larger ‘sampsize’ for training the random forest model for MM (1,011 + 1,200 + 1,011 + 1,100 = 4,322) compared to MA (1,011), IG (1,011), and MS (826, see Table 6.3-1). Consequently, the balancing introduced by making use of the ‘sampsize’ argument (see Section 6.3) is getting out of balance, resulting in higher classification success rates for MM at the expense of the three other classes. Second, taking the sum of votes entangles the two different questions to be answered by a single classification model, which is impermissible.

Votes of the ‘setting’ scheme are shown as kernel density maps in four ternary plots to represent each setting class (Figure 6.4-1a). The voting result of each individual observation from the database is solely plotted in one of the four ternary plots, that is the plot representing the three highest votes. The vast majority of the votes plots close to the apexes of the corresponding correct class. Only very minor overlaps occur for MM versus MA, MM versus IG, and MM versus MS. This is obvious in the corresponding majority vote bar plot showing that on average >95 % are assigned to their correct class (Figure 6.4-1a).

Table 6.4-1:
Classification rates and confusion matrix of the ‘setting and metamorphic facies’ random forest model based on the out-of-bag estimate.

		True class						
		MA	BS/GS	AM	GR	EC/UHP	IG	MS
<i>Correct classification: 88.4 %</i>								
Predicted class	MA	3,292	0	0	3	90	0	0
	BS/GS	0	1,047	139	5	147	13	3
	AM	1	86	2,166	29	165	28	0
	GR	4	4	91	839	136	13	13
	EC/UHP	142	46	122	100	2,890	13	4
	IG	0	12	74	10	24	1,001	4
	MS	0	9	13	25	4	6	802
Correct classification		95.7 %	87.0 %	83.1 %	83.0 %	83.6 %	93.2 %	97.1 %

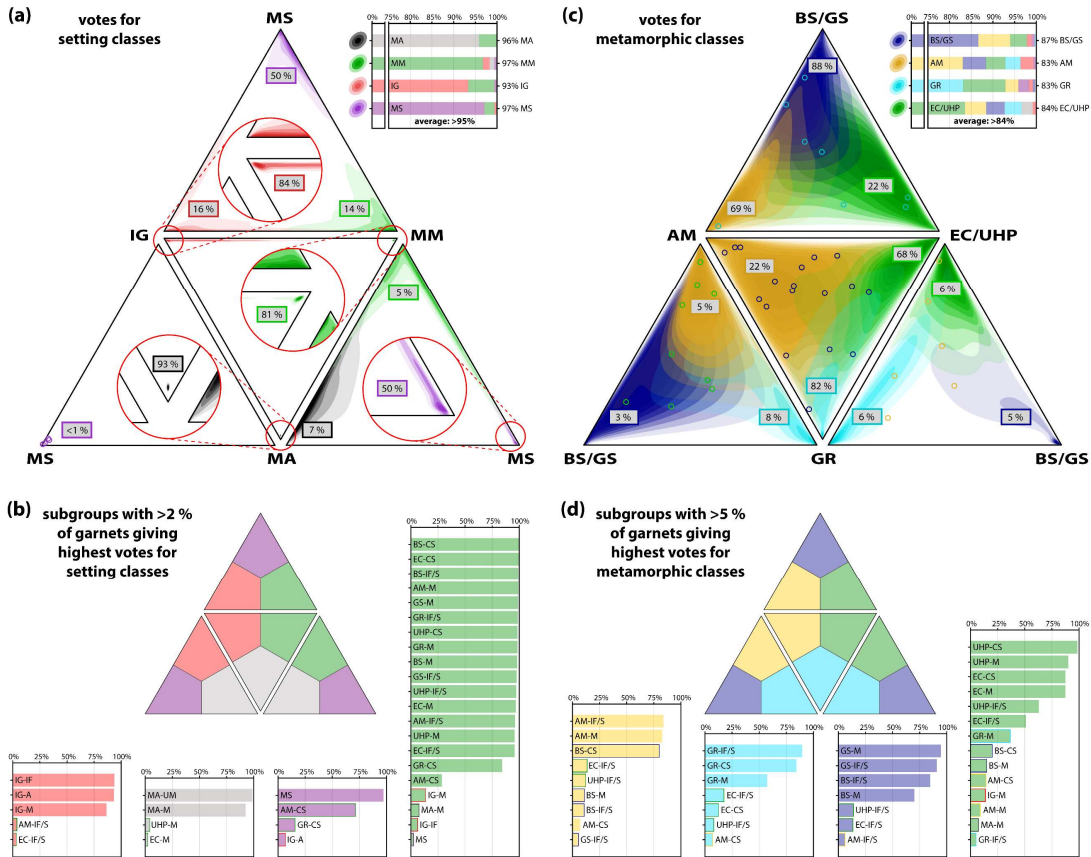


Figure 6.4-1: Performance of the ‘setting and metamorphic facies’ model based on the out-of-bag error. The distribution of votes for ‘setting’ classes (a) and ‘metamorphic facies’ classes (c) are shown as kernel density estimate maps in four ternary diagrams that represent the sides of a tetrahedron: MS – metasomatic rocks, IG – igneous rocks, MA – mantle rocks, MM – metamorphic rocks, BS/GS – blueschist/greenschist facies, AM – amphibolite facies, GR – granulite facies, and EC/UHP – eclogite/ultrahigh-pressure facies. Individual observations are included only in the ternary diagram that represents the three highest votes. Note that MM represents the maximum vote for BS/GS, AM, GR, or EC/UHP. Kernel density bandwidth calculated after Venables & Ripley (2002). Corresponding classification success rates based on the majority vote are shown as barplots (note break in scale at 75 %). Proportions of observations from each class vote occurring in the individual ternary diagrams are given in small rectangular boxes within the ternary diagrams of (a) and (c). The proportions of observations from individual subgroups assigned to the prediction classes are shown as barplots for the ‘setting’ (b) and ‘metamorphic facies’ (d) scheme (see Table 6.2-1 for abbreviations). Bars representing misclassifying votes are highlighted by frames that are color coded according to the true class.

Considering solely the discrimination of MA versus crustal garnet (MM, IG, and MS), MA are correctly classified in 96 % and crustal garnet in 99 %, giving a class average of 97 %. Thus, the prediction success excels the graphical mantle-versus-crustal garnet discrimination after Hardman et al. (2018), that is 95 % based on the presented database (Appendix 6-C). In the developed model, MA-M is the only mantle subgroup exceeding 2 % of the observations misclassified as MM, and EC-M as well as UHP-M are the only crustal subgroups exceeding 2 % of the observations misclassified as MA (Figure 6.4-1b). However, even these challenging groups show high success rates: 93 % for MA-M, 97 % for EC-M, and 96 % for UHP-M.

Garnets of class MS are correctly identified in >97 % and only minor amounts (<3 %) are misclassified as MM (Figure 6.4-1a and b). Contrary, metamorphic calc–silicates that formed at high temperature,

which are subgroups AM-CS and GR-CS, are often misclassified as MS. Besides their chemical similarity, this is caused by the underrepresentation of observations from metamorphic calc–silicates compared to mafic and intermediate–felsic/metasedimentary host-rock compositions, in particular for AM (Table 6.2-1). In addition to calc–silicates, some of the alkaline igneous garnets (7 %) are misclassified as MS.

IG garnet is correctly classified in >93 % (Figure 6.4-1a). The highest success rates are given for subgroups IG-IF and IG-A with 94 % (6 % misclassified as MM) and 93 % (7 % misclassified as MS), respectively. IG-M shows a slightly lower success with 86 %, which still represents a well-discriminated subgroup. Noteworthy, very low amounts of garnet from other subgroups are misclassified as IG, with AM-IF/S and EC-IF/S being the only subgroups exceeding 2 % misclassification as IG (Figure 6.4-1b).

Garnets of the setting class MM are correctly classified in >96 % (Figure 6.4-1a), with 15 of the 17 metamorphic subgroups listed in Table 6.2-1 being correctly assigned in >95 %. Subgroups showing lower success rates are restricted to calc–silicates (GR-CS and AM-CS; Figure 6.4-1b).

Votes of the ‘metamorphic facies’ scheme are as well shown as kernel density maps in four ternary plots to represent each metamorphic class (Figure 6.4-1c). The plot includes all observations giving the highest votes for MM in the ‘setting’ scheme. The voting result of each individual observation is solely plotted in the ternary diagram representing the three highest votes. Compared to the ‘setting’ scheme, the spread in votes and overlaps are more pronounced but the maxima are clearly located close to the apexes of the corresponding class. The barplot in Figure 6.4-1c shows that classification success rates of the individual classes range from 83 % to 87 %, giving an average of >84 % correctly classified garnets. Beyond the additional and separate prediction of garnet sourced from BS/GS, classification clearly improved compared to the scheme of Tolosana-Delgado et al. (2018), which shows an average classification success rate of 65 % for metamorphic classes (Appendix 6-C).

The barplots in Figure 6.4-1d show that (i) the correct subgroups constitute the vast majority of observations assigned to the individual metamorphic classes, except for several of the CS subgroups; (ii) garnet from IF/S host-rock composition is better classified for GR, AM, and BS/GS subgroups than for EC/UHP subgroups and vice versa; and (iii) misclassifications are mainly restricted to adjacent classes in P – T space, that is BS/GS and GR with AM and EC/UHP, respectively, while AM and EC/UHP share borders with all other classes (see also barplot in Figure 6.4-1c). Points (i) and (ii) can be related to the distribution of observations from the individual subgroups (Table 6.2-1), but point (iii) implies a rather continuous change in garnet composition with changing P – T conditions, which is well-known from metamorphic petrology and reflected by the votes (Appendix 6-D).

6.4.2 Performance of the ‘composition’ model

The ‘composition’ model predicts the correct class out of five for >92 % of all observations included in the database based on the OOB error estimate (Table 6.4-2). It discriminates garnet from intermediate–felsic/metasedimentary (IF/S), mafic (M), ultramafic (UM), calc–silicates (CS), and alkaline (A) host rocks.

Table 6.4-2:
Classification rates and confusion matrix of the ‘composition’
random forest model based on the out-of-bag estimate.

		True class				
		IF/S	M	UM	CS	A
<i>Correct classification: 92.3 %</i>						
Predicted class	IF/S	4,209	340	1	14	0
	M	353	5,480	145	10	0
	UM	1	145	1,626	0	0
	CS	11	14	5	1,167	6
	A	0	0	0	5	83
Correct classification		92.0 %	91.7 %	91.5 %	97.6 %	93.3 %

Votes of the ‘composition’ scheme are shown as kernel density maps in four ternary plots to represent four of the five classes (Figure 6.4-2a). Because alkaline garnet has the lowest number of observations, is rarely misclassified, and misclassifications are restricted to class CS (Table 6.4-2), class A is excluded from the plots. Thus, plots include all observations giving not the highest votes for class A. As in the preceding plots, voting results for each individual observation from the database is solely plotted in one of the four ternary plots, that is the plot representing the three highest votes. The vast majority of the votes plots close to the apexes of the corresponding correct class. However, overlaps occur for M versus IF/S and M versus UM. This is highlighted in the corresponding majority vote bar plot showing that on

average >93 % are assigned to their correct class (Figure 6.4-2a).

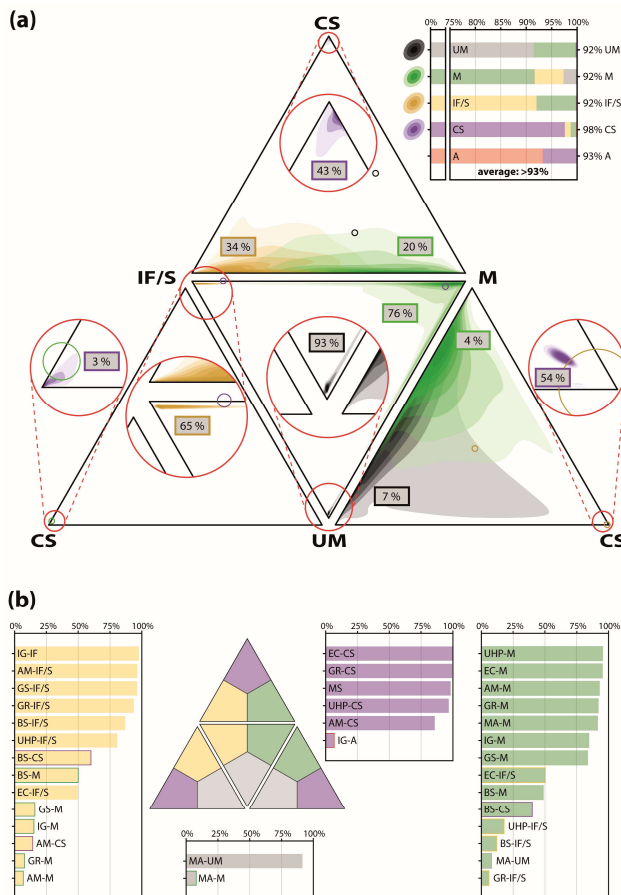


Figure 6.4-2: Performance of the ‘composition’ model based on the out-of-bag error. (a) Distribution of votes shown as kernel density estimate maps in four ternary diagrams that represent the sites of a tetrahedron: CS – calc-silicates, IF/S – intermediate-felsic/metasedimentary, UM – ultramafic, and M – mafic. Votes for alkaline (A) composition are not shown. Individual observations are included only in the ternary diagram that represents the three highest votes. Kernel density bandwidth calculated after Venables & Ripley (2002). Corresponding classification success rates based on the majority vote are shown as barplots (note break in scale at 75 %). Proportions of observations from each class occurring in the individual ternary diagrams are given in small rectangular boxes. (b) Proportions of observations from individual subgroups assigned to the prediction classes shown as barplots (see Table 6.2-1 for abbreviations). Bars that represent misclassifying votes are highlighted by color coded frames according to the true class.

The barplots in Figure 6.4-2b show that the correct subgroups constitute the vast majority of observations assigned to the individual composition classes. In particular, garnet classified as CS and UM are well represented and only scarcely garnet of subgroups IG-A and MA-M receive the highest votes for CS or UM, respectively. Garnets classified as IF/S and M are dominated by the correct subgroups, too. However, up to almost 16 % of the M subgroups are assigned to IF/S and IF/S subgroups to M. Conspicuously, EC-IF/S (50 %), BS-M (50 %), and BS-CS (100 %, 60 % in M, 40 % in IF/S) show high misclassifications.

6.5 Understanding the models

The two presented garnet discrimination models consist of 3,400 and 3,200 trees (Table 6.3-1), each based on a different bootstrapped random sample and deeply grown without pruning leading to between 1,619 and 1,949 decision nodes for each tree of the ‘setting and metamorphic facies’ model and between 1,033 and 1,269 nodes for the ‘composition’ model. Thus, following the decision process in detail is not feasible, giving random forest models a kind of ‘black box’ character.

In order to understand the basic discrimination decisions performed by the models, the importance of variables is explored in three ways: (i) Considering the mean decrease in Gini impurity (Appendix 6-A) for individual variables, that is the weighted average of the decrease in Gini impurity between parent and child nodes in all trees of the trained forest when the values of an individual variable are permuted; (ii) considering the mean decrease in accuracy for individual variables, that is the decrease of prediction accuracy when an individual variable is removed from the OOB test set; and (iii) considering the increase in misclassification rates for individual classes when individual oxides are removed from the database for training the forest. Note that the exclusion of each oxide means that all seven log-ratios that include this oxide are removed. Finally, the most important variables to discriminate individual classes and subgroups are retraced and their origin is discussed.

6.5.1 Variable importance of the ‘setting and metamorphic facies’ model

The highest variable importance based on the mean decrease in Gini impurity and accuracy is given by log-ratios involving MgO. This particularly includes $\ln(\text{FeO}_{\text{total}} \times \text{MgO}^{-1})$, followed by $\ln(\text{SiO}_2 \times \text{MgO}^{-1})$ and $\ln(\text{Al}_2\text{O}_3 \times \text{MgO}^{-1})$ (Figure 6.5-1, upper). All three show a high spread for observations of the dataset with distinct ranges for the individual classes (Figure 6.5-1, lower). Notably, values of these ratios decrease from metasomatic garnet (MS), over low-temperature metamorphic (BS/GS and AM) and igneous garnet (IG), to high-grade metamorphic garnet (GR and EC/UHP), and mantle garnet (MA) shows the lowest values.

The next important set of log-ratios includes CaO versus Al_2O_3 , SiO_2 , MgO, MnO, and $\text{FeO}_{\text{total}}$ (Figure 6.5-1, upper). This is dominated by the importance of discriminating class MS which shows higher CaO values than the other classes (Figure 6.5-1, lower). Another major difference between class MS and all other classes is the high range of values for $\ln(\text{SiO}_2 \times \text{Al}_2\text{O}_3^{-1})$ for MS compared to the very tight range of the other classes, which is also visible in the values for $\ln(\text{SiO}_2 \times \text{FeO}_{\text{total}}^{-1})$ and $\ln(\text{Al}_2\text{O}_3 \times \text{FeO}_{\text{total}}^{-1})$. In contrast to class MS, garnets of class GR and to a lesser extent IG show high values for log-ratios including CaO in the denominator, even higher than those for the other metamorphic classes, making

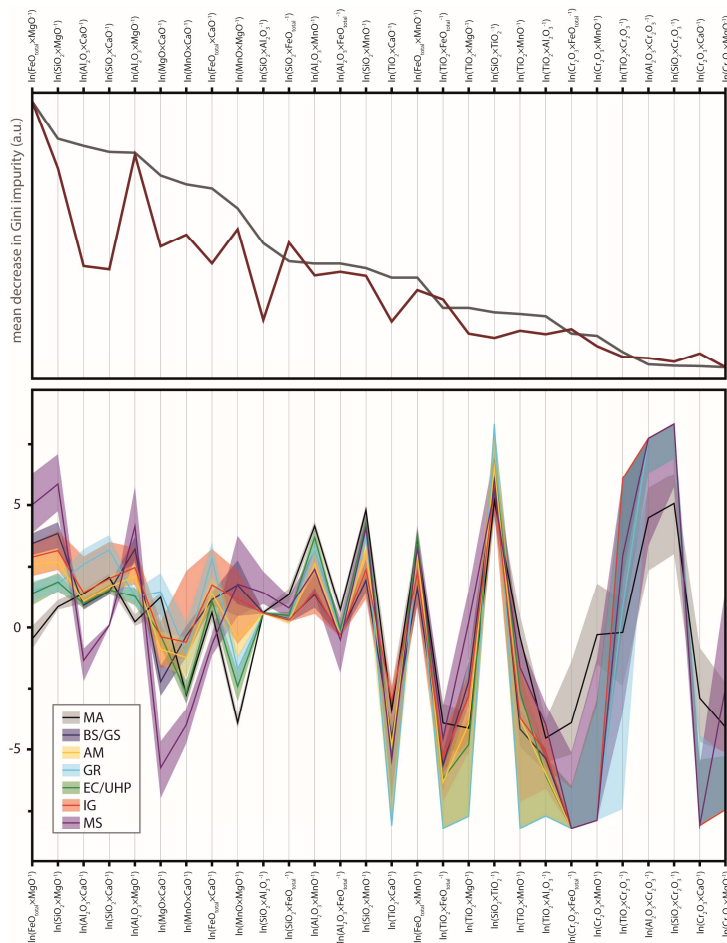


Figure 6.5-1: Variable importance for the 'setting and metamorphic facies' model. Upper diagram shows the mean decrease in Gini impurity and mean decrease in accuracy for individual variables ordered from the highest decrease in Gini impurity (left) to lowest (right). Lower diagram shows corresponding variable values for individual classes as 25 % quantile, median, and 75 % quantile (see Table 6.2-1 for abbreviations). For some variables, nominator or denominator are often below detection limit, resulting in similar values for median and quantiles (lines overlap).

garnet showing higher similarities with low-grade metamorphic garnet for $\ln(\text{MnO} \times \text{MgO}^{-1})$ and $\ln(\text{Al}_2\text{O}_3 \times \text{MnO}^{-1})$, and higher similarities with high-grade metamorphic garnet for $\ln(\text{SiO}_2 \times \text{MnO}^{-1})$ and $\ln(\text{FeO}_{\text{total}} \times \text{MnO}^{-1})$.

Considering the mean decrease in Gini impurity and accuracy of the entire tree ensemble, the individual log-ratios including TiO_2 or Cr_2O_3 are placed in a subordinate role for creating high purity splits. However, some specific log-ratios are important for splitting individual classes. In particular, $\ln(\text{TiO}_2 \times \text{CaO}^{-1})$ is essential for purifying the discrimination of class IG versus metamorphic classes. The variables $\ln(\text{Cr}_2\text{O}_3 \times \text{FeO}_{\text{total}}^{-1})$, $\ln(\text{Cr}_2\text{O}_3 \times \text{MnO}^{-1})$, $\ln(\text{Cr}_2\text{O}_3 \times \text{CaO}^{-1})$, $\ln(\text{TiO}_2 \times \text{FeO}_{\text{total}}^{-1})$ and $\ln(\text{TiO}_2 \times \text{MnO}^{-1})$ are important for discriminating MA versus EC/UHP (Figure 6.5-1).

In addition to the exploration of variable importance based on the decrease in Gini impurity and accuracy, Figure 6.5-2 shows the implications for misclassification rates when individual oxides are

log-ratios including CaO useful to separate garnet of classes GR and IG. Besides MS and GR, $\ln(\text{MgO} \times \text{CaO}^{-1})$ is particularly important for the discrimination of IG versus BS/GS, which are in most other respects compositionally similar (Figure 6.5-1, lower).

Behind the log-ratios mainly dictated by MgO and CaO along with $\text{FeO}_{\text{total}}$, a set of log-ratios including MnO becomes next most important (Figure 6.5-1, upper). Remarkably, values for log-ratios with MnO in the denominator versus MgO, Al_2O_3 , SiO_2 , and $\text{FeO}_{\text{total}}$ show a reverse trend to log-ratios with MgO in the denominator (Figure 6.5-1, lower). Values successively increase from lower-temperature metamorphic and igneous garnet, over higher-temperature metamorphic garnet, to high-grade metamorphic garnet, and finally mantle garnet. Distinct is the behavior of metasomatic

excluded for the development of a random forest ‘setting and metamorphic facies’ discrimination model. Misclassification rates for all classes show the highest increase when MnO is excluded, followed by TiO₂ (strongly influencing the correct classification of IG), MgO (with notable contribution to the quality of BS/GS and MS reclassification), CaO, Al₂O₃, FeO_{total}, SiO₂, and Cr₂O₃ in decreasing order of global importance (Figure 6.5-2, bold grey line). The higher importance of MnO and TiO₂ compared to MgO, CaO, and FeO_{total} is contrary to the importance order based on the mean decrease in Gini impurity (Figure 6.5-1). This indicates that MnO and TiO₂ either gain their importance by considering many log-ratios including MnO and TiO₂ or by being specifically important for the discrimination of individual classes, or a combination of both. A detailed description of consequences for individual classes by excluding individual oxides is provided in Appendix 6-E.

6.5.2 Variable importance of the ‘composition’ model

The highest variable importance based on the mean decrease in Gini impurity and accuracy is given by log-ratios with CaO versus Al₂O₃, SiO₂, FeO_{total}, MnO, and MgO (Figure 6.5-3, upper). Calc–silicate (CS) and alkaline (A) garnet show low values for all of these ratios and thus can be discriminated from all other groups (Figure 6.5-3, lower). Mafic garnet (M) shows higher values than CS and A, but lower values than intermediate–felsic/metasedimentary (IF/S),

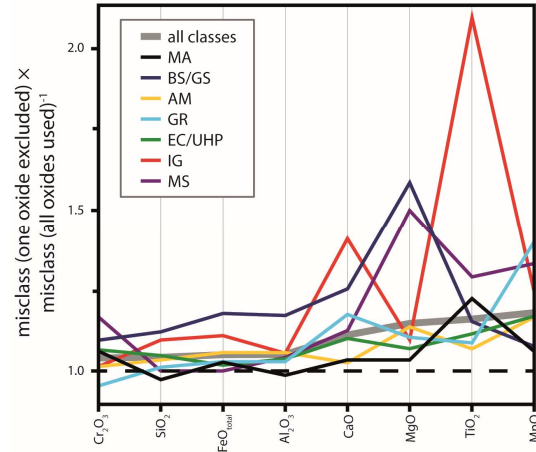


Figure 6.5-2: Misclassification rates of the ‘setting and metamorphic facies’ model for individual oxides excluded compared to the full model with all oxides used (see Table 6.2-1 for abbreviations).

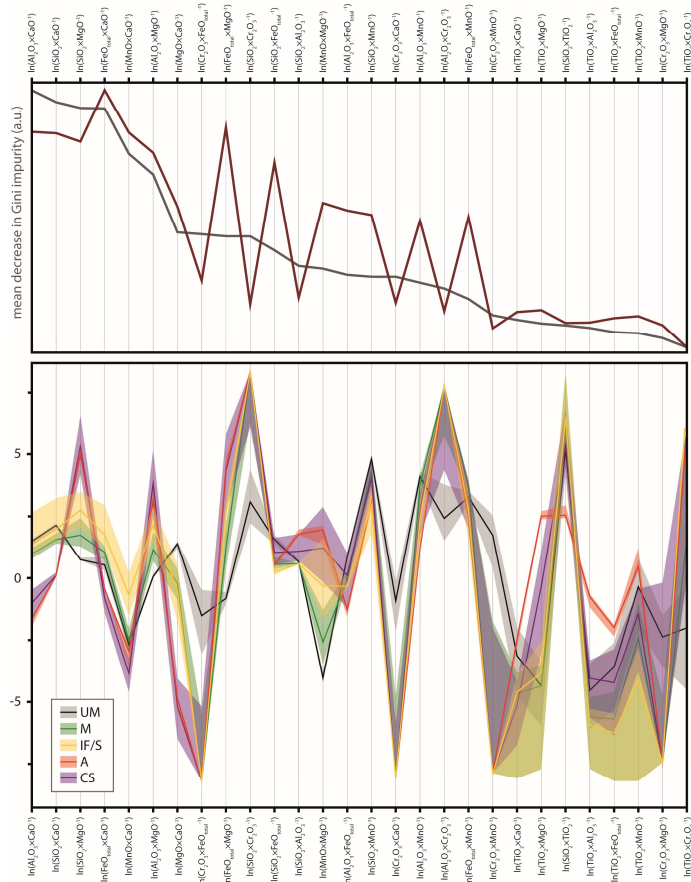


Figure 6.5-3: Variable importance for the ‘composition’ model. Upper diagram shows the mean decrease in Gini impurity and mean decrease in accuracy for individual variables ordered from the highest decrease in Gini impurity (left) to lowest (right). Lower diagram shows corresponding variable values for individual classes as 25 % quantile, median, and 75 % quantile (see Table 6.2-1 for abbreviations).

enabling to create high-purity splits. In addition, the ratios with CaO versus $\text{FeO}_{\text{total}}$, as well as MgO, are useful to separate ultramafic (UM) and M garnet.

The next important set of log-ratios includes MgO versus SiO_2 , Al_2O_3 , $\text{FeO}_{\text{total}}$, and MnO (Figure 6.5-3, upper). This is not solely related to the creation of high purity splits but also to highly increase the model accuracy. Like log-ratios with CaO, the ratios with MgO allow the separation of most CS and A garnet (high values) from M and IF/S garnet (intermediate values), and UM garnet (low values) (Figure 6.5-3, lower).

Besides $\ln(\text{FeO}_{\text{total}} \times \text{CaO}^{-1})$ and $\ln(\text{FeO}_{\text{total}} \times \text{MgO}^{-1})$, other ratios that include $\text{FeO}_{\text{total}}$ like $\ln(\text{SiO}_2 \times \text{FeO}_{\text{total}}^{-1})$, $\ln(\text{Al}_2\text{O}_3 \times \text{FeO}_{\text{total}}^{-1})$, and $\ln(\text{FeO}_{\text{total}} \times \text{MnO}^{-1})$ show only intermediate importance for the decrease in Gini impurity. Nevertheless, they are highly important for the accuracy of the model (Figure 6.5-3, upper). By contrast, log-ratios that include Cr_2O_3 also show intermediate importance for the purity of splits, but much lower importance for the model accuracy. However, these ratios are obviously useful to separate UM garnet (Figure 6.5-3, lower).

The log-ratios including TiO_2 are placed in a subordinate role for the mean decrease in Gini impurity and accuracy (Figure 6.5-3, upper). By contrast, excluding TiO_2 when developing the ‘composition’ discrimination model leads to the highest increase in misclassification rates (owing to its dramatic influence in the correct reclassification of alkaline garnets), followed by CaO, MgO, MnO, Cr_2O_3 , $\text{FeO}_{\text{total}}$, SiO_2 , and Al_2O_3 in decreasing order of importance (Figure 6.5-4). A detailed description of consequences for individual classes by excluding individual oxides is provided in Appendix 6-E.

6.5.3 Origin of main discriminators

The discrimination of classes in the ‘setting and metamorphic facies’ as well as the ‘composition’ model is complex, and for sufficient separation, individual subgroups have to be considered individually. A detailed exploration of main discriminators for individual subgroups is provided in Appendix 6-F. Here we focus on the most important class discriminators.

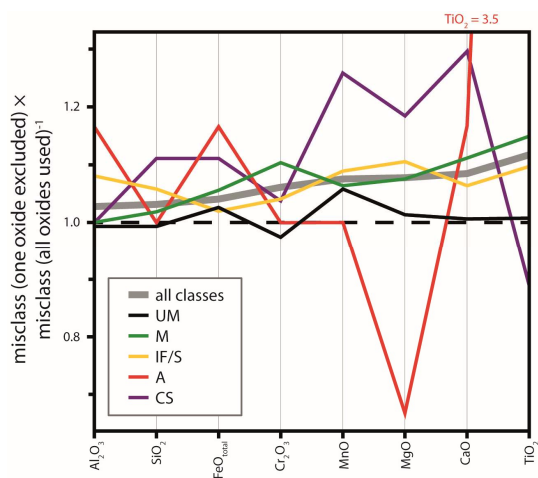
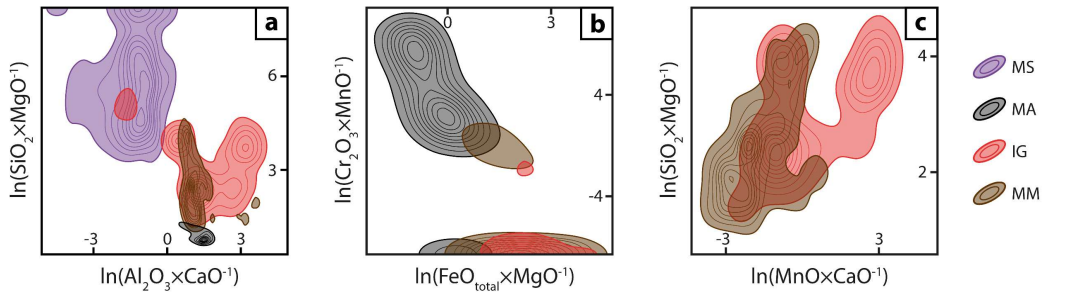


Figure 6.5-4: Misclassification rates of the ‘composition’ model for individual oxides excluded compared to the full model with all oxides used (see Table 6.2-1 for abbreviations).

Garnet of class MS in the ‘setting and metamorphic facies’ model shows the highest classification success (Table 6.4-1), reflecting its distinct chemical composition. MS garnet is CaO rich, MgO poor, and shows a broad range in Al_2O_3 contents with an average lower than the other classes (Figure 6.5-5a). The distinct composition is strongly related to the formation environment. Although skarn garnet can form in a wide range of settings and different protolith lithologies, by far the most are associated with igneous activity that leads to contact metamorphism of carbonates by heat supply and infiltrating metasomatic fluids at depth <12 km (e.g., Meinert 1992). Garnet mainly forms at the

separate setting classes



separate metamorphic facies classes

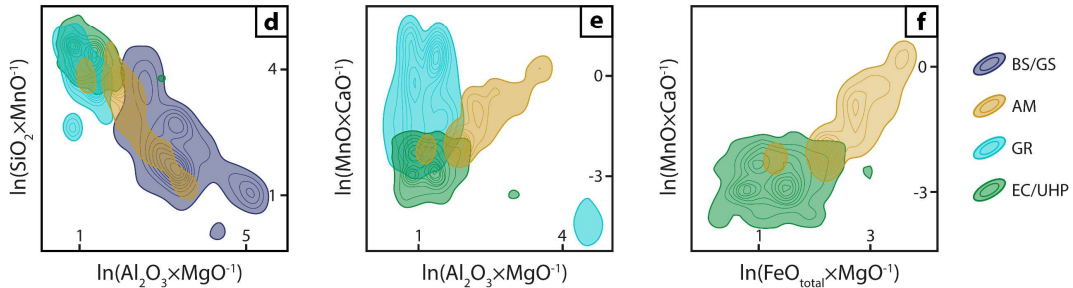


Figure 6.5-5: Main discriminators to separate setting (a–c) and metamorphic facies classes (d–f). (a) MS versus MA, IG, and MM; (b) MA versus IG and MM; (c) IG versus MM; (d) BS/GS versus GR, AM, and EC/UHP; (e) GR versus AM and EC/UHP; (f) AM versus EC/UHP (see Table 6.2-1 for abbreviations). Data shown as kernel density estimate maps.

prograde anhydrous stage together with clinopyroxene, both being high in Ca^{2+} due to the availability given by the chemical composition of the protolith. Furthermore, high oxygen fugacity enables the stabilization of andradite (end member composition: $\text{Ca}_3\text{Fe}_2\text{Si}_3\text{O}_{12}$), that involves the substitution of Al^{3+} by Fe^{3+} compared to grossular ($\text{Ca}_3\text{Al}_2\text{Si}_3\text{O}_{12}$), resulting in a garnet solid solution rich in grossular–andradite (e.g., Zhang & Saxena 1991). In contrast, clinopyroxene crystallizes mainly as solid solutions between diopside ($\text{CaMgSi}_2\text{O}_6$) and hedenbergite ($\text{CaFeSi}_2\text{O}_6$), and thus much of the available Mg^{2+} and Fe^{2+} are incorporated in clinopyroxene (Bin & Barton 1988). An exceptional case includes skarns that formed under low oxygen fugacity conditions like those associated with tungsten and tin mineralization, where some garnet populations are rich in Al^{3+} (e.g., Zhang & Saxena 1991; Meinert 1992). However, considering recently published compositions of garnet from these reduced environments (Duan et al. 2020; Im et al. 2020), >87 % are correctly classified as MS, and the remaining are mainly classified as GR garnet of CS composition.

Garnet of class MA shows the second highest classification success in the ‘setting and metamorphic facies’ model (Table 6.4-1). In particular, the comparatively high content of MgO and Cr_2O_3 and the low content of $\text{FeO}_{\text{total}}$ and MnO in mantle rocks compared to crustal rocks represent the most important difference (Figure 6.5-5b). In addition, a high importance of TiO_2 is observed for the discrimination of some subgroups (Appendix 6-E). The enrichment of Cr in MA garnet is mainly related to the lithophile behavior of Cr, resulting in the accumulation of Cr in mantle mineral phases like chromium spinel during partial melting of the upper mantle (e.g., Matrosova et al. 2020), while spinel is replaced by garnet at greater depths (e.g., Klemme et al. 2009). The higher TiO_2 content of MA garnet is probably related to the higher formation temperatures, resulting in increasing solubility of Ti in garnet (Aulbach

2020). Notably, caution should be taken for some rare UHP-IF/S garnets that can have extremely high MgO contents (Chopin 1984) leading to a misclassification as MA garnet.

Compared to MS and MA garnet, the discrimination of IG versus MM garnet is more challenging. Very distinct are only IG garnets of alkaline composition (Appendix 6-F). Otherwise, the higher content of MnO and lower content of MgO as well as CaO represent the main discriminators (Figure 6.5-5c). This is related to the much higher abundance of garnet in felsic igneous rocks compared to alkaline or mafic igneous rocks. High MnO contents reflect the abundant crystallization from highly fractionated Al- and Mn-rich magmas (e.g., Dahlquist et al. 2007), enabling garnet growth at pressures as low as 3 kbar (e.g., Green 1977). The low-pressure formation conditions also agree with low CaO contents, and Ca-rich garnet in igneous rocks only occurs in deeply emplaced intrusions (e.g., Anderson et al. 2008). In addition, at crystallization temperatures of felsic melts, Mg is partitioning into the melt, resulting in low-Mg garnet (Green 1977). However, this superordinate trend is only sufficient to separate parts of class IG and subpopulations have to be considered individually. Particularly notable is the classification improvement given by the higher content of TiO₂ in IG garnet compared to MM. Besides the relevance for garnet of alkaline igneous rocks, which are very rich in Ti (e.g., Huggins et al. 1977), TiO₂ is highly important for garnet from intermediate–felsic igneous rocks (Appendix 6-E). Understanding the partitioning of Ti in garnet of igneous versus metamorphic systems is not straightforward, but the observed preferred incorporation of Ti into igneous biotite (Samadi et al. 2021) may also apply to garnet.

With regard to the discrimination of individual MM classes, the most important variables to separate BS/GS from other metamorphic classes include MgO and MnO (Figure 6.5-5d). The low content of MgO agrees with the low-temperature formation conditions and the many exchange thermometers that imply increasing $\text{Fe} \times (\text{Fe} + \text{Mg})^{-1}$ with decreasing temperature (Reverdatto et al. 2019, and references therein). High MnO contents are consistent with the increasing stability field of garnet to lower P – T conditions with increasing MnO content of the protolith. Thus, the earliest grown garnet typically shows the highest MnO contents (e.g., Carlson 1989) and removes MnO from the effective bulk composition leading to an up-temperature shift of garnet stability and bell-shaped Mn-zoning patterns (Evans 2004).

For the discrimination of GR from AM and EC/UHP garnet, the combination of high MgO and low CaO is most important (Figure 6.5-5e). This highlights the fundamentals of Fe–Mg exchange thermometry (decreasing $\text{Fe} \times (\text{Fe} + \text{Mg})^{-1}$ with increasing temperature) and the garnet–aluminosilicate–plagioclase–quartz geothermobarometer based on the higher stability of anorthite at high-temperature/low-pressure (low Ca in garnet) compared to the higher stability of grossular + aluminosilicate + quartz at low-temperature/high-pressure (e.g., Ghent 1976; Koziol & Newton 1988). Similarly, the best separation of AM and EC/UHP is observed by considering the higher values of $\text{FeO}_{\text{total}}$ versus MgO (lower temperature) and MnO versus CaO (lower pressure) for AM (Figure 6.5-5f).

Concerning composition, class CS shows the highest discrimination success, followed by A (Table 6.4-2). CS and A garnet are well separated from all other classes by their higher CaO content (Figure 6.5-6a), reflecting the high host-rock CaO content. The high TiO₂ content of A garnet allows the discrimination to CS (Figure 6.5-6b). Furthermore, UM garnet separates from IF/S and M garnet by the higher MgO and Cr₂O₃ content in combination with the lower $\text{FeO}_{\text{total}}$ content (Figure 6.5-6c), in line

separate composition classes

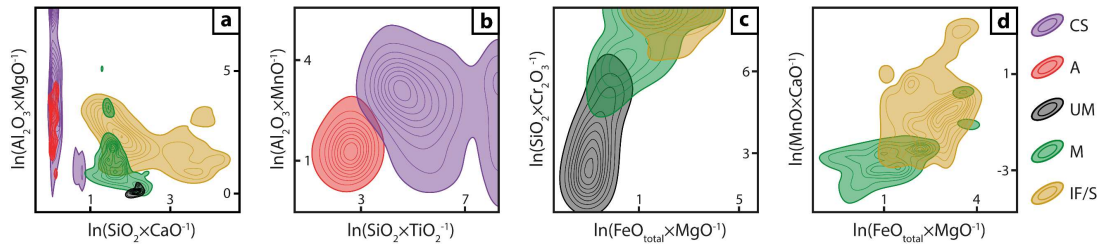


Figure 6.5-6: Main discriminators to separate composition classes. (a) CS and A versus UM, M, and IF/S; (b) CS versus A; (c) UM versus M and IF/S; (d) M versus IF/S (see Table 6.2-1 for abbreviations). Data shown as kernel density estimate maps.

with the element availability defined by the host-rock composition as well as the high-temperature formation conditions of mantle rocks. For the discrimination of IF/S and M garnet, $\ln(\text{FeO}_{\text{total}} \times \text{MgO}^{-1})$ and $\ln(\text{MnO} \times \text{CaO}^{-1})$ are the most important variables, both being higher for IF/S compared to M garnet (Figure 6.5-6d). This agrees with the often higher CaO content of M host rocks and the stabilization effect of garnet at lower temperatures by increased host-rock MnO contents that are mainly observed from IF/S protoliths.

6.6 Sensitivity and Applicability

One of the major aims in sedimentary provenance analysis is the reconstruction of source rock assemblages of sediments and the climatic–physiographic conditions under which they formed (von Eynatten & Dunkl 2012). The main potential of garnet single-grain analysis lies in reflecting variations in metamorphic conditions of rocks located in the source region, in particular when other characteristic minerals are lost due to their lower mechanical and/or chemical stability (Morton 1985). Thus, to represent a robust tool, predictions of the introduced garnet discrimination scheme should (i) be sensitive to changes in P – T conditions, (ii) reflect catchment specific host-rock characteristics, and (iii) be able to identify provenance shifts occurring in sedimentary successions or between samples.

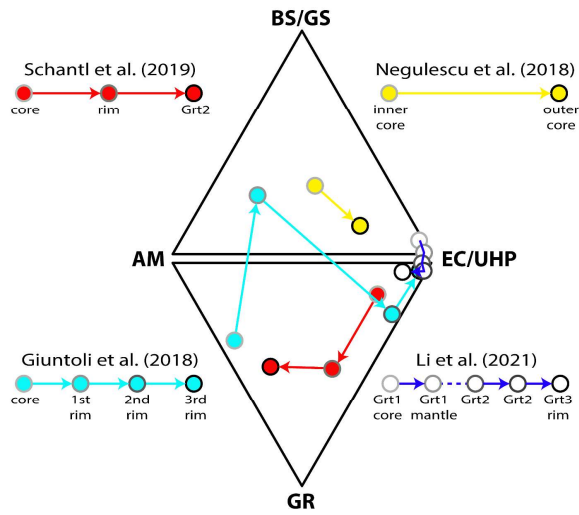
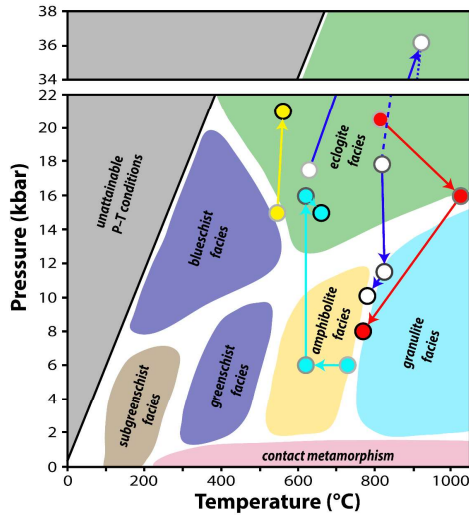
6.6.1 Sensitivity to P – T changes

The sensitivity to variations in P – T conditions during garnet growth is tested by comparing the proposed discrimination scheme predictions for different garnet growth zones and/or different garnet populations from samples that record multistage garnet growth based on geo-thermo-barometric investigations.

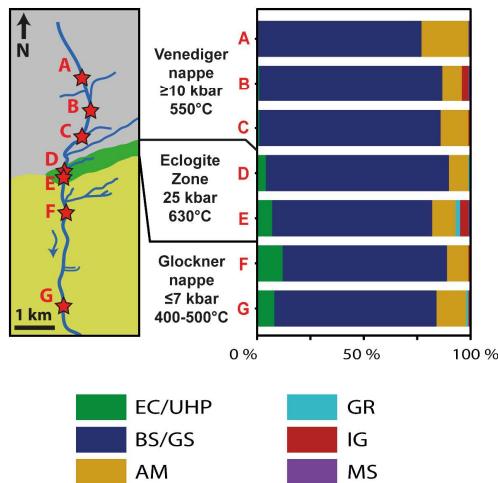
Schantl et al. (2019) studied garnet-bearing granulites from the Moldanubian Zone in Lower Austria by a combination of rutile thermometry, biotite breakdown reactions, Ti content of biotite, garnet–aluminosilicate–plagioclase–quartz and amphibole–plagioclase thermobarometry as well as thermodynamic modelling. For a sample set of five felsic granulites, the authors deduced 810–820 °C and 16–25 kbar for garnet core formation (eclogite facies), after which the core composition has been entirely reset by diffusion during decompression under increasing temperature to 1000–1050 °C and 15–17 kbar (eclogite–granulite facies transition). Subsequent fast decompression cooling to 770 °C and 8 kbar (granulite–amphibolite facies transition) led to diffusional modification of the rim composition and minor modification of the core composition, as well as the formation of a second garnet generation

(Figure 6.6-1a, red path in P - T facies diagram for MORB composition). This P - T evolution is well reflected by the arithmetic mean votes for garnet core ($n = 5$), garnet rim ($n = 5$), and retrograde garnet ($n = 2$, only observed in one sample) compositions (Figure 6.6-1a, red path in ternary vote plots). Core

(a) pressure-temperature variations



(b) catchment specific characteristics



(c) provenance shifts

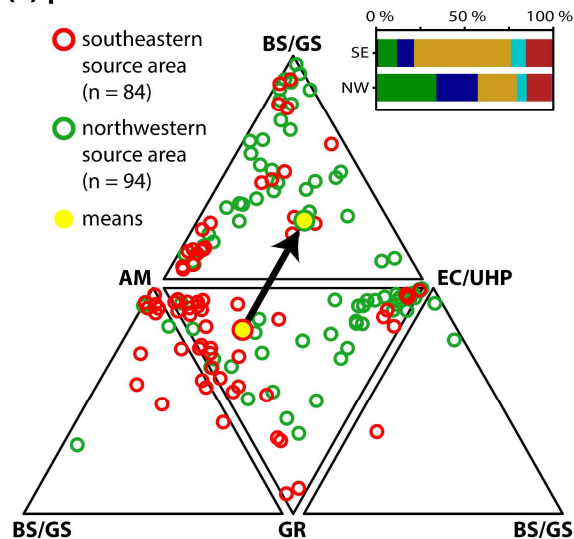


Figure 6.6-1: Sensitivity and applicability of the introduced garnet discrimination scheme. (a) Sensitivity to changes in pressure and temperature during garnet growth tested by crystalline rock examples. Tested examples are from Giuntoli et al. (2018), Negulescu et al. (2018), Schantl et al. (2019), and Li et al. (2021). Conditions of individual growth zones are shown in a pressure-temperature diagram with metamorphic facies for MORB composition after Bucher & Frey (2002), modified from Schönig et al. (2018b). Vote results for individual growth zones by the introduced discrimination scheme are shown in ternary diagrams. (b) Sensitivity to reflect catchment specific characteristics tested on an example case study of Krippner et al. (2015). Simplified geological map of the Hohe Tauern area shows the sampling locations. Class assignments of garnets from individual samples by the introduced discrimination scheme are shown as barplots. (c) Sensitivity to identify shifts in provenance tested on an example case study by von Eynatten & Gaupp (1999). Individual votes as well as arithmetic mean votes for garnet grains of sediments sourced from southeast and northwest are shown in the ternary ‘metamorphic facies’ plot. Barplot shows the corresponding class assignment (see Table 6.2-1 for abbreviations).

compositions received the highest votes for EC/UHP being five times higher than for AM and GR, rim compositions received highest votes for GR followed by EC/UHP, and retrograde garnet compositions show the highest votes for GR followed by slightly lower votes for AM, both being more than two times higher than for EC/UHP.

Giuntoli et al. (2018) investigated complexly zoned garnets from micaschists of the Sesia Zone in the Western Italian Alps. Thermodynamic modelling of garnet growth zones records two orogenic cycles, most completely preserved by sample 1249. The pre-alpine metamorphic event gives 730 °C and 6 kbar for garnet core formation (high-temperature amphibolite facies), followed by isobaric cooling to 620 °C and 6 kbar recorded by the first rim (amphibolite facies) (Figure 6.6-1a, pale-blue path in P - T facies diagram). Alpine metamorphism at 620 °C and 16 kbar leads to diffusional re-equilibration of the outermost rim and in proximity to fractures, denoted as the second rim (eclogite facies). Growth of a third rim resulted from subsequent temperature increase to 660 °C at almost isobaric conditions of 15 kbar (eclogite facies). This complex path is nicely reflected by the discrimination scheme votes (Figure 6.6-1a, pale-blue path in ternary vote plots). For the high-temperature amphibolite-facies core formation, predictions are highest for class AM followed by GR with very minor votes for BS/GS and EC/UHP. Votes for the composition of the first rim that formed under isobaric cooling within the amphibolite facies stay highest for AM, but the second highest votes switched to BS/GS reflecting the colder conditions. The strong increase in pressure recorded by the second and third rim results in dominant votes for EC/UHP. Such increase in votes for EC/UHP is also observed for the increased pressure conditions from the innermost garnet core (545 °C and 15 kbar, blueschist-eclogite facies transition) to the outermost core (560 °C and 21 kbar, eclogite facies) of a chloritoid-bearing micaschist studied by Negulescu et al. (2018) (Figure 6.6-1a, yellow path). It is important to note that in all three P - T paths tested, the host-rock composition for stages outside the eclogite facies are correctly predicted as IF/S, but growth stages within the eclogite facies are misclassified as M. This highlights the difficulty of assigning the correct composition class to subgroup EC-IF/S (cf. Figure 6.5-2b).

Li et al. (2021) studied mafic granulite lenses from the South Altyn Orogen in West China by thermodynamic modelling including garnet and plagioclase isopleth thermobarometry. The authors observed three garnet generations, whereby conditions of 600–655 °C and 15.8–19.2 kbar (eclogite facies) are recorded by the core of garnet one, followed by garnet one mantle growth at 920 °C and 36.2 kbar (ultrahigh-pressure eclogite facies), formation of garnet two from 820 °C and 17.8 kbar (eclogite facies) to 826 °C and 11.5 kbar (high-pressure granulite facies), and rim formation of garnet three at 826–735 °C and 11.5–8.7 kbar (high-pressure granulite-amphibolite facies transition) (Figure 6.6-1a, dark-blue path and white points in P - T facies diagram). While the formation of garnet one is correctly predicted as EC/UHP by the discrimination scheme, decompression is not well reflected, and although votes for GR increase, they stay highest for EC/UHP (Figure 6.6-1a, dark-blue path and white points in ternary vote plots). This agrees with the issue of the metamorphic class prediction for garnet of subgroup GR-M (cf. Figure 6.4-1d).

6.6.2 Reflecting catchment specific garnet host-rock characteristics

In order to test the sensitivity of the discrimination scheme to reflect changes in the relative abundance of different garnet-bearing host rocks contributing erosional material to sediments, a modern sand case

study is chosen with a well-known geological framework of the catchments. Thereby, we focus on the discrimination between blueschist/greenschist and eclogite facies sources, an issue that is not tackled by previous schemes.

Krippner et al. (2015) studied detrital garnets from tributaries draining the western Hohe Tauern window in the central Eastern Alps, Austria. The Dorfertal stream section was sampled by seven modern sand samples, here renamed as A–G (Figure 6.6-1b). Along the profile, the stream drains (i) the Venediger nappe that preserves few pre-Alpine eclogites (e.g., von Quadt et al. 1997) and underwent alpine peak metamorphic conditions of ~ 550 °C and ≥ 10 kbar mainly corresponding to the blueschist facies (Selverstone 1993), (ii) the eclogite zone that records peak conditions of ~ 630 °C and ~ 25 kbar corresponding to the eclogite facies (Hoschek 2007), and (iii) the Glockner nappe that underwent metamorphism at 400 – 500 °C and ≤ 7 kbar mainly corresponding to the greenschist facies (Selverstone 1993). This drainage path is well represented by the discrimination scheme predictions, showing that (i) garnets of samples A–C collected within the Venediger nappe are dominantly assigned to a BS/GS origin, (ii) an increasing amount of EC/UHP assigned garnet is observed once the eclogite zone is entered (samples D and E) which is becoming highest directly downstream of the eclogite zone (sample F), and (iii) the proportion of EC/UHP assigned garnet dilutes further downstream in sample G of the Glockner nappe (Figure 6.6-1b, barplot).

6.6.3 *Detecting provenance shifts*

To test the capability of the new garnet discrimination scheme regarding the identification of shifts in provenance, a multi-method provenance study of Cretaceous sedimentary rocks from the Northern Calcareous Alps is chosen (von Eynatten & Gaupp 1999). Based on framework petrography, heavy mineral analysis, and the chemical composition of amphiboles, white mica, tourmaline, garnet, and chloritoid, the authors distinguished two contrasting source regions. Particularly the occurrence of glaucophane and phengite indicate the contribution of erosional material from low-temperature/high-pressure metamorphic rocks located in a north-western source area, which are absent in sediments sourced from a south-western source.

Re-evaluation of the detrital garnet data by the introduced discrimination scheme strongly supports this observation. Garnet grains from the south-eastern source are dominantly classified as AM (~ 56 %), while class assignments to BS/GS, GR, and EC/UHP are each < 11 % (Figure 6.6-1c). By contrast, garnet grains sourced from northwest are dominantly assigned to EC/UHP (~ 34 %) with significant but much lower proportions of AM (~ 22 %), and much higher proportions of BS/GS (~ 23 %). This is further highlighted by the arithmetic mean votes that shift from the AM–GR–EC/UHP diagram (39 % AM, 12 % GR, 14 % EC/UHP, 11 % BS/GS) for the south-eastern source, to the AM–BS/GS–EC/UHP diagram (24 % AM, 8 % GR, 31 % EC/UHP, 19 % BS/GS) for the north-western source (Figure 6.6-1c, black arrow).

6.7 The ‘garnetRF’ web application

To enable a user-friendly application of the garnet random forest discrimination scheme without the need for installing software and having programming expertise, we developed a freely and worldwide

accessible web application called ‘garnetRF v1.1’. The app was developed using the ‘shiny’ R package of Chang et al. (2019) and the ‘shinydashboard’ package of Chang & Ribeiro (2018). Used packages further include those mentioned in Section 6.3 as well as ‘readxl’ (Wickham & Bryan 2019) and ‘openxlsx’ (Schauberger & Walker 2020) for importing spreadsheet files, as well as ‘colourpicker’ (Attali 2020) and ‘cowplot’ (Wilke 2020) for visualization.

The ‘garnetRF’ app is standalone and users are guided by an ‘instructions’ tab. By five quick steps, users get from their garnet major-element data to discrimination scheme results and corresponding plots:

1. Visit the ‘garnetRF’ app via web browser at <http://134.76.17.86:443/garnetRF/>, hosted at the servers of GWDG, the data and IT service company of the University of Göttingen and the Max Planck Institute in Göttingen.
2. Give your project a title. This is optional but facilitates data handling as any file output includes the project title.
3. Download the .xlsx template via ‘Data Preparation’ and copy your garnet chemical data to the template. Note that all analyses from each individual sample should have the same sample name for adequate data visualization and calculation of means. Individual grain or spot names can optionally be assigned in the ‘grain_no’ column. Ensure the right order of oxides, give values in wt%, use a point as decimal separator, give a numeric value <0.03 for oxide contents below detection limit, and leave cells empty for not-analyzed oxides. Empty cells are only allowed for Cr₂O₃ and TiO₂ (Note that this reduces prediction accuracy: cf. Figure 6.5-2 and Figure 6.5-4).
4. Upload your prepared data. Once upload and calculations are complete, results can be found and downloaded in the ‘Data Tables’ tab. Individual results for each grain, the arithmetic mean for each sample, and class assignments (majority vote) for each sample are given.
5. Click ‘Create Plots’ to visualize individual and mean votes as ternary plots for each scheme as well as barplots for class assignments. Marker size, shape, and color can be modified and plots can be downloaded as .pdf, and thus easily be modified via graphical vector programs.

6.8 Conclusions

A large database including 13,615 observations of chemical garnet major-element analyses is compiled from the literature. Observations are subdivided into 23 petrogenetic subgroups with regard to host-rock type, metamorphic facies, and composition. With this database, a new discrimination scheme is developed that aims at predicting the original host-rock of detrital garnet grains. In order to focus on the most substantial information in terms of sedimentary provenance, database subgroups are merged into seven classes to predict the ‘setting and metamorphic facies’ of the garnet-bearing host rock as well as five classes to predict the ‘composition’. For both prediction issues, the random forest classification machine-learning algorithm is applied.

The final discrimination scheme is easily applicable via a provided web app. Considering the out-of-bag error, the scheme is able to correctly predict (i) the host-rock setting with a class average of >95 %, and

(ii) the host-rock metamorphic facies with a class average of >84 %, and (iii) the host-rock composition with a class average of >93 %.

Success rates for individual classes included in setting, metamorphic facies, and composition predictions differ ≤ 5 % from the class average, emphasizing substantial discrimination balance. However, balancing between individual subgroups merged in the prediction classes is much less pronounced. Particularly notable are higher misclassification rates in (i) setting prediction for metamorphic calc–silicate garnet (misclassified as metasomatic) and mafic igneous garnet (misclassified as metamorphic), (ii) metamorphic facies prediction for intermediate–felsic/metasedimentary eclogite/ultrahigh-pressure facies garnet (misclassified as granulite, blueschist/greenschist, and amphibolite facies) and mafic granulite facies garnet (misclassified as eclogite/ultrahigh-pressure facies), and (iii) composition prediction for mafic blueschist/greenschist facies as well as mafic igneous garnet (misclassified as intermediate–felsic/metasedimentary) and intermediate–felsic/metasedimentary eclogite/ultrahigh-pressure garnet (misclassified as mafic).

Detailed exploration of the discrimination models reveals that decisions mainly follow characteristic partitioning trends that are the building blocks of geothermobarometry. The strength of the developed model is the step-wise consideration of many of those element ratios in a randomized way that leads to a significant increase in classification success without compromising generalization. This procedure also uses individual decision lines for subpopulations occurring within the prediction classes, which seems to be the main reason for high classification success rates for the host-rock metamorphic facies without knowledge of the host-rock composition and vice versa. In addition, model exploration uncovers the high potential of minor variations in TiO_2 to strongly increase prediction accuracy, underlining the importance to include TiO_2 in the standard protocol of in-situ chemical analysis of garnet.

Application examples to crystalline rocks that record multiple stages of garnet growth, to modern sand samples from tributaries draining variable lithologies, and to sedimentary successions that received erosional material from different sources demonstrate that the discrimination scheme is sensitive to identify (i) variations in P – T conditions, (ii) catchment specific host-rock characteristics, and (iii) shifts in provenance. Although the scheme is designed for provenance applications and subsists on a statistically significant number of grains analyzed, it may also be useful in crystalline rock petrology to quickly narrow down sample sets to the most interesting samples in order to study these in more detail.

6.9 Outlook and call on the community

Although garnet host-rock predictions clearly enhanced compared to previous discrimination schemes, there is still potential for improvement, in particular with regard to robustness and balance within individual classes. One issue is the underrepresentation of some individual groups/subgroups, especially BS, GS, EC/UHP-IF/S, IG-M, and low-temperature MM-CS. These are also those groups/subgroups that show the lowest classification success. Another issue is the separate treatment of ‘setting and metamorphic facies’ and ‘composition’.

We suggest that a combined model with a prediction of detailed classes and derivation of the most important information is the best future direction. For example, class GR could be split into GR-IF/S, GR-M, and GR-CS, and after prediction, the maximum vote of the three classes defines the GR prediction, similar to the approach for MM in the presented setting scheme. In the same way, the maximum vote of all mafic classes, that would be MA-M, IG-M, BS/GS-M, AM-M, GR-M, and EC/UHP-M, defines the prediction for M. This also allows to balance all subgroups during the training phase of model development.

To reach this aim, the dataset has to be extended, in particular for underrepresented groups/subgroups mentioned. In many works, solely the most representative garnet compositions are reported, but it is clear that a much higher amount of data was acquired during the project. Thus, we want to encourage the community to contribute their supplementary as well as newly published garnet data with known host-rock type, metamorphic grade, and composition to the dataset. We also appreciate hints on references that are so far not included in the dataset. In addition, we welcome any kind of criticism or detected problems. Based on feedback and new data acquisition, we plan to submit an updated scheme within the next couple of years.

Acknowledgements

This work was supported by the German Research Foundation [DFG grant EY 23/27-1]. We thank Pierre Lanari and an anonymous reviewer for detailed and valuable comments and Daniela Rubatto for the editorial work.

The sedimentary record of ultrahigh-pressure metamorphism: a perspective review

Jan Schönig¹, Hilmar von Eynatten¹, Guido Meinhold^{1,2,3}, and N. Keno Lünsdorf¹

¹*Geosciences Center Göttingen, University of Göttingen, Germany*

²*School of Geography, Geology and the Environment, Keele University, United Kingdom*

³*Institute for Geology, TU Bergakademie Freiberg, Germany*

manuscript in preparation

(planned submission to Earth-Science Reviews)

Tracing ultrahigh-pressure (UHP) metamorphism of crustal rocks through the geological record is a key for understanding the evolution of plate tectonics on Earth due to the linkage with deep subduction processes. Until recently, UHP research was almost exclusively based on the investigation of crystalline rocks, but findings of coesite and diamond inclusions in detrital mineral grains demonstrate that the sedimentary record archives mineralogical evidence for UHP metamorphism. We here review previous attempts to link sediments to UHP sources and the recent findings of detrital UHP garnet, and thoroughly discuss the new approach in the search for UHP metamorphism. The indicative UHP minerals were identified by Raman spectroscopy and include monomineralic coesite and bimineralic coesite + quartz inclusions in detrital garnets from the Scandinavian Caledonides of Norway, the D'Entrecasteaux Metamorphic Complex of Papua New Guinea, and the Central European Variscides of Germany, as well as diamond inclusions in the latter. Garnet chemistry and inclusion assemblages are used to gain information about the origin of these mineral grains and to discriminate different UHP sources. Presumably, the value of information will increase in future studies by considering other detrital containers of UHP minerals such as the ultrastable heavy minerals zircon, rutile, and tourmaline, for which also a range of single-grain provenance tools exist. The enrichment of monomineralic coesite inclusions in detrital minerals enables the investigation of coesite preservation factors and potentially elastic geothermobarometry in the coesite stability field. Altogether, the method allows for (i) screening large regions systematically for the presence of UHP rocks, (ii) studying the exhumation history of UHP terranes, and (iii) monitoring the former existence of UHP terranes on the Earth's surface.

7.1 Introduction

Ultrahigh-pressure (UHP) metamorphism of continental crust is intimately connected to deep (>100 km) subduction processes (e.g., Hawkesworth et al. 2016), which are characteristic of modern-style plate tectonics (e.g., Stern 2005). Tracking these processes through the geological record is of first-order significance in Earth Sciences to draw conclusions on the evolution of subduction tectonics in Earth history. Although several mineralogical indicators have been proposed and were controversially discussed, the best and unequivocal indicators for UHP metamorphism are inclusions of coesite and

diamond in mechanically robust host minerals (e.g., Chopin 2003; Kotková et al. 2011). This is well known since the breakthrough studies in the 1980s reporting bimineralic coesite + quartz inclusions in garnet and omphacite (Chopin 1984; Smith 1984), and diamond inclusions in garnet of crustal rocks in the early 1990s (Sobolev & Shatsky 1990). Since then, a great number of terranes have been identified that experienced deep subduction processes and were subsequently exhumed, making UHP metamorphism a common phenomenon in Earth's metamorphic record since the late Neoproterozoic (Liou et al. 2009).

Studies identifying UHP metamorphism are primarily based on the investigation of crystalline rocks, and approaches using the sedimentary record to constrain the erosion of UHP rocks are extremely scarce. The few studies available are sedimentary provenance studies, where chemical and isotopic characteristics of detrital single grains are roughly linked to the characteristics of known UHP terranes, which could represent a potential source of the sediments (e.g., Grimmer et al. 2003; Li et al. 2005). These techniques, however, are unable to verify UHP sources or explore regions on the existence of these rocks. The identification of coesite inclusions in zircons of cobbles from conglomerates reported by Wan et al. (2005) is restricted to coarse clastic sediments, and thus this technique is only suitable in certain circumstances. In contrast, in an individual case, coesite inclusions were reported from single detrital zircon grains (Chen et al. 2005). Recently, a novel method has been developed using Raman spectroscopy to systematically screen detrital mineral grains on the presence of coesite inclusions with a focus on garnet, which allows to pinpoint an UHP origin (Schönig et al. 2018a). This approach was first successfully applied on detrital garnet from the Western Gneiss Region of Norway and proof of concept has been demonstrated by application to modern sand samples from the Saxonian Erzgebirge of Germany (Schönig et al. 2019, 2020) and Earth's youngest UHP terrane in Papua New Guinea (Baldwin et al. 2021). Besides the frequent inclusions of coesite in detrital garnets of the Erzgebirge, also diamond inclusions were detected.

In this paper, we review early attempts to link sediments to UHP sources, the recent findings of UHP mineral inclusions in detrital garnet, and the related method of capturing the distribution and characteristics of UHP metamorphic rocks by combining mineral inclusion data with garnet chemistry. This also includes the benefits as well as challenges, which have to be carefully considered, and the prospective enhancements of the method. Furthermore, we discuss the potential of detrital UHP host minerals beyond garnet, with particular emphasis on heavy minerals which are ultrastable in the sedimentary cycle. Finally, we give an outlook on fields of application by considering the sedimentary record as an archive for UHP metamorphism.

7.2 Attempts to link sediments to UHP sources

Early attempts to link sedimentary successions to the erosion of UHP source rocks are restricted to the Dabie Shan and Sulu terranes located in the eastern part of the Qinling–Dabie–Sulu Orogen in China (Figure 7.2-1A). This orogen and accompanied UHP rocks were formed during collision of the North and South China blocks in the Triassic (Li et al. 2005). To evaluate the timing of exposure, sedimentary rocks of various basins surrounding the Qinling–Dabie–Sulu Orogen were considered to be sourced from the Dabie and Sulu UHP rocks.

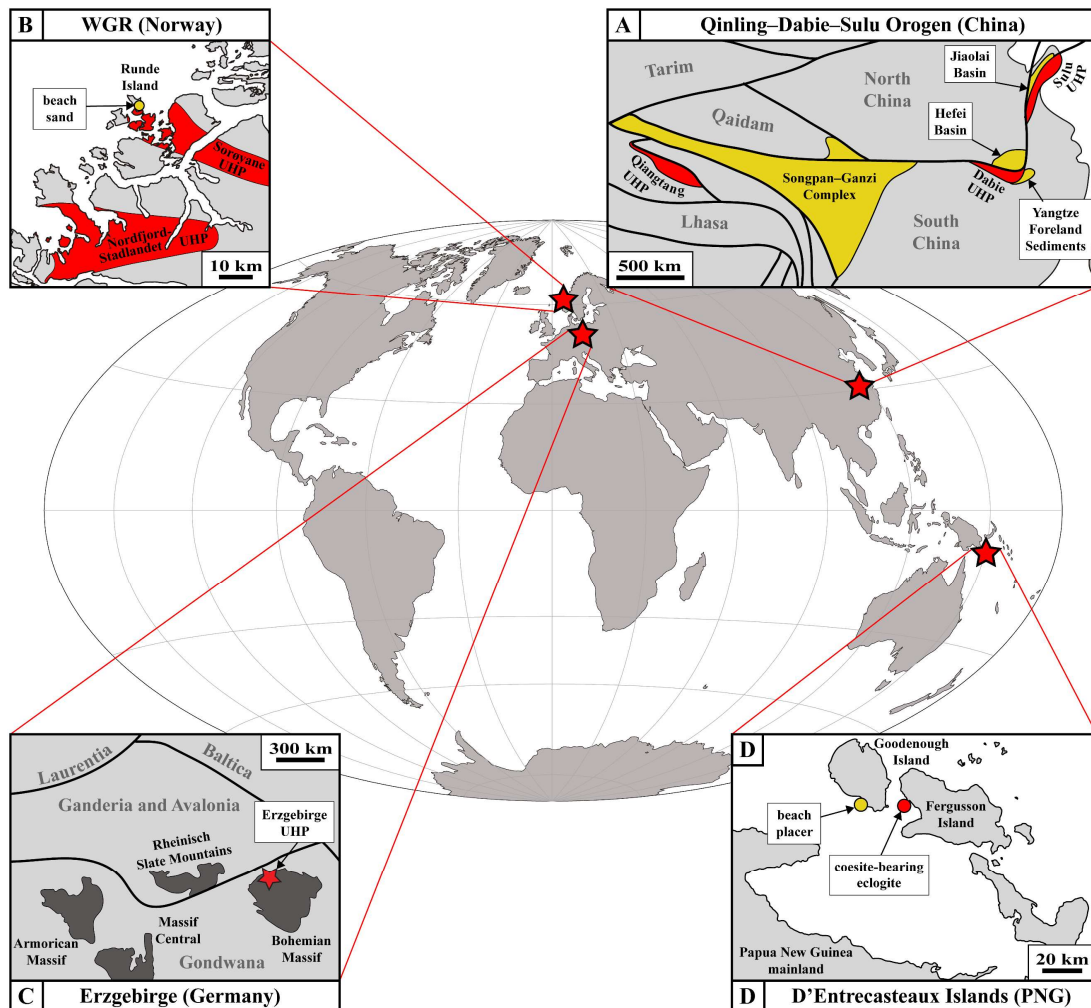


Figure 7.2-1: Global map showing locations where detrital approaches have been applied to trace the erosion of UHP rocks. (A) Qinling–Dabie–Sulu Orogen (China) modified from Zhang et al. (2012); (B) Western Gneiss Region (Norway) modified from Root et al. (2005), Krippner et al. (2016), and Schönig et al. (2018a); (C) Saxonian Erzgebirge (Germany) modified from Linnemann et al. (2012) and Schönig et al. (2020); and (D) D'Entrecasteaux metamorphic complex (Papua New Guinea) modified from Baldwin et al. (2021).

Considerable attention has been given to the large volumes of Triassic turbidites of the Songpan–Ganzi Complex located ~1000 km west of the present-day outcropping UHP rocks of the Dabie Shan (Figure 7.2-1A). By comparing the age and volume of the Songpan–Ganzi Complex with the amount of material proposed to have overburden the Dabie UHP rocks, Nie et al. (1994) proposed that the majority of the Triassic sediments were sourced from the eroding Qinling–Dabie Orogen during exhumation of the UHP rocks. Besides possible pitfalls in this mass balance attempt, doubts on this interpretation have been raised due to the missing mineralogical evidence for the contribution of eroded material from both UHP and the formerly overlying high-pressure (HP) rocks (Avigad 1995). Later, detrital zircon U–Pb ages revealed that the Songpan–Ganzi Complex consists of multiple depocenters with different sources and that low Th/U detrital zircons, which are typical for the UHP rocks from Dabie as well as metamorphic zircon in general (e.g., Rubatto 2017, and references therein), show different ages than their supposed source rocks (Weislogel et al. 2006, 2010). Yet, the sediment sources of the Triassic

turbidites of the Songpan–Ganzi Complex are still a matter of debate; various sources are proposed including the Dabie UHP rocks, the Qinling–Dabie Orogen, the Qaidam Block (Kunlun Arc), the South China Block, the Qiantang UHP rocks, and the Qiantang Block (e.g., Zhang et al. 2012, and references therein, Figure 7.2-1A). Studies suggesting the presence or absence of an UHP source are based on the occurrence of HP minerals like omphacite, the chemical composition of garnet, a high Si content in white mica, and comparison of zircon U–Pb or white mica $^{40}\text{Ar}/^{39}\text{Ar}$ ages with supposed UHP source terranes (e.g., Enkelmann et al. 2007; Zhang et al. 2008). In contrast to the supposed long transport to the Songpan–Ganzi Basin, Grimmer et al. (2003) assume deposition of erosional material sourced from the Dabie UHP rocks in closer proximity in the Yangtze foreland, located south-east of the Dabie UHP terrane (Figure 7.2-1A). To link the investigated sediments to a Dabie source, the authors compared $^{40}\text{Ar}/^{39}\text{Ar}$ ages of white mica. Because a few of these micas in the Middle Jurassic successions show Si values of >3.5 apfu (atoms per formula units), the authors propose a first limited exposure of Dabie UHP rocks at this time.

In addition, it is also considered that eroded material from the Dabie UHP rocks was accumulated in the Hefei Basin (Figure 7.2-1A). Li et al. (2005) recognized a prominent change in the Si content of white mica within the Lower Jurassic Fanghushan Formation from dominantly <3.3 apfu to dominantly >3.3 apfu. This trend continues in the younger formations. Based on the Triassic age of some zircons, the authors link the Lower Jurassic sediments to a Dabie source. Most convincingly, evidence for the exposure and erosion of UHP rocks is given by coesite inclusions in detrital zircon from sandstone of the Fanghushan Formation (Chen et al. 2005) and also by coesite inclusions in zircon of a granitic gneiss cobble from an Upper Jurassic conglomerate of the Fenghuangta Formation (Wan et al. 2005).

A similar approach of comparing chemical composition and U–Pb ages of detrital zircon with a known UHP terrane was performed by Xie et al. (2012). The authors analyzed zircons from the Lower Cretaceous Laiyang Group of the Jiaolai Basin (Figure 7.2-1A), which is adjacent to the Sulu UHP terrane that in turn is supposed to be the eastern extension of the Dabie UHP terrane (e.g., Hacker et al. 1998). Because the analyzed zircons show low Th/U ratios, indicating a metamorphic origin, and U–Pb ages similar to those of metamorphic rocks of the Sulu terrane, UHP rocks of the latter are proposed as sediment source, and thus were probably exposed on the Earth's surface during early Cretaceous time (Xie et al. 2012). As outlined by the provenance studies from sedimentary basins in China, attempts to trace UHP metamorphism through the sedimentary record are mainly based on mineral chemical composition of mica and rarely garnet, and the comparison of chronologic ages from detrital mineral grains and known potential UHP source rocks. Although determining the Si content of white mica is an important tool in sedimentary provenance analysis because the substitution of Si + (Mg, Fe) for two Al strongly depends on pressure conditions (e.g., Massonne & Schreyer 1987), it is not possible to confidently discriminate HP and UHP sources. Similarly, garnet composition is useful to identify different metamorphic sources, but UHP garnet does not show a unique composition clearly differing from that of HP garnets (Krippner et al. 2014; Tolosana-Delgado et al. 2018; Schönig et al. in press). Chronologic ages of single grains are useful to obtain information about the source regions, but discriminating HP and UHP source rocks from the same region is not resolvable.

Thus, techniques to identify UHP metamorphism in the detritus are limited to mineralogical indicator phases, whereby coesite and diamond are the most important. Ideally, these minerals do not occur as

single grains but show some paragenetic context of their source rock. Otherwise, a differentiation between UHP metamorphism of crustal rocks and a mantle origin (i.e. peridotites, pyroxenites, mantle eclogites, or kimberlites) is open for interpretation (e.g., Kueter et al. 2016). In addition, shock metamorphism resulting from impact events represent another formation environment of coesite (e.g., Chao et al. 1960). Thus, a coesite inclusion in zircon of a cobble-sized clast like reported by Wan et al. (2005) is exceptionally beneficial because very coarse clastic material can provide important source rock information (e.g., Cuthbert 1991; Dunkl et al. 2009; Kellett et al. 2018). However, these gravel-sized clasts are usually a feature of proximal sedimentary successions which do not represent the majority of clastic sediments and sedimentary rocks. In contrast, sand-sized grains are widespread in modern as well as ancient clastic sediments and sedimentary rocks and can be easily analyzed by a wide range of analytical techniques, making it the preferred grain-size range in single-grain provenance analysis (e.g., von Eynatten & Dunkl 2012). Consequently, the identification of UHP mineral inclusions in detrital single grains, like reported by Chen et al. (2005), is the most promising attempt to trace UHP metamorphism through the sedimentary record.

7.3 UHP mineral inclusions in detrital garnet

As outlined above, the detection of coesite and diamond inclusions in detrital mineral grains is the most desirable method to trace UHP metamorphism through the sedimentary record. Although a first report of coesite in detrital zircon was given by Chen et al. (2005), and the findings were subsequently used by Li et al. (2005), a first detailed report of a technique to systematically trace UHP metamorphism at the catchment scale by analyzing inclusions in detrital garnet was given by Schönig et al. (2018a), and further developed and verified by Schönig et al. (2019, 2020, 2021b) and Baldwin et al. (2021).

7.3.1 Documented findings

7.3.1.1 Western Gneiss Region of Norway

Schönig et al. (2018a) analyzed 732 garnets from a modern sand sample taken at the beach at the mouth of a small stream on the south-eastern coast of the island of Runde, located in the Sorøyane UHP domain of the Western Gneiss Region in south-west Norway (Figure 7.2-1B). This sample represents a relatively small present-day catchment of ~1 km². The analyzed grain-size range of very-fine to medium sand was split into the three fractions 63–125 µm, 125–250 µm, and 250–500 µm. The garnets were mounted in epoxy, grounded with SiC, polished with Al₂O₃, and the inclusions were analyzed by Raman spectroscopy.

Detrital garnets containing inclusions ≥ 2 µm are frequent in the sample (>80 %). In contrast to many other analytical in-situ techniques that are limited to the polished surface, Raman spectroscopy enables inclusion analysis in the entire grain volume. A total of 13 coesite inclusions were detected in six of the analyzed garnet grains, being the first report of coesite inclusions in detrital garnet single grains and directly reflecting an UHP source. These coesite inclusions are most frequent in garnets of the 63–125 µm fraction, less frequent in the 125–250 µm fraction, and absent in the 250–500 µm fraction.

All detected coesite inclusions are small (<12 μm , longest axis in plane view), mainly spheroidal to spherical in shape, and preserve residual strains resulting from the entrapment at UHP conditions and differential thermoelastic properties of the garnet host and the entrapped coesite. In addition, all coesite inclusions are monomineralic, and thus they lack the typical petrographic structures of bimineralic coesite + quartz inclusions resulting from the partial coesite-to-quartz transformation, like radial fracturing of the host garnet (Figure 7.3-1A).

7.3.1.2 Saxonian Erzgebirge of Germany

By applying the analytical concept of Schönig et al. (2018a) to seven modern sand samples from tributaries draining the central part of the Saxonian Erzgebirge in Germany (Schönig et al. 2019), the method of tracing UHP metamorphism by analyzing detrital garnet was tested for present-day catchments ranging from sizes as small as Runde ($\sim 1 \text{ km}^2$; Schönig et al. 2018a), over catchments being up to ten times larger, and finally to a regional river catchment draining an area $> 500 \text{ km}^2$. One-hundred inclusion-bearing garnets per sample (700 grains in total) from the 125–250 μm grain-size fraction were analyzed by Schönig et al. (2019). In a follow-up study, inclusion analysis of each sample was extended to 100 garnet grains from the 63–125 μm as well as the 250–500 μm grain-size fractions (Schönig et al. 2020). Out of the 2100 studied grains, 93 garnets were identified that contain a total of 193 coesite inclusions. This includes garnet grains from all studied catchments, showing that UHP rocks in the Erzgebirge are more frequent and wider distributed than previously expected.

A detailed investigation of the coesite inclusions by Schönig et al. (2021b) using hyperspectral two-dimensional Raman imaging revealed that small coesite inclusions $< 9 \mu\text{m}$ are primary monomineralic, mainly spherical to spheroidal in shape with few inclusions showing sharp edges (Figure 7.3-1A), and

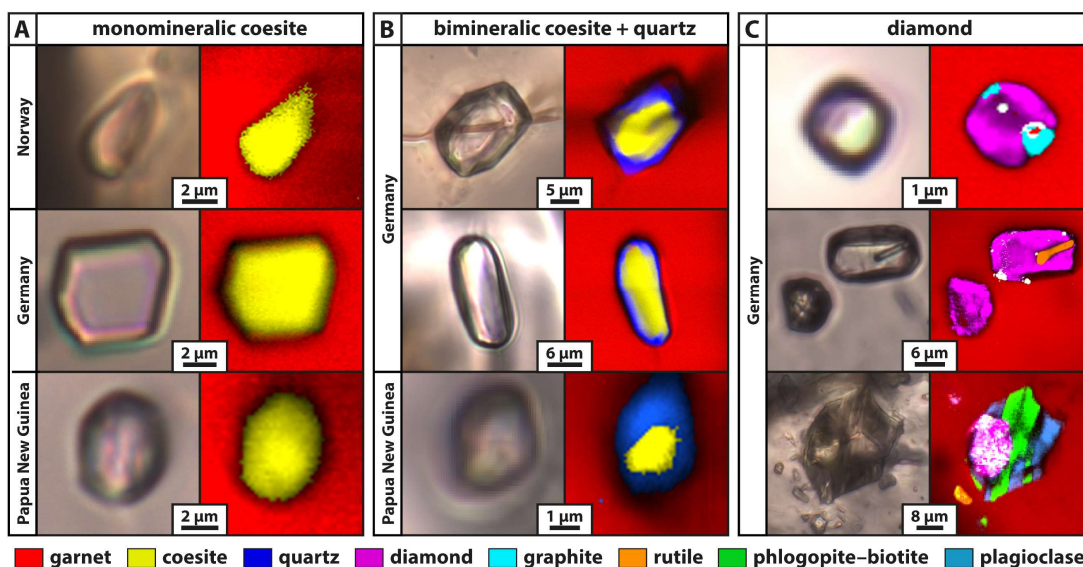


Figure 7.3-1: Photomicrographs and Raman images of UHP inclusions in detrital garnet. (A) Monomineralic coesite inclusions. (B) Coesite inclusions partially transformed to quartz. (C) Diamond inclusions. White pixels correspond to inhomogeneities or unidentified phases. Modified from Schönig et al. (2018a) for the Western Gneiss Region in Norway, from Schönig et al. (2019, 2020, 2021b) for the Saxonian Erzgebirge in Germany, and Baldwin et al. (2021) for the D’Entrecasteaux metamorphic complex in Papua New Guinea.

preserve residual strains, which is in line with observations from Norway (Schönig et al. 2018a). In contrast, larger inclusions often partially transformed to quartz (Schönig et al. 2021b; Figure 7.3-1B). This size dependence is a general trend that is also observed in single grains containing multiple inclusions of small monomineralic coesite and larger bimineralic coesite + quartz (cf. figs. 10 and 11 in Schönig et al. 2021b, here Figure 5.4-9 and Figure 5.4-10). The replacement of coesite by quartz is observed to start at the inclusion-host boundary and progresses towards the inclusion center. Occasionally, the bimineralic inclusions show a filigree of fine fractures spreading into the host garnet (Figure 7.3-1B). As fluid availability is crucial for the coesite-to-quartz transformation (e.g., Liu & Zhang 1996; Mosenfelder & Bohlen 1997; Mosenfelder et al. 2005; Liu et al. 2017), this led to the conclusion that inclusion size is a superordinate factor controlling the potential of the inclusion to fracture the host garnet, and thus enable fluid infiltration (Schönig et al. 2021b). Carbonaceous material detected at host-inclusion boundaries of bimineralic and fractured inclusions record peak temperatures of ~330 °C based on the Raman geothermometer of Lünsdorf et al. (2017), indicating that fracturing and fluid infiltration is a late process during exhumation (Schönig et al. 2021b). The size dependence is probably related to the initial fracture length, that is the length of the inclusion–host boundary which is defined by inclusion size (Whitney et al. 2000). Large and small inclusions entrapped in the same garnet and at the same pressure–temperature (P – T) conditions develop similar non-lithostatic inclusion strains during exhumation, but larger inclusions have a larger initial fracture length, which requires less stress to propagate into the host garnet (Schönig et al. 2021b).

Besides coesite, a total of 145 diamond inclusions were found in 54 detrital garnets of two samples (Schönig et al. 2019, 2020). The vast majority (53 diamond-bearing garnets) are from a sample taken very proximal to felsic diamond-bearing rock lenses (e.g., Nasdala & Massonne 2000), while one diamond-bearing grain was detected in the sample that represents the regional river catchment. However, as this catchment also encompasses the known diamond-bearing rock lenses, this finding does not necessarily point to another diamond-bearing source (Schönig et al. 2020).

Diamond-bearing inclusions are up to 30 μm in dimension and mainly show an irregular shape. Some of them are monomineralic but most diamonds occur in polyphase inclusions together with varying amounts of minerals like quartz, plagioclase, graphite, rutile, apatite, and phyllosilicates (Figure 7.3-1C). Particularly the co-existence with quartz + feldspar + phyllosilicates indicate the entrapment as a melt, which agrees with the many other melt inclusions found in the detrital garnets that sometimes include rare polymorphs like cristobalite, kokchetavite, and kumdykolite (Schönig et al. 2020). The reported diamonds represent the first record of diamond-grade UHP metamorphism of crustal rocks by analyzing the detritus, and shows that diamond-bearing rocks are capable to transfer prominent signatures to the sedimentary record (Schönig et al. 2019).

7.3.1.3 *D'Entrecasteaux Islands of Papua New Guinea*

The D'Entrecasteaux metamorphic complex in eastern Papua New Guinea records the youngest UHP rocks exposed on Earth's surface (Baldwin et al. 2008), dated to be of late Miocene age (e.g., Monteleone et al. 2007; Baldwin et al. 2012). However, direct mineralogical evidence for UHP metamorphism in form of coesite is restricted to a single eclogite lens (Baldwin et al. 2008; Faryad et al. 2019; Osborne et al. 2019). As further attempts to find coesite in crystalline rock samples have been

unsuccessful, Baldwin et al. (2021) considered the detrital garnet record as a potential archive, similar to the approach applied in Norway and Germany (Sections 7.3.1.1 and 7.3.1.2). The authors studied the inclusion assemblage of 354 sand-sized detrital garnets from a modern beach placer. Two coesite-bearing grains were identified, one showing a monomineralic coesite inclusion (Figure 7.3-1A) and one showing a coesite inclusion that partially transformed to quartz (Figure 7.3-1B). These findings strongly increased evidences for UHP metamorphism in the actively exhuming metamorphic complex and demonstrates that the detrital garnet record is capable to trace sparsely preserved UHP relicts at the catchment scale.

7.3.2 UHP source rock reconstruction using garnet chemistry and inclusion assemblages

7.3.2.1 Verifying a subduction-related crustal origin

Although inclusions of coesite and diamond serve as powerful indicators for UHP conditions, it must be considered that their formation is not restricted to deep subduction of crustal rocks. Both coesite and diamond also occur in rocks that experienced shock metamorphism during impact events (e.g., French & Koeberl 2010, and references therein) as well as in rocks of mantle origin (e.g., Smyth & Hatton 1977; Schulze et al. 2000). Most mantle rocks are transported to Earth's surface as xenoliths by alkaline volcanism, i.e., by kimberlites and lamproites (e.g., Field et al. 2008). In addition, fragments of mantle rocks are emplaced into subducting continental crust at convergent plate margins and are subsequently exhumed together with their crustal country rocks (e.g., Medaris 1980). Though this process is subduction related, the crustal rocks and intruded mantle rocks are often not iso-facial, and mantle rocks may originate from much greater depth than reached by the subducted and exhumed slab (e.g., Spengler et al. 2006). Thus, to link detrital coesite- and diamond-bearing garnet to the deep subduction of crustal rocks, both an impact-related origin as well as a mantle origin have to be excluded.

While impact-related coesite and diamond show unique characteristics (e.g., Ferrière & Osinski 2012) and typically do not occur as inclusions in garnet, the features of coesite- and diamond-bearing mantle and crustal garnet are similar and challenging to discriminate. A first look on the heavy mineral suite of a sediment sample can provide hints whether detritus supplied from mantle rocks has to be considered, for example by the presence of chrome spinel (e.g., Nowicki et al. 2007). The chemical composition of chrome spinel can further be used as a petrogenetic indicator (Irvine 1967; Dick & Bullen 1984; Cookenboo et al. 1997; Mange & Morton 2007; Han et al. 2019), but mantle and crustal chrome spinel show high compositional overlap (Gurney & Zweistra 1995). More indicative is the major-element composition of the detrital garnet grains that entrapped coesite and diamond inclusions. Mantle garnet of ultramafic host-rock composition can be confidently identified by comparatively high Cr_2O_3 content as well as high MgO content compared to $\text{FeO}_{\text{total}}$ (Schulze 2003; Grütter et al. 2004; Tolosana-Delgado et al. 2018). However, particularly challenging is the discrimination of chromium-poor mantle garnet, mainly originating from mantle eclogites, and crustal eclogite-facies garnet (Hardman et al. 2018).

Two multivariate discrimination schemes are available that enable the distinction of chromium-rich as well as chromium-poor mantle garnet from crustal garnet (Hardman et al. 2018; Schönig et al. in press). Figure 7.3-2 shows the discrimination results of this schemes for the detrital coesite- and diamond-

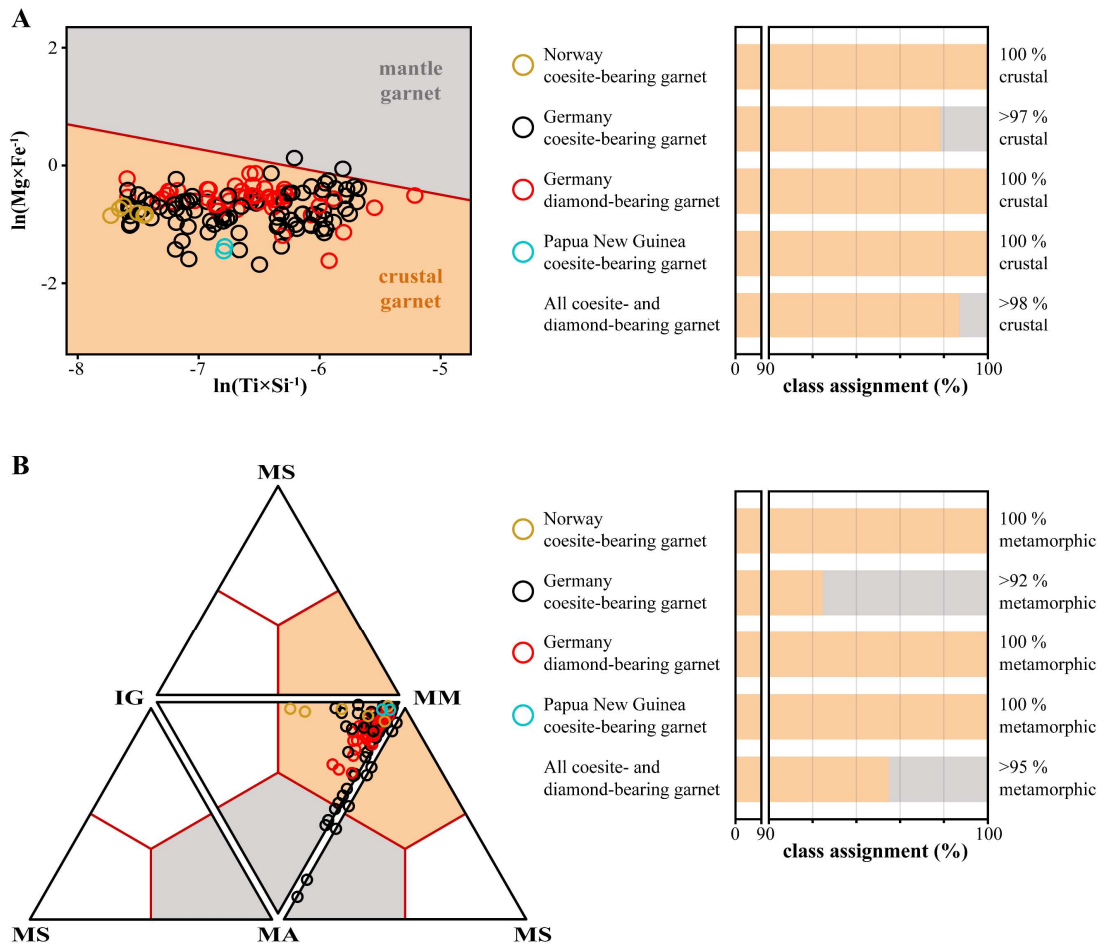


Figure 7.3-2: Discrimination scheme classification for crustal vs. mantle origin of coesite- and diamond-bearing detrital garnet. (A) Graphical discrimination scheme of Hardman et al. (2018) for mean compositions of individual garnet grains. (B) Mean votes for ‘setting’ classes of individual garnet grains using the ‘setting and metamorphic facies’ model of Schönig et al. (in press). IG – igneous; MS – metasomatic; MM – metamorphic; and MA – mantle. Garnet compositions of the Western Gneiss Region in Norway from Schönig et al. (2018a), of the Saxonian Erzgebirge in Germany from Schönig et al. (2019, 2020), and the D’Entrecasteaux metamorphic complex in Papua New Guinea from Baldwin et al. (2021).

bearing garnet grains. Both approaches assign the vast majority of the detrital UHP garnet grains to a crustal origin with >98 % (Figure 7.3-2A) and >95 % (Figure 7.3-2B), respectively. Solely a minor portion of coesite-bearing garnet grains from the Saxonian Erzgebirge are assigned to be derived from mantle rocks with <3 % (Figure 7.3-2A) and <8 % (Figure 7.3-2B), respectively. Most likely, the high temperatures >850 °C at UHP conditions (e.g., Schmädicke et al. 1992) led to higher MgO contents compared to $\text{FeO}_{\text{total}}$ and higher TiO_2 contents in garnet, resulting in compositional overlap with garnet of mantle origin for some grains. Besides these rare exceptions, both discrimination schemes clearly indicate a crustal origin of coesite- and diamond-bearing garnet grains; thus, fulfilling the definition of UHP metamorphism that refers to crustal rocks that experienced P – T conditions high enough for the formation of coesite (Carswell & Compagnoni 2003).

7.3.2.2 Mafic versus felsic origin

Since a mantle origin is precluded (Section 7.3.2.1), an important question to be answered is whether the coesite- and/or diamond-bearing garnet grains are sourced from metamorphic rocks of mafic or felsic bulk composition. The close association of mafic and metasedimentary UHP rock lenses and bodies within large volumes of medium- to high-pressure felsic country rocks is a common feature of UHP terranes, and often interpreted as *mélanges* of metamorphic rocks that do not share a joint P – T path (e.g., Liou et al. 2009). In contrast, a large and growing number of studies report findings of coesite and diamond in felsic country rocks of UHP terranes, which indicates subduction and exhumation as largely coherent geological units (e.g., Faryad & Cuthbert 2020, and references therein). The felsic rocks often underwent strong retrogression or re-crystallization during exhumation that, based on the mineral assemblage, obliterates a precursor UHP stage (e.g., Hermann et al. 2006). Proving or disproving the involvement of voluminous felsic rocks in the cycle of UHP metamorphism has strong implications for the size and buoyancy of UHP terranes to be considered in subduction and exhumation models (Zhang & Wang 2020). Investigating the detrital record enables to systematically sample a mixture of lithologies that are potentially involved in the UHP rock cycle (including the felsic country rocks) and to screen those for inclusions of coesite and diamond preserved in resistant host minerals like garnet (Schönig et al. 2018a, 2019).

The scheme of Schönig et al. (in press) facilitates the discrimination of garnet sourced from alkaline, calc-silicate, ultramafic, mafic, and intermediate–felsic/metasedimentary host-rock composition solely based on garnet major-element composition acquired by electron microprobe analysis. As shown in Figure 7.3-3A, the scheme assigns a significant proportion of 40 % of the coesite- and diamond-bearing detrital garnets to an intermediate–felsic/metasedimentary source, including all studied regions, except the two grains from the D’Entrecasteaux Islands of Papua New Guinea. Unfortunately, host-rock composition predictions for garnet from intermediate–felsic/metasedimentary eclogite-facies and UHP rocks are most challenging and show the highest misclassification rates with 50 % incorrectly assigned to a mafic source (see fig. 2 of Schönig et al. in press, here Figure 6.4-2). Nevertheless, garnets from mafic eclogite-facies and UHP rocks are correctly assigned in 96 % of the cases and rarely misclassified as intermediate–felsic/metasedimentary. Thus, the 40 % of detrital UHP garnets assigned to an intermediate–felsic/metasedimentary source are rather a minimum estimation, clearly exceed misclassification rates, and indicate significant involvement of felsic rocks in the UHP rock cycle.

To gain further information about the source rocks of the garnets containing UHP mineral inclusions, it turned out that a combination of detrital garnet chemistry and mineral inclusion assemblages is of great value, particularly when compared to garnet of local crystalline rocks (Schönig et al. 2018a, 2018b, 2021b; Baldwin et al. 2021). This can be done by using garnet endmember plots or discrimination schemes (Krippner et al. 2014, and references therein; Tolosana-Delgado et al. 2018; Schönig et al. in press).

Figure 7.3-3B (left diagram) shows a compositional comparison of detrital coesite-bearing garnet from Norway to garnet from local eclogite and felsic gneiss in the $X_{\text{Fe+Mn}}-X_{\text{Mg}}-X_{\text{Ca}}$ ternary diagram. The coesite-bearing garnet grains show a considerable variability in X_{Ca} , indicating more than a single source. Based on the compositional similarity to garnet from local felsic gneiss, abundant inclusions of

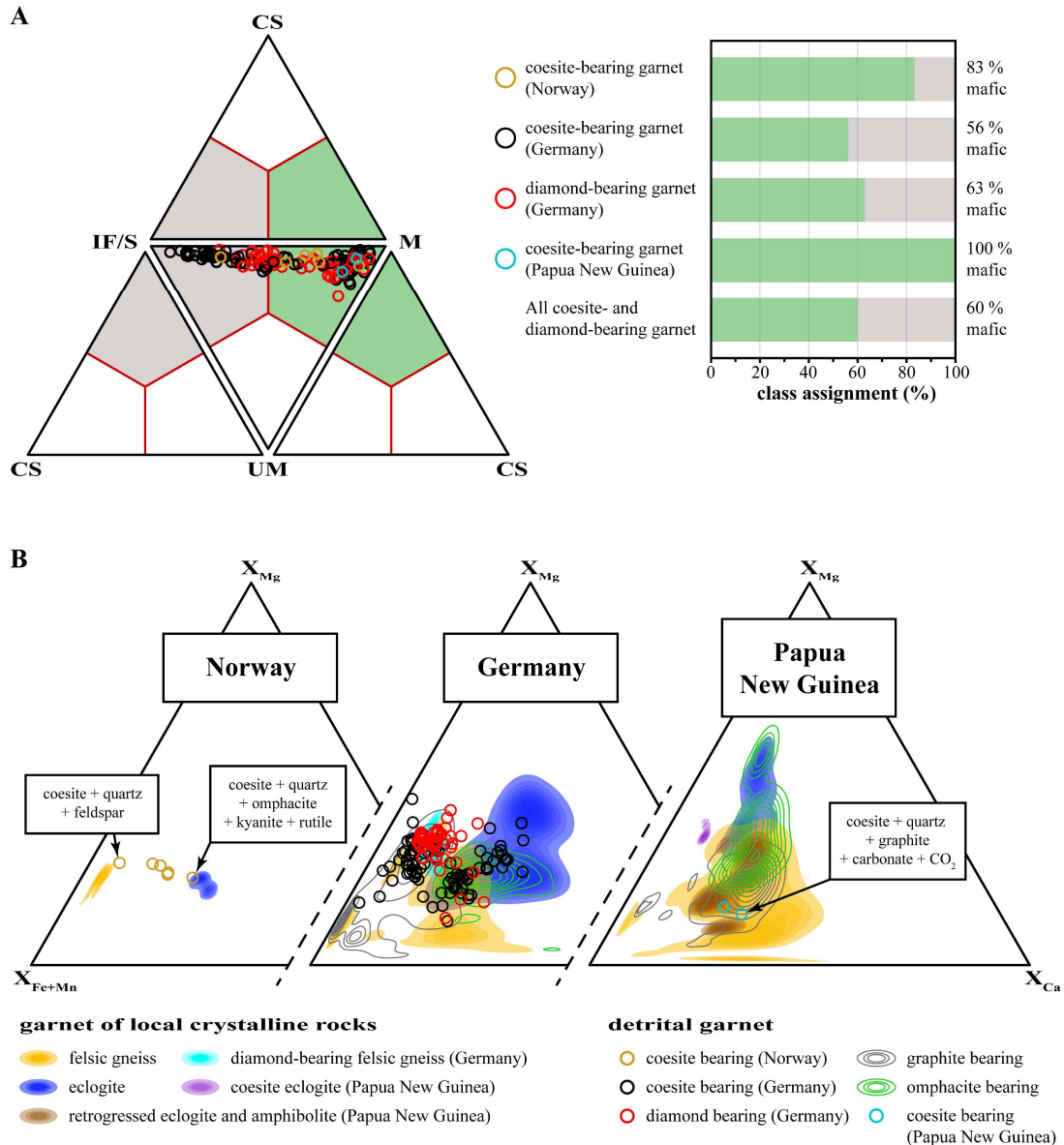


Figure 7.3-3: Comparison of detrital UHP garnet composition with regard to source-rock composition. (A) Mean votes for 'composition' classes of individual UHP garnet grains after Schönig et al. (in press). IF/S – intermediate–felsic/metasedimentary; CS – calc–silicate; M – mafic; and UM – ultramafic. (B) Comparison of detrital UHP garnet mean composition and inclusion-assemblage with garnet from local crystalline rocks in the X_{Fe+Mn} – X_{Mg} – X_{Ca} ternary diagram (molar proportions). Garnet compositions and inclusion assemblages of the Western Gneiss Region in Norway from Schönig et al. (2018a), of the Saxonian Erzgebirge in Germany from Schönig et al. (2019, 2020, 2021b), and the D'Entrecasteaux metamorphic complex in Papua New Guinea from Baldwin et al. (2021). Crystalline and detrital graphite- and omphacite-bearing garnet compositions shown as kernel density estimate maps, with bandwidths calculated after Venables & Ripley (2002).

quartz, and the presence of an alkali feldspar inclusion, Schönig et al. (2018a) supposed a felsic source as most likely for coesite-bearing garnet showing the lowest X_{Ca} content (Figure 7.3-3B, left). In contrast, coesite-bearing garnet with the highest X_{Ca} content shows an inclusion assemblage of coesite + quartz + omphacite + kyanite + rutile, making a mafic source (i.e., eclogite) most likely.

The dataset of inclusion assemblages in detrital garnets from Germany studied by Schönig et al. (2019, 2020, 2021b) is much more extended compared to Norway, and includes 2100 inclusion-bearing garnets (93 coesite-bearing, 54 diamond-bearing). This enables to compare compositional characteristics of garnets containing specific inclusion types with garnet compositions from local crystalline rocks. Garnet grains hosting inclusions of omphacite and graphite have been found particularly useful. As shown in Figure 7.3-3B (middle diagram), the composition of omphacite-bearing garnet resembles the composition of garnet from local eclogites, whereas graphite-bearing garnet resembles the composition of garnet from local felsic rocks. Consequently, coesite- and diamond-bearing detrital garnets that additionally entrapped omphacite or are compositionally similar to omphacite-bearing garnet are mainly sourced from mafic lithologies (eclogites), and those that additionally contain graphite or are compositionally similar to graphite-bearing garnet are mainly sourced from felsic rocks. Based on a detailed comparison of detrital and crystalline garnet composition, as well as the consideration of other inclusion assemblages besides omphacite and graphite that are more frequent in felsic rocks (alkali feldspar, phlogopite–biotite, quartz, and cristobalite), Schönig et al. (2021b) assigned ~76 % of the coesite-bearing garnets to a felsic source and ~24 % to a mafic source. This highlights the importance of felsic lithologies in UHP rock cycles and supports that the prediction of a felsic origin for detrital UHP garnet after Schönig et al. (in press) in Figure 7.3-3A represents a lower bound estimate.

In addition to frequent hints for UHP garnets sourced from felsic lithologies, Schönig et al. (2020) observed that the composition of ~10 % of the coesite-bearing and ~7 % of the diamond-bearing grains only matches with garnet compositions from the felsic country rocks (yellow kernel density distribution map in Figure 7.3-3B, middle diagram), which previously have been supposed to never underwent pressure conditions in excess of ~2.1 GPa (Willner et al. 1997; Tichomirowa et al. 2018). Main differences to garnet from eclogite lenses (dark blue distribution map) and diamond-bearing felsic rock lenses (sky-blue distribution map) are the higher values of X_{Mn} and X_{Fe} versus X_{Mg} (Figure 7.3-3B, middle diagram), which is even more obvious in a scatter plots of these ratios (see figs. 2 and 3 of Schönig et al. 2020, here Figure 3.4-1 and Figure 3.4-2). Thus, it was concluded that the felsic country rocks, diamond-bearing felsic lenses, and eclogites were subducted to UHP conditions as a largely coherent slab (Schönig et al. 2020). This supports individual opinions of the studied area (Gose & Schmädicke 2018) as well as worldwide observations (Faryad & Cuthbert 2020, and references therein), but strongly contradicts the view of a mixture of rocks that reached different maximum depth and amalgamated during exhumation (Massonne 2005, 2011b). Consequently, this provocative interpretation led to a relaunch of the debate about the geodynamic context of the UHP terrane of the central Saxonian Erzgebirge (Massonne 2021; Schönig et al. 2021a).

Like in the Erzgebirge of Germany, a comparison of detrital and crystalline garnet chemistry in the D'Entrecasteaux metamorphic complex of Papua New Guinea as well as inclusions of graphite and omphacite come in handy. By solely considering garnet composition after Schönig et al. (in press), the coesite-bearing grains are assigned to a mafic source (Figure 7.3-3A, right diagram). However, felsic UHP garnet is prone to be misclassified and Baldwin et al. (2021) suppose a felsic origin, probably metasedimentary, based on a number of arguments.

First of all, detrital coesite-bearing garnet composition differs strongly from garnet of the coesite-bearing eclogite discovered by Baldwin et al. (2008), pre-investigated by Monteleone et al. (2007), and

further studied by Faryad et al. (2019) and Osborne et al. (2019) (Figure 7.3-3B, right diagram, purple distribution map). This observation is particularly important as the sample of the single eclogite lens outcropping at a single location previously represented the only find of coesite in the UHP terrane of eastern Papua New Guinea, and thus the detrital coesite-bearing garnets expand the range of lithologies involved in the UHP rock cycle (Baldwin et al. 2021).

Secondly, both coesite-bearing garnets are also compositionally distinct from garnet of other local eclogites as well as detrital garnet containing omphacite inclusions (Figure 7.3-3B, right diagram, dark-blue and green distribution maps), making a pristine eclogite source very unlikely. Furthermore, one of the coesite-bearing garnets contains abundant inclusions of graphite. As graphite is more likely to occur in metasedimentary rocks, and the composition of graphite-bearing detrital garnet resembles the composition of garnet from felsic rocks as well retrogressed eclogites and amphibolites (Figure 7.3-3B, right diagram, grey, yellow, and brown distribution maps) but no inclusions of graphite have been found in garnet of a nearby retrogressed eclogite (see supplementary data 2 of Baldwin et al. 2021, here Electronic Appendix 4e-B), a metasedimentary source is supposed to be most likely. Consequently, the detrital coesite-bearing garnets close the young (<10 Ma) and still active UHP rock cycle from protolith generation at the Earth's surface, over subduction to mantle depth, return to Earth's surface by exhumation, followed by erosion and final deposition as a beach placer (Baldwin et al. 2021).

7.3.3 Methodological benefits and limits

Almost all previous studies dealing with UHP metamorphism are based on analyzing crystalline rocks, whereby potential rocks are sampled following targeted field mapping. When the aim is to examine the existence and/or extent of UHP rocks this approach suffers in some respects, particularly when large rock volumes have to be screened (Schönig et al. 2018a).

First of all, crystalline rocks are often poorly or not accessible in the area of interest. Depending on climate conditions and lithology, bedrocks may be covered by soil, dense vegetation, or ice. Even if a large area may be well exposed and lithologies have been comprehensively mapped, the selection of sampling spots might be challenging and sometimes subjective regarding the large volumes of rocks. Equilibration under UHP metamorphic conditions may depend on fluid infiltration, which can result in co-existing domains of different metamorphic grade on a very small scale (e.g., John & Schenk 2003). To make matters worse, UHP terranes are often exhumed by nearly isothermal decompression or even heating before cooling and thus metamorphic peak assemblages are often not preserved and/or obliterated by retrogression (e.g., Ernst 2006). Particularly felsic rocks are prone to be retrogressed due to melting induced by the breakdown of hydrous phases like phengite (Hermann et al. 2006). UHP minerals like coesite and diamond may survive retrogression when shielded from the external conditions by their entrapment as inclusions in resistant host minerals like garnet; however, this is difficult to assess during sampling in the field. In contrast, analyzing detrital grains takes advantage of natural processes such as erosion and sedimentary transport to sample potential host minerals from a variety of rocks in the investigated catchment (e.g., Schönig et al. 2018a). This also includes grains from rocks which have undergone weathering, soil formation and/or are covered by vegetation or ice (sampled by meltwater).

A tremendous advantage is the possibility to apply the method to ancient clastic sedimentary rocks (e.g., Schönig et al. 2018a; Baldwin et al. 2021). Because garnet (i) represents a frequent detrital mineral in sediments originating from orogenic settings (e.g., Andò et al. 2014), (ii) can preserve UHP mineral inclusions (e.g., Schönig et al. 2018a, 2019) even when exhumed under high-temperature conditions (Schönig et al. 2020; Baldwin et al. 2021), and (iii) is comparatively stable during transport, surface weathering, and deep burial (Morton & Hallsworth 1999), it can be expected that coesite- and/or diamond-bearing garnets are preserved in ancient sedimentary successions shed from UHP terranes, like already shown for coesite-bearing zircon (Chen et al. 2005). Thus, garnet is a major target mineral to study the erosion and exposure of ancient UHP terranes with high potential regarding, for instance, dimensions of rock bodies affected by UHP conditions, timing and rates of UHP rock exhumation to Earth's surface, as well as the occurrence of UHP terranes throughout Earth's history. However, the preservation in ancient sedimentary rocks has still to be tested and validated.

Although the detection of UHP sources by analyzing detrital minerals offers several benefits, it is also accompanied by some challenges. First and foremost, some powerful techniques of metamorphic petrology cannot be directly applied. Metamorphic thermobarometry is based on exchange reactions, exsolution temperature of solid solutions, net-transfer reactions, major-element contents, trace-element partitioning, multi-equilibria calculations, petrogenetic grids, and thermodynamic modelling. All these methods can provide detailed information on P - T evolution but most of them depend on two or more co-existing minerals and/or knowledge of the (effective) bulk-rock composition (e.g., Reverdatto et al. 2019). Because this information is highly limited concerning detrital single grains, detailed P - T information is not available and can only roughly be estimated by using garnet discrimination schemes and combine the results with inclusion information (Section 7.3.2) or by applying elastic geothermobarometry (Baldwin et al. 2021). Nevertheless, the method of analyzing inclusions in detrital garnet provides a first glance overview of the distribution and characteristics of UHP metamorphic rocks located in the study area, and thus can be seen as an effective starting point to plan further exploration – or not. It is capable of verifying the presence of UHP rocks and providing source rock characteristics, as long as the eventuality of a mantle origin is carefully considered (Section 7.3.2.1).

A major challenge is that, by analyzing detrital grains, the eventuality of sediment recycling has to be considered. Although detrital garnet containing coesite and/or diamond inclusions provides evidence for material of UHP origin located in the present-day catchment, it is uncertain whether the UHP garnets originated directly from crystalline rocks or, if present, may be reworked from sediments or sedimentary rocks within the catchment. This is a difficulty, but remains a minor problem if the catchment area is relatively small, clearly arranged, and geologically well known. However, it becomes tricky for large catchments, remote areas, and when analyzing sedimentary rocks with unknown origin. Thus, tackling the recycling issue strongly depends on the respective geological situation and the objectives of the study.

One of the key objectives is to link detrital coesite- and/or diamond-bearing garnet to a specific metamorphic/orogenic event. In this case, dating zircon, monazite, rutile, and/or apatite grains from the bulk sediment sample will reveal whether more than a single event or an exotic input has to be considered. If not, sediment recycling with respect to UHP minerals can be neglected. If yes, direct in-situ dating of the host mineral containing UHP inclusions is the method of choice. Unfortunately,

aluminum-rich garnet is typically poor in uranium, hampering the ability of U–Pb dating. However, first successful approaches of dating uranium-poor aluminum-rich garnet in the U–Pb system (Millonig et al. 2020) and the Sm–Nd system (Maneiro et al. 2019) provide an optimistic outlook. Other suitable dating techniques strongly depend on mineral inclusions co-existing with the UHP phases and have to be adjusted to the specific case. For instance, (U, Th)–Pb dating of monazite (e.g., Harrison et al. 1997; Martin et al. 2007), zircon (e.g., Usui et al. 2002; Bruguier et al. 2017), or rutile inclusions (e.g., Bruguier et al. 2017; Zhou et al. 2020) in close proximity to UHP inclusions would be a possibility. In addition, expanding the technique to other host minerals that can be confidently dated in the U–Pb system, like zircon and rutile, would certainly increase the precision in age determinations.

If contamination from sediments in the catchment cannot be excluded and dating is not feasible or data remains ambiguous, the information provided by the detrital garnets is still very useful to quickly narrow down the potential source rocks by comparing their chemical characteristics and inclusion assemblages with that of garnet from local crystalline rocks located in the catchment.

7.3.4 Enhancing efficiencies

It has been shown, for three different UHP terranes of different age and with continental as well as oceanic upper plates, that analyzing detrital garnet grains is effective in identifying UHP metamorphic rocks and less time consuming than analyzing many crystalline rock samples from large volumes of potential lithologies occurring in the catchment. However, the user-assisted time needed for analyzing mineral inclusion assemblages in a large number of detrital garnet grains by Raman spectroscopy is still expensive. Enhancing efficiencies of the method becomes particularly important when considering perspective applications to large regions where many samples from large drainage systems shall be screened for the presence of coesite- and diamond-bearing garnet. Techniques that enable a statistically based pre-selection of potential UHP garnet grains seems most promising to reduce the overall analytical time, while automated measurement routines are most promising to reduce the user-assisted time.

7.3.4.1 Selecting the grain-size window

The analyzed grain size can have a strong control on the composition (Krippner et al. 2015, 2016; Schönig et al. 2021b) and mineral inclusion assemblages of detrital garnet (Schönig et al. 2018b, 2021b). On the one hand, variations in composition and inclusions leads to variations in garnet density, which in turn affects the hydrodynamic behavior. However, stronger control has been observed regarding the initial garnet crystal size at the source, that varies markedly between different garnet-bearing rocks and is prone to be inherited in their erosional material, i.e., sediments (Krippner et al. 2015, 2016; Schönig et al. 2021b). This raises the question whether garnet sourced from UHP rocks is enriched in a specific grain-size window, and thus whether a pre-selection of the grain-size window can enhance analytical efficiencies.

The grain-size distribution of coesite- and diamond-bearing detrital garnet from the Saxonian Erzgebirge has been studied in detail by Schönig et al. (2021b). Reports of garnet composition for different grain-size windows indicate that garnet sourced from high-grade metamorphic rocks is often enriched in the medium-sand fraction compared to fine-sand (see fig. 1 of Schönig et al. 2021b, here

Figure 5.1-1). While diamond-bearing garnet follows this trend, the grain-size distribution of coesite-bearing garnet is highly heterogeneous. It turned out that this effect comes along with variations in source-rock composition. UHP garnet shed from mafic rocks contains a low number of coesite inclusions and is typically enriched in coarser grain-size fractions due to grain-size inheritance. In contrast, UHP garnet derived from felsic rocks contains variable amounts of coesite inclusions, whereby coesite-poor grains are enriched in coarser fractions (similar to mafic UHP garnet), but coesite-rich grains are enriched in fine fractions. Due to different elastic properties of coesite and garnet, strains developing during exhumation cause a high degree of fracturing and fracture connections to smaller inclusions for coesite-rich grains, allowing fluid infiltration and the transformation to quartz, which in turn further promotes garnet disintegration (see figs. 13 and 14 of Schönig et al. 2021b, here Figure 5.4-11 and Figure 5.4-12).

In order to figure out the most efficient grain-size fraction for tracing UHP metamorphism, Schönig et al. (2021b) put the abundance of coesite- and diamond-bearing garnet in different grain-size fractions into relation of the analytical time needed, which is increasing with increasing garnet grain size. Due to the heterogeneous grain-size distribution of coesite-bearing garnet, the most efficient grain-size fraction varies between catchments that comprise varying proportions of mafic and felsic host rocks. On average, none of the grain-size fractions was found to be more efficient compared to any other with regard to the number of UHP garnets detected per time (see fig. SM5 of Schönig et al. 2021b, here Figure Appendix 5-D 1), and thus the fraction that provides the highest value of information should be defined as most efficient. Solely the 250–500 μm fraction recorded (i) UHP metamorphism in all studied catchments, (ii) coesite-bearing garnet from mafic as well as felsic sources for individual catchments, and (iii) diamond-bearing garnet in the respective catchments (Schönig et al. 2021b). This also holds for detrital garnet from Papua New Guinea, where coesite-bearing garnet has only been detected in the >200 μm fraction (Baldwin et al. 2021). In contrast, detrital coesite-bearing garnet from Norway is absent in the 250–500 μm but most frequent in the 63–125 μm fraction (Schönig et al. 2018a). In conclusion, to reduce the analytical time in order to screen large rock volumes by a large number of samples on the occurrence of UHP rocks, the 250–500 μm grain-size fraction is most efficient for initial analysis. An absence of UHP garnet in this fraction does not exclusively rule out the existence, but makes it much less likely in particular on a statistical base by considering multiple samples (Schönig et al. 2021b).

7.3.4.2 *Geochemical pre-screening*

Garnet major-element composition is mainly a function of pressure, temperature, effective bulk-rock composition, and fluid availability. As information about the bulk-rock composition as well as fluids is very limited from a detrital perspective, multivariate quantitative empirical approaches applied to large natural datasets are most promising to estimate the metamorphic grade of garnet formation solely based on garnet major-element composition (Tolosana-Delgado et al. 2018; Schönig et al. in press). These discrimination schemes may allow to screen out garnet grains that are less likely to have crystallized during UHP metamorphism, and thus to reduce the number of grains selected for the time-consuming inclusion analysis.

The discrimination scheme of Tolosana-Delgado et al. (2018) rests on a model developed by applying linear discriminant analysis to a major-element dataset of 3,188 garnets. As a result, it assigns garnet grains with certain probabilities to five major host-rock types, that are (i) ultramafic rocks, (ii) felsic igneous rocks, (iii) amphibolite-facies metamorphic rocks, (iv) granulite-facies metamorphic rocks, and (v) eclogite-facies metamorphic rocks. Notably, the scheme does not differentiate between eclogite-facies garnet of crustal and mantle affinity. Thus, a mantle origin should be additionally considered by applying the scheme of Hardman et al. (2018) or Schönig et al. (in press) (Section 7.3.2.1).

Considering the arithmetic mean probabilities of individual detrital coesite- and diamond-bearing garnet grains analyzed at 9–20 spots per grain, the scheme of Tolosana-Delgado et al. (2018) assigns all grains to a metamorphic source using the prior probability ‘equal-M’. Figure 7.3-4A shows the probabilities

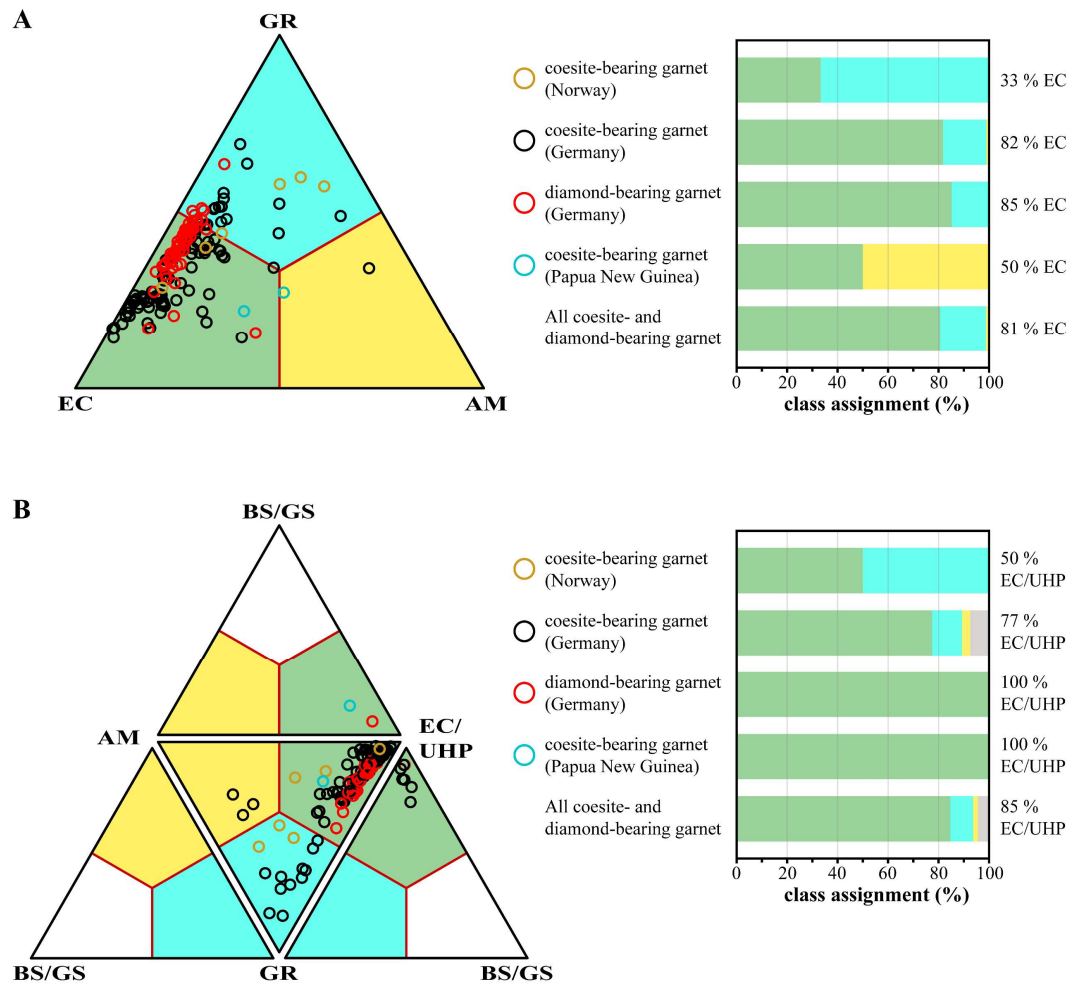


Figure 7.3-4: Prediction of metamorphic host-rock facies based on major-element composition of detrital coesite- and diamond-bearing garnet grains. (A) Discrimination according to mean probabilities after Tolosana-Delgado et al. (2018) using prior ‘equal-M’. EC – eclogite facies; GR – granulite facies; and AM – amphibolite facies. (B) Discrimination according to mean votes of the ‘setting and metamorphic facies’ model of Schönig et al. (in press). BS/GS – blueschist/greenschist facies, AM – amphibolite facies; GR – granulite facies; and EC/UHP – eclogite/ultrahigh-pressure facies. Grey bars indicate an assignment to mantle rocks. Garnet compositions of the Western Gneiss Region in Norway from Schönig et al. (2018a), of the Saxonian Erzgebirge in Germany from Schönig et al. (2019, 2020, 2021b), and the D’Entrecasteaux metamorphic complex in Papua New Guinea from Baldwin et al. (2021).

of the individual grains for the three considered metamorphic rock types. The scheme assigns ~81 % of the grains with the highest probability of belonging to an eclogite-facies metamorphic source. This rate decreases to ~79 % or ~76 % when additionally sorting out grains that are assigned to a mantle origin based on the schemes of Hardman et al. (2018) or Schönig et al. (in press), respectively (Figure 7.3-2).

The discrimination scheme of Schönig et al. (in press) is based on a model trained on a major-element dataset of 13,615 garnets using the random forest machine-learning algorithm. The “setting and metamorphic facies” model consists of an ensemble of 3,400 deeply grown classification trees. For a specific garnet composition, each tree votes for one of seven host-rock classes, that are (i) mantle rocks, (ii) metasomatic rocks, (iii) igneous rocks, (iv) blueschist-/greenschist-facies metamorphic rocks, (v) amphibolite-facies metamorphic rocks, (vi) granulite-facies metamorphic rocks, and (vii) eclogite-facies/ultrahigh-pressure metamorphic rocks. Garnet grains are assigned to the class that receives the majority of the votes from the 3,400 trees.

Considering the arithmetic mean votes of 9–20 spots per grain after Schönig et al. (in press), none of the detrital coesite- and diamond-bearing garnet grains is assigned to an igneous or metasomatic origin, but <5 % received a higher number of votes for a mantle origin than the maximum of votes for the four metamorphic classes (Figure 7.3-2B). Figure 7.3-4B shows the individual votes for the metamorphic classes for garnet grains that are assigned to a metamorphic origin in Figure 7.3-2B. The scheme assigns the majority of votes to metamorphic garnet of the eclogite-facies/ultrahigh-pressure class for ~85 % of the coesite- and diamond-bearing grains, and thus provides a higher success rate compared to Tolosana-Delgado et al. (2018) shown in Figure 7.3-4A and allows an efficient pre-screening.

By using the arithmetic mean probabilities or votes for the single grains in the two tested schemes, the eventuality of major-element zonation is ignored. Strong zonation of detrital garnet derived from regional metamorphic rocks is rather scarce, but can lead to misclassification (Krippner et al. 2014). To estimate the impact of zonation, Figure 7.3-5 shows the discrimination results of all individual analyses (9–20 spots per grain) for coesite- and diamond-bearing garnet grains that have not been classified as being sourced from eclogite-facies rocks by mean probabilities after Tolosana-Delgado et al. (2018) and mean votes after Schönig et al. (in press) (cf. Figure 7.3-4). In both schemes, the vast majority of analyses is still classified as granulite- or amphibolite-facies garnet, but 15–16 % are assigned to the eclogite facies. Transferring this to the number of grains, this corresponds to an increase in UHP garnet assigned to the class of eclogite-facies garnet from 81 to 90 % for the scheme of Tolosana-Delgado et al. (2018) and from 85 to 94 % for the scheme of Schönig et al. (in press). However, this increase in success is expensive as the number of electron microprobe analyses considered has been increased from 155 to 1,439, that is by >800 %. Consequently, although zonation and/or heterogeneity is an issue, it is more efficient from a statistical perspective to pre-screen a larger number of grains by one spot and except that some UHP grains may be sorted out than pre-screening a smaller number of grains by multiple spots.

Such a geochemical pre-screening technique becomes particularly powerful for large catchments that drain a variety of potential garnet source rocks. A striking example is sample JS-Erz-14s of Schönig et al. (2019, 2020). This modern sand sample represents erosional material from a regional river catchment that drains an area >500 km², comprising the UHP terrane of the central Saxonian Erzgebirge as well

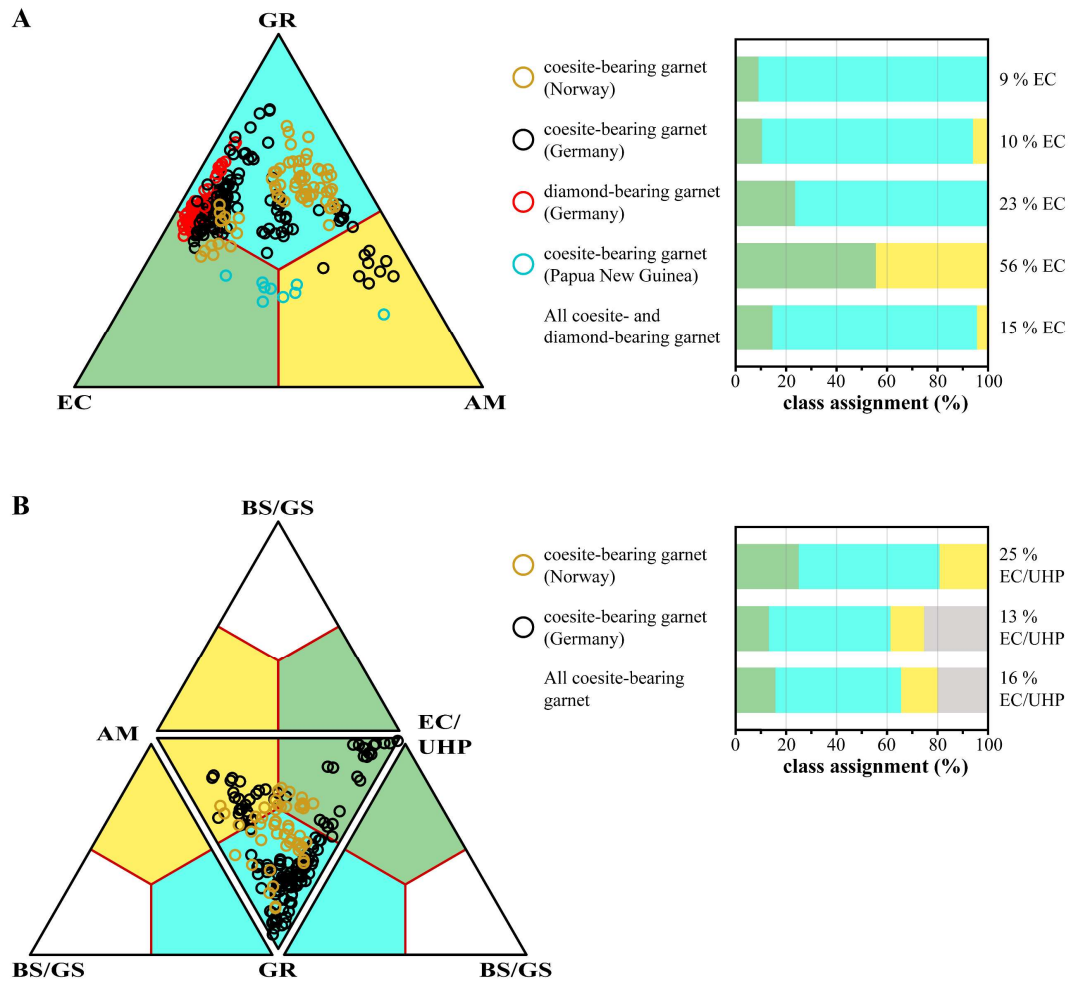


Figure 7.3-5: Prediction of metamorphic host-rock facies based on major-element composition of all individual analyses (9–20 spots per grain) for coesite- and diamond-bearing garnet grains that have not been classified as being sourced from eclogite-facies rocks in Figure 7.3-4. (A) Discrimination according to probabilities after Tolosana-Delgado et al. (2018) using prior 'equal-M'. EC – eclogite facies; GR – granulite facies; and AM – amphibolite facies. (B) Discrimination according to votes of the 'setting and metamorphic facies' model of Schönig et al. (in press). BS/GS – blueschist/greenschist facies, AM – amphibolite facies; GR – granulite facies; and EC/UHP – eclogite/ultrahigh-pressure facies. Grey bars indicate an assignment to mantle rocks. Garnet compositions of the Western Gneiss Region in Norway from Schönig et al. (2018a), of the Saxonian Erzgebirge in Germany from Schönig et al. (2019, 2020, 2021b), and the D'Entrecasteaux metamorphic complex from Baldwin et al. (2021).

as the surrounding nappes of lower metamorphic grade. A total of 300 inclusion-bearing garnet grains have been investigated regarding inclusion assemblages, including 100 grains from each, the 63–125 μm , 125–250 μm , and 250–500 μm grain-size fraction. Coesite inclusions occur in six of the grains, that are two grains of the 125–250 μm fraction and four grains of the 250–500 μm fraction. In addition, one diamond-bearing garnet has been found in the 250–500 μm fraction. Figure 7.3-6 shows the discrimination results of all inclusion-bearing garnets in the 'setting and metamorphic facies' scheme after Schönig et al. (in press). Grains that contain UHP mineral inclusions (coesite or diamond) and grains that do not contain UHP inclusions are marked individually for the different grain-size fractions. Votes in the 'setting' plot (Figure 7.3-6, upper diagram) assign the vast majority of garnets (>95 %) to a metamorphic source. For these garnets, individual votes for the four metamorphic-facies classes are

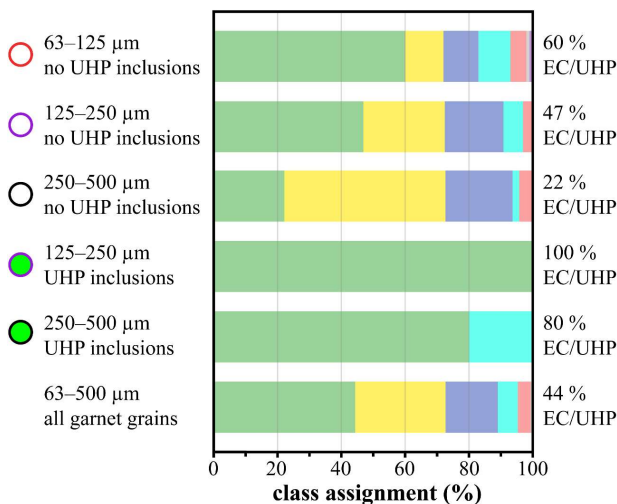
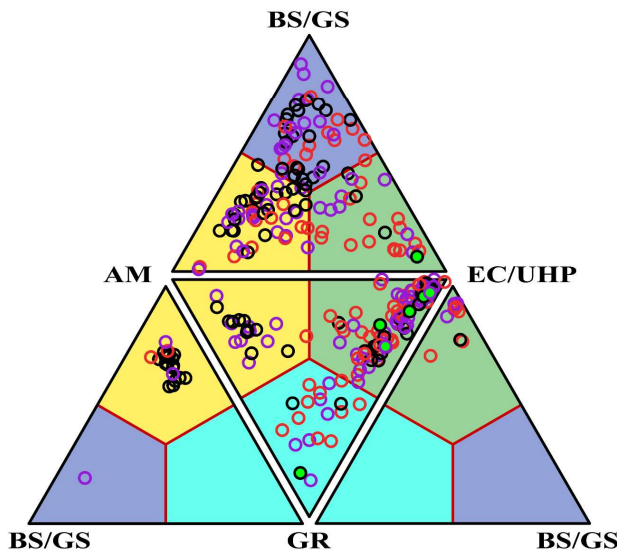
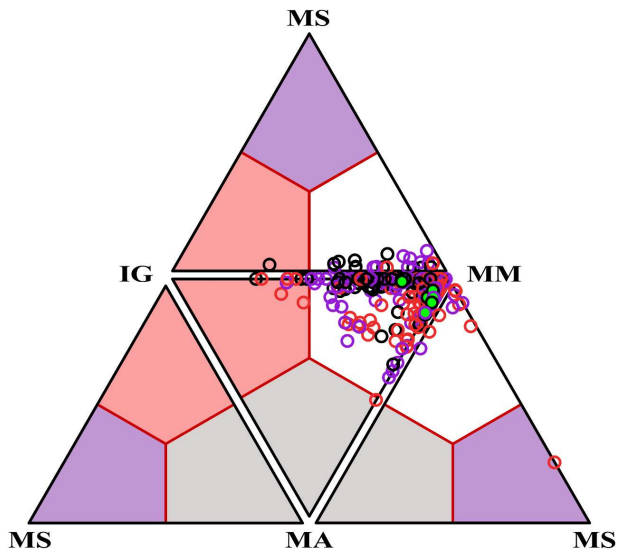


Figure 7.3-6: Discrimination results of all inclusion-bearing garnets from sample JS-Erz-14s after the ‘setting and metamorphic facies’ model after Schönig et al. (in press). Shown are the mean votes for individual grains regarding ‘setting’ (upper diagram), ‘metamorphic facies’ (middle diagram), as well as their corresponding class assignment based on the majority vote (lower diagram). Symbols of UHP inclusion-bearing garnets are filled in bright green. IG – igneous; MS – metasomatic; MM – metamorphic; MA – mantle; BS/GS – blueschist/greenschist facies, AM – amphibolite facies; GR – granulite facies; and EC/UHP – eclogite/ultrahigh-pressure facies. Garnet compositions from Schönig et al. (2019, 2020, 2021b).

shown in the ‘metamorphic facies’ plot (Figure 7.3-6, middle diagram). Considering a pre-screening where all garnet grains that are not assigned to the eclogite/ultrahigh-pressure class are sorted out, ~56 % of all grains are excluded prior to inclusion analysis (Figure 7.3-6, lower diagram), being accompanied by a considerable saving of analytical time. Thereby, all UHP garnets from the 125–250 μm as well as 80 % of the 250–500 μm fraction are maintained. The rate is even more impressive when the most potential grain-size fraction 250–500 μm (Section 7.3.4.1) is individually considered, where ~78 % of the grains are sorted out by maintaining 80 % of the UHP garnets.

7.3.4.3 Hyperspectral 3D Raman imaging

Analyzing inclusions in a large number of detrital mineral grains by manually focusing on the individual inclusions is a time-consuming procedure (Schönig et al. 2021b). In addition, to run labs efficient, techniques that enable to acquire data at weekends and nights are highly welcome. Raman imaging by

largely automated systems provide this option. Figure 7.3-7 shows a hyperspectral cuboid acquired from a $70 \times 60 \times 20 \mu\text{m}$ garnet volume at three different resolutions.

Analysis was performed at the Geosciences Center Göttingen, Germany. The experimental setup includes a WITec alpha 300R fiber-coupled ultra-high throughput Raman spectrometer, a 532 nm laser, an automatically adjusted laser power of 20 mW, a $300 \text{ l}\times\text{mm}^{-1}$ grating, a $100\times$ long working distance objective with a numerical aperture of 0.75, an acquisition time of 20 ms per spectrum, and an electron multiplying charge-coupled device. The cuboid with the highest resolution with a step size of $0.25 \times 0.25 \times 0.25 \mu\text{m}$ offers many details, including the thin rim of quartz in the largest inclusion and the detection of a very small coesite inclusion with a size of $<2 \mu\text{m}$. However, the total duration of the experiment of >40 hours is inefficient for the objective of solely detecting and identifying inclusion in a large number of garnets. By adjusting the step size to $1.00 \times 1.00 \times 1.00 \mu\text{m}$, the smallest inclusion is not detected but all other inclusions as well as the bimineralic character of the largest. This also holds for a step size of $2.00 \times 2.00 \times 2.00 \mu\text{m}$, whereby the total duration is only ~ 7 min. This setup was tested on several detrital garnet grains from the Saxonian Erzgebirge, revealing that most mineral inclusions $\geq 4 \mu\text{m}$ are confidently identified. Smaller inclusions $\leq 3 \mu\text{m}$ are identified for strong Raman active phases like coesite, quartz, diamond, and rutile. For the coesite-bearing garnet grains from the Erzgebirge, 84 of the 93 garnets ($\sim 90\%$) have at least one coesite inclusion $\geq 3 \mu\text{m}$. Thus, hyperspectral

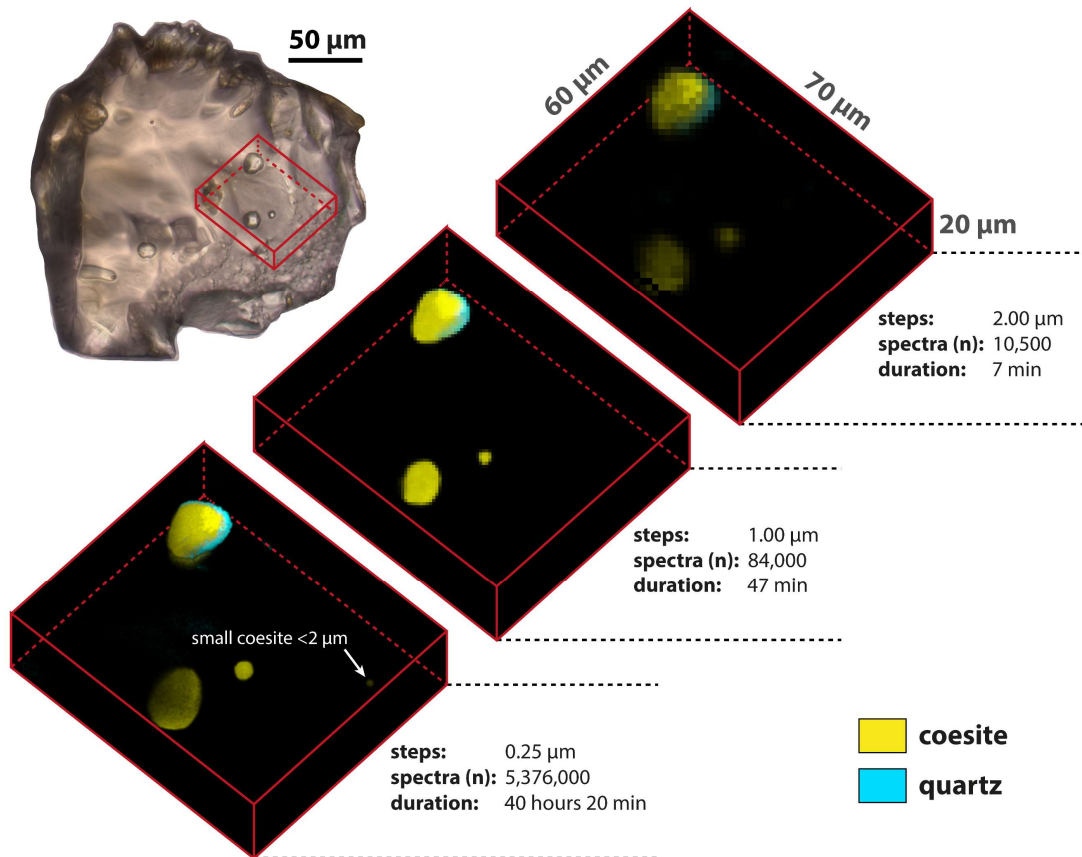


Figure 7.3-7: Photomicrograph and three-dimensional hyperspectral Raman images of coesite-bearing garnet. Garnet number 90 from sample JS-Erz-3s (cf. fig. 2A of Schönig et al. 2019, here Figure 2.2-1). See main text for instrumental setup.

Raman imaging offers a great option to reduce the user-assisted analytical time needed for inclusion analysis.

7.4 Other potential UHP host minerals

Besides garnet, coesite and diamond inclusions have been frequently detected in other host minerals like zircon (e.g., Parkinson & Katayama 1999; Massonne 2003), clinopyroxene (e.g., Smith 1984; Shatsky & Sobolev 1993), and chromite (e.g., Robinson et al. 2004; Yamamoto et al. 2009). In addition, they were also found in tourmaline (e.g., Ota et al. 2008; Marschall et al. 2009), rutile (e.g., Hart et al. 2016; Rezvukhina et al. 2021), kyanite (e.g., Massonne 2003; Taguchi et al. 2019), titanite (Ogasawara et al. 2002), zoisite (Shatsky & Sobolev 1993), epidote (Zhang et al. 1995), and dolomite (Zhang & Liou 1996).

For the sedimentary record of UHP metamorphism, the so-called ultrastable minerals are of particular importance, namely zircon, rutile, and tourmaline. These are common in high-grade metamorphic rocks, and due to their extreme stability against mechanical abrasion and chemical weathering, they are also common phases in mature clastic sediments and sedimentary rocks (e.g., Hubert 1962). Additionally, they survive in deeply buried sedimentary successions (>3000 m), at depths where garnet (especially grossular-rich garnet) may break down by intrastratal solution (e.g., Morton & Hallsworth 1999). Thus, these ultrastable minerals have high potential to archive UHP metamorphism in the sedimentary record.

7.4.1 Zircon

In addition to the possibility of screening very mature sediments on the presence of erosional material sourced from UHP rocks, a major advantage of finding UHP inclusion in detrital zircon is the straightforward application of geo- and thermochronometric methods. The low contents of non-radiogenic lead and the high closure temperature of >900 °C (Dahl 1997) make zircon the most commonly utilized mineral for determining crystallization ages (e.g., Corfu et al. 2003). This is nowadays routinely performed by, for instance, laser ablation inductively coupled plasma mass spectroscopy (e.g., Frei & Gerdes 2009) or secondary ion mass spectroscopy (e.g., Ireland & Williams 2003). Simultaneous analysis of rare-earth-element (REE) concentrations and patterns furthermore enables to discriminate mantle and crustal zircon. Compared to crustal zircon, zircon from mantle rocks shows low REE concentrations, a flat REE pattern, and low thorium and uranium contents (Belousova et al. 1998; Hoskin & Ireland 2000; Belousova et al. 2002). Combining those high-spatial-resolution techniques with cathodoluminescence and/or back-scattered-electron imaging enables to directly link a growth zone of a detrital zircon that contains coesite and/or diamond to a specific metamorphic event that includes deep subduction of continental crust (Wan et al. 2005). Notably, caution must be taken to rule out a secondary origin of UHP mineral inclusions (pseudo-inclusions) as demonstrated by coesite inclusions found in magmatic zircon that were introduced during UHP metamorphism via cracks that provide fluid pathways (Gebauer et al. 1997; Zhang et al. 2009; Schertl et al. 2019).

Besides the determination of UHP crystallization ages, thermochronological methods can be applied, that is the determination of cooling ages by zircon fission track (e.g., Kohn et al. 2019) or (U–Th)/He dating (e.g., Reiners 2005). Both methods may be combined with U–Pb crystallization ages derived

from the same grain (Carter & Moss 1999; Rahl et al. 2003; Reiners et al. 2004, 2005; Campbell et al. 2005; Bernet et al. 2006; McInnes et al. 2009; Evans et al. 2013), enabling to estimate exhumation rates (e.g., Enkelmann et al. 2008; Wang et al. 2014). In addition, the titanium content in zircon mainly depends on temperature and to lesser extent on pressure, allowing to estimate crystallization temperatures (Watson & Harrison 2005; Watson et al. 2006; Ferry & Watson 2007).

Despite the wealth of information provided by zircon, the applicability of using inclusions in zircon to trace the erosion of UHP rocks is hampered by the strong dilution of high-grade metamorphic zircon in the sediment factory. First of all, the vast majority of zircon is formed in intermediate–felsic igneous rocks, and thus igneous zircon dominates the detrital record (e.g., Balica et al. 2020). Secondly, the timing of zircon growth in metamorphic systems is a further aggravating factor. Zirconium mass balancing models indicate that zircon in equilibrium with co-existing mineral phases primarily dissolves on the prograde metamorphic path and mainly grows during exhumation and cooling, thus often postdates peak-pressure conditions (Kohn et al. 2015). However, prograde growth of zircon from fluids is facilitated by dehydration reactions (e.g., Gauthiez-Putallaz et al. 2016). In addition, dissolution of inherited zircon and formation of new metamorphic zircon from released zirconium (dissolution–precipitation process) enables prograde zircon growth in a virtually closed system without the need of significant amounts of free fluids with high zirconium solubility (e.g., Tomaschek et al. 2003; Rubatto et al. 2008). Inclusions of coesite and/or diamond in zircon of the Kokchetav massif (e.g., Parkinson & Katayama 1999; Hermann et al. 2001), the Saxonian Erzgebirge (Massonne 2003; Massonne et al. 2007), and the Qinling–Dabie–Sulu Orogen (e.g., Parkinson & Katayama 1999; Ye et al. 2000; Liu et al. 2008) demonstrate the growth of zircon at UHP conditions, and the preservation of those zircons in the sedimentary record (Chen et al. 2005). Thus, from a detrital perspective, finding an efficient pre-screening technique to get rid of the overwhelming amount of igneous and low-pressure metamorphic zircon poses the major challenge.

To discriminate magmatic from metamorphic zircon, considering the ratio of thorium-to-uranium is a simple and powerful tool, whereby the majority of magmatic zircon shows values >0.1 and metamorphic zircons <0.1 (Rubatto & Gebauer 2000; Belousova et al. 2002; Rubatto 2002; Grimes et al. 2015). Notably, this threshold should be used with caution (Harley et al. 2007; Rubatto 2017), as several cases of metamorphic zircon with higher thorium-to-uranium ratios have been reported (Pidgeon 1992; Vavra et al. 1996, 1999; Carson et al. 2002; Möller et al. 2002, 2003; Hokada & Harley 2004; Kelly & Harley 2005; Ewing et al. 2013; Korhonen et al. 2013; Stepanov et al. 2016). However, a compilation by Rubatto (2017) shows that by far the most UHP zircons have a thorium-to-uranium ratio <0.2 , and higher values are restricted to rare cases of ultrahigh-temperatures (UHT) at UHP conditions (Stepanov et al. 2016). This is related to the high solubility of monazite in melts produced at UHT metamorphic conditions (Stepanov et al. 2012, 2014), leading to thorium enrichment in zircon crystallized from the UHT melt (Rubatto 2017).

In addition to the thorium-to-uranium ratio, REE patterns are potentially useful to identify HP/UHP metamorphic zircon. First, HP/UHP zircon primarily crystallizes in the presence of garnet. As garnet preferentially incorporates heavy REEs (HREE), co-genetic zircon is characterized by a flat HREE pattern (e.g., Rubatto 2002, 2017, and references therein). Notably, a similar pattern can also be produced by abundant co-existing orthopyroxene that is able to incorporate high amounts of HREE

(Fornelli et al. 2014). Second, albite – a main carrier of europium – breaks down in the HP blueschist and eclogite facies to form quartz and jadeite (Holland 1980), leaving an europium-enriched effective bulk-rock composition. Thus, zircon crystallized at eclogite-facies condition is often characterized by a weak or absent negative europium anomaly (e.g., Rubatto 2002; Baldwin et al. 2004), but exceptions exist for bulk-rock compositions with very strong depletion in europium or enrichment in HREE (Rubatto 2017, and references therein). It is important to mention that deeply crystallized magmatic zircon also shows a less pronounced negative europium anomaly due to the decreasing stability of plagioclase and increasing stability of garnet and amphibole (Tang et al. 2021a). This observation has been used to infer crustal thickness through time on a regional and global scale (Tang et al. 2021a, 2021b).

In summary, a statistically-based pre-selection scheme to enrich the strongly diluted detrital zircons sourced from HP/UHP metamorphic rocks should consider a combination of indicators. Particularly, an absence of oscillatory zoning, a low thorium-to-uranium ratio, a flat HREE pattern, and a weak or absent negative europium anomaly constitutes a high probability of facing zircon of HP/UHP origin. In order to not ablate significant amounts of the zircon crystals for geochemical pre-screening prior to inclusion analysis, ion microprobe micro sampling (e.g., Ireland & Williams, 2003) is preferred over laser ablation inductively coupled plasma mass spectroscopy.

7.4.2 Rutile

In contrast to zircon, rutile growth is more common in HP metamorphic rocks and less frequent in mantle rocks, igneous rocks, and hydrothermal systems (e.g., Force 1980; Zack & Kooijman 2017). Consequently, rutile of high-pressure metamorphic origin is inherently enriched in the sediment factory and rutile growth at UHP conditions is confirmed by reports of coesite (Hart et al. 2016) and diamond inclusions (Massonne 2003; Rezvukhina et al. 2021). Furthermore, the chemical composition of rutile enables to discriminate (i) mantle rutile by higher aluminum and magnesium contents (Smythe et al. 2008) as well as higher zirconium to hafnium ratios (Pereira et al. 2019) compared to crustal rutile, and (ii) igneous and hydrothermal rutile from metamorphic rutile by concentrations and ratios of niobium, tantalum, zirconium, hafnium, tungsten, antimony, zinc, vanadium, chromium, and iron (Clark & Williams-Jones 2004; Agangi et al. 2019; Pereira et al. 2019).

A tremendous advantage of considering rutile as detrital UHP recorder is the possibility to date the specific metamorphic event in the U–Pb system even when zircon growth at UHP conditions was lacking. While zircon may miss specific metamorphic stages (Thiessen et al. 2019) or even the entire tectonothermal events (Moecher & Samson 2006; Krippner & Bahlburg 2013), rutile typically records the last orogenic event (von Eynatten & Dunkl 2012, and references therein). This is because rutile is prone to break down and form low-pressure titanium-rich phases like titanite, ilmenite, or biotite during subsequent metamorphic cycles even at greenschist-facies conditions (Zack et al. 2004a; Luvizotto et al. 2009; Luvizotto & Zack 2009; Meinhold 2010; Triebold et al. 2012). In comparison to zircon, important to note is the much lower U–Pb closure temperature of 400–600 °C (Vry & Baker 2006; Kooijman et al. 2010; Blackburn et al. 2011; Zack et al. 2011). Thus, rutile U–Pb ages primarily reflect cooling ages of UHP rocks, except for extremely low geothermal gradients.

In addition, finding coesite or diamond inclusions in detrital rutile is particularly attractive to enhance information about the UHP source rocks. Niobium versus chromium contents are useful for discriminating mafic versus felsic sources (Zack et al. 2004a; Triebold et al. 2007; Meinhold et al. 2008; Triebold et al. 2012), whereby a felsic source can further be supported by a large spread and on average elevated Hf concentrations (Meinhold 2010). Rutile further serves as a geothermometer, due to the temperature-dependent partitioning of zirconium when co-existing with zircon and quartz (Zack et al. 2004b; Watson et al. 2006; Tomkins et al. 2007; Kohn 2020). Notably, niobium versus chromium host-rock classification and zirconium-in-rutile thermometry are not always valid for temperatures >900 °C (Hart et al. 2018, and references therein).

Challenging factors for analyzing mineral inclusions is the intrinsic color of rutile (less transparent than garnet and zircon) and the intense Raman activity. This hampers the optical inclusion detection and obscures the Raman signal emitted by the inclusions. Thus, analytical techniques probably have to be customized, for example by grinding/polishing in several steps. Regardless of this minor shortcoming to be tackled, rutile has a high potential for detrital UHP studies with regard to source rock chronology, thermometry, and composition.

7.4.3 *Tourmaline*

Tourmaline is a common mineral in metasedimentary rocks, but is even more frequent in felsic igneous rocks (e.g., Henry & Guidotti 1985; von Eynatten & Dunkl 2012). Although scarce, tourmaline growth at UHP conditions is proven by quartz pseudomorphs after coesite in tourmaline of the Dora Maira Massif in the Western Alps (Ertl et al. 2010) and coesite-bearing tourmaline from Lago di Cignana in the Western Alps (Reinecke 1991; Bebout & Nakamura 2003) and the Saxonian Erzgebirge in the Northeastern Bohemian Massif (Marschall et al. 2009). In addition, diamond-bearing tourmaline is reported from the Kokchetav Massif in Kazakhstan, although tourmaline growth in the diamond stability field is unconfident (Ota et al. 2008).

Major element chemistry is useful to discriminate metamorphic from igneous tourmaline. Metamorphic tourmaline shows high proportions of Mg compared igneous tourmaline, and igneous tourmaline additionally has high concentrations of Al, Fe, and Li (Henry & Guidotti 1985; von Eynatten & Gaupp 1999; Morton et al. 2005a; Trumbull et al. 2009). In addition, boron isotopes can provide valuable source rock information (Guo et al. 2021). The high closure temperature in isotopic systems like K–Ar, ^{40}Ar – ^{39}Ar , Rb–Sr, Sm–Nd, and U–Th–Pb also provide the opportunity for geochronological dating of tourmaline (Marschall & Jiang 2011), although this has not been utilized much yet (e.g., Martínez-Martínez et al. 2010).

7.5 **Fields of application**

7.5.1 *Exhumation history of UHP terranes*

Sedimentary provenance analysis often aims at reconstructing the exhumation history of orogens in the hinterland by investigating sedimentary successions of foreland basins. As a major advantage, the timing of exhumation and sometimes even rates may be constrained by stratigraphic means. However,

identifying the metamorphic grade of eroded source rocks is challenging because most grains lost their paragenetic context. Thus, unless gravel-sized material is available, diagnostic associations of minerals in mutual grain contact, i.e., metamorphic mineral assemblages, cannot be observed and information must be extracted from detrital single grains (von Eynatten & Dunkl 2012).

While a distinct change in the heavy mineral spectra may mark the onset of metamorphic input into a basin, for instance by the first significant appearance of metamorphic minerals like epidote, garnet, and/or hornblende, the exposure of HP and UHP units in the hinterland is often difficult to assess, especially in mature sedimentary successions. Diagnostic index minerals, like omphacite, glaucophane, and lawsonite for HP metamorphism or coesite and diamond for UHP metamorphism, are rarely archived in the sedimentary record. Often these minerals are either replaced by low-pressure phases during exhumation of their initial source rocks, or, when preserved and exposed to the surface, they progressively disappear when subjected to processes of the sedimentary cycle such as weathering and transport. Therefore, in most cases single-grain techniques like the determination of the Si content in white mica (e.g., von Eynatten et al. 1996; Grimmer et al. 2003), garnet chemistry (e.g., Morton 1985; Krippner et al. 2016), rutile chemistry (e.g., Triebold et al. 2007; Meinhold et al. 2008) or the comparison of chronological data with known ages from potential source rocks (e.g., Li et al. 2005; Weislogel et al. 2006) are applied to detect the exposure and erosion of high-grade metamorphic rocks. Although these methods are generally suitable to evaluate the exhumation history of crystalline rock packages, detailed information on exhumation stage and metamorphic grade of exposed rocks is open for interpretation.

In contrast, by applying the concept of analyzing inclusions in mechanically and chemically stable host minerals, the first supply of material sourced from HP/UHP metamorphic rocks can be pinpointed, even in mature sediments. The host mineral shields inclusions from retrogression and modifications during surface weathering, transport, and burial diagenesis. Inclusions of omphacite in garnet directly reflect an eclogitic source and thus the exposure and erosion of HP rocks in the source area (Schönig et al. 2018b). Although not reported from the detritus so far, inclusions of glaucophane or lawsonite would reflect low-temperature HP source rocks. Continued exhumation and exposure of UHP rocks can be verified by inclusions of coesite and, at higher pressures, diamond (Schönig et al. 2018a, 2019, 2020; Baldwin et al. 2021). This opens new opportunities to investigate the timing of exposure of HP and UHP rocks, respectively, and trace the exhumation history, for example by estimating the exhumation rates of ancient HP/UHP terranes.

7.5.2 Modern-style plate tectonics in Earth history

Plate tectonics is a unique feature of planet Earth (e.g., Stern 2018; Dewey et al. 2021), driven by the global-scale operation of subduction, i.e., the sinking of cold dense lithosphere into the mantle (Forsyth & Ueda 1975; Conrad & Lithgow-Bertelloni 2002). Thus, the time interval where subduction started to exert a dominant control on continental crust generation and preservation marks the onset of plate tectonics (e.g., Dhuime et al. 2012; Hawkesworth et al. 2016). Several lines of arguments, like the first appearance of paired metamorphic belts (Brown 2006, 2014), the formation of large continental masses (e.g., Korenaga 2013; Hawkesworth et al. 2016; Reimink et al. 2021), the decrease in the rate of continental growth (e.g., Belousova et al. 2010; Dhuime et al. 2012, 2015, 2017; Spencer et al. 2017),

geochemical data (Cawood et al. 2006; Shirey & Richardson 2011; Tang et al. 2016; Satkoski et al. 2017), and petrological-thermomechanical numerical modelling (Sizova et al. 2010) indicate an onset of subduction in the Mesoarchean to early Paleoproterozoic (e.g., Palin et al. 2020). In contrast, some authors argue for an even earlier onset of subduction during late Hadean to early Archean times (e.g., Komiya et al. 1999; Nutman et al. 2002, 2020; Hopkins et al. 2008, 2010; Pease et al. 2008; Shirey et al. 2008; Ernst 2017; Greber et al. 2017; Maruyama et al. 2018), and others argue for an onset as late as the Neoproterozoic (Stern 2005; Hamilton 2011; Stern et al. 2016).

While Hadean to early Archean plate tectonic phenomena may be related to local subduction in an otherwise global stagnant-lid regime (Toth & Gurnis 1998; Gurnis et al. 2004; Ueda et al. 2008; Burov & Cloetingh 2010; Gerya et al. 2015; Davaille et al. 2017; Palin et al. 2020), the key argument for a late (Neoproterozoic) onset of plate tectonics is the lacking evidence for ophiolites, low T/P rocks, and UHP rocks from the geological record prior to that time (Stern 2005). Important to note is that low T/P and UHP rocks define the modern-style of plate tectonics that includes cold and deep subduction, and not plate tectonics in general which may have operated with global-scale subduction under warmer conditions and shallower depths (Sizova et al. 2010, 2014; Hawkesworth et al. 2016; Brown & Johnson 2018; Holder et al. 2019) in response to higher potential mantle temperatures (Davies 2009; Korenaga 2013; Condie et al. 2016; Ganne & Feng 2017). Thus, the Neoproterozoic can only be considered as marking the onset of modern-style plate tectonics. However, pre-Neoproterozoic ophiolites exist (Scott et al. 1992; Peltonen et al. 1996; Dann 1997) and many works report Paleoproterozoic low T/P rocks indicative for modern-style plate tectonics (Möller et al. 1995; Collins et al. 2004; Mints et al. 2010; Ganne et al. 2012; Dokukina et al. 2014; Glassley et al. 2014; Perchuk & Morgunova 2014; Weller & St-Onge 2017; François et al. 2018; Müller et al. 2018a, 2018b; Xu et al. 2018; de Oliveira Chaves & Porcher 2020). In addition, a lower proportion of low T/P rocks in the pre-Neoproterozoic may be related to the fragmentary geological record through time (e.g., Goodwin 1996; Palin et al. 2020), including biased preservation due to erosion, retrograde metamorphism, and supercontinent cycles (e.g., Wei & Clarke 2011; Cawood & Hawkesworth 2014; Weller & St-Onge 2017; Keller & Schoene 2018; Chowdhury et al. 2021), restriction of lawsonite-bearing rocks to extremely cold conditions (Penniston-Dorland et al. 2015; Hernández-Urbe & Palin 2019), and variations in protolith composition (Palin & Dyck 2018; Palin et al. 2021).

In conclusion, indications for modern-style plate tectonics in the Paleoproterozoic are convincing, but whether these are local or global phenomena and whether deep subduction to UHP conditions was involved are unresolved issues, especially when considering the fragmentary crystalline rock record (e.g., Goodwin 1996), the supposed higher metamorphic gradients (Holder et al. 2019), and the oldest evidence for UHP metamorphism in the form of coesite at ~620 Ma (Jahn et al. 2001). To tackle these issues, large regions have to be screened on the presence of low T/P and UHP rocks and also material sourced from eroded orogens should be considered to utilize the entire geological record. As targeted field mapping and thin-section analysis to find UHP relicts suffers in screening large rock volumes and is limited to the preserved crystalline rock record, benefits of the technique of analyzing inclusions in detrital minerals (e.g., garnet), as reviewed here, are becoming increasingly important. Thus, this method represents a complimentary and preferable approach to trace UHP metamorphism, and consequently modern-style plate tectonics, through the Precambrian geological record.

7.5.3 Elastic geothermobarometry

Elastic geothermobarometry is independent from chemical equilibrium of a mineral assemblage (Mazzucchelli et al. 2018), which is particularly attractive for estimating conditions in the UHP field, where phase transformations are rare and only roughly reflect minimal conditions, i.e., >2.9 GPa for coesite, >4 GPa for diamond, and >7 GPa for stishovite at $T = 800$ °C (e.g., Bundy 1980; Bose & Ganguly 1995; Yong et al. 2012). In addition, elastic geothermometry can be applied to detrital inclusion-bearing mineral grains that otherwise mainly lost their paragenetic context (Baldwin et al. 2021). Such elastic approaches require (i) knowledge of the host–inclusion equation of state parameters (Angel et al. 2014); (ii) the determination of inclusion strains resulting from different thermoelastic properties of host–inclusion pairs (Angel et al. 2015), for example by the Raman shifts of multiple bands and calculations based on the phonon-mode Grüneisen tensor (Angel et al. 2019); (iii) calculation of the mean stress, that is inclusion pressure; and (iv) calculation of the isomeke, that is a line of uniform stress and strain in P – T space (Angel et al. 2017a; Murri et al. 2018; Mazzucchelli et al. 2021). These complex models are successfully developed for anisotropic mineral inclusions of quartz and zircon in an isotropic garnet host, and applied in several studies and in combination with other thermobarometric methods (e.g., Gonzalez et al. 2019; Zhong et al. 2019; Alvaro et al. 2020; Spear & Wolfe 2020).

The field of elastic geothermobarometry is continuing to develop rapidly, and a recently introduced model for anisotropic mineral inclusions in anisotropic host minerals by Gonzalez et al. (2021) gives cause for optimism to cope complex systems in future. However, the subject of coesite-in-garnet has not been touched so far. First of all, the lower symmetry of coesite (monoclinic) compared to quartz (trigonal, hexagonal) and zircon (tetragonal) require complex and resource-intensive density-functional theory simulations to determine the phonon-mode Grüneisen tensor components (e.g., Zicovich-Wilson et al. 2004; Prencipe 2012). Secondly, motivations have probably been hampered because it has been shown that optically monomineralic coesite inclusions often turned out to be bimineralic (coesite + quartz) when investigated by detailed Raman imaging, making the host-inclusion system to a complex three-shelled model (e.g., Korsakov et al. 2007; Zhukov & Korsakov 2015). However, transmission electron microscopy proved the occurrence of monomineralic coesite in kyanite (Taguchi et al. 2019) and garnet (Taguchi et al. 2021) of crystalline rocks from the Sulu orogen and the Western Alps, making a two-component host–inclusion model sufficient.

The frequent occurrence of monomineralic coesite in the detrital garnet fraction (Schönig et al. 2018a, 2019, 2020, 2021b; Baldwin et al. 2021) highlight the efficiency of the detrital approach to find a statistically significant number of monomineralic coesite inclusions. We hope this encourage experts to tackle the issue of elastic coesite-in-garnet geothermobarometry, potentially providing new insights into the P – T evolution of UHP rocks, particularly when combined with titanium-in-coesite thermometry (Osborne et al. 2019).

7.6 Summary

UHP metamorphism is directly interlinked with deep subduction processes characteristic for modern-style plate tectonics. Studying rocks that experienced these extreme conditions through time has so far been limited to the investigation of crystalline rocks. The novel approach of considering the sedimentary

record as an archive for UHP metamorphism was recently introduced by Schönig et al. (2018a, 2019), and further applied by Schönig et al. (2020, 2021b) and Baldwin et al. (2021). These studies report the first findings of inclusions of the unequivocal mineral indicators for UHP metamorphism, i.e., coesite and diamond, in detrital single garnet grains sourced from crustal rocks. Mineral chemistry and co-existing inclusions of the garnets are useful to characterize and discriminate different sources, for instance felsic vs. mafic. The method of analyzing the detritus has several benefits compared to sampling crystalline rocks, mainly with regard to reducing the subjectivity of point sampling and the number of samples needed to cover large rock volumes, and the possibility to detect UHP terranes that have been exposed to Earth's surface in the geological past. The possibilities of a mantle origin and/or recycling have to be carefully considered before linking the detrital signal to deep subduction processes of a specific metamorphic event. Whereas garnet chemistry is appropriate to distinguish between crustal and mantle origin, the effect of recycling is more difficult to handle and depends on the specific case study. In general, the detritus can provide an overview of the characteristics and distribution of UHP rocks and/or their erosional products. UHP detritus may be linked to deep subduction processes of a specific orogenic event and may be used to plan further investigation of the crystalline record, provided that they have not yet been eroded.

Future enhancements of the method include a reduction of the analytical time needed and increasing the information value from the detrital UHP grains. This will be achieved by focusing on garnets of a specific grain-size range and composition, and by considering ultrastable minerals as hosts for UHP inclusions. Zircon, rutile, and tourmaline offer great potential for source rock discrimination, geochronology, and thermochronology. In particular, *in situ* geochronologic methods are important to assign detrital grains containing UHP inclusions to a specific metamorphic event. In addition, hyperspectral Raman imaging represents an option to reduce the user-assisted analytical time.

Overall, the findings and potential enhancements regarding the method of tracing UHP metamorphism in the sedimentary record provide an effective and complimentary approach for capturing the distribution and characteristics of UHP rocks exposed on the Earth's surface at the time of sediment generation and deposition. This opens new opportunities to search for UHP events in Earth's history and study the exhumation of UHP terranes. Furthermore, the enrichment of monomineralic coesite inclusions in detrital mineral grains will significantly increase the findings of these inclusions, which are useful to systematically study the coesite-to-quartz transformation and coesite preservation during exhumation. We may speculate that monomineralic coesite inclusions could allow performing elastic geothermobarometry in the future.

Acknowledgements

This work was supported by the German Research Foundation [DFG grant EY 23/27-1]. We thank Suzanne L. Baldwin, Joseph P. Gonzalez, Hugh Davies, Raimon Tolosana-Delgado, Arne P. Willner, and Bernhard Schulz for collaboration and discussion during projects intimately related to this contribution.

Concluding Remarks and Future Research Directions

8.1 General Conclusions

UHP metamorphism is interlinked with deep subduction processes, which are indicative for modern-style plate tectonics. Numerous hints, particularly from the detrital zircon record, indicate that plate tectonics exert a dominant control on crustal growth and destruction since the Archean–Proterozoic transition. However, how plate tectonics evolved until present and when the modern-style deep subduction regime initiated is highly controversial. While the detrital zircon record provides important insights regarding the onset of plate tectonics on a global scale, techniques that enable to investigate the sedimentary archive on deep subduction processes through time are in great demand but virtually absent. The findings of coesite inclusions in detrital garnet from a small catchment of the Western Gneiss Region of Norway (Schönig et al. 2018a) introduced a novel technique to systematically screen sediments for erosional material sourced from UHP rocks. Building up on this approach, this thesis aimed at answering fundamental questions (Section 1.2) regarding methodological robustness, benefits, and advancements, as well as applicability to tackle issues that remained open in Phanerozoic UHP terranes despite extensive investigation of crystalline rocks. Key conclusions of the papers and manuscripts presented in Chapters 2 to 7 include:

1. Eroded UHP rocks leave their traces in the sedimentary record in the form of coesite inclusions in detrital garnet. This is a general and not a local phenomenon as demonstrated in three spatially and chronologically distributed Phanerozoic UHP terranes including the Devonian Western Gneiss Region of Norway (Schönig et al. 2018a), the Carboniferous Saxonian Erzgebirge of Germany (Schönig et al. 2019, 2020; Chapters 2 and 3), and the Neogene D'Entrecasteaux metamorphic complex of Papua New Guinea (Baldwin et al. 2021; Chapter 4).
2. Diamond-bearing rocks effectively transfer their signatures to the sediment factory and can be detected by the detrital garnet approach as proven for the Saxonian Erzgebirge (Schönig et al. 2019, 2020; Chapters 2 and 3).
3. The technique is applicable to trace UHP metamorphism in larger catchments than tested before ($\sim 1 \text{ km}^2$, Schönig et al. 2018a), up to regional river catchments $> 500 \text{ km}^2$ (Schönig et al. 2019, 2020; Chapters 2 and 3).
4. By combining information from detrital garnet inclusion assemblages and garnet major-element chemistry, important new insights are gained regarding the size of the rock body affected by UHP metamorphism and the lithologies involved. This leads to the conclusion of a largely coherent slab subducted to UHP conditions in the Erzgebirge (Schönig et al. 2020; Chapter 3), and UHP metamorphism of crustal rocks in D'Entrecasteaux metamorphic complex, closing

the rock cycle from a sedimentary protolith, over deep subduction, exhumation, and erosion, to sediment deposition (Baldwin et al. 2021; Chapter 4).

5. The occurrence of polyphase inclusions containing mineral assemblages characteristic for granitic melts, including rare SiO₂ (cristobalite) and feldspar (kokchetavite, kumdykolite) polymorphs, track partial melting during the metamorphic cycle in the Erzgebirge (Schönig et al. 2020; Chapter 3) and the D'Entrecasteaux metamorphic complex (Baldwin et al. 2021; Chapter 4). For the Erzgebirge, melt inclusions and garnet chemistry indicate that garnet of felsic country rocks is compositionally modified as a result of diffusion during exhumation under high-temperature conditions, while evidence for UHP metamorphism is preserved in form of coesite and diamond inclusions (Schönig et al. 2020; Chapter 3). In the D'Entrecasteaux metamorphic complex, melt inclusions and elastic geothermobarometry support a supposed heating event during exhumation of the UHP terrane (Baldwin et al. 2021; Chapter 4).
6. The heterogenous grain-size distribution of coesite-bearing garnet highlight the necessity to consider a large grain-size window to achieve thorough provenance information from mineral inclusions, especially in terms of UHP source rocks (Schönig et al. 2020; Chapter 3). Nevertheless, to tackle key questions in the least amount of invested time, i.e., whether rocks underwent UHP conditions, whether they reached the diamond-stability field, and whether mafic and felsic lithologies were involved, the 250–500 µm fraction is most efficient (Schönig et al. 2021b; Chapter 5).
7. A small coesite inclusion size <9 µm and low abundance per garnet host grain promote the preservation of coesite, particularly in the monomineralic state, because the small initial fracture length and the absence of overlapping strain fields reduce the fracturing potential. Thus, metastable coesite inclusions are shielded from external conditions and metamorphic fluids, hampering the transformation to quartz. Both mafic and felsic UHP garnets mainly have an initially large crystal size. While mafic garnet typically contains low amounts of coesite inclusions per grain and show minor disintegration, felsic garnets show variable amounts of coesite inclusions, whereby coesite-rich grains intensively disintegrate into smaller fragments during exhumation and processes of the sedimentary cycle (Schönig et al. 2021b; Chapter 5).
8. The novel major-element garnet discrimination scheme, developed by considering a large database and using the random forest machine-learning algorithm, overcomes many issues related to previous schemes, particularly with respect to a wide coverage of potential host rocks, detailed prediction classes, and high discrimination rates (Schönig et al. in press; Chapter 6). This improves provenance interpretations based on garnet composition, and also allows for a pre-screening and pre-selection of garnet grains that have a high potential to be sourced from HP/UHP rocks, and thus enhancing the methodological efficiency (Schönig et al. in preparation; Chapter 7). Additional technical advances include the choice of the grain size (point 6) and hyperspectral Raman imaging to reduce the user-assisted analytical time.

In summary, the technique of analyzing mineral inclusions in detrital garnet to trace the erosion of UHP rocks brings many advantages, is robust, efficient, and has a high potential to prove or disprove the

hypothesis that deep subduction, and consequently modern-style plate tectonics, has operated in pre-Neoproterozoic times.

8.2 Outlook

The oldest irrefutable UHP rock is of Neoproterozoic age (Jahn et al. 2001). As outlined, seeking for metamorphic coesite and/or diamond in the pre-Neoproterozoic record is of first-order significance in Earth Sciences because any finding would, at least locally, indisputably prove that not only cold subduction, but also deep subduction operated, both being characteristic for the modern-style plate tectonic regime. To search for pre-Neoproterozoic traces of UHP metamorphism, it is probably most effective to start in Paleoproterozoic terranes, which are already suspect of having experienced UHP metamorphism or conditions close to it. Because these rocks are still exposed at the Earth's surface, analyzing modern-sand samples from catchments draining these rocks and their surroundings should be able to prove or disprove if coesite- and/or diamond-bearing UHP rocks occur.

Potential Paleoproterozoic targets that experienced low T/P conditions include the Belomorian Belt of Russia, the Usagaran Belt of Tanzania, the West African Craton of Burkina Faso, the Kasai Block of the Democratic Republic of Congo, the Nagssugtoqidian Orogen of Greenland, the Trans-Hudson Orogen of Canada, the North China Craton of China, and the São Francisco Craton of Brazil (Figure 1.1 1D). Considering the maximum P - T conditions reported, Burkina Faso (~1.1 GPa at ~425 °C; Gannet et al. 2012), Tanzania (~1.8 GPa at ~750 °C; Möller et al. 1995; Collins et al. 2004), Brazil (~1.85 GPa at ~650 °C; de Oliveira Chaves & Porcher 2020), and the Democratic Republic of Congo (~2.0 GPa at ~525 °C; François et al. 2018) have less potential in terms of UHP metamorphism compared to China (~2.65 GPa at ~660 °C; Xu et al. 2018), Russia (~3 GPa at ~660 °C; Perchuk & Morgunova 2014), Canada (~2.5 GPa at ~735 °C; Weller & St-Onge 2017), and Greenland (~7.0 GPa at ~975 °C; Glassley et al. 2014). Because the P - T conditions reported from China correspond to eclogite xenoliths in carbonatites (Xu et al. 2018), and Russia is difficult to access, Greenland and Canada have been declared as prime targets as part of the ongoing DFG project (grant EY 23/27-1, funding until September 2022). While field work in Canada had to be postponed to summer 2022 due to pandemic-related travel restrictions, field work in Greenland could be performed in a small time slot without travel restrictions in August 2020 by Guido Meinhold and Jan Schönig.

The Paleoproterozoic Nagssugtoqidian Orogen extends from East to West over Southern Greenland (Kolb 2014; Müller et al. 2018a). The orogenic cycle included northward accretion of microcontinents to the Rae craton and subsequent collision of the Rae craton with the North Atlantic craton at ~1.86–1.84 Ga (St-Onge et al. 2009; Kolb 2014), accompanied by south-directed tectonic transport and northward subduction (van Gool et al. 2002; Nutman et al. 2008). The Nordre Strømfjord Shear Zone in the western part of the orogen is of particular interest based on the work of Glassley et al. (2014). The authors reported olivine-garnet-clinopyroxene-quartz-(graphite) gneisses with preferred oriented chlorine-bearing hydrous mineral inclusions in garnet, interpreted as retrograded orthopyroxene originally formed by exsolution from a majoritic precursor, and thus, indicating extreme UHP conditions of ~7 GPa (Figure 1.1-1D). Graphitized diamond inclusions are also reported, but their identification and metamorphic origin are questionable due to the presented low-quality Raman spectra

and the usage of diamond abrasives for sample preparation. The suggested incomplete graphitization process is described as being similar to findings of diamonds from Norway by Smith & Godard (2013), for which Nasdala et al. (2016) already argued that the UHP assignment is questionable. Other arguments for the existence of an UHP domain are oriented rutile inclusions in garnet, interpreted as exsolution, orthopyroxene lamellae in clinopyroxene, and quartz needles in fayalite (Glassley et al. 2014). Overall, the indications for UHP metamorphism are speculative and vulnerable, but if this region underwent the supposed extreme conditions, some coesite and diamond inclusions should be preserved in robust host minerals like garnet.

Fifteen modern-sand samples have been taken in order to cover a large proportion of catchments surrounding the UHP rock occurrences reported by Glassley et al. (2014). Samples have been prepared for the investigation of garnet chemistry and mineral inclusion assemblages, while data acquisition is ongoing. The final dataset is expected to prove or disprove the hypothesis of the operation of deep subduction to UHP conditions during the Paleoproterozoic Nagssugtoqidian Orogeny.

REFERENCES

- Abers GA, Eilon Z, Gaherty JB, Jin G, Kim YH, Obrebski M, Dieck C (2016): Southeast Papuan crustal tectonics: Imaging extension and buoyancy of an active rift. *Journal of Geophysical Research: Solid Earth* 121, 951–971, <https://doi.org/10.1002/2015JB012621>.
- Adam J, Rushmer T, O'Neil J, Francis D (2012): Hadean greenstones from the Nuvvuagittuq fold belt and the origin of the Earth's early continental crust. *Geology* 40, 363–366, <https://doi.org/10.1130/G32623.1>.
- Agangi A, Reddy SM, Plavsa D, Fougereuse D, Clark C, Roberts M, Johnson TE (2019): Antimony in rutile as a pathfinder for orogenic gold deposits. *Ore Geology Reviews* 106, 1–11, <https://doi.org/10.1016/j.oregeorev.2019.01.018>.
- Agard P, Yamato P, Jolivet L, Burov E (2009): Exhumation of oceanic blueschists and eclogites in subduction zones: timing and mechanisms. *Earth-Science Reviews* 92, 53–79, <https://doi.org/10.1016/j.earscirev.2008.11.002>.
- Aitchison J (1986): *The Statistical Analysis of Compositional Data*. Chapman and Hall, London/New York, pp. 416.
- Aitchison J, Egozcue JJ (2005): Compositional data analysis: where are we and where should we be heading? *Mathematical Geology* 37, 829–850.
- Alvaro M, Mazzucchelli ML, Angel RJ, Murri M, Campomenosi N, Scambelluri M, Nestola F, Korsakov A, Tomilenko AA, Marone F, Morana M (2020): Fossil subduction recorded by quartz from the coesite stability field. *Geology* 48, 24–28, <https://doi.org/10.1130/G46617.1>.
- Anderson JL, Barth AP, Wooden JL, Mazdab F (2008): Thermometers and thermobarometers in granitic systems. *Reviews in Mineralogy and Geochemistry* 69, 121–142, <https://doi.org/10.2138/rmg.2008.69.4>.
- Andò S, Morton AC, Garzanti E (2014): Metamorphic grade of source rocks revealed by chemical fingerprints of detrital amphibole and garnet. In: Scott RA, Smyth HR, Morton AC, Richardson N (Eds), *Sediment Provenance Studies in Hydrocarbon Exploration and Production*. Geological Society of London, Special Publications 386, 351–371, <https://doi.org/10.1144/SP386.5>.
- Angel RJ, Mazzucchelli ML, Alvaro M, Nimis P, Nestola F (2014): Geobarometry from host-inclusion systems: the role of elastic relaxation. *American Mineralogist* 99, 2146–2149, <https://doi.org/10.2138/am-2014-5047>.
- Angel RJ, Nimis P, Mazzucchelli ML, Alvaro M, Nestola F (2015): How large are departures from lithostatic pressure? Constraints from host-inclusion elasticity. *Journal of Metamorphic Geology* 33, 801–813, <https://doi.org/10.1111/jmg.12138>.
- Angel RJ, Mazzucchelli ML, Alvaro M, Nestola F (2017a): EosFit-Pinc: A simple GUI for host-inclusion elastic thermobarometry. *American Mineralogist* 102, 1957–1960, <https://doi.org/10.2138/am-2017-6190>.
- Angel RJ, Alvaro M, Miletich R, Nestola F (2017b): A simple and generalised P–T–V EoS for continuous phase transitions, implemented in EosFit and applied to quartz. *Contributions to Mineralogy and Petrology* 172, 29, <https://doi.org/10.1007/s00410-017-1349-x>.
- Angel RJ, Murri M, Mihailova B, Alvaro M (2019): Stress, strain and Raman shifts. *Zeitschrift für Kristallographie - Crystalline Materials* 234, 129–140, <https://doi.org/10.1515/zkri-2018-2112>.
- Angiboust S, Harlov D (2017): Ilmenite breakdown and rutile-titanite stability in metagranitoids: natural observations and experimental results. *American Mineralogist* 102, 1696–1708, <https://doi.org/10.2138/am-2017-6064>.
- Arndt NT, Goldstein SL (1987): Use and abuse of crust-formation ages. *Geology* 15, 893–895, [https://doi.org/10.1130/0091-7613\(1987\)15<893:UAAOCA>2.0.CO;2](https://doi.org/10.1130/0091-7613(1987)15<893:UAAOCA>2.0.CO;2).
- Attali D (2020): colourpicker: A Colour Picker Tool for Shiny and for Selecting Colours in Plots. R package version 1.1.0, <https://CRAN.R-project.org/package=colourpicker>.

- Aubrecht R, Méres S, Sýkora M, Mikuš T (2009): Provenance of the detrital garnets and spinels from the Albian sediments of the Czorsztyn Unit (Pieniny Klippen Belt, Western Carpathians, Slovakia). *Geologica Carpathica* 60, 463–483, <https://doi.org/10.2478/v10096-009-0034-z>.
- Aulbach S (2020): Temperature-dependent rutile solubility in garnet and clinopyroxene from mantle eclogite: Implications for continental crust formation and V-based oxybarometry. *Journal of Petrology* 61, ega065, <https://doi.org/10.1093/petrology/egaa065>.
- Avigad D, Nie S, Yin A, Rowley DB, Jin Y (1995): Exhumation of the Dabie Shan ultra–high-pressure rocks and accumulation of the Songpan-Ganzi flysch sequence, central China: Comment and Reply. *Geology* 23, 764–766.
- Babuška V, Fiala J, Kumazawa M, Ohno I, Sumino Y (1978): Elastic properties of garnet solid-solution series. *Physics of the Earth and Planetary Interiors* 16, 157–176, [https://doi.org/10.1016/0031-9201\(78\)90086-9](https://doi.org/10.1016/0031-9201(78)90086-9).
- Bache SM, Wickham H (2014): magrittr: A Forward-Pipe Operator for R. R package version 1.5, <https://CRAN.R-project.org/package=magrittr>.
- Baldwin SL, Das JP (2015): Atmospheric Ar and Ne returned from mantle depths to the Earth’s surface by forearc recycling. *Proceedings of the National Academy of Sciences* 112, 14174–14179, <https://doi.org/10.1073/pnas.1424122112>.
- Baldwin SL, Lister GS, Hill EJ, Foster DA, McDougall I (1993): Thermochronologic constraints on the tectonic evolution of active metamorphic core complexes, D’Entrecasteaux Islands, Papua New Guinea. *Tectonics* 12, 611–628, <https://doi.org/10.1029/93TC00235>.
- Baldwin SL, Monteleone BD, Webb LE, Fitzgerald PG, Grove M, Hill EJ (2004): Pliocene eclogite exhumation at plate tectonic rates in eastern Papua New Guinea. *Nature* 431, 263–267, <https://doi.org/10.1038/nature02846>.
- Baldwin SL, Webb LE, Monteleone BD (2008): Late Miocene coesite-eclogite exhumed in the Woodlark Rift. *Geology* 36, 735–738, <https://doi.org/10.1130/G25144A.1>.
- Baldwin SL, Fitzgerald PG, Webb LE (2012): Tectonics of the New Guinea region. *Annual Review of Earth and Planetary Sciences* 40, 495–520, <https://doi.org/10.1146/annurev-earth-040809-152540>.
- Baldwin SL, Schönig J, Gonzalez JP, Davies H, von Eynatten H (2021): Garnet sand reveals rock recycling processes in the youngest exhumed high- and ultrahigh-pressure terrane on Earth. *Proceedings of the National Academy of Sciences* 118, e2017231118, <https://doi.org/10.1073/pnas.2017231118>.
- Balica C, Ducea MN, Gehrels GE, Kirk J, Roban RD, Luffi P, Chapman JB, Triantafyllou A, Guo J, Stoica AM, Ruiz J (2020): A zircon petrochronologic view on granitoids and continental evolution. *Earth and Planetary Science Letters* 531, 116005, <https://doi.org/10.1016/j.epsl.2019.116005>.
- Barley ME, Brown SJA, Krapez B (2006): Felsic volcanism in the eastern Yilgarn craton, Western Australia: Evolution of a late Archean convergent margin. *Geochimica et Cosmochimica Acta* 70, A35.
- Baxter EF, Caddick MJ, Ague JJ (2013): Garnet: Common mineral, uncommonly useful. *Elements* 9, 415–419, <https://doi.org/10.2113/gselements.9.6.415>.
- Bebout GE, Nakamura E (2003): Record in metamorphic tourmalines of subduction-zone devolatilization and boron cycling. *Geology* 31, 407–410, [https://doi.org/10.1130/0091-7613\(2003\)031<0407:RIMTOS>2.0.CO;2](https://doi.org/10.1130/0091-7613(2003)031<0407:RIMTOS>2.0.CO;2).
- Bebout GE, Penniston-Dorland SC (2016): Fluid and mass transfer at subduction interfaces — The field metamorphic record. *Lithos* 240, 228–258, <https://doi.org/10.1016/j.lithos.2015.10.007>.
- Belgiu M, Drăguț L (2016): Random forest in remote sensing: A review of applications and future directions. *ISPRS Journal of Photogrammetry and Remote Sensing* 114, 24–31, <https://doi.org/10.1016/j.isprsjprs.2016.01.011>.
- Belousova EA, Griffin WL, Pearson NJ (1998): Trace element composition and cathodoluminescence properties of southern African kimberlitic zircons. *Mineralogical Magazine* 62, 355–366, <https://doi.org/10.1180/002646198547747>.

- Belousova EA, Griffin WL, O'Reilly SY, Fisher NI (2002): Igneous zircon: trace element composition as an indicator of source rock type. *Contributions to Mineralogy and Petrology* 143, 602–622, <https://doi.org/10.1007/s00410-002-0364-7>.
- Belousova EA, Kostitsyn YA, Griffin WL, Begg GC, O'Reilly SY, Pearson NJ (2010): The growth of the continental crust: constraints from zircon Hf-isotope data. *Lithos* 119, 457–466, <https://doi.org/10.1016/j.lithos.2010.07.024>.
- Bernet M, van der Beek P, Pik R, Huyghe P, Mugnier JL, Labrinz E, Szulc A (2006): Miocene to Recent exhumation of the central Himalaya determined from combined detrital zircon fission track and U/Pb analysis of Siwalik sediments, western Nepal: *Basin Research* 18, 393–412, <https://doi.org/10.1111/j.1365-2117.2006.00303.x>.
- Biau G, Scornet E (2016): A random forest guided tour. *TEST* 25, 197–227, <https://doi.org/10.1007/s11749-016-0481-7>.
- Bin Z, Barton MD (1988): Compositional characteristics of garnets and pyroxenes in contact-metamorphic skarn deposits and their relationship with metallization. *Chinese Journal of Geochemistry* 7, 329–335, <https://doi.org/10.1007/BF02842337>.
- Blackburn T, Bowring S, Schoene B, Mahan K, Dudas F (2011): U–Pb thermochronology: creating a temporal record of lithosphere thermal evolution. *Contributions to Mineralogy and Petrology* 162, 479–500, <https://doi.org/10.1007/s00410-011-0607-6>.
- Bohlen SR, Boettcher AL (1982): The quartz–coesite transformation: a precise determination and the effects of other components. *Journal of Geophysical Research: Solid Earth* 87, 7073–7078, <https://doi.org/10.1029/JB087iB08p07073>.
- Boily M, Dion C (2002): Geochemistry of boninite-type volcanic rocks in the Frotet-Evans greenstone belt, Opatica subprovince, Quebec: implications for the evolution of Archaean greenstone belts. *Precambrian Research* 115, 349–371, [https://doi.org/10.1016/S0301-9268\(02\)00016-5](https://doi.org/10.1016/S0301-9268(02)00016-5).
- Bolton MS, Jensen BJ, Wallace K, Praet N, Fortin D, Kaufman D, De Batist M (2020): Machine learning classifiers for attributing tephra to source volcanoes: an evaluation of methods for Alaska tephra. *Journal of Quaternary Science* 35, 81–92, <https://doi.org/10.1002/jqs.3170>.
- Bonazzi M, Tumiati S, Thomas JB, Angel RJ, Alvaro M (2019): Assessment of the reliability of elastic geobarometry with quartz inclusions. *Lithos* 350–351, 105201, <https://doi.org/10.1016/j.lithos.2019.105201>.
- Borghini A, Ferrero S, O'Brien PJ, Laurent O, Günter C, Ziemann MA (2020): Cryptic metasomatic agent measured in situ in Variscan mantle rocks: Melt inclusions in garnet of eclogite, Granulitgebirge, Germany. *Journal of Metamorphic Geology* 38, 207–234, <https://doi.org/10.1111/jmg.12519>.
- Bose K, Ganguly J (1995): Quartz-coesite transition revisited: Reversed experimental determination at 500–1200 °C and retrieved thermochemical properties. *American Mineralogist* 80, 231–238, <https://doi.org/10.2138/am-1995-3-404>.
- Boulesteix AL, Janitza S, Kruppa J, König IR (2012): Overview of random forest methodology and practical guidance with emphasis on computational biology and bioinformatics. *Wiley Interdisciplinary Reviews: Data Mining and Knowledge Discovery* 2, 493–507, <https://doi.org/10.1002/widm.1072>.
- Breiman L (2001): Random forests. *Machine learning* 45, 5–32, <https://doi.org/10.1023/A:1010933404324>.
- Brown M (2006): Duality of thermal regimes is the distinctive characteristic of plate tectonics since the Neoproterozoic. *Geology* 34, 961–964, <https://doi.org/10.1130/G22853A.1>.
- Brown M (2014): The contribution of metamorphic petrology to understanding lithosphere evolution and geodynamics. *Geoscience Frontiers* 5, 553–569, <https://doi.org/10.1016/j.gsf.2014.02.005>.
- Brown M, Johnson T (2018): Secular change in metamorphism and the onset of global plate tectonics. *American Mineralogist* 103, 181–196, <https://doi.org/10.2138/am-2018-6166>.
- Bruguier O, Bosch D, Caby R, Vitale-Brovarone A, Fernandez L, Hammor D, Laouar R, Ouabadi A, Abdallah N, Mechat M (2017): Age of UHP metamorphism in the Western Mediterranean: insight from rutile and

- minute zircon inclusions in a diamond-bearing garnet megacryst (Edough Massif, NE Algeria). *Earth and Planetary Science Letters* 474, 215–225, <https://doi.org/10.1016/j.epsl.2017.06.043>.
- Buchan KL, Mitchell RN, Bleeker W, Hamilton MA, LeCheminant AN (2016): Paleomagnetism of ca. 2.13–2.11 Ga Indian and ca. 1.885 Ga Ghost dyke swarms of the Slave craton: Implications for the Slave craton APW path and relative drift of Slave, Superior and Siberian cratons in the Paleoproterozoic. *Precambrian Research* 275, 151–175, <https://doi.org/10.1016/j.precamres.2016.01.012>.
- Bucher K, Frey M (2002) *Petrogenesis of Metamorphic Rocks*. Springer-Verlag, Berlin-Heidelberg, pp. 341.
- Bundy FP (1980): The P, T phase and reaction diagram for elemental carbon, 1979. *Journal of Geophysical Research: Solid Earth* 85, 6930–6936, <https://doi.org/10.1029/JB085iB12p06930>.
- Burov E, Cloetingh S (2010): Plume-like upper mantle instabilities drive subduction initiation. *Geophysical Research Letters* 37, L03309, <https://doi.org/10.1029/2009GL041535>.
- Caddick MJ, Konopásek J, Thompson AB (2010): Preservation of garnet growth zoning and the duration of prograde metamorphism. *Journal of Petrology* 51, 2327–2347, <https://doi.org/10.1093/petrology/egq059>.
- Campbell IH, Reiners PW, Allen CM, Nicolescu S, Upadhyay R (2005): He–Pb double dating of detrital zircons from the Ganges and Indus Rivers: implication for quantifying sediment recycling and provenance studies. *Earth and Planetary Science Letters* 237, 402–432, <https://doi.org/10.1016/j.epsl.2005.06.043>.
- Campomenosi N, Mazzucchelli ML, Mihailova B, Scambelluri M, Angel RJ, Nestola F, Reali A, Alvaro M (2018): How geometry and anisotropy affect residual strain in host-inclusion systems: Coupling experimental and numerical approaches. *American Mineralogist* 103, 2032–2035, <https://doi.org/10.2138/am-2018-6700CCBY>.
- Campomenosi N, Rubatto D, Hermann J, Mihailova B, Scambelluri M, Alvaro M (2020): Establishing a protocol for the selection of zircon inclusions in garnet for Raman thermobarometry. *American Mineralogist* 105, 992–1001, <https://doi.org/10.2138/am-2020-7246>.
- Carlson WD (1989): The significance of intergranular diffusion to the mechanisms and kinetics of porphyroblast crystallization. *Contributions to Mineralogy and Petrology* 103, 1–24, <https://doi.org/10.1007/BF00371361>.
- Carson CJ, Ague JJ, Coath CD (2002): U–Pb geochronology from Tonagh Island, East Antarctica: implications for the timing of ultra-high temperature metamorphism of the Napier Complex. *Precambrian Research* 116, 237–263, [https://doi.org/10.1016/S0301-9268\(02\)00023-2](https://doi.org/10.1016/S0301-9268(02)00023-2).
- Carswell DA, Compagnoni R (2003): Introduction with review of the definition, distribution and geotectonic significance of ultrahigh pressure metamorphism. In: Carswell DA, Compagnoni R, Rolfó F (eds), *Ultrahigh pressure metamorphism*. The Mineralogical Society of Great Britain and Ireland, 3–9.
- Carswell DA, Zhang RY (1999): Petrographic characteristics and metamorphic evolution of ultrahigh-pressure eclogites in plate-collision belts. *International Geology Review* 41, 781–798, <https://doi.org/10.1080/00206819909465169>.
- Carter A, Moss SJ (1999): Combined detrital-zircon fission-track and U–Pb dating: A new approach to understanding hinterland evolution. *Geology* 27, 235–238, [https://doi.org/10.1130/0091-7613\(1999\)027<0235:CDZFTA>2.3.CO;2](https://doi.org/10.1130/0091-7613(1999)027<0235:CDZFTA>2.3.CO;2).
- Cawood PA, Hawkesworth CJ (2014): Earth’s middle age. *Geology* 42, 503–506, <https://doi.org/10.1130/G35402.1>.
- Cawood PA, Kroner A, Pisarevsky S (2006): Precambrian plate tectonics: criteria and evidence. *GSA Today* 16, 4–11, <https://doi.org/10.1130/GSAT01607.1>.
- Cawood PA, Hawkesworth CJ, Pisarevsky SA, Dhuime B, Capitanio FA, Nebel O (2018): Geological archive of the onset of plate tectonics. *Philosophical Transactions of the Royal Society A* 376, 20170405, <https://doi.org/10.1098/rsta.2017.0405>.
- Cesare B, Ferrero S, Salvioli-Mariani E, Pedron D, Cavallo A (2009): “Nanogranite” and glassy inclusions: The anatexitic melt in migmatites and granulites. *Geology* 37, 627–630, <https://doi.org/10.1130/G25759A.1>.

- Chang W, Ribeiro BB (2018): shinydashboard: Create Dashboards with 'Shiny'. R package version 0.7.1, <https://CRAN.R-project.org/package=shinydashboard>.
- Chang W, Cheng J, Allaire JJ, Xie Y, McPherson J (2019): shiny: Web Application Framework for R, R package version 1.3.2, <https://CRAN.R-project.org/package=shiny>.
- Chao EC, Shoemaker EM, Madsen BM (1960): First natural occurrence of coesite. *Science* 132, 220–222, <https://doi.org/10.1126/science.132.3421.220>.
- Chayes F (1960): On correlation between variables of constant sum. *Journal of Geophysical Research* 65, 4185–4193, <https://doi.org/10.1029/JZ065i012p04185>.
- Chen C, Liaw A, Breiman L (2004): Using random forest to learn imbalanced data. Technical report, # 666, Department of Statistics, University of California, Berkeley, CA, <http://www.stat.berkeley.edu/tech-reports/666.pdf> (Accessed 29th May 2021).
- Chen Z, Zhou J, Li R, Wan Y (2005): Mineral inclusions and internal structure of detrital zircons from lower Jurassic sedimentary rocks of Fanghushan Formation in Hefei Basin. *Acta Mineralogica Sinica* 25, 89–96.
- Chopin C (1984): Coesite and pure pyrope in high-grade blueschists of the Western Alps: a first record and some consequences. *Contributions to Mineralogy and Petrology* 86, 107–118, <https://doi.org/10.1007/BF00381838>.
- Chopin C (2003): Ultrahigh-pressure metamorphism: tracing continental crust into the mantle. *Earth and Planetary Science Letters* 212, 1–14, [https://doi.org/10.1016/S0012-821X\(03\)00261-9](https://doi.org/10.1016/S0012-821X(03)00261-9).
- Chowdhury P, Chakraborty S, Gerya TV (2021): Time can tell: Secular change in metamorphic timescales and the tectonic implications. *Gondwana Research* 93, 291–310, <https://doi.org/10.1016/j.gr.2021.02.003>.
- Clark JR, Williams-Jones AE (2004): Rutile as a potential indicator mineral for metamorphosed metallic ore deposits. *Rapport Final de DIVEX, Sous-projet SC2, Montréal, Canada*, pp. 17.
- Collins AS, Reddy SM, Buchan C, Mruma A (2004): Temporal constraints on Palaeoproterozoic eclogite formation and exhumation (Usagaran Orogen, Tanzania). *Earth and Planetary Science Letters* 224, 175–192, <https://doi.org/10.1016/j.epsl.2004.04.027>.
- Compston W, Pidgeon RT (1986): Jack Hills, evidence of more very old detrital zircons in Western Australia. *Nature* 321, 766–769, <https://doi.org/10.1038/321766a0>.
- Condie KC (2015): Changing tectonic settings through time: indiscriminate use of geochemical discriminant diagrams. *Precambrian Research* 266, 587–591, <https://doi.org/10.1016/j.precamres.2015.05.004>.
- Condie KC, Kröner A (2008): When did plate tectonics begin? Evidence from the geologic record. In: Condie KC, Pease V (eds), *When did plate tectonics begin on planet Earth?* GSA Special Paper 440, 281–294.
- Condie KC, Aster RC, van Hunen J (2016): A great thermal divergence in the mantle beginning 2.5 Ga: Geochemical constraints from greenstone basalts and komatiites. *Geoscience Frontiers* 7, 543–553, <https://doi.org/10.1016/j.gsf.2016.01.006>.
- Conrad CP, Lithgow-Bertelloni C (2002): How mantle slabs drive plate tectonics. *Science* 298, 207–209, <https://doi.org/10.1126/science.1074161>.
- Cookenboo HO, Bustin RM, Wilks KR (1997): Detrital chromian spinel compositions used to reconstruct the tectonic setting of provenance; implications for orogeny in the Canadian Cordillera. *Journal of Sedimentary Research* 67, 116–123.
- Čopjaková R, Sulovský P, Paterson BA (2005): Major and trace elements in pyrope–almandine garnets as sediment provenance indicators of the Lower Carboniferous Culm sediments, Drahaný Uplands, Bohemian Massif. *Lithos* 82, 51–70, <https://doi.org/10.1016/j.lithos.2004.12.006>.
- Corfu F, Hanchar JM, Hoskin PW, Kinny P (2003): Atlas of zircon textures. *Reviews in Mineralogy and Geochemistry* 53, 469–500.
- Cuthbert SJ (1991): Evolution of the Devonian Hornelen Basin, west Norway: new constraints from petrological studies of metamorphic clasts. In: Morton AC, Todd SP, Haughton PDW (eds), *Developments in*

Sedimentary Provenance Studies. Geological Society of London, Special Publications 57, 343–360, <https://doi.org/10.1144/GSL.SP.1991.057.01.25>.

- Cutts KA, Kinny PD, Strachan RA, Hand M, Kelsey DE, Emery M, Friend CRL, Leslie AG (2010): Three metamorphic events recorded in a single garnet: Integrated phase modelling, in situ LA-ICPMS and SIMS geochronology from the Moine Supergroup, NW Scotland. *Journal of Metamorphic Geology* 28, 249–267, <https://doi.org/10.1111/j.1525-1314.2009.00863.x>.
- Cutts KA, Stevens G, Hoffmann JE, Buick IS, Frei D, Münker C (2014): Paleo- to Mesoproterozoic polymetamorphism in the Barberton Granite-Greenstone Belt, South Africa: Constraints from U-Pb monazite and Lu-Hf garnet geochronology on the tectonic processes that shaped the belt. *GSA Bulletin* 126, 251–270, <https://doi.org/10.1130/B30807.1>.
- Dahl PS (1980): The thermal-compositional dependence of Fe²⁺-Mg distributions between coexisting garnet and pyroxene: applications to geothermometry. *American Mineralogist* 65, 852–866.
- Dahl PS (1997): A crystal-chemical basis for Pb retention and fission-track annealing systematics in U-bearing minerals, with implications for geochronology. *Earth and Planetary Science Letters* 150, 277–290, [https://doi.org/10.1016/S0012-821X\(97\)00108-8](https://doi.org/10.1016/S0012-821X(97)00108-8).
- Dahlquist JA, Galindo C, Pankhurst RJ, Rapela CW, Alasino PH, Saavedra J, Fanning CM (2007): Magmatic evolution of the Peñón Rosado granite: petrogenesis of garnet-bearing granitoids. *Lithos* 95, 177–207, <https://doi.org/10.1016/j.lithos.2006.07.010>.
- Dann JC (1997): Pseudostratigraphy and origin of the Early Proterozoic Payson ophiolite, central Arizona. *GSA Bulletin* 109, 347–365, [https://doi.org/10.1130/0016-7606\(1997\)109<0347:PAOOTE>2.3.CO;2](https://doi.org/10.1130/0016-7606(1997)109<0347:PAOOTE>2.3.CO;2).
- Davaille A, Smrekar SE, Tomlinson S (2017): Experimental and observational evidence for plume-induced subduction on Venus. *Nature Geoscience* 10, 349–355, <https://doi.org/10.1038/ngeo2928>.
- Davies GF (2009): Effect of plate bending on the Urey ratio and the thermal evolution of the mantle. *Earth and Planetary Science Letters* 287, 513–518, <https://doi.org/10.1016/j.epsl.2009.08.038>.
- Davies HL, Warren RG (1992): Eclogites of the D'Entrecasteaux Islands. *Contributions to Mineralogy and Petrology* 112, 463–474, <https://doi.org/10.1007/BF00310778>.
- de Oliveira Chaves A, Porcher CC (2020): Petrology, geochemistry and Sm-Nd systematics of the Paleoproterozoic Itaguara retroeclogite from São Francisco/Congo Craton: one of the oldest records of the modern-style plate tectonics. *Gondwana Research* 87, 224–237, <https://doi.org/10.1016/j.gr.2020.06.014>.
- DesOrmeau JW, Gordon SM, Little TA, Bowring SA, Chatterjee N (2017): Rapid time scale of Earth's youngest known ultrahigh-pressure metamorphic event, Papua New Guinea. *Geology* 45, 795–798, <https://doi.org/10.1130/G39296.1>.
- Dewey JF, Kiseeva ES, Pearce JA, Robb LJ (2021): Precambrian tectonic evolution of Earth: an outline. *South African Journal of Geology* 124, 141–162, <https://doi.org/10.25131/sajg.124.0019>.
- Dhuime B, Hawkesworth CJ, Cawood PA, Storey CD (2012): A change in the geodynamics of continental growth 3 billion years ago. *Science* 335, 1334–1336, <https://doi.org/10.1126/science.1216066>.
- Dhuime B, Wuestefeld A, Hawkesworth CJ (2015): Emergence of modern continental crust about 3 billion years ago. *Nature Geoscience* 8, 552–555, <https://doi.org/10.1038/ngeo2466>.
- Dhuime B, Hawkesworth CJ, Delavault H, Cawood PA (2017): Continental growth seen through the sedimentary record. *Sedimentary Geology* 357, 16–32, <https://doi.org/10.1016/j.sedgeo.2017.06.001>.
- Dick HJ, Bullen T (1984): Chromian spinel as a petrogenetic indicator in abyssal and alpine-type peridotites and spatially associated lavas. *Contributions to Mineralogy and Petrology* 86, 54–76, <https://doi.org/10.1007/BF00373711>.
- Dobrzhinetskaya LF, Wirth R, Green HW, Schreiber A, O'Bannon E (2013): First find of polycrystalline diamond in UHP metamorphic terrane of Erzgebirge, Germany. *Journal of Metamorphic Geology* 31, 5–18, <https://doi.org/10.1111/jmg.12010>.

- Dokukina KA, Kaulina TV, Konilov AN, Mints MV, Van KV, Natapov L, Belousova E, Simakin SG, Lepkhina EN (2014): Archaean to Palaeoproterozoic high-grade evolution of the Belomorian eclogite province in the Gridino area, Fennoscandian Shield: Geochronological evidence. *Gondwana Research* 25, 585–613, <https://doi.org/10.1016/j.gr.2013.02.014>.
- Duan XX, Ju YF, Chen B, Wang ZQ (2020): Garnet Geochemistry of Reduced Skarn System: Implications for Fluid Evolution and Skarn Formation of the Zhuxiling W (Mo) Deposit, China. *Minerals* 10, 1024, <https://doi.org/10.3390/min10111024>.
- Dunkl I, Frisch W, Kuhlemann J, Brügel A (2009): Pebble population dating as an additional tool for provenance studies — examples from the Eastern Alps. In: Lisker F, Ventura B, Glasmacher UA (eds), *Thermochronological Methods: From Palaeotemperature Constraints to Landscape Evolution Models*. Geological Society of London, Special Publications 324, 125–140, <https://doi.org/10.1144/SP324.10>.
- Ellis SM, Little TA, Wallace LM, Hacker BR, Buijter SJH (2011): Feedback between rifting and diapirism can exhume ultrahigh-pressure rocks. *Earth and Planetary Science Letters* 311, 427–438, <https://doi.org/10.1016/j.epsl.2011.09.031>.
- Enkelmann E, Weislogel A, Ratschbacher L, Eide E, Renno A, Wooden J (2007): How was the Triassic Songpan-Ganzi basin filled? A provenance study. *Tectonics* 26, TC4007, <https://doi.org/10.1029/2006TC002078>.
- Enkelmann E, Garver JI, Pavlis TL (2008): Rapid exhumation of ice-covered rocks of the Chugach–St. Elias orogen, Southeast Alaska. *Geology* 36, 915–918, <https://doi.org/10.1130/G2252A.1>.
- Ernst WG (2006): Preservation/exhumation of ultrahigh-pressure subduction complexes. *Lithos* 92, 321–335, <https://doi.org/10.1016/j.lithos.2006.03.049>.
- Ernst WG (2017): Earth's thermal evolution, mantle convection, and Hadean onset of plate tectonics. *Journal of Asian Earth Sciences* 145, 334–348, <https://doi.org/10.1016/j.jseaes.2017.05.037>.
- Ertl A, Marschall HR, Giester G, Henry DJ, Schertl HP, Ntaflos T, Luvizotto GL, Nasdala L, Tillmanns E (2010): Metamorphic ultrahigh-pressure tourmaline: Structure, chemistry, and correlations to P-T conditions. *American Mineralogist* 95, 1–10, <https://doi.org/10.2138/am.2010.3283>.
- Evans TP (2004): A method for calculating effective bulk composition modification due to crystal fractionation in garnet-bearing schist: implications for isopleth thermobarometry. *Journal of Metamorphic Geology* 22, 547–557, <https://doi.org/10.1111/j.1525-1314.2004.00532.x>.
- Evans DA, Pisarevsky SA (2008): Plate tectonics on early Earth? Weighing the paleomagnetic evidence. In: Condie KC, Pease V (eds), *When did plate tectonics begin on planet Earth*. GSA Special Paper 440, 249–263, [https://doi.org/10.1130/2008.2440\(12\)](https://doi.org/10.1130/2008.2440(12)).
- Evans NJ, McInnes BIA, McDonald B, Danišik M, Jourdan F, Mayers C, Thern E, Corbett D (2013): Emplacement age and thermal footprint of the diamondiferous Ellendale E9 lamproite pipe, Western Australia. *Mineralium Deposita* 48, 413–421, <https://doi.org/10.1007/s00126-012-0430-7>.
- Ewing TA, Hermann J, Rubatto D (2013): The robustness of the Zr-in-rutile and Ti-in-zircon thermometers during high-temperature metamorphism (Ivrea-Verbano Zone, northern Italy). *Contributions to Mineralogy and Petrology* 165, 757–779, [10.1007/s00410-012-0834-5](https://doi.org/10.1007/s00410-012-0834-5).
- Fabricius KE, Langdon C, Uthicke S, Humphrey C, Noonan S, De'ath G, Okazaki R, Muehllehner N, Glas MS, Lough JM (2011): Losers and winners in coral reefs acclimatized to elevated carbon dioxide concentrations. *Nature Climate Change* 1, 165–169, <https://doi.org/10.1038/nclimate1122>.
- Faryad SW, Cuthbert SJ (2020): High-temperature overprint in (U)HPM rocks exhumed from subduction zones; A product of isothermal decompression or a consequence of slab break-off (slab rollback)? *Earth-Science Reviews* 103108, <https://doi.org/10.1016/j.earscirev.2020.103108>.
- Faryad SW, Baldwin SL, Jedlicka R, Ježek J (2019): Two-stage garnet growth in coesite eclogite from the southeastern Papua New Guinea (U)HP terrane and its geodynamic significance. *Contributions to Mineralogy and Petrology* 174, 1–16, <https://doi.org/10.1007/s00410-019-1612-4>.
- Ferrero S, Angel RJ (2018): Micropetrology: are inclusions grains of truth? *Journal of Petrology* 59, 1671–1700, <https://doi.org/10.1093/petrology/egy075>.

- Ferrero S, Ziemann MA, Angel RJ, O'Brien PJ, Wunder B (2016): Kumdykolite, kokchetavite, and cristobalite crystallized in nanogranites from felsic granulites, Orlica-Snieznik Dome (Bohemian Massif): not evidence for ultrahigh-pressure conditions. *Contributions to Mineralogy and Petrology* 171, 3, <https://doi.org/10.1007/s00410-015-1220-x>.
- Ferrero S, O'Brien PJ, Borghini A, Wunder B, Wälle M, Günter C, Ziemann MA (2019): A treasure chest full of nanogranitoids: an archive to investigate crustal melting in the Bohemian Massif. In: Ferrero S, Lanari P, Goncalves P, Grosch EG (eds), *Metamorphic Geology: Microscale to Mountain Belts*. Geological Society of London, Special Publications 478, 13–38, <https://doi.org/10.1144/SP478.19>.
- Ferrière L, Osinski GR (2012): Shock metamorphism. In: Osinski GR, Pierazzo E (eds), *Impact Cratering: Processes and Products*. John Wiley & Sons, 106–124.
- Ferry JT, Spear FS (1978): Experimental calibration of the partitioning of Fe and Mg between biotite and garnet. *Contributions to Mineralogy and Petrology* 66, 113–117.
- Ferry JM, Watson EB (2007): New thermodynamic models and revised calibrations for the Ti-in-zircon and Zr-in-rutile thermometers. *Contributions to Mineralogy and Petrology* 154, 429–437, <https://doi.org/10.1007/s00410-007-0201-0>.
- Field M, Stiefenhofer J, Robey J, Kurszlaukis S (2008): Kimberlite-hosted diamond deposits of southern Africa: a review. *Ore Geology Reviews* 34, 33–75, <https://doi.org/10.1016/j.oregeorev.2007.11.002>.
- Force ER (1980): The provenance of rutile. *Journal of Sedimentary Research* 50, 485–488, <https://doi.org/10.1306/212F7A31-2B24-11D7-8648000102C1865D>.
- Fornelli A, Langone A, Micheletti F, Pascazio A, Piccarreta G (2014): The role of trace element partitioning between garnet, zircon and orthopyroxene on the interpretation of zircon U–Pb ages: an example from high-grade basement in Calabria (Southern Italy). *International Journal of Earth Sciences* 103, 487–507, <https://doi.org/10.1007/s00531-013-0971-8>.
- Forsyth D, Uyeda S (1975): On the relative importance of the driving forces of plate motion. *Geophysical Journal International* 43, 163–200, <https://doi.org/10.1111/j.1365-246X.1975.tb00631.x>.
- François C, Debaille V, Paquette JL, Baudet D, Javaux EJ (2018): The earliest evidence for modern-style plate tectonics recorded by HP–LT metamorphism in the Paleoproterozoic of the Democratic Republic of the Congo. *Scientific Reports* 8, 15452, <https://doi.org/10.1038/s41598-018-33823-y>.
- Frei D, Gerdes A (2009): Precise and accurate in situ U–Pb dating of zircon with high sample throughput by automated LA-SF-ICP-MS. *Chemical Geology* 261, 261–270, <https://doi.org/10.1016/j.chemgeo.2008.07.025>.
- French BM, Koeberl C (2010): The convincing identification of terrestrial meteorite impact structures: What works, what doesn't, and why. *Earth-Science Reviews* 98, 123–170, <https://doi.org/10.1016/j.earscirev.2009.10.009>.
- Furnes H, Dilek YD, de Wit M (2015): Precambrian greenstone sequences represent different ophiolite types. *Gondwana Research* 27, 649–685, <https://doi.org/10.1016/j.gr.2013.06.004>.
- Galvez ME, Pubellier M (2019): How do subduction zones regulate the carbon cycle? In: Orcutt BN, Daniel I, Dasgupta R (eds), *Deep carbon: Past to present*. Cambridge University Press, 276–312, <https://doi.org/10.1017/9781108677950>.
- Ganguly J (1979): Garnet and clinopyroxene solid solutions, and geothermometry based on Fe-Mg distribution coefficient. *Geochimica et Cosmochimica Acta* 43, 1021–1029, [https://doi.org/10.1016/0016-7037\(79\)90091-7](https://doi.org/10.1016/0016-7037(79)90091-7).
- Ganne J, Feng X (2017): Primary magmas and mantle temperatures through time. *Geochemistry, Geophysics, Geosystems* 18, 872–888, <https://doi.org/10.1002/2016GC006787>.
- Ganne J, De Andrade V, Weinberg RF, Vidal O, Dubacq B, Kagambega N, Naba S, Baratoux L, Jessell M, Allibon J (2012): Modern-style plate subduction preserved in the Palaeoproterozoic West African craton. *Nature Geoscience* 5, 60–65, <https://doi.org/10.1038/ngeo1321>.

- Garzanti E, Andò S, Vezzoli G (2009): Grain-size dependence of sediment composition and environmental bias in provenance studies. *Earth and Planetary Science Letters* 277, 422–432, <https://doi.org/10.1016/j.epsl.2008.11.007>.
- Gauthiez-Putallaz L, Rubatto D, Hermann J (2016): Dating prograde fluid pulses during subduction by in situ U–Pb and oxygen isotope analysis. *Contributions to Mineralogy and Petrology* 171, 15, <https://doi.org/10.1007/s00410-015-1226-4>.
- Gebauer D, Schertl HP, Brix M, Schreyer W (1997): 35 Ma old ultrahigh-pressure metamorphism and evidence for very rapid exhumation in the Dora Maira Massif, Western Alps. *Lithos* 41, 5–24, [https://doi.org/10.1016/S0024-4937\(97\)82002-6](https://doi.org/10.1016/S0024-4937(97)82002-6).
- Gerya TV, Stern RJ, Baes M, Sobolev SV, Whattam SA (2015): Plate tectonics on the Earth triggered by plume-induced subduction initiation. *Nature* 527, 221–225, <https://doi.org/10.1038/nature15752>.
- Ghent ED (1976): Plagioclase–garnet–Al₂SiO₅–quartz: a potential geobarometer–geothermometer. *American Mineralogist* 61, 710–714.
- Gilotti JA, Ravna EJK (2002): First evidence for ultrahigh-pressure metamorphism in the North-East Greenland Caledonides. *Geology* 30, 551–554, [https://doi.org/10.1130/0091-7613\(2002\)030<0551:FEFUPM>2.0.CO;2](https://doi.org/10.1130/0091-7613(2002)030<0551:FEFUPM>2.0.CO;2).
- Giuntoli F, Lanari P, Engi M (2018): Deeply subducted continental fragments: I. Fracturing, dissolution-precipitation and diffusion processes recorded by garnet textures of the central Sesia Zone (Western Italian Alps). *Solid Earth* 9, 167–189, <https://doi.org/10.5194/se-2017-87>.
- Glassley WE, Korstgård JA, Sørensen K, Platou SW (2014): A new UHP metamorphic complex in the ~1.8 Ga Nagssugtoqidian Orogen of West Greenland. *American Mineralogist* 99, 1315–1334, <https://doi.org/10.2138/am.2014.4726>.
- Gonzalez JP, Thomas JB, Baldwin SL, Alvaro M (2019): Quartz-in-garnet and Ti-in-quartz thermobarometry: Methodology and first application to a quartzofeldspathic gneiss from eastern Papua New Guinea. *Journal of Metamorphic Geology* 37, 1193–1208, <https://doi.org/10.1111/jmg.12508>.
- Gonzalez JP, Mazzucchelli ML, Angel RJ, Alvaro M (2021): Elastic Geobarometry for Anisotropic Inclusions in Anisotropic Host Minerals: Quartz-in-Zircon. *Journal of Geophysical Research: Solid Earth* 126, 2021JB022080, <https://doi.org/10.1029/2021JB022080>.
- Goodwin AM (1996): Principles of Precambrian geology. Academic Press London, pp. 327.
- Gordon SM, Little TA, Hacker BR, Bowring SA, Korchinski M, Baldwin SL, Kylander-Clark ARC (2012): Multi-stage exhumation of young UHP–HP rocks: Timescales of melt crystallization in the D’Entrecasteaux Islands, southeastern Papua New Guinea. *Earth and Planetary Science Letters* 351–352, 237–246, <https://doi.org/10.1016/j.epsl.2012.07.014>.
- Gose J, Schmädicke E (2018): Water incorporation in garnet: Coesite versus quartz eclogite from Erzgebirge and Fichtelgebirge. *Journal of Petrology* 59, 207–232, <https://doi.org/10.1093/petrology/egy022>.
- Greber ND, Dauphas N, Bekker A, Ptáček MP, Bindeman IN, Hofmann A (2017): Titanium isotopic evidence for felsic crust and plate tectonics 3.5 billion years ago. *Science* 357, 1271–1274, <https://doi.org/10.1126/science.aan8086>.
- Green TH (1977): Garnet in silicic liquids and its possible use as a PT indicator. *Contributions to Mineralogy and Petrology* 65, 59–67.
- Grimes CB, Wooden JL, Cheadle MJ, John BE (2015): “Fingerprinting” tectono-magmatic provenance using trace elements in igneous zircon. *Contributions to Mineralogy and Petrology* 170, 1–26, <https://doi.org/10.1007/s00410-015-1199-3>.
- Grimmer JC, Ratschbacher L, McWilliams M, Franz L, Gaitzsch I, Tichomirowa M, Hacker BR, Zhang Y (2003): When did the ultrahigh-pressure rocks reach the surface? A ²⁰⁷Pb/²⁰⁶Pb zircon, ⁴⁰Ar/³⁹Ar white mica, Si-in-white mica, single-grain provenance study of Dabie Shan synorogenic foreland sediments. *Chemical Geology* 197, 87–110, [https://doi.org/10.1016/S0009-2541\(02\)00321-2](https://doi.org/10.1016/S0009-2541(02)00321-2).

- Grütter HS, Gurney JJ, Menzies AH, Winter F (2004): An updated classification scheme for mantle-derived garnet, for use by diamond explorers. *Lithos* 77, 841–857, <https://doi.org/10.1016/j.lithos.2004.04.012>.
- Guo R, Hu X, Garzanti E, Lai W (2021): Boron isotope composition of detrital tourmaline: A new tool in provenance analysis. *Lithos* 400, 106360, <https://doi.org/10.1016/j.lithos.2021.106360>.
- Gurney JJ, Zweistra P (1995): The interpretation of the major element compositions of mantle minerals in diamond exploration. *Journal of Geochemical Exploration* 53, 293–309, [https://doi.org/10.1016/0375-6742\(94\)00021-3](https://doi.org/10.1016/0375-6742(94)00021-3).
- Gurnis M, Hall C, Lavier L (2004): Evolving force balance during incipient subduction. *Geochemistry, Geophysics, Geosystems* 5, Q07001, <https://doi.org/10.1029/2003GC000681>.
- Hacker BR, Ratschbacher L, Webb L, Ireland T, Walker D, Shuwen D (1998): U/Pb zircon ages constrain the architecture of the ultrahigh-pressure Qinling–Dabie Orogen, China. *Earth and Planetary Science Letters* 161, 215–230, [https://doi.org/10.1016/S0012-821X\(98\)00152-6](https://doi.org/10.1016/S0012-821X(98)00152-6).
- Hamilton WB (2011): Plate tectonics began in Neoproterozoic time, and plumes from deep mantle have never operated. *Lithos* 123, 1–20, <https://doi.org/10.1016/j.lithos.2010.12.007>.
- Hamilton NE, Ferry M (2018): ggtern: Ternary diagrams using ggplot2. *Journal of Statistical Software* 87, 1–17, <https://doi.org/10.18637/jss.v087.c03>.
- Han S, Li M, Ren Q (2019): Discriminating among tectonic settings of spinel based on multiple machine learning algorithms. *Big Earth Data* 3, 67–82, <https://doi.org/10.1080/20964471.2019.1586074>.
- Hardman MF, Pearson DG, Stachel T, Sweeney RJ (2018): Statistical approaches to the discrimination of crust- and mantle-derived low-Cr garnet–major-element-based methods and their application in diamond exploration. *Journal of Geochemical Exploration* 186, 24–35, <https://doi.org/10.1016/j.gexplo.2017.11.012>.
- Harley SL, Kelly NM, Möller A (2007): Zircon behaviour and the thermal histories of mountain chains. *Elements* 3, 25–30, <https://doi.org/10.2113/gselements.3.1.25>.
- Harlow GE, Tsujimori T, Sorensen SS (2015): Jadeitites and plate tectonics. *Annual Review of Earth and Planetary Sciences* 43, 105–138, <https://doi.org/10.1146/annurev-earth-060614-105215>.
- Harrison TM, Ryerson FJ, Le Fort P, Yin A, Lovera OM, Catlos EJ (1997): A late Miocene-Pliocene origin for the central Himalayan inverted metamorphism. *Earth and Planetary Science Letters* 146, E1–E7, [https://doi.org/10.1016/S0012-821X\(96\)00215-4](https://doi.org/10.1016/S0012-821X(96)00215-4).
- Hart E, Storey C, Bruand E, Schertl HP, Alexander BD (2016): Mineral inclusions in rutile: A novel recorder of HP-UHP metamorphism. *Earth and Planetary Science Letters* 446, 137–148, <https://doi.org/10.1016/j.epsl.2016.04.035>.
- Hart E, Storey C, Harley SL, Fowler M (2018): A window into the lower crust: Trace element systematics and the occurrence of inclusions/intergrowths in granulite-facies rutile. *Gondwana Research* 59, 76–86, <https://doi.org/10.1016/j.gr.2018.02.021>.
- Hawkesworth CJ, Dhuime B, Pietranik AB, Cawood PA, Kemp AI, Storey CD (2010): The generation and evolution of the continental crust. *Journal of the Geological Society* 167, 229–248, <https://doi.org/10.1144/0016-76492009-072>.
- Hawkesworth C, Cawood PA, Dhuime B (2013): Continental growth and the crustal record. *Tectonophysics* 609, 651–660, <https://doi.org/10.1016/j.tecto.2013.08.013>.
- Hawkesworth CJ, Cawood PA, Dhuime B (2016): Tectonics and crustal evolution. *GSA Today* 26, 4–11, <https://doi.org/10.1130/GSATG272A.1>.
- Hawkesworth CJ, Cawood PA, Dhuime B, Kemp TI (2017): Earth's continental lithosphere through time. *Annual Review of Earth and Planetary Sciences* 45, 169–198, <https://doi.org/10.1146/annurev-earth-063016-020525>.
- Henry DJ, Guidotti CV (1985): Tourmaline as a petrogenetic indicator mineral: an example from the staurolite-grade metapelites of NW Maine. *American Mineralogist* 70, 1–15.

- Hermann J, Rubatto D (2014): Subduction of continental crust to mantle depth: geochemistry of ultrahigh-pressure rocks. In: Holland HD, Turekian KK (eds), *Treatise on Geochemistry* (2nd Edition) 4, 309–340, <https://doi.org/10.1016/B978-0-08-095975-7.00309-0>.
- Hermann J, Rubatto D, Korsakov A, Shatsky VS (2001): Multiple zircon growth during fast exhumation of diamondiferous, deeply subducted continental crust (Kokchetav Massif, Kazakhstan). *Contribution to Mineralogy and Petrology* 141, 66–82, <https://doi.org/10.1007/s004100000218>.
- Hermann J, Spandler C, Hack A, Korsakov AV (2006): Aqueous fluids and hydrous melts in high-pressure and ultra-high pressure rocks: Implications for element transfer in subduction zones. *Lithos* 92, 399–417, <https://doi.org/10.1016/j.lithos.2006.03.055>.
- Hernández-Uribe D, Palin RM (2019): A revised petrological model for subducted oceanic crust: Insights from phase equilibrium modelling. *Journal of Metamorphic Geology* 37, 745–768, <https://doi.org/10.1111/jmg.12483>.
- Hill EJ (1994): Geometry and kinematics of shear zones formed during continental extension in eastern Papua New Guinea. *Journal of Structural Geology* 16, 1093–1105, [https://doi.org/10.1016/0191-8141\(94\)90054-X](https://doi.org/10.1016/0191-8141(94)90054-X).
- Hokada T, Harley SL (2004): Zircon growth in UHT leucosome: constraints from zircon-garnet rare earth elements (REE) relations in Napier Complex, East Antarctica. *Journal of Mineralogical and Petrological Sciences* 99, 180–190, <https://doi.org/10.2465/jmps.99.180>.
- Holder RM, Viete DR, Brown M, Johnson TE (2019): Metamorphism and the evolution of plate tectonics. *Nature* 572, 378–381, <https://doi.org/10.1038/s41586-019-1462-2>.
- Holland TJ (1980): The reaction albite = jadeite + quartz determined experimentally in the range 600–1200°C. *American Mineralogist* 65, 129–134.
- Hong D, Jian X, Fu L, Zhang W (2020): Garnet trace element geochemistry as a sediment provenance indicator: An example from the Qaidam basin, northern Tibet. *Marine and Petroleum Geology* 116, 104316, <https://doi.org/10.1016/j.marpetgeo.2020.104316>.
- Hopkins M, Harrison TM, Manning CE (2008): Low heat flow inferred from >4 Gyr zircons suggests Hadean plate boundary interactions. *Nature* 456, 493–496, <https://doi.org/10.1038/nature07465>.
- Hopkins MD, Harrison TM, Manning CE (2010): Constraints on Hadean geodynamics from mineral inclusions in >4 Ga zircons. *Earth and Planetary Science Letters* 298, 367–376, <https://doi.org/10.1016/j.epsl.2010.08.010>.
- Hoschek G (2007): Metamorphic peak conditions of eclogites in the Tauern Window, Eastern Alps, Austria: Thermobarometry of the assemblage garnet + omphacite + phengite + kyanite + quartz. *Lithos* 93, 1–16, <https://doi.org/10.1016/j.lithos.2006.03.042>.
- Hoskin PW, Ireland TR (2000): Rare earth element chemistry of zircon and its use as a provenance indicator. *Geology* 28, 627–630, [https://doi.org/10.1130/0091-7613\(2000\)28<627:REECOZ>2.0.CO;2](https://doi.org/10.1130/0091-7613(2000)28<627:REECOZ>2.0.CO;2).
- Howell D, Wood IG, Dobson DP, Jones AP, Nasdala L, Harris JW (2010): Quantifying strain birefringence halos around inclusions in diamond. *Contributions to Mineralogy and Petrology* 160, 705–717, <https://doi.org/10.1007/s00410-010-0503-5>.
- Hubert JF (1962): A zircon-tourmaline-rutile maturity index and the interdependence of the composition of heavy mineral assemblages with the gross composition and texture of sandstones. *Journal of Sedimentary Research* 32, 440–450, <https://doi.org/10.1306/74D70CE5-2B21-11D7-8648000102C1865D>.
- Huggins FE, Virgo D, Huckenholz HG (1977): Titanium-containing silicate garnet; I, The distribution of Al, Fe³⁺, and Ti⁴⁺ between octahedral and tetrahedral sites. *American Mineralogist* 62, 475–490.
- Hülscher J, Bahlburg H, Pfänder J (2018): New geochemical results indicate a non-alpine provenance for the Alpine Spectrum (epidote, garnet, hornblende) in quaternary Upper Rhine sediment. *Sedimentary Geology* 375, 134–144, <https://doi.org/10.1016/j.sedgeo.2018.02.010>.

- Hwang SL, Shen P, Chu HT, Yui TF, Liou JG, Sobolev NV, Zhang RY, Shatsky VS, Zayachkovsky AA (2004): Kokchetavite: a new potassium-feldspar polymorph from the Kokchetav ultrahigh-pressure terrane. *Contributions to Mineralogy and Petrology* 148, 380–389, <https://doi.org/10.1007/s00410-004-0610-2>.
- Hwang SL, Shen P, Chu HT, Yui TF, Liou JG, Sobolev NV (2009): Kumdykolite, an orthorhombic polymorph of albite, from the Kokchetav ultrahigh-pressure massif, Kazakhstan. *European Journal of Mineralogy* 21, 1325–1334, <https://doi.org/10.1127/0935-1221/2009/0021-1970>.
- Ibañez-Mejia M, Pullen A, Pepper M, Urbani F, Ghoshal G, Ibañez-Mejia JC (2018): Use and abuse of detrital zircon U-Pb geochronology — A case from the Río Orinoco delta, eastern Venezuela. *Geology* 46, 1019–1022, <https://doi.org/10.1130/G45596.1>.
- Im H, Jeong JY, Shin D (2020): Genetic environment of W skarn and Pb-Zn vein mineralization associated with the Imog granite in the Taebaeksan Mineralized District, South Korea. *Ore Geology Reviews* 126, 103721, <https://doi.org/10.1016/j.oregeorev.2020.103721>.
- Ireland TR, Williams IS (2003): Considerations in zircon geochronology by SIMS. *Reviews in Mineralogy and Geochemistry* 53, 215–241, <https://doi.org/10.2113/0530215>.
- Irvine TN (1967): Chromian spinel as a petrogenetic indicator: Part 2. Petrologic applications. *Canadian Journal of Earth Sciences* 4, 71–103.
- Itano K, Ueki K, Iizuka T, Kuwatani T (2020): Geochemical discrimination of monazite source rock based on machine learning techniques and multinomial logistic regression analysis. *Geosciences* 10, 63, <https://doi.org/10.3390/geosciences10020063>.
- Jahn BM, Cabry R, Monie P (2001): The oldest UHP eclogites of the World: age of UHP metamorphism, nature of protoliths and tectonic implications. *Chemical Geology* 178, 143–158, [https://doi.org/10.1016/S0009-2541\(01\)00264-9](https://doi.org/10.1016/S0009-2541(01)00264-9).
- Jicha BR, Jagoutz O (2015): Magma production rates for intraoceanic arcs. *Elements* 11, 105–111, <https://doi.org/10.2113/gselements.11.2.105>.
- John T, Schenk V (2003): Partial eclogitisation of gabbroic rocks in a late Precambrian subduction zone (Zambia): prograde metamorphism triggered by fluid infiltration. *Contributions to Mineralogy and Petrology* 146, 174–191, <https://doi.org/10.1007/s00410-003-0492-8>.
- Keller B, Schoene B (2018): Plate tectonics and continental basaltic geochemistry throughout Earth history. *Earth and Planetary Science Letters* 481, 290–304, <https://doi.org/10.1016/j.epsl.2017.10.031>.
- Kellett DA, Weller OM, Zagorevski A, Regis D (2018): A petrochronological approach for the detrital record: Tracking mm-sized eclogite clasts in the northern Canadian Cordillera. *Earth and Planetary Science Letters* 494, 23–31, <https://doi.org/10.1016/j.epsl.2018.04.036>.
- Kelly NM, Harley SL (2005): An integrated microtextural and chemical approach to zircon geochronology: refining the Archaean history of the Napier Complex, east Antarctica. *Contributions to Mineralogy and Petrology* 149, 57–84, <https://doi.org/10.1007/s00410-004-0635-6>.
- Kitahara S, Kennedy GC (1964): The quartz-coesite transition. *Journal of Geophysical Research* 69, 5395–5400, <https://doi.org/10.1029/JZ069i024p05395>.
- Klemme S, Ivanić TJ, Connolly JAD, Harte B (2009): Thermodynamic modelling of Cr-bearing garnets with implications for diamond inclusions and peridotite xenoliths. *Lithos* 112, 986–991, <https://doi.org/10.1016/j.lithos.2009.05.007>.
- Klonowska I, Janák M, Majka J, Petrik I, Froitzheim N, Gee DG, Sasinková V (2017): Microdiamond on Åreskutan confirms regional UHP metamorphism in the Seve Nappe Complex of the Scandinavian Caledonides. *Journal of Metamorphic Geology* 35, 541–564, <https://doi.org/10.1111/jmg.12244>.
- Kohn MJ (2020): A refined zirconium-in-rutile thermometer. *American Mineralogist* 105, 963–971, <https://doi.org/10.2138/am-2020-7091>.
- Kohn MJ, Corrie SL, Markley C (2015): The fall and rise of metamorphic zircon. *American Mineralogist* 100, 897–908, <https://doi.org/10.2138/am-2015-5064>.

- Kohn B, Chung L, Gleadow A (2019): Fission-track analysis: field collection, sample preparation and data acquisition. In: Malusà MG, Fitzgerald PG (eds), *Fission-Track Thermochronology and its Application to Geology*, Springer, Cham, 25–48, https://doi.org/10.1007/978-3-319-89421-8_2.
- Kolb J (2014): Structure of the Palaeoproterozoic Nagssugtoqidian Orogen, South-East Greenland: model for the tectonic evolution. *Precambrian Research* 255, 809–822, <https://doi.org/10.1016/j.precamres.2013.12.015>.
- Komiya T, Maruyama S, Masuda T, Nohda S, Hayashi M, Okamoto K (1999): Plate tectonics at 3.8–3.7 Ga: Field evidence from the Isua accretionary complex, southern West Greenland. *The Journal of Geology* 107, 515–554.
- Kooijman E, Mezger K, Berndt J (2010): Constraints on the U–Pb systematics of metamorphic rutile from in situ LA-ICP-MS analysis. *Earth and Planetary Science Letters* 293, 321–330, <https://doi.org/10.1016/j.epsl.2010.02.047>.
- Korenaga J (2013): Initiation and evolution of plate tectonics on Earth: theories and observations. *Annual Review of Earth and Planetary Sciences* 41, 117–151, <https://doi.org/10.1146/annurev-earth-050212-124208>.
- Korhonen FJ, Clark C, Brown M, Bhattacharya S, Taylor R (2013): How long-lived is ultrahigh temperature (UHT) metamorphism? Constraints from zircon and monazite geochronology in the Eastern Ghats orogenic belt, India. *Precambrian Research* 234, 322–350, <https://doi.org/10.1016/j.precamres.2012.12.001>.
- Korsakov AV, Hutsebaut D, Theunissen K, Vandenaabeele P, Stepanov AS (2007): Raman mapping of coesite inclusions in garnet from the Kokchetav Massif (Northern Kazakhstan). *Spectrochimica Acta Part A: Molecular and Biomolecular Spectroscopy* 68, 1046–1052, <https://doi.org/10.1016/j.saa.2007.04.005>.
- Kossmat F, Rheinisch R (1931): *Geologische Karte von Sachsen Nr. 116, Blatt Lengefeld*. Leipzig: Giesecke & Devrient.
- Kotková J, O'Brien PJ, Ziemann MA (2011): Diamond and coesite discovered in Saxony-type granulite: Solution to the Variscan garnet peridotite enigma. *Geology* 39, 667–670, <https://doi.org/10.1130/G31971.1>.
- Kotková J, Škoda R, Machovič V (2014): Kumdykolite from the ultrahigh-pressure granulite of the Bohemian Massif. *American Mineralogist* 99, 1798–1801, <https://doi.org/10.2138/am.2014.4889>.
- Koziol AM, Newton RC (1988): Redetermination of the anorthite breakdown reaction and improvement of the plagioclase–garnet–Al₂SiO₅–quartz geobarometer. *American Mineralogist* 73, 216–223.
- Krippner A, Bahlburg H (2013): Provenance of Pleistocene Rhine River Middle Terrace sands between the Swiss–German border and Cologne based on U–Pb detrital zircon ages. *International Journal of Earth Sciences* 102, 917–932, <https://doi.org/10.1007/s00531-012-0842-8>.
- Krippner A, Meinhold G, Morton AC, von Eynatten H (2014): Evaluation of garnet discrimination diagrams using geochemical data of garnets derived from various host rocks. *Sedimentary Geology* 306, 36–52, <https://doi.org/10.1016/j.sedgeo.2014.03.004>.
- Krippner A, Meinhold G, Morton AC, Russell E, von Eynatten H (2015): Grain-size dependence of garnet composition revealed by provenance signatures of modern stream sediments from the western Hohe Tauern (Austria). *Sedimentary Geology* 321, 25–38, <https://doi.org/10.1016/j.sedgeo.2015.03.002>.
- Krippner A, Meinhold G, Morton AC, Schöning J, von Eynatten H (2016): Heavy minerals and garnet geochemistry of stream sediments and bedrocks from the Almklovdalen area, Western Gneiss Region, SW Norway: Implications for provenance analysis. *Sedimentary Geology* 336, 96–105, <https://doi.org/10.1016/j.sedgeo.2015.09.009>.
- Krishnamurti D (1954): The Raman spectrum of diamond: *Proceedings of the Indian Academy of Sciences-Section A* 40, 211–216.
- Kroner U, Romer RL (2013): Two plates — Many subduction zones: The Variscan orogeny reconsidered. *Gondwana Research* 24, 298–329, <https://doi.org/10.1016/j.gr.2013.03.001>.

- Kröner A, Willner AP (1998): Time of formation and peak of Variscan HP–HT metamorphism of quartz-feldspar rocks in the central Erzgebirge, Saxony, Germany. *Contributions to Mineralogy and Petrology* 132, 1–20, <https://doi.org/10.1007/s004100050401>.
- Kröner A, Willner AP, Hegner E, Frischbutter A, Hofmann J, Bergner R (1995): Latest Precambrian (Cadomian) zircon ages, Nd isotopic systematics and PT evolution of granitoid orthogneisses of the Erzgebirge, Saxony and Czech Republic. *Geologische Rundschau* 84, 437–456.
- Kruger FJ, Kamber BS, Harris PD (1998): Isotopic peculiarities of an Archaean pegmatite (Union Mine, Mica, South Africa): Geochemical and geochronological implications. *Precambrian Research* 91, 253–267, [https://doi.org/10.1016/S0301-9268\(98\)00052-7](https://doi.org/10.1016/S0301-9268(98)00052-7).
- Kueter N, Soesilo J, Fedortchouk Y, Nestola F, Belluco L, Troch J, Wälle M, Guillong M, von Quadt A, Driesner T (2016): Tracing the depositional history of Kalimantan diamonds by zircon provenance and diamond morphology studies. *Lithos* 265, 159–176, <https://doi.org/10.1016/j.lithos.2016.05.003>.
- Kusky TM (1998): Tectonic setting and terrane accretion of the Archean Zimbabwe craton. *Geology* 26, 163–166, [https://doi.org/10.1130/0091-7613\(1998\)026<0163:TSATAO>2.3.CO;2](https://doi.org/10.1130/0091-7613(1998)026<0163:TSATAO>2.3.CO;2).
- Kusky T, Wang J, Wang L, Huang B, Ning W, Fu D, Peng H, Deng H, Polat A, Zhong Y, Shi G (2020): Mélanges through time: Life cycle of the world's largest Archean mélange compared with Mesozoic and Paleozoic subduction-accretion-collision mélanges. *Earth-Science Reviews* 209, 103303, <https://doi.org/10.1016/j.earscirev.2020.103303>.
- Kylander-Clark AR, Hacker BR, Mattinson CG (2012): Size and exhumation rate of ultrahigh-pressure terranes linked to orogenic stage. *Earth and Planetary Science Letters* 321, 115–120, <https://doi.org/10.1016/j.epsl.2011.12.036>.
- Kylander-Clark AR, Hacker BR, Cottle JM (2013): Laser-ablation split-stream ICP petrochronology. *Chemical Geology* 345, 99–112, <https://doi.org/10.1016/j.chemgeo.2013.02.019>.
- Lafuente B, Downs RT, Yang H, Stone N (2015): The power of databases: The RRUFF project. In: Armbruster T, Danisi RM (eds), *Highlights in Mineralogical Crystallography*. Berlin, De Gruyter, 1–30.
- Lanari P, Engi M (2017): Local bulk composition effects on metamorphic mineral assemblages. *Reviews in Mineralogy and Geochemistry* 83, 55–102, <https://doi.org/10.2138/rmg.2017.83.3>.
- Lanari P, Giuntoli F, Loury C, Burn M, Engi M (2017): An inverse modelling approach to obtain P–T conditions of metamorphic stages involving garnet growth and resorption. *European Journal of Mineralogy* 29, 181–199, <https://doi.org/10.1127/ejm/2017/0029-2597>.
- Lang HM, Gilotti JA (2015): Modeling the exhumation path of partially melted ultrahigh-pressure metapelites, North-East Greenland Caledonides. *Lithos* 226, 131–146, <https://doi.org/10.1016/j.lithos.2014.10.010>.
- Lathe C, Koch-Müller M, Wirth R, van Westrenen W, Mueller HJ, Schilling F, Lauterjung J (2005): The influence of OH in coesite on the kinetics of the coesite-quartz phase transition. *American Mineralogist* 90, 36–43, <https://doi.org/10.2138/am.2005.1662>.
- Lawrence RL, Cox R, Mapes RW, Coleman DS (2011): Hydrodynamic fractionation of zircon age populations. *GSA Bulletin* 123, 295–305, <https://doi.org/10.1130/B30151.1>.
- Li R, Wan Y, Cheng Z, Zhou J, Li S, Jin F, Meng Q, Li Z, Jiang M (2005): Provenance of Jurassic sediments in the Hefei Basin, east-central China and the contribution of high-pressure and ultrahigh-pressure metamorphic rocks from the Dabie Shan. *Earth and Planetary Science Letters* 231, 279–294, <https://doi.org/10.1016/j.epsl.2004.12.021>.
- Li C, Arndt NT, Tang Q, Ripley EM (2015): Trace element indiscriminability diagrams. *Lithos* 232, 76–83, <https://doi.org/10.1016/j.lithos.2015.06.022>.
- Li X, Liu L, Liao X, Gai Y, Ma T, Geng G, Li T (2021): Metamorphic evolution of mafic granulites in the Kuruksayi area of the South Altyn Orogen, West China: Insights from petrography, phase equilibria modelling and geochronology. *Journal of Asian Earth Sciences* 213, 104766, <https://doi.org/10.1016/j.jseaes.2021.104766>.

- Liao J, Malusà MG, Zhao L, Baldwin SL, Fitzgerald PG, Gerya T (2018): Divergent plate motion drives rapid exhumation of (ultra)high pressure rocks. *Earth and Planetary Science Letters* 491, 67–80, <https://doi.org/10.1016/j.epsl.2018.03.024>.
- Liati A, Gebauer D (2009): Crustal origin of zircon in a garnet peridotite: a study of U-Pb SHRIMP dating, mineral inclusions and REE geochemistry (Erzgebirge, Bohemian Massif). *European Journal of Mineralogy* 21, 737–750, <https://doi.org/10.1127/0935-1221/2009/0021-1939>.
- Liaw A, Wiener M (2002): Classification and Regression by randomForest. *R News* 2, 18–22.
- Linnemann U, Herbolch A, Liégeois JP, Pin C, Gärtner A, Hofmann M (2012): The Cambrian to Devonian odyssey of the Brabant Massif within Avalonia: A review with new zircon ages, geochemistry, Sm–Nd isotopes, stratigraphy and palaeogeography. *Earth-Science Reviews* 112, 126–154, <https://doi.org/10.1016/j.earscirev.2012.02.007>.
- Liou JG, Zhang RY (1996): Occurrences of intergranular coesite in ultrahigh-P rocks from the Sulu region, eastern China: Implications for lack of fluid during exhumation. *American Mineralogist* 81, 1217–1221, <https://doi.org/10.2138/am-1996-9-1020>.
- Liou JG, Ernst WG, Zhang RY, Tsujimori T, Jahn BM (2009): Ultrahigh-pressure minerals and metamorphic terranes – the view from China. *Journal of Asian Earth Sciences* 35, 199–231, <https://doi.org/10.1016/j.jseaes.2008.10.012>.
- Little TA, Baldwin SL, Fitzgerald PG, Monteleone BD (2007): Continental rifting and metamorphic core complex formation ahead of the Woodlark spreading ridge, D'Entrecasteaux Islands, Papua New Guinea. *Tectonics* 26, TC1002, <https://doi.org/10.1029/2005TC001911>.
- Liu F, Gerdes A, Zeng L, Xue H (2008): SHRIMP U–Pb dating, trace elements and the Lu–Hf isotope system of coesite-bearing zircon from amphibolite in the SW Sulu UHP terrane, eastern China. *Geochimica et Cosmochimica Acta* 72, 2973–3000, <https://doi.org/10.1016/j.gca.2008.04.007>.
- Liu P, Massonne HJ, Zhang J, Wu Y, Jin Z (2017): Intergranular coesite and coesite inclusions in dolomite from the Dabie Shan: Constraints on the preservation of coesite in UHP rocks. *Terra Nova* 29, 154–161, <https://doi.org/10.1111/ter.12258>.
- Lubnina NV, Pisarevsky SA, Stepanova AV, Bogdanova SV, Sokolov SJ (2017): Fennoscandia before Nuna/Columbia: Paleomagnetism of 1.98–1.96 Ga mafic rocks of the Karelian craton and paleogeographic implications. *Precambrian Research* 292, 1–12, <https://doi.org/10.1016/j.precamres.2017.01.011>.
- Lünsdorf NK, Lünsdorf JO (2016): Evaluating Raman spectra of carbonaceous matter by automated, iterative curve-fitting. *International Journal of Coal Geology* 160, 51–62, <https://doi.org/10.1016/j.coal.2016.04.008>.
- Lünsdorf NK, Dunkl I, Schmidt BC, Rantitsch G, von Eynatten H (2017): Towards a higher comparability of geothermometric data obtained by Raman spectroscopy of carbonaceous material. Part 2: a revised geothermometer. *Geostandards and Geoanalytical Research* 41, 593–612, <https://doi.org/10.1111/ggr.12178>.
- Luvizotto GL, Zack T (2009): Nb and Zr behavior in rutile during high-grade metamorphism and retrogression: an example from the Ivrea–Verbano Zone. *Chemical Geology* 261, 303–317, <https://doi.org/10.1016/j.chemgeo.2008.07.023>.
- Luvizotto GL, Zack T, Triebold S, von Eynatten H (2009): Rutile occurrence and trace element behavior in medium-grade metasedimentary rocks: example from the Erzgebirge, Germany. *Mineralogy and Petrology* 97, 233–249, [10.1007/s00710-009-0092-z](https://doi.org/10.1007/s00710-009-0092-z).
- MacGregor ID, Manton WI (1986): Roberts Victor eclogites: ancient oceanic crust. *Journal of Geophysical Research: Solid Earth* 91, 14063–14079, <https://doi.org/10.1029/JB091iB14p14063>.
- Malusà MG, Faccenna C, Baldwin SL, Fitzgerald PG, Rossetti F, Balestrieri ML, Danišik M, Ellero A, Ottria G, Piromallo C (2015): Contrasting styles of (U)HP rock exhumation along the Cenozoic Adria-Europe plate boundary (Western Alps, Calabria, Corsica). *Geochemistry, Geophysics, Geosystems* 16, 1786–1824, <https://doi.org/10.1002/2015GC005767>.

- Maneiro KA (2016): Development of a detrital garnet geochronometer and the search for Earth's oldest garnet. Doctoral dissertation, Boston University, pp. 353.
- Maneiro KA, Baxter EF, Samson SD, Marschall HR, Hietpas J (2019): Detrital garnet geochronology: Application in tributaries of the French Broad River, Southern Appalachian Mountains, USA. *Geology* 47, 1189–1192, <https://doi.org/10.1130/G46840.1>.
- Mange MA, Morton AC (2007): Geochemistry of heavy minerals. In: Mange MA, Wright DT (eds), *Developments in Sedimentology* 58, 345–391, [https://doi.org/10.1016/S0070-4571\(07\)58013-1](https://doi.org/10.1016/S0070-4571(07)58013-1).
- Marschall HR, Jiang SY (2011): Tourmaline isotopes: no element left behind. *Elements* 7, 313–319, <https://doi.org/10.2113/gselements.7.5.313>.
- Marschall HR, Korsakov AV, Luvizotto GL, Nasdala L, Ludwig T (2009): On the occurrence and boron isotopic composition of tourmaline in (ultra) high-pressure metamorphic rocks. *Journal of the Geological Society* 166, 811–823, <https://doi.org/10.1144/0016-76492008-042>.
- Martin AJ, Gehrels GE, DeCelles PG (2007): The tectonic significance of (U,Th)/Pb ages of monazite inclusions in garnet from the Himalaya of central Nepal. *Chemical Geology* 244, 1–24, <https://doi.org/10.1016/j.chemgeo.2007.05.003>.
- Martínez-Martínez JM, Torres-Ruiz J, Pesquera A, Gil-Crespo PP (2010): Geological relationships and U–Pb zircon and ⁴⁰Ar/³⁹Ar tourmaline geochronology of gneisses and tourmalinites from the Nevado–Filabride complex (western Sierra Nevada, Spain): tectonic implications. *Lithos* 119, 238–250, <https://doi.org/10.1016/j.lithos.2010.07.002>.
- Maruyama S, Liou JG, Terabayashi M (1996): Blueschists and eclogites of the world and their exhumation. *International Geology Review* 38, 485–594, <https://doi.org/10.1080/00206819709465347>.
- Maruyama S, Santosh M, Azuma S (2018): Initiation of plate tectonics in the Hadean: Eclogitization triggered by the ABEL Bombardment. *Geoscience Frontiers* 9, 1033–1048, <https://doi.org/10.1016/j.gsf.2016.11.009>.
- Massonne HJ (2001): First find of coesite in the UHP metamorphic area of the central Erzgebirge, Germany. *European Journal of Mineralogy* 13, 565–570, <https://doi.org/10.1127/0935-1221/2001/0013-0565>.
- Massonne HJ (2003): A comparison of the evolution of diamondiferous quartz-rich rocks from the Saxonian Erzgebirge and the Kokchetav Massif: are so-called diamondiferous gneisses magmatic rocks? *Earth and Planetary Science Letters* 216, 347–364, [https://doi.org/10.1016/S0012-821X\(03\)00512-0](https://doi.org/10.1016/S0012-821X(03)00512-0).
- Massonne HJ (2005): Involvement of crustal material in delamination of the lithosphere after continent-continent collision. *International Geology Reviews* 47, 792–804, <https://doi.org/10.2747/0020-6814.47.8.792>.
- Massonne HJ (2011a): Occurrences and PT conditions of high and ultrahigh pressure rocks in the Bohemian Massif. *Geolines* 23, 18–26.
- Massonne HJ (2011b): German part of the Saxonian Erzgebirge. 9th International Eclogite Conference, Pre-Conference Excursion. *Geolines* 23, 29–59.
- Massonne HJ (2021): Comment to “Deep subduction of felsic rocks hosting UHP lenses in the central Saxonian Erzgebirge: Implications for UHP terrane exhumation” by Schönig et al. (2020). *Gondwana Research* 98, 317–319, <https://doi.org/10.1016/j.gr.2020.12.028>.
- Massonne HJ, Czambor A (2007): Geochemical signatures of Variscan eclogites from the Saxonian Erzgebirge, central Europe. *Chemie der Erde - Geochemistry* 67, 69–83, <https://doi.org/10.1016/j.chemer.2006.07.001>.
- Massonne HJ, Nasdala L (2003): Characterization of an early metamorphic stage through inclusions in zircon of a diamondiferous quartzofeldspathic rock from the Erzgebirge, Germany. *American Mineralogist* 88, 883–889, <https://doi.org/10.2138/am-2003-5-618>.
- Massonne HJ, Schreyer W (1987): Phengite geobarometry based on the limiting assemblage with K-feldspar, phlogopite, and quartz. *Contributions to Mineralogy and Petrology* 96, 212–224, <https://doi.org/10.1007/BF00375235>.

- Massonne HJ, Tu W (2007): $\delta^{13}\text{C}$ signature of early graphite and subsequently formed microdiamond from the Saxonian Erzgebirge, Germany. *Terra Nova* 19, 476–480, <https://doi.org/10.1111/j.1365-3121.2007.00774.x>.
- Massonne HJ, Kennedy A, Nasdala L, Theye T (2007): Dating of zircon and monazite from diamondiferous quartzofeldspathic rocks of the Saxonian Erzgebirge – hints at burial and exhumation velocities, <https://doi.org/10.1180/minmag.2007.071.4.407>.
- Matrosova EA, Bobrov AV, Bindi L (2020): *Geochemistry of Chromium in the Earth's Mantle*. Springer Nature Switzerland, Cham, <https://doi.org/10.1007/978-3-030-27018-6>.
- Mazzucchelli ML, Burnley P, Angel RJ, Morganti S, Domeneghetti MC, Nestola F, Alvaro M (2018): Elastic geothermobarometry: Corrections for the geometry of the host-inclusion system. *Geology* 46, 231–234, <https://doi.org/10.1130/G39807.1>.
- Mazzucchelli ML, Reali A, Morganti S, Angel RJ, Alvaro M (2019): Elastic geobarometry for anisotropic inclusions in cubic hosts. *Lithos* 350–351, 105218, <https://doi.org/10.1016/j.lithos.2019.105218>.
- Mazzucchelli ML, Angel RJ, Alvaro M (2021): EntraPT: an online application for elastic geothermobarometry. *American Mineralogist* 106, 830–837, <https://doi.org/10.2138/am-2021-7693CCBYNCND>.
- McInnes BIA, Evans NJ, McDonald BJ, Kinny PD, Jakimowicz J (2009): Zircon U–Th–Pb–He double dating of the Merlin kimberlite field, northern territory, Australia. *Lithos* 112, 592–599, <https://doi.org/10.1016/j.lithos.2009.05.006>.
- McKenzie D, Parker R (1967): The North Pacific: An Example of Tectonics on a Sphere. *Nature* 216, 1276–1280, <https://doi.org/10.1038/2161276a0>.
- Medaris LG (1980): Convergent metamorphism of eclogite and garnet-bearing ultramafic rocks at Lien, West Norway. *Nature* 283, 470–472, <https://doi.org/10.1038/283470a0>.
- Meinert LD (1992): Skarns and Skarn Deposits. *Geoscience Canada* 19, 145–162, <https://journals.lib.unb.ca/index.php/GC/article/view/3773>.
- Meinhold G (2010): Rutile and its applications in earth sciences. *Earth-Science Reviews* 102, 1–28, <https://doi.org/10.1016/j.earscirev.2010.06.001>.
- Meinhold G, Anders B, Kostopoulos D, Reischmann T (2008): Rutile chemistry and thermometry as provenance indicator: an example from Chios Island, Greece. *Sedimentary Geology* 203, 98–111, <https://doi.org/10.1016/j.sedgeo.2007.11.004>.
- Milani S, Nestola F, Alvaro M, Pasqual D, Mazzucchelli ML, Domeneghetti MC, Geiger CA (2015): Diamond–garnet geobarometry: The role of garnet compressibility and expansivity. *Lithos* 227, 140–147, <https://doi.org/10.1016/j.lithos.2015.03.017>.
- Milani S, Angel RJ, Scandolo L, Mazzucchelli ML, Ballaran TB, Klemme S, Domeneghetti MC, Miletich R, Scheidl KS, Derzsi M, Tokár K, Prencipe M, Alvaro M, Nestola F (2017) Thermo-elastic behavior of grossular garnet at high pressures and temperatures. *American Mineralogist* 102, 851–859, <https://doi.org/10.2138/am-2017-5855>.
- Miller SR, Baldwin SL, Fitzgerald PG (2012): Transient fluvial incision and active surface uplift in the Woodlark Rift of eastern Papua New Guinea. *Lithosphere* 4, 131–149, <https://doi.org/10.1130/L135.1>.
- Millonig LJ, Albert R, Gerdes A, Avigad D, Dietsch C (2020): Exploring laser ablation U–Pb dating of regional metamorphic garnet – The Straits Schist, Connecticut, USA. *Earth and Planetary Science Letters* 552, 116589, <https://doi.org/10.1016/j.epsl.2020.116589>.
- Mints MV, Belousova EA, Konilov AN, Natapov LM, Shchipansky AA, Griffin WL, O'Reilly SY, Dokukina KA, Kaulina TV (2010): Mesoarchean subduction processes: 2.87 Ga eclogites from the Kola Peninsula, Russia. *Geology* 38, 739–742, <https://doi.org/10.1130/G31219.1>.
- Mitchell RN, Bleeker W, van Breemen O, Lecheminant TN, Peng P, Nilsson MK, Evans DA (2014): Plate tectonics before 2.0 Ga: Evidence from paleomagnetism of cratons within supercontinent Nuna. *American Journal of Science* 314, 878–894, <https://doi.org/10.2475/04.2014.03>.

- Moecher DP, Samson SD (2006): Differential zircon fertility of source terranes and natural bias in the detrital zircon record: implications for sedimentary provenance analysis. *Earth and Planetary Science Letters* 247, 252–266, <https://doi.org/10.1016/j.epsl.2006.04.035>.
- Möller A, Appel P, Mezger K, Schenk V (1995): Evidence for a 2 Ga subduction zone: eclogites in the Usagaran belt of Tanzania. *Geology* 23, 1067–1070, [https://doi.org/10.1130/0091-7613\(1995\)023<1067:EFAGSZ>2.3.CO;2](https://doi.org/10.1130/0091-7613(1995)023<1067:EFAGSZ>2.3.CO;2).
- Möller A, O'Brien PJ, Kennedy A, Kröner A (2002): Polyphase zircon in ultrahigh-temperature granulites (Rogaland, SW Norway): Constraints for Pb diffusion in zircon. *Journal of Metamorphic Geology* 20, 727–740, <https://doi.org/10.1046/j.1525-1314.2002.00400.x>.
- Möller A, O'Brien PJ, Kennedy A, Kröner A (2003): Linking growth episodes of zircon and metamorphic textures to zircon chemistry: an example from the ultrahigh-temperature granulites of Rogaland (SW Norway). In: Vance D, Müller W, Villa IM (eds), *Geochronology: Linking the Isotopic Record with Petrology and Textures*. Geological Society of London, Special Publications 220, 65–81, <https://doi.org/10.1144/GSL.SP.2003.220.01.04>.
- Monteleone BD, Baldwin SL, Webb LE, Fitzgerald PG, Grove M, Schmitt AK (2007): Late Miocene–Pliocene eclogite facies metamorphism, D'Entrecasteaux Islands, SE Papua New Guinea. *Journal of Metamorphic Geology* 25, 245–265, <https://doi.org/10.1111/j.1525-1314.2006.00685.x>.
- Morton AC (1985): A new approach to provenance studies: electron microprobe analysis of detrital garnets from Middle Jurassic sandstones of the northern North Sea. *Sedimentology* 32, 553–566, <https://doi.org/10.1111/j.1365-3091.1985.tb00470.x>.
- Morton AC (1991): Geochemical studies of detrital heavy minerals and their application to provenance research. In: Morton AC, Todd SP, Haughton PDW (eds), *Developments in Sedimentary Provenance Studies*. Geological Society of London, Special Publications 57, 31–45, <https://doi.org/10.1144/GSL.SP.1991.057.01.04>.
- Morton AC, Hallsworth CR (1999): Processes controlling the composition of heavy mineral assemblages in sandstones. *Sedimentary Geology* 124, 3–29, [https://doi.org/10.1016/S0037-0738\(98\)00118-3](https://doi.org/10.1016/S0037-0738(98)00118-3).
- Morton AC, Hallsworth C, Chalton B (2004): Garnet compositions in Scottish and Norwegian basement terrains: a framework for interpretation of North Sea sandstone provenance. *Marine and Petroleum Geology* 21, 393–410, <https://doi.org/10.1016/j.marpetgeo.2004.01.001>.
- Morton AC, Whitham AG, Fanning CM (2005a): Provenance of Late Cretaceous to Paleocene submarine fan sandstones in the Norwegian Sea: integration of heavy mineral, mineral chemical and zircon age data. *Sedimentary Geology* 182, 3–28, <https://doi.org/10.1016/j.sedgeo.2005.08.007>.
- Morton AC, Whitham AG, Fanning CM, Claoué-Long J (2005b): The role of East Greenland as a source of sediment to the Vøring Basin during the Late Cretaceous. In: Wandås BTG, Nystuen JP, Eide E, Gradstein F (eds), *Onshore-Offshore Relationships on the North Atlantic Margin*. Norwegian Petroleum Society Special Publications 12, 83–110, [https://doi.org/10.1016/S0928-8937\(05\)80045-1](https://doi.org/10.1016/S0928-8937(05)80045-1).
- Mosenfelder JL (2000): Pressure dependence of hydroxyl solubility in coesite. *Physics and Chemistry of Minerals* 27, 610–617, <https://doi.org/10.1007/s002690000105>.
- Mosenfelder JL, Bohlen SR (1997): Kinetics of the coesite to quartz transformation. *Earth and Planetary Science Letters* 153, 133–147, [https://doi.org/10.1016/S0012-821X\(97\)00159-3](https://doi.org/10.1016/S0012-821X(97)00159-3).
- Mosenfelder JL, Schertl HP, Smyth JR, Liou JG (2005): Factors in the preservation of coesite: The importance of fluid infiltration. *American Mineralogist* 90, 779–789, <https://doi.org/10.2138/am.2005.1687>.
- Mueller WU, Corcoran PL (2001): Volcano-sedimentary processes operating on a marginal continental arc: the Archean Raquette Lake Formation, Slave Province, Canada. *Sedimentary Geology* 141, 169–196, [https://doi.org/10.1016/S0037-0738\(01\)00074-4](https://doi.org/10.1016/S0037-0738(01)00074-4).
- Mueller WU, Daigneault R, Mortensen JK, Chown EH (1996): Archean terrane docking: upper crust collision tectonics, Abitibi greenstone belt, Quebec, Canada. *Tectonophysics* 265, 127–150, [https://doi.org/10.1016/S0040-1951\(96\)00149-7](https://doi.org/10.1016/S0040-1951(96)00149-7).

- Müller S, Dziggel A, Kolb J, Sindern S (2018a): Mineral textural evolution and PT-path of relict eclogite-facies rocks in the Paleoproterozoic Nagssugtoqidian Orogen, South-East Greenland. *Lithos* 296, 212–232, <https://doi.org/10.1016/j.lithos.2017.11.008>.
- Müller S, Dziggel A, Sindern S, Kokfelt TF, Gerdes A, Kolb J (2018b): Age and temperature-time evolution of retrogressed eclogite-facies rocks in the Paleoproterozoic Nagssugtoqidian Orogen, South-East Greenland: Constrained from U-Pb dating of zircon, monazite, titanite and rutile. *Precambrian Research* 314, 468–486, <https://doi.org/10.1016/j.precamres.2018.07.002>.
- Murri M, Mazzucchelli ML, Campomenosi N, Korsakov AV, Prencipe M, Mihailova BD, Scambelluri M, Angel RJ, Alvaro M (2018): Raman elastic geobarometry for anisotropic mineral inclusions. *American Mineralogist* 103, 1869–1872, <https://doi.org/10.2138/am-2018-6625CCBY>.
- Nagel TJ, Hoffmann JE, Münker C (2012): Generation of Eoarchean tonalite-trondhjemite-granodiorite series from thickened mafic arc crust. *Geology* 40, 375–378, <https://doi.org/10.1130/G32729.1>.
- Nakamura Y, Yoshino T, Satish-Kumar M (2020): Pressure dependence of graphitization: implications for rapid recrystallization of carbonaceous material in a subduction zone. *Contributions to Mineralogy and Petrology* 175, 32, <https://doi.org/10.1007/s00410-020-1667-2>.
- Nasdala L, Massonne HJ (2000): Microdiamonds from the Saxonian Erzgebirge, Germany: in situ micro-Raman characterization. *European Journal of Mineralogy* 12, 495–498, <https://doi.org/10.1127/0935-1221/2000/0012-0495>.
- Nasdala L, Steger S, Reissner C (2016): Raman study of diamond-based abrasives, and possible artefacts in detecting UHP microdiamond. *Lithos* 265, 317–327, <https://doi.org/10.1016/j.lithos.2016.03.009>.
- Negulescu E, Săbău G, Massonne HJ (2018): Growth of chloritoid and garnet along a nearly isothermal burial path to 70 km depth: an example from the Bughea Metamorphic Complex, Leaota Massif, South Carpathians. *Mineralogy and Petrology* 112, 535–553, <https://doi.org/10.1007/s00710-017-0552-9>.
- Nie S, Yin A, Rowley DB, Jin Y (1994): Exhumation of the Dabie Shan ultra-high-pressure rocks and accumulation of the Songpan-Ganzi flysch sequence, central China. *Geology* 22, 999–1002, [https://doi.org/10.1130/0091-7613\(1994\)022<0999:EOTDSU>2.3.CO;2](https://doi.org/10.1130/0091-7613(1994)022<0999:EOTDSU>2.3.CO;2).
- Nowicki TE, Moore RO, Gurney JJ, Baumgartner MC (2007): Diamonds and associated heavy minerals in kimberlite: a review of key concepts and applications. *Developments in Sedimentology* 58, 1235–1267, [https://doi.org/10.1016/S0070-4571\(07\)58046-5](https://doi.org/10.1016/S0070-4571(07)58046-5).
- Nutman AP, Friend CR, Bennett VC (2002): Evidence for 3650–3600 Ma assembly of the northern end of the Itsaq Gneiss Complex, Greenland: implication for early Archaean tectonics. *Tectonics* 21, TC001203, <https://doi.org/10.1029/2000TC001203>.
- Nutman AP, Kalsbeek F, Friend CR (2008): The Nagssugtoqidian orogen in South-East Greenland: Evidence for Paleoproterozoic collision and plate assembly. *American Journal of Science* 308, 529–572, <https://doi.org/10.2475/04.2008.06>.
- Nutman AP, Bennett VC, Friend CR, Yi K (2020): Eoarchean contrasting ultra-high-pressure to low-pressure metamorphisms (<250 to >1000°C/GPa) explained by tectonic plate convergence in deep time. *Precambrian Research* 344, 105770, <https://doi.org/10.1016/j.precamres.2020.105770>.
- O'Brien PJ, Ziemann MA (2008): Preservation of coesite in exhumed eclogite: insights from Raman mapping. *European Journal of Mineralogy* 20, 827–834, <https://doi.org/10.1127/0935-1221/2008/0020-1883>.
- Ogasawara Y, Fukasawa K, Maruyama S (2002): Coesite exsolution from supersilicic titanite in UHP marble from the Kokchetav Massif, northern Kazakhstan. *American Mineralogist* 87, 454–461, <https://doi.org/10.2138/am-2002-0409>.
- Okay AI (1993): Petrology of a diamond and coesite-bearing metamorphic terrain: Dabie Shan, China. *European Journal of Mineralogy* 5, 659–675.
- Osborne ZR, Thomas JB, Nachlas WO, Baldwin SL, Holycross ME, Spear FS, Watson EB (2019): An experimentally calibrated thermobarometric solubility model for titanium in coesite (TitaniC). *Contributions to Mineralogy and Petrology* 174, 1–13, <https://doi.org/10.1007/s00410-019-1575-5>.

- Ota T, Kobayashi K, Kunihiro T, Nakamura E (2008): Boron cycling by subducted lithosphere; insights from diamondiferous tourmaline from the Kokchetav ultrahigh-pressure metamorphic belt. *Geochimica et Cosmochimica Acta* 72, 3531–3541, <https://doi.org/10.1016/j.gca.2008.05.002>.
- Palin RM, Dyck B (2018): Metamorphic consequences of secular changes in oceanic crust composition and implications for uniformitarianism in the geological record. *Geoscience Frontiers* 9, 1009–1019, <https://doi.org/10.1016/j.gsf.2018.04.004>.
- Palin RM, White RW (2016): Emergence of blueschists on Earth linked to secular changes in oceanic crust composition. *Nature Geoscience* 9, 60–64, <https://doi.org/10.1038/ngeo2605>.
- Palin RM, Santosh M, Cao W, Li SS, Hernández-Uribe D, Parsons A (2020): Secular change and the onset of plate tectonics on Earth. *Earth-Science Reviews* 207, 103172, <https://doi.org/10.1016/j.earscirev.2020.103172>.
- Palin RM, Moore JD, Zhang Z, Huang G, Wade J, Dyck B (2021): Mafic Archean continental crust prohibited exhumation of orogenic UHP eclogite. *Geoscience Frontiers* 12, 101225, <https://doi.org/10.1016/j.gsf.2021.101225>.
- Parkinson CD, Katayama I (1999): Present-day UHP conditions of coesite inclusions in zircon and garnet: Evidence from laser Raman microspectroscopy. *Geology* 27, 979–982, [https://doi.org/10.1130/0091-7613\(1999\)027<0979:PDUPCO>2.3.CO;2](https://doi.org/10.1130/0091-7613(1999)027<0979:PDUPCO>2.3.CO;2).
- Parman SW, Grove TL, Dann JC (2001): The production of Barberton komatiites in an Archean subduction zone. *Geophysical Research Letters* 28, 2513–2516, <https://doi.org/10.1029/2000GL012713>.
- Payne JL, Ferris G, Barovich KM, Hand M (2010): Pitfalls of classifying ancient magmatic suites with tectonic discrimination diagrams: An example from the Paleoproterozoic Tunkillia Suite, southern Australia. *Precambrian Research* 177, 227–240, <https://doi.org/10.1016/j.precamres.2009.12.005>.
- Pearce JA (2008): Geochemical fingerprinting of oceanic basalts with applications to ophiolite classification and the search for Archean oceanic crust. *Lithos* 100, 14–48, <https://doi.org/10.1016/j.lithos.2007.06.016>.
- Pease V, Percival J, Smithies H, Stevens G, van Kranendonk M (2008): When did plate tectonics begin? Evidence from the orogenic record. In: Condie KC, Pease V (eds), *When did plate tectonics begin on planet Earth?* GSA Special Paper 440, 199–228.
- Peltonen P, Kontinen A, Huhma H (1996): Petrology and geochemistry of metabasalts from the 1.95 Ga Jormua ophiolite, northeastern Finland. *Journal of Petrology* 37, 1359–1383, <https://doi.org/10.1093/petrology/37.6.1359>.
- Peng H, Kusky T, Deng H, Wang L, Wang J, Huang Y, Huang B, Ning W (2020): Identification of the Neoproterozoic Jianping pyroxenite-mélange in the Central Orogenic Belt, North China Craton: A fore-arc accretional assemblage. *Precambrian Research* 336, 105495, <https://doi.org/10.1016/j.precamres.2019.105495>.
- Penniston-Dorland SC, Kohn MJ, Manning CE (2015): The global range of subduction zone thermal structures from exhumed blueschists and eclogites: Rocks are hotter than models. *Earth and Planetary Science Letters* 428, 243–254, <https://doi.org/10.1016/j.epsl.2015.07.031>.
- Perchuk LL (1991): Derivation of a thermodynamically consistent set of geothermometers and geobarometers for metamorphic and magmatic rocks. In: Perchuk LL (ed), *Progress in metamorphic and magmatic petrology*. Cambridge University Press, Cambridge, 93–112, <https://doi.org/10.1017/CBO9780511564444>.
- Perchuk AL, Morgunova AA (2014): Variable P–T paths and HP-UHP metamorphism in a Precambrian terrane, Gridino, Russia: Petrological evidence and geodynamic implications. *Gondwana Research* 25, 614–629, <https://doi.org/10.1016/j.gr.2012.09.009>.
- Pereira I, Storey CD, Darling JR, Lana C, Alkmim AR (2019): Two billion years of evolution enclosed in hydrothermal rutile: recycling of the São Francisco Craton Crust and constraints on gold remobilisation processes. *Gondwana Research* 68, 69–92, <https://doi.org/10.1016/j.gr.2018.11.008>.
- Pereira I, Storey CD, Darling JR, Moreira H, Strachan RA, Cawood PA (2021): Detrital rutile tracks the first appearance of subduction zone low T/P paired metamorphism in the Palaeoproterozoic. *Earth and Planetary Science Letters* 570, 117069, <https://doi.org/10.1016/j.epsl.2021.117069>.

- Petersen KD, Buck WR (2015): Eduction, extension, and exhumation of ultrahigh-pressure rocks in metamorphic core complexes due to subduction initiation. *Geochemistry, Geophysics, Geosystems* 16, 2564–2581, <https://doi.org/10.1002/2015GC005847>.
- Petrelli M, Perugini D (2016): Solving petrological problems through machine learning: the study case of tectonic discrimination using geochemical and isotopic data. *Contributions to Mineralogy and Petrology* 171, 1–15, <https://doi.org/10.1007/s00410-016-1292-2>.
- Petrelli M, Bizzarri R, Morgavi D, Baldanza A, Perugini D (2017): Combining machine learning techniques, microanalyses and large geochemical datasets for tephrochronological studies in complex volcanic areas: New age constraints for the Pleistocene magmatism of central Italy. *Quaternary Geochronology* 40, 33–44, <https://doi.org/10.1016/j.quageo.2016.12.003>.
- Pidgeon RT (1992): Recrystallisation of oscillatory zoned zircon: some geochronological and petrological implications. *Contributions to Mineralogy and Petrology* 110, 463–472, <https://doi.org/10.1007/BF00344081>.
- Polat A, Kerrich R (1999): Formation of an Archean tectonic mélange in the Schreiber-Hemlo greenstone belt, Superior Province, Canada: Implications for Archean subduction-accretion process. *Tectonics* 18, 733–755, <https://doi.org/10.1029/1999TC900032>.
- Prencipe M (2012): Simulation of vibrational spectra of crystals by ab initio calculations: an invaluable aid in the assignment and interpretation of the Raman signals. The case of jadeite (NaAlSi₂O₆). *Journal of Raman Spectroscopy* 43, 1567–1569, <https://doi.org/10.1002/jrs.4040>.
- Puetz SJ (2018): A relational database of global U–Pb ages. *Geoscience Frontiers* 9, 877–891, <https://doi.org/10.1016/j.gsf.2017.12.004>.
- Rahl JM, Reiners PW, Campbell IH, Nicolescu S, Allen CM (2003): Combined single-grain (U–Th)/He and U/Pb dating of detrital zircons from the Navajo Sandstone, Utah. *Geology* 31, 761–764, <https://doi.org/10.1130/G19653.1>.
- R Core Team (2019): R: a language and environment for statistical computing. R Foundation for Statistical Computing, Vienna, Austria, <https://www.R-project.org/>.
- Reimink JR, Davies JHFL, Ielpi A (2021): Global zircon analysis records a gradual rise of continental crust throughout the Neoproterozoic. *Earth and Planetary Science Letters* 554, 116654, <https://doi.org/10.1016/j.epsl.2020.116654>.
- Reinecke T (1991): Very-high-pressure metamorphism and uplift of coesite-bearing metasediments from the Zermatt-Saas zone, Western Alps. *European Journal of Mineralogy* 3, 7–18, <https://doi.org/10.1127/ejm/3/1/0007>.
- Reiners PW (2005): Zircon (U–Th)/He thermochronometry. *Reviews in Mineralogy and Geochemistry* 58, 151–179, <https://doi.org/10.2138/rmg.2005.58.6>.
- Reiners PW, Campbell IH, Nicolescu S, Allen CM, Garver JI, Hourigan JK, Cowan DS (2004): Double- and triple-dating of single detrital zircons with (U–Th)/He, fission-track, and U/Pb systems, and examples from modern and ancient sediments of the western US. American Geophysical Union, Fall Meeting 2004, Abstract T51D-01.
- Reiners PW, Campbell IH, Nicolescu S, Allen CM, Hourigan JK, Garver JI, Mattinson JM, Cowan DS (2005): (U–Th)/(He–Pb) double dating of detrital zircons. *American Journal of Science* 305, 259–311, <https://doi.org/10.2475/ajs.305.4.259>.
- Ren Q, Li M, Han S, Zhang Y, Zhang Q, Shi J (2019): Basalt tectonic discrimination using combined machine learning approach. *Minerals* 9, 376, <https://doi.org/10.3390/min9060376>.
- Reverdatto VV, Likhanov II, Polyansky OP, Sheplev VS, Kolobov VY (2019): Mineral Geothermobarometry. In: Reverdatto VV, Likhanov II, Polyansky OP, Sheplev VS, Kolobov VY (eds), *The Nature and Models of Metamorphism*. Springer Nature Switzerland, Cham, pp. 55–82, https://doi.org/10.1007/978-3-030-03029-2_2.

- Rezvukhina OV, Skublov SG, Rezvukhin DI, Korsakov AV (2021): Rutile in diamondiferous metamorphic rocks: New insights from trace-element composition, mineral/fluid inclusions, and U-Pb ID-TIMS dating. *Lithos* 394, 106172, <https://doi.org/10.1016/j.lithos.2021.106172>.
- Robinson PT, Bai WJ, Malpas J, Yang JS, Zhou MF, Fang Q, Hu XFS, Cameron S, Staudigel H (2004): Ultrahigh-pressure minerals in the Luobusa Ophiolite, Tibet, and their tectonic implications. In: Malpas J, Fletcher CJN, Ali JR, Aitchison JC (eds), *Aspects of the Tectonic Evolution of China*. Geological Society of London, Special Publications 226, 247–271, <https://doi.org/10.1144/GSL.SP.2004.226.01.14>.
- Rolf T, Coltice N, Tackley PJ (2012): Linking continental drift, plate tectonics and the thermal state of the Earth's mantle. *Earth and Planetary Science Letters* 351, 134–146, <https://doi.org/10.1016/j.epsl.2012.07.011>.
- Root DB, Hacker BR, Gans PB, Ducea MN, Eide EA, Mosenfelder JL (2005): Discrete ultrahigh-pressure domains in the Western Gneiss Region, Norway: implications for formation and exhumation. *Journal of Metamorphic Geology* 23, 45–61, <https://doi.org/10.1111/j.1525-1314.2005.00561.x>.
- Rosenfeld JL, Chase AB (1961): Pressure and temperature of crystallization from elastic effects around solid inclusions in minerals? *American Journal of Science* 259, 519–541, <https://doi.org/10.2475/ajs.259.7.519>.
- Rötzler K, Schumacher R, Maresch WV, Willner AP (1998): Characterization and geodynamic implications of contrasting metamorphic evolution in juxtaposed high-pressure units of the Western Erzgebirge (Saxony, Germany). *European Journal of Mineralogy* 10, 261–280, <https://doi.org/10.1127/ejm/10/2/0261>.
- Rubatto D (2002): Zircon trace element geochemistry: partitioning with garnet and the link between U–Pb ages and metamorphism. *Chemical Geology* 184, 123–138, [https://doi.org/10.1016/S0009-2541\(01\)00355-2](https://doi.org/10.1016/S0009-2541(01)00355-2).
- Rubatto D (2017): Zircon: the metamorphic mineral. *Reviews in Mineralogy and Geochemistry* 83, 261–295, <https://doi.org/10.2138/rmg.2017.83.9>.
- Rubatto D, Gebauer D (2000): Use of cathodoluminescence for U-Pb zircon dating by ion microprobe: some examples from the Western Alps. In: Pagel M, Barbin V, Blanc P, Ohnenstetter D (eds), *Cathodoluminescence in Geosciences*. Springer, Berlin, Heidelberg, 373–400, https://doi.org/10.1007/978-3-662-04086-7_15.
- Rubatto D, Hermann J (2001): Exhumation as fast as subduction? *Geology* 29, 3–6, [https://doi.org/10.1130/0091-7613\(2001\)029<0003:EAFAS>2.0.CO;2](https://doi.org/10.1130/0091-7613(2001)029<0003:EAFAS>2.0.CO;2).
- Rubatto D, Müntener O, Barnhoorn A, Gregory C (2008): Dissolution-reprecipitation of zircon at low-temperature, high-pressure conditions (Lanzo Massif, Italy). *American Mineralogist* 93, 1519–1529, <https://doi.org/10.2138/am.2008.2874>.
- Russell JK, Dipple GM, Lang JR, Lueck B (1999): Major-element discrimination of titanium andradite from magmatic and hydrothermal environments; an example from the Canadian Cordillera. *European Journal of Mineralogy* 11, 919–935.
- Ryan WB, Carbotte SM, Coplan JO, O'Hara S, Melkonian A, Arko R, Weissel RA, Ferrini V, Goodwillie A, Nitsche F, Bonczkowski J (2009): Global multi-resolution topography synthesis. *Geochemistry, Geophysics, Geosystems* 10, Q03014, <https://doi.org/10.1029/2008GC002332>.
- Samadi R, Torabi G, Kawabata H, Miller NR (2021): Biotite as a petrogenetic discriminator: Chemical insights from igneous, meta-igneous and meta-sedimentary rocks in Iran. *Lithos* 386, 106016, <https://doi.org/10.1016/j.lithos.2021.106016>.
- Sandwell DT, Schubert G (1992): Evidence for retrograde lithospheric subduction on Venus. *Science* 257, 766–770, <https://doi.org/10.1126/science.257.5071.766>.
- Satkoski AM, Fralick P, Beard BL, Johnson CM (2017): Initiation of modern-style plate tectonics recorded in Mesoarchean marine chemical sediments. *Geochimica et Cosmochimica Acta* 209, 216–232, <https://doi.org/10.1016/j.gca.2017.04.024>.
- Schantl P, Hauzenberger C, Finger F, Müller T, Linner M (2019): New evidence for the prograde and retrograde PT-path of high-pressure granulites, Moldanubian Zone, Lower Austria, by Zr-in-rutile thermometry and garnet diffusion modelling. *Lithos* 342, 420–439, <https://doi.org/10.1016/j.lithos.2019.05.041>.

- Schauberger P, Walker A (2020): openxlsx: Read, Write and Edit xlsx Files. R package version 4.2.3, <https://CRAN.R-project.org/package=openxlsx>.
- Schertl HP, Hertwig A, Maresch WV (2019): Cathodoluminescence microscopy of zircon in HP- and UHP-metamorphic rocks: A fundamental technique for assessing the problem of inclusions versus pseudo-inclusions. *Journal of Earth Science* 30, 1095–1107, <https://doi.org/10.1007/s12583-019-1246-5>.
- Schmädicke E, Okrusch M, Schmidt W (1992): Eclogite-facies rocks in the Saxonian Erzgebirge, Germany: high pressure metamorphism under contrasting PT conditions. *Contributions to Mineralogy and Petrology* 110, 226–241, <https://doi.org/10.1007/BF00310740>.
- Schmädicke E, Mezger K, Cosca MA, Okrusch M (1995): Variscan Sm–Nd and Ar–Ar ages of eclogite facies rocks from the Erzgebirge, Bohemian Massif. *Journal of Metamorphic Geology* 13, 537–552, <https://doi.org/10.1111/j.1525-1314.1995.tb00241.x>.
- Schönig J, Meinhold G, von Eynatten H, Lünsdorf, NK (2018a): Tracing ultrahigh pressure metamorphism at the catchment scale. *Scientific Reports* 8, 2931, <https://doi.org/10.1038/s41598-018-21262-8>.
- Schönig J, Meinhold G, von Eynatten H, Lünsdorf NK (2018b): Provenance information recorded by mineral inclusions in detrital garnet. *Sedimentary Geology* 376, 32–49, <https://doi.org/10.1016/j.sedgeo.2018.07.009>.
- Schönig J, von Eynatten H, Meinhold G, Lünsdorf NK (2019): Diamond and coesite inclusions in detrital garnet of the Saxonian Erzgebirge, Germany. *Geology* 47, 715–718, <https://doi.org/10.1130/G46253.1>.
- Schönig J, von Eynatten H, Meinhold G, Lünsdorf NK, Willner AP, Schulz B (2020): Deep subduction of felsic rocks hosting UHP lenses in the central Saxonian Erzgebirge: Implications for UHP terrane exhumation. *Gondwana Research* 87, 320–329, <https://doi.org/10.1016/j.gr.2020.06.020>.
- Schönig J, von Eynatten H, Meinhold G, Lünsdorf NK, Willner AP, Schulz B (2021a): Reply to comment on “Deep subduction of felsic rocks hosting UHP lenses in the central Saxonian Erzgebirge: Implications for UHP terrane exhumation”. *Gondwana Research* 98, 320–323, <https://doi.org/10.1016/j.gr.2020.12.029>.
- Schönig J, von Eynatten H, Meinhold G, Lünsdorf NK (2021b): Life-cycle analysis of coesite-bearing garnet. *Geological Magazine* 158, 1421–1440, <https://doi.org/10.1017/S0016756821000017>.
- Schönig J, von Eynatten H, Tolosana-Delgado R, Meinhold G (in press): Garnet major-element composition as an indicator of host-rock type: A machine-learning approach using the random forest classifier. *Contributions to Mineralogy and Petrology* (not yet issued), <https://doi.org/10.1007/s00410-021-01854-w>.
- Schönig J, von Eynatten H, Meinhold G, Lünsdorf NK (in preparation): The sedimentary record of ultrahigh-pressure metamorphism: A perspective review.
- Schubert G, Sandwell DT (1995): A global survey of possible subduction sites on Venus. *Icarus* 117, 173–196, <https://doi.org/10.1006/icar.1995.1150>.
- Schuling RD, Scholten MJ, de Meijer RJ, Riezebos HJ (1985): Grain size distribution of different minerals in a sediment as a function of their specific density. *Geologie en Mijnbouw* 64, 199–203.
- Schulze DJ (2003): A classification scheme for mantle-derived garnets in kimberlite: a tool for investigating the mantle and exploring for diamonds. *Lithos* 71, 195–213, [https://doi.org/10.1016/S0024-4937\(03\)00113-0](https://doi.org/10.1016/S0024-4937(03)00113-0).
- Schulze DJ, Valley JW, Spicuzza MJ (2000): Coesite eclogites from the Roberts Victor kimberlite, South Africa. *Lithos* 54, 23–32, [https://doi.org/10.1016/S0024-4937\(00\)00031-1](https://doi.org/10.1016/S0024-4937(00)00031-1).
- Schulze DJ, Harte B, Valley JW, Brenan JM, Dominic MDR (2003): Extreme crustal oxygen isotope signatures preserved in coesite in diamond. *Nature* 423, 68–70, <https://doi.org/10.1038/nature01615>.
- Schumacher R, Rötzler K, Maresch WV (1999): Subtle oscillatory zoning in garnet from regional metamorphic phyllites and mica schists, western Erzgebirge, Germany. *Canadian Mineralogist* 37, 381–403.

- Scott DJ, Helmstaedt H, Bickle MJ (1992): Purtuniq ophiolite, Cape Smith belt, northern Quebec, Canada: A reconstructed section of Early Proterozoic oceanic crust. *Geology* 20, 173–176, [https://doi.org/10.1130/0091-7613\(1992\)020<0173:POCSBN>2.3.CO;2](https://doi.org/10.1130/0091-7613(1992)020<0173:POCSBN>2.3.CO;2).
- Selverstone J (1993): Micro- to macroscale interactions between deformational and metamorphic processes, Tauern window, Eastern Alps. *Schweizerische Mineralogische und Petrographische Mitteilungen* 73, 229–239.
- Seman S, Stockli DF, McLean NM (2017): U-Pb geochronology of grossular-andradite garnet. *Chemical Geology* 460, 106–116, <https://doi.org/10.1016/j.chemgeo.2017.04.020>.
- Shatsky VS, Sobolev NV (1993): Some specific features of the origin of diamonds in metamorphic rocks. *Doklady Akademii Nauk* 331, 217–219.
- Shirey SB, Richardson SH (2011): Start of the Wilson cycle at 3 Ga shown by diamonds from subcontinental mantle. *Science* 333, 434–436, <https://doi.org/10.1126/science.1206275>.
- Shirey SB, Kamber BS, Whitehouse MJ, Mueller PA, Basu AR (2008): A review of the isotopic and trace element evidence for mantle and crustal processes. In: Condie KC, Pease V (eds), *When did plate tectonics begin on planet Earth?* GSA Special Paper 440, 1–29.
- Sizova E, Gerya T, Brown M, Perchuk LL (2010): Subduction styles in the Precambrian: Insight from numerical experiments. *Lithos* 116, 209–229, <https://doi.org/10.1016/j.lithos.2009.05.028>.
- Sizova E, Gerya T, Brown M (2014): Contrasting styles of Phanerozoic and Precambrian continental collision. *Gondwana Research* 25, 522–545, <https://doi.org/10.1016/j.gr.2012.12.011>.
- Smart KA, Tappe S, Stern RA, Webb SJ, Ashwal LD (2016): Early Archaean tectonics and mantle redox recorded in Witwatersrand diamonds. *Nature Geoscience* 9, 255–259, <https://doi.org/10.1038/ngeo2628>.
- Smit MA, Scherer EE, Mezger K (2013): Lu–Hf and Sm–Nd garnet geochronology: chronometric closure and implications for dating petrological processes. *Earth and Planetary Science Letters* 381, 222–233, <https://doi.org/10.1016/j.epsl.2013.08.046>.
- Smit KV, Shirey SB, Hauri EH, Stern RA (2019): Sulfur isotopes in diamonds reveal differences in continent construction. *Science* 364, 383–385, [10.1126/science.aaw9548](https://doi.org/10.1126/science.aaw9548).
- Smith DC (1984): Coesite in clinopyroxene in the Caledonides and its implications for geodynamics. *Nature* 310, 641–644, <https://doi.org/10.1038/310641a0>.
- Smith DC, Godard G (2013): A Raman spectroscopic study of diamond and disordered sp³-carbon in the coesite-bearing Straumen Eclogite Pod, Norway. *Journal of Metamorphic Geology* 31, 19–33, <https://doi.org/10.1111/jmg.12007>.
- Smyth JR, Hatton CJ (1977): A coesite-sanidine grosspydite from the Roberts Victor kimberlite. *Earth and Planetary Science Letters* 34, 284–290, [https://doi.org/10.1016/0012-821X\(77\)90012-7](https://doi.org/10.1016/0012-821X(77)90012-7).
- Smythe DJ, Schulze DJ, Brenan JM (2008): Rutile as a kimberlite indicator mineral: minor and trace element geochemistry. 9th International Kimberlite Conference, Extended Abstract, No. 9IKC-A-00193.
- Sobolev NV, Shatsky VS (1990): Diamond inclusions in garnets from metamorphic rocks: a new environment for diamond formation. *Nature* 343, 742–745, <https://doi.org/10.1038/343742a0>.
- Spear FS (1993): *Metamorphic Phase Equilibria and Pressure–Temperature–Time Paths*. Mineralogical Society of America, Monograph 1, Washington DC, pp. 799.
- Spear FS, Wolfe OM (2020): Reevaluation of “equilibrium” PT paths from zoned garnet in light of quartz inclusion in garnet (QuiG) barometry. *Lithos* 372, 105650, <https://doi.org/10.1016/j.lithos.2020.105650>.
- Spencer CJ, Cawood PA, Hawkesworth CJ, Raub TD, Prave AR, Roberts NM (2014): Proterozoic onset of crustal reworking and collisional tectonics: Reappraisal of the zircon oxygen isotope record. *Geology* 42, 451–454, <https://doi.org/10.1130/G35363.1>.
- Spencer CJ, Cawood PA, Hawkesworth CJ, Prave AR, Roberts NM, Horstwood MS, Whitehouse MJ (2015): Generation and preservation of continental crust in the Grenville Orogeny. *Geoscience Frontiers* 6, 357–372, <https://doi.org/10.1016/j.gsf.2014.12.001>.

- Spencer CJ, Roberts NMW, Santosh M (2017): Growth, destruction, and preservation of Earth's continental crust. *Earth-Science Reviews* 172, 87–106, <https://doi.org/10.1016/j.earscirev.2017.07.013>.
- Spengler D, van Roermund HLM, Drury MR, Ottolini L, Mason PR, Davies GR (2006): Deep origin and hot melting of an Archaean orogenic peridotite massif in Norway. *Nature* 440, 913–917, <https://doi.org/10.1038/nature04644>.
- Spengler D, Alifirova TA, van Roermund HLM (2021): Subcratonic and tectonic evolution of pyroxenite and eclogite with lamellar inclusions in garnet, Western Gneiss Region, Norway. *Journal of Petrology* 62, egab008, <https://doi.org/10.1093/petrology/egab008>.
- Stepanov AS, Hermann J, Rubatto D, Rapp RP (2012): Experimental study of monazite/melt partitioning with implications for the REE, Th and U geochemistry of crustal rocks. *Chemical Geology* 300, 200–220, <https://doi.org/10.1016/j.chemgeo.2012.01.007>.
- Stepanov AS, Hermann J, Korsakov AV, Rubatto D (2014): Geochemistry of ultrahigh-pressure anatexis: fractionation of elements in the Kokchetav gneisses during melting at diamond-facies conditions. *Contributions to Mineralogy and Petrology* 167, 1002, [10.1007/s00410-014-1002-x](https://doi.org/10.1007/s00410-014-1002-x).
- Stepanov AS, Rubatto D, Hermann J, Korsakov AV (2016): Contrasting PT paths within the Barchi-Kol UHP terrain (Kokchetav Complex): Implications for subduction and exhumation of continental crust. *American Mineralogist* 101, 788–807, <https://doi.org/10.2138/am-2016-5454>.
- Stern RJ (2005): Evidence from ophiolites, blueschists, and ultrahigh-pressure metamorphic terranes that the modern episode of subduction tectonics began in Neoproterozoic time. *Geology* 33, 557–560, <https://doi.org/10.1130/G21365.1>.
- Stern RJ (2018): The evolution of plate tectonics. In: Hawkesworth C, Brown M (eds), *Earth dynamics and the development of plate tectonics*. *Philosophical Transactions of the Royal Society A* 376, 20170406, <https://doi.org/10.1098/rsta.2017.0406>.
- Stern RJ, Reagan M, Ishizuka O, Ohara Y, Whattam S (2012): To understand subduction initiation, study forearc crust: To understand forearc crust, study ophiolites. *Lithosphere* 4, 469–483, <https://doi.org/10.1130/L183.1>.
- Stern RJ, Leybourne MI, Tsujimori T (2016): Kimberlites and the start of plate tectonics. *Geology* 44, 799–802, <https://doi.org/10.1130/G38024.1>.
- Stöckhert B, Trepmann CA, Massonne HJ (2009): Decrepitated UHP fluid inclusions: about diverse phase assemblages and extreme decompression rates (Erzgebirge, Germany). *Journal of Metamorphic Geology* 27, 673–684, <https://doi.org/10.1111/j.1525-1314.2009.00835.x>.
- St-Onge MR, van Gool JA, Garde AA, Scott DJ (2009): Correlation of Archaean and Palaeoproterozoic units between northeastern Canada and western Greenland: constraining the pre-collisional upper plate accretionary history of the Trans-Hudson orogen. In: Cawood PA, Kröner A (eds), *Earth Accretionary Systems in Space and Time*. Geological Society of London, Special Publications 318, 193–235, <https://doi.org/10.1144/SP318.7>.
- Suggate SM, Hall R (2014): Using detrital garnet compositions to determine provenance: a new compositional database and procedure. In: Scott RA, Smyth HR, Morton AC, Richardson N (eds), *Sediment Provenance Studies in Hydrocarbon Exploration and Production*. Geological Society of London, Special Publications 386, 373–393, <https://doi.org/10.1144/SP386.8>.
- Swainson IP, Dove MT, Palmer DC (2003): Infrared and Raman spectroscopy studies of the α - β phase transition in cristobalite. *Physics and Chemistry of Minerals* 30, 353–365, <https://doi.org/10.1007/s00269-003-0320-8>.
- Tang M, Chen K, Rudnick RL (2016): Archean upper crust transition from mafic to felsic marks the onset of plate tectonics. *Science* 351, 372–375, <https://doi.org/10.1126/science.aad5513>.
- Tang M, Ji WQ, Chu X, Wu A, Chen C (2021a): Reconstructing crustal thickness evolution from europium anomalies in detrital zircons. *Geology* 49, 76–80, <https://doi.org/10.1130/G47745.1>.
- Tang M, Chu X, Hao J, Shen B (2021b): Orogenic quiescence in Earth's middle age. *Science* 371, 728–731, <https://doi.org/10.1126/science.abf1876>.

- Taguchi T, Igami Y, Miyake A, Masaki E (2019): Factors affecting preservation of coesite in ultrahigh-pressure metamorphic rocks: Insights from TEM observations of dislocations within kyanite. *Journal of Metamorphic Geology* 37, 401–414, <https://doi.org/10.1111/jmg.12470>.
- Taguchi T, Kouketsu Y, Igami Y, Kobayashi T, Miyake A (2021): Hidden intact coesite in deeply subducted rocks. *Earth and Planetary Science Letters* 558, 116763, <https://doi.org/10.1016/j.epsl.2021.116763>.
- Tappert R, Stachel T, Harris JW, Muehlenbachs K, Ludwig T, Brey GP (2005): Subducting oceanic crust: The source of deep diamonds. *Geology* 33, 565–568, <https://doi.org/10.1130/G21637.1>.
- Tardieu A, Cansell F, Petit JP (1990): Pressure and temperature dependence of the first-order Raman mode of diamond. *Journal of Applied Physics* 68, 3243–3245, <https://doi.org/10.1063/1.346375>.
- Teraoka Y, Suzuki M, Kawakami K (1998): Provenance of Cretaceous and Paleogene sediments in the Median Zone of Southwest Japan. *Bulletin of the Geological Society of Japan* 49, 395–411.
- Thiessen EJ, Gibson HD, Regis D, Pehrsson SJ, Cutts JA, Smit MA (2019): High-grade metamorphism flying under the radar of accessory minerals. *Geology* 47, 568–572, <https://doi.org/10.1130/G45979.1>.
- Thomson AR, Kohn SC, Prabhu A, Walter MJ (2021): Evaluating the formation pressure of diamond-hosted majoritic garnets: A machine learning majorite barometer. *Journal of Geophysical Research: Solid Earth* 126, p.e2020JB020604, <https://doi.org/10.1029/2020JB020604>.
- Tichomirowa M, Whitehouse M, Gerdes A, Schulz B (2018): Zircon (Hf, O isotopes) as melt indicator: Melt infiltration and abundant new zircon growth within melt rich layers of granulite-facies lenses versus solid-state recrystallization in hosting amphibolite-facies gneisses (central Erzgebirge, Bohemian Massif). *Lithos* 302, 65–85, <https://doi.org/10.1016/j.lithos.2017.12.020>.
- Tolosana-Delgado R, von Eynatten H, Krippner A, Meinhold G (2018): A multivariate discrimination scheme of detrital garnet chemistry for use in sedimentary provenance analysis. *Sedimentary Geology* 375, 14–26, <https://doi.org/10.1016/j.sedgeo.2017.11.003>.
- Tomaschek F, Kennedy AK, Villa IM, Lagos M, Ballhaus C (2003): Zircons from Syros, Cyclades, Greece — recrystallization and mobilization of zircon during high-pressure metamorphism. *Journal of Petrology* 44, 1977–2002, <https://doi.org/10.1093/petrology/egg067>.
- Tomkins HS, Powell R, Ellis DJ (2007): The pressure dependence of the zirconium-in-rutile thermometer. *Journal of Metamorphic Geology* 25, 703–713, <https://doi.org/10.1111/j.1525-1314.2007.00724.x>.
- Toth J, Gurnis M (1998): Dynamics of subduction initiation at preexisting fault zones. *Journal of Geophysical Research: Solid Earth* 103, 18053–18067, <https://doi.org/10.1029/98JB01076>.
- Tracy RJ (1982): Compositional zoning and inclusions in metamorphic minerals. In: Ferry JM (ed), *Characterization of metamorphism through mineral equilibria. Reviews in Mineralogy and Geochemistry* 10, 354–398, <https://doi.org/10.1515/9781501508172-013>.
- Tracy RJ, Robinson P, Thompson AB (1976): Garnet composition and zoning in the determination of temperature and pressure of metamorphism, central Massachusetts. *American Mineralogist* 61, 762–775.
- Triebold S, von Eynatten H, Luvizotto GL, Zack T (2007): Deducing source rock lithology from detrital rutile geochemistry: an example from the Erzgebirge, Germany. *Chemical Geology* 244, 421–436, <https://doi.org/10.1016/j.chemgeo.2007.06.033>.
- Triebold S, von Eynatten H, Zack T (2012): A recipe for the use of rutile in sedimentary provenance analysis. *Sedimentary Geology* 282, 268–275, <https://doi.org/10.1016/j.sedgeo.2012.09.008>.
- Trumbull RB, Krienitz MS, Grundmann G, Wiedenbeck M (2009): Tourmaline geochemistry and $\delta^{11}\text{B}$ variations as a guide to fluid–rock interaction in the Habachtal emerald deposit, Tauern Window, Austria. *Contributions to Mineralogy and Petrology* 157, 411–427, <https://doi.org/10.1007/s00410-008-0342-9>.
- Tsai CH, Liou JG (2000): Eclogite-facies relics and inferred ultrahigh-pressure metamorphism in the North Dabie Complex, central-eastern China. *American Mineralogist* 85, 1–8, <https://doi.org/10.2138/am-2000-0101>.
- Tsujimori T, Ernst WG (2014): Lawsonite blueschists and lawsonite eclogites as proxies for palaeo-subduction zone processes: A review. *Journal of Metamorphic Geology* 32, 437–454, <https://doi.org/10.1111/jmg.12057>.

- Ueda K, Gerya T, Sobolev SV (2008): Subduction initiation by thermal–chemical plumes: numerical studies. *Physics of the Earth and Planetary Interiors* 171, 296–312, <https://doi.org/10.1016/j.pepi.2008.06.032>.
- Usui T, Kobayashi K, Nakamura E (2002): U–Pb isotope systematics of micro-zircon inclusions: Implications for the age and origin of eclogite xenolith from the Colorado Plateau. *Proceedings of the Japan Academy* 78, 51–56, <https://doi.org/10.2183/pjab.78.51>.
- Valley JW, Cavosie AJ, Ushikubo T, Reinhard DA, Lawrence DF, Larson DJ, Clifton PH, Kelly TF, Wilde SA, Moser DE, Spicuzza MJ (2014): Hadean age for a post-magma-ocean zircon confirmed by atom-probe tomography. *Nature Geoscience* 7, 219–223, <https://doi.org/10.1038/ngeo2075>.
- van den Boogaart KG, Tolosana-Delgado R (2008): “Compositions”: a unified R package to analyze compositional data. *Computers & Geosciences* 34, 320–338, <https://doi.org/10.1016/j.cageo.2006.11.017>.
- van der Molen I, van Roermund HLM (1986): The pressure path of solid inclusions in minerals: the retention of coesite inclusions during uplift. *Lithos* 19, 317–324, [https://doi.org/10.1016/0024-4937\(86\)90030-7](https://doi.org/10.1016/0024-4937(86)90030-7).
- van Gool JA, Connelly JN, Marker M, Mengel FC (2002): The Nagssugtoqidian Orogen of West Greenland: tectonic evolution and regional correlations from a West Greenland perspective. *Canadian Journal of Earth Sciences* 39, 665–686, <https://doi.org/10.1139/e02-027>.
- van Hunen J, Moyen JF (2012): Archean subduction: fact or fiction? *Annual Review of Earth and Planetary Sciences* 40, 195–219, <https://doi.org/10.1146/annurev-earth-042711-105255>.
- van Hunen J, van den Berg AP (2008): Plate tectonics on the early Earth: limitations imposed by strength and buoyancy of subducted lithosphere. *Lithos* 103, 217–235, <https://doi.org/10.1016/j.lithos.2007.09.016>.
- van Kranendonk MJ, Smithies HR, Hickman AH, Champion DC (2007): Secular tectonic evolution of Archean continental crust: interplay between horizontal and vertical processes in the formation of the Pilbara Craton, Australia. *Terra Nova* 19, 1–38, <https://doi.org/10.1111/j.1365-3121.2006.00723.x>.
- Vavra G, Gebauer D, Schmid R, Compston W (1996): Multiple zircon growth and recrystallization during polyphase Late Carboniferous to Triassic metamorphism in granulites of the Ivrea Zone (Southern Alps): an ion microprobe (SHRIMP) study. *Contributions to Mineralogy and Petrology* 122, 337–358, <https://doi.org/10.1007/s004100050132>.
- Vavra G, Schmid R, Gebauer D (1999): Internal morphology, habit and U–Th–Pb microanalysis of amphibolite- to granulite-facies zircons: geochronology of the Ivrea Zone (Southern Alps). *Contributions to Mineralogy and Petrology* 134, 380–404, <https://doi.org/10.1007/s004100050492>.
- Venables WN, Ripley BD (2002): *Modern Applied Statistics with S*. Springer-Verlag, New York, <https://doi.org/10.1007/978-0-387-21706-2>.
- Viator DB (2003): Detrital tourmaline as an indicator of provenance: a chemical and sedimentological study of modern sands from the Black Hills, South Dakota. M.Sc. Thesis, Louisiana State University, https://digitalcommons.lsu.edu/gradschool_theses/1520/.
- von Eynatten H, Dunkl I (2012): Assessing the sediment factory: the role of single grain analysis. *Earth-Science Reviews* 115, 97–120, <https://doi.org/10.1016/j.earscirev.2012.08.001>.
- von Eynatten H, Gaupp R (1999): Provenance of Cretaceous synorogenic sandstones in the Eastern Alps: constraints from framework petrography, heavy mineral analysis and mineral chemistry. *Sedimentary Geology* 124, 81–111, [https://doi.org/10.1016/S0037-0738\(98\)00122-5](https://doi.org/10.1016/S0037-0738(98)00122-5).
- von Eynatten H, Gaupp R, Wijbrans JR (1996): $^{40}\text{Ar}/^{39}\text{Ar}$ laser-probe dating of detrital white micas from Cretaceous sedimentary rocks of the Eastern Alps: evidence for Variscan high-pressure metamorphism and implications for Alpine orogeny. *Geology* 24, 691–694, [https://doi.org/10.1130/0091-7613\(1996\)024<0691:AALPDO>2.3.CO;2](https://doi.org/10.1130/0091-7613(1996)024<0691:AALPDO>2.3.CO;2).
- von Eynatten H, Pawlowsky-Glahn V, Egozcue JJ (2002): Understanding perturbation on the simplex: A simple method to better visualize and interpret compositional data in ternary diagrams. *Mathematical Geology* 34, 249–257, <https://doi.org/10.1023/A:1014826205533>.

- von Quadt A, Günther D, Frischknecht R (1997): The evolution of pre-Variscan eclogites of the Tauern Window (Eastern Alps): a Sm/Nd-, conventional and Laser ICP-MS zircon U–Pb study. *Schweizerische Mineralogische und Petrographische Mitteilungen* 77, 265–279.
- Vry JK, Baker JA (2006): LA-MC-ICPMS Pb–Pb dating of rutile from slowly cooled granulites: confirmation of the high closure temperature for Pb diffusion in rutile. *Geochimica et Cosmochimica Acta* 70, 1807–1820, <https://doi.org/10.1016/j.gca.2005.12.006>.
- Wallace LM, Stevens C, Silver E, McCaffrey R, Lorantung W, Hasiata S, Stanaway R, Curley R, Rosa R, Taugaloidi J (2004): GPS and seismological constraints on active tectonics and arc-continent collision in Papua New Guinea: Implications for mechanics of microplate rotations in a plate boundary zone. *Journal of Geophysical Research: Solid Earth* 109, B05404, <https://doi.org/10.1029/2003JB002481>.
- Wan Y, Li R, Wilde SA, Liu D, Chen Z, Yan L, Song T, Yin X (2005): UHP metamorphism and exhumation of the Dabie Orogen, China: evidence from SHRIMP dating of zircon and monazite from a UHP granitic gneiss cobble from the Hefei Basin. *Geochimica et Cosmochimica Acta* 69, 4333–4348, <https://doi.org/10.1016/j.gca.2005.03.055>.
- Wang CY, Campbell IH, Reiners PW, Allen CM (2014): Detrital zircon U–Pb–He double dating: A method of quantifying long-and short-term exhumation rates in collisional orogens. *Science China Earth Sciences* 57, 2702–2711, <https://doi.org/10.1007/s11430-014-4970-9>.
- Wang C, Mitchell RN, Murphy JB, Peng P, Spencer CJ (2021): The role of megacontinents in the supercontinent cycle. *Geology* 49, 402–406, <https://doi.org/10.1130/G47988.1>.
- Watson EB, Harrison TM (2005): Zircon thermometer reveals minimum melting conditions on earliest Earth. *Science* 308, 841–844, <https://doi.org/10.1126/science.1110873>.
- Watson EB, Wark D, Thomas J (2006): Crystallization thermometers for zircon and rutile. *Contributions to Mineralogy and Petrology* 151, 413–433, <https://doi.org/10.1007/s00410-006-0068-5>.
- Webb LE, Baldwin SL, Little TA, Fitzgerald PG (2008): Can microplate rotation drive subduction inversion? *Geology* 36, 823–826, <https://doi.org/10.1130/G25134A.1>.
- Webb LE, Baldwin SL, Fitzgerald PG (2014): The early-middle Miocene subduction complex of the Louisiade Archipelago, southern margin of the Woodlark Rift. *Geochemistry, Geophysics, Geosystems* 15, 4024–4046, <https://doi.org/10.1002/2014GC005500>.
- Webb AAG, Müller T, Zuo J, Haproff PJ, Ramírez-Salazar A (2020): A non–plate tectonic model for the Eoarchean Isua supracrustal belt. *Lithosphere* 12, 166–179, <https://doi.org/10.1130/L1130.1>.
- Wei CJ, Clarke GL (2011): Calculated phase equilibria for MORB compositions: a reappraisal of the metamorphic evolution of lawsonite eclogite. *Journal of Metamorphic Geology* 29, 939–952, <https://doi.org/10.1111/j.1525-1314.2011.00948.x>.
- Weislogel AL, Graham SA, Chang EZ, Wooden JL, Gehrels GE, Yang H (2006): Detrital zircon provenance of the Late Triassic Songpan-Ganzi complex: Sedimentary record of collision of the North and South China blocks. *Geology* 34, 97–100, <https://doi.org/10.1130/G21929.1>.
- Weislogel AL, Graham SA, Chang EZ, Wooden JL, Gehrels GE (2010): Detrital zircon provenance from three turbidite depocenters of the Middle–Upper Triassic Songpan-Ganzi complex, central China: Record of collisional tectonics, erosional exhumation, and sediment production. *GSA Bulletin* 122, 2041–2062, <https://doi.org/10.1130/B26606.1>.
- Weller OM, St-Onge MR (2017): Record of modern-style plate tectonics in the Palaeoproterozoic Trans-Hudson orogen. *Nature Geoscience* 10, 305–311, <https://doi.org/10.1038/ngeo2904>.
- Werner O, Lippolt HJ (2000): White mica $^{40}\text{Ar}/^{39}\text{Ar}$ ages of Erzgebirge metamorphic rocks: simulating the chronological results by a model of Variscan crustal imbrication. In: Franke W, Haak V, Oncken O, Tanner D (eds), *Orogenic Processes: Quantification and Modelling in the Variscan Belt*. Geological Society of London, Special Publications 179, 323–336, <https://doi.org/10.1144/GSL.SP.2000.179.01.19>.
- Whitney DL, Cooke ML, Du Frane SA (2000): Modeling of radial microcracks at corners of inclusions in garnet using fracture mechanics. *Journal of Geophysical Research: Solid Earth* 105, 2843–2853, <https://doi.org/10.1029/1999JB900375>.

- Wickham H, Bryan J (2019): readxl: Read Excel Files. R package version 1.3.1, <https://CRAN.R-project.org/package=readxl>.
- Wickham H, François R, Henry L, Müller K (2019): dplyr: A Grammar of Data Manipulation. R package version 0.8.3, <https://CRAN.R-project.org/package=dplyr>.
- Wilde SA, Valley JW, Peck WH, Graham CM (2001): Evidence from detrital zircons for the existence of continental crust and oceans on the Earth 4.4 Gyr ago. *Nature* 409, 175–178, <https://doi.org/10.1038/35051550>.
- Wilke CO (2020): cowplot: Streamlined Plot Theme and Plot Annotations for 'ggplot2'. R package version 1.1.1, <https://CRAN.R-project.org/package=cowplot>.
- Willner AP, Rötzler K, Maresch WV (1997): Pressure-temperature and fluid evolution of quartzo-feldspathic metamorphic rocks with a relic high-pressure, granulite-facies history from the Central Erzgebirge (Saxony, Germany). *Journal of Petrology* 38, 307–336, <https://doi.org/10.1093/ptroj/38.3.307>.
- Willner AP, Krohe A, Maresch WV (2000): Interrelated P–T–t–d paths in the Variscan Erzgebirge dome (Saxony, Germany): Constraints on the rapid exhumation of high-pressure rocks from the root zone of a collisional orogen. *International Geology Review* 42, 64–85, <https://doi.org/10.1080/00206810009465070>.
- Willner AP, Sebazungu E, Gerya TV, Maresch WV, Krohe A (2002): Numerical modelling of PT-paths related to rapid exhumation of high-pressure rocks from the crustal root in the Variscan Erzgebirge Dome (Saxony/Germany). *Journal of Geodynamics* 33, 281–314, [https://doi.org/10.1016/S0264-3707\(01\)00071-0](https://doi.org/10.1016/S0264-3707(01)00071-0).
- Xie S, Wu Y, Zhang Z, Qin Y, Liu X, Wang H, Qin Z, Liu Q, Yang S (2012): U–Pb ages and trace elements of detrital zircons from Early Cretaceous sedimentary rocks in the Jiaolai Basin, north margin of the Sulu UHP terrane: Provenances and tectonic implications. *Lithos* 154, 346–360, <https://doi.org/10.1016/j.lithos.2012.08.002>.
- Xu C, Kynický J, Song W, Tao R, Lü Z, Li Y, Yang Y, Pohanka M, Galiova MV, Zhang L, Fei Y (2018): Cold deep subduction recorded by remnants of a Paleoproterozoic carbonated slab. *Nature Communications* 9, 2790, <https://doi.org/10.1038/s41467-018-05140-5>.
- Yamamoto S, Senshu H, Rino S, Omori S, Maruyama S (2009): Granite subduction: Arc subduction, tectonic erosion and sediment subduction. *Gondwana Research* 15, 443–453, <http://dx.doi.org/10.1016/j.gr.2008.12.009>.
- Ye K, Yao Y, Katayama I, Cong B, Wang Q, Maruyama S (2000): Large areal extent of ultrahigh-pressure metamorphism in the Sulu ultrahigh-pressure terrane of East China: new implications from coesite and omphacite inclusions in zircon of granitic gneiss. *Lithos* 52, 157–164, [https://doi.org/10.1016/S0024-4937\(99\)00089-4](https://doi.org/10.1016/S0024-4937(99)00089-4).
- Yong W, Dachs E, Benisek A, Secco RA (2012): Heat capacity, entropy and phase equilibria of stishovite. *Physics and Chemistry of Minerals* 39, 153–162, <https://doi.org/10.1007/s00269-011-0470-z>.
- Zack T, Kooijman E (2017): Petrology and geochronology of rutile. *Reviews in Mineralogy and Geochemistry* 83, 443–467, <https://doi.org/10.2138/rmg.2017.83.14>.
- Zack T, Luvizotto GL (2006): Application of rutile thermometry to eclogites. *Mineralogy and Petrology* 88, 69–85, <https://doi.org/10.1007/s00710-006-0145-5>.
- Zack T, von Eynatten H, Kronz A (2004a): Rutile geochemistry and its potential use in quantitative provenance studies. *Sedimentary Geology* 171, 37–58, <https://doi.org/10.1016/j.sedgeo.2004.05.009>.
- Zack T, Moraes R, Kronz A (2004b): Temperature dependence of Zr in rutile: empirical calibration of a rutile thermometer. *Contributions to Mineralogy and Petrology* 148, 471–488, <https://doi.org/10.1007/s00410-004-0617-8>.
- Zack T, Stockli DF, Luvizotto GL, Barth MG, Belousova E, Wolfe MR, Hinton RW (2011): In situ U–Pb rutile dating by LA-ICP-MS: ²⁰⁸Pb correction and prospects for geological applications. *Contributions to Mineralogy and Petrology* 162, 515–530, <https://doi.org/10.1007/s00410-011-0609-4>.

- Zhang RY, Liou JG (1996): Coesite inclusions in dolomite from eclogite in the southern Dabie Mountains, China: the significance of carbonate minerals in UHPM rocks. *American Mineralogist* 81, 181–186, <https://doi.org/10.2138/am-1996-1-222>.
- Zhang Z, Saxena SK (1991): Thermodynamic properties of andradite and application to skarn with coexisting andradite and hedenbergite. *Contributions to Mineralogy and Petrology* 107, 255–263.
- Zhang L, Wang Y (2020): The exhumation of high- and ultrahigh-pressure metamorphic terranes in subduction zone: Questions and discussions. *Science China Earth Sciences* 63, 1884–1903, <https://doi.org/10.1007/s11430-020-9579-3>.
- Zhang RY, Hirajima T, Banno S, Cong B, Liou JG (1995): Petrology of ultrahigh-pressure rocks from the southern Su-Lu region, eastern China. *Journal of Metamorphic Geology* 13, 659–675, <https://doi.org/10.1111/j.1525-1314.1995.tb00250.x>.
- Zhang KJ, Li B, Wei QG, Cai JX, Zhang YX (2008): Proximal provenance of the western Songpan–Ganzi turbidite complex (Late Triassic, eastern Tibetan plateau): Implications for the tectonic amalgamation of China. *Sedimentary Geology* 208, 36–44, <https://doi.org/10.1016/j.sedgeo.2008.04.008>.
- Zhang ZM, Schertl HP, Wang JL, Shen K, Liou JG (2009): Source of coesite inclusions within inherited magmatic zircon from Sulu UHP rocks, eastern China, and their bearing for fluid–rock interaction and SHRIMP dating. *Journal of Metamorphic Geology* 27, 317–333, <https://doi.org/10.1111/j.1525-1314.2009.00819.x>.
- Zhang KJ, Li B, Wei QG (2012): Diversified provenance of the Songpan–Ganzi Triassic turbidites, central China: constraints from geochemistry and Nd isotopes. *Journal of Geology* 120, 69–82, <https://doi.org/10.1086/662716>.
- Zhong X, Andersen NH, Dabrowski M, Jamtveit B (2019): Zircon and quartz inclusions in garnet used for complementary Raman thermobarometry: application to the Holsnøy eclogite, Bergen Arcs, Western Norway. *Contributions to Mineralogy and Petrology* 174, 50, <https://doi.org/10.1007/s00410-019-1584-4>.
- Zhong X, Moulas E, Tajčmanová L (2020): Post-entrapment modification of residual inclusion pressure and its implications for Raman elastic thermobarometry. *Solid Earth* 11, 223–240, <https://doi.org/10.5194/se-11-223-2020>.
- Zhou T, Li Q, Klemd R, Shi Y, Tang X, Li C, Liu Y (2020): Multi-system geochronology of North Dabie eclogite: Ineffective garnet ‘shielding’ on rutile inclusions under multi-thermal conditions. *Lithos* 368, 105573, <https://doi.org/10.1016/j.lithos.2020.105573>.
- Zhukov VP, Korsakov AV (2015): Evolution of host-inclusion systems: a visco-elastic model. *Journal of Metamorphic Geology* 33, 815–828, <https://doi.org/10.1111/jmg.12149>.
- Zicovich-Wilson CM, Pascale F, Roetti C, Saunders VR, Orlando R, Dovesi R (2004): Calculation of the vibration frequencies of α -quartz: The effect of Hamiltonian and basis set. *Journal of Computational Chemistry* 25, 1873–1881, <https://doi.org/10.1002/jcc.20120>.
- Ziegler A, König IR (2014): Mining data with random forests: current options for real-world applications. *Wiley Interdisciplinary Reviews: Data Mining and Knowledge Discovery* 4, 55–63, <https://doi.org/10.1002/widm.1114>.
- Zirakparvar NA, Baldwin SL, Vervoort JD (2011): Lu–Hf garnet geochronology applied to plate boundary zones: Insights from the (U)HP terrane exhumed within the Woodlark Rift. *Earth and Planetary Science Letters* 309, 56–66, <https://doi.org/10.1016/j.epsl.2011.06.016>.
- Zirakparvar NA, Baldwin SL, Vervoort JD (2013): The origin and geochemical evolution of the Woodlark Rift of Papua New Guinea. *Gondwana Research* 23, 931–943, <https://doi.org/10.1016/j.gr.2012.06.013>.
- Zirakparvar NA, Baldwin SL, Schmitt AK (2014): Zircon growth in (U)HP quartzo-feldspathic host gneisses exhumed in the Woodlark Rift of Papua New Guinea. *Geochemistry, Geophysics, Geosystems* 15, 1258–1282, <https://doi.org/10.1002/2013GC004964>.

Supplementary Information – Chapter 2

Electronic Appendix 2e-A

Mineral inclusion data

– *schoenig_2021_PhD_thesis_electronic_appendix_2e-A.xlsx*

Electronic Appendix 2e-B

Coesite inclusion data

– *schoenig_2021_PhD_thesis_electronic_appendix_2e-B.xlsx*

Electronic Appendix 2e-C

Diamond inclusion data

– *schoenig_2021_PhD_thesis_electronic_appendix_2e-C.xlsx*

Electronic Appendix 2e-D

Detrital garnet composition

– *schoenig_2021_PhD_thesis_electronic_appendix_2e-D.xlsx*

Electronic Appendix 2e-E

Garnet composition of local crystalline rocks

– *schoenig_2021_PhD_thesis_electronic_appendix_2e-E.xlsx*

Appendix 2-A

Samples

Coordinates of the seven investigated modern sand samples marked in Figure 2.1-1 are given in Table Appendix 2-A 1.

Modern sands were wet sieved to extract the 125–250 μm grain-size fraction, treated with acetic acid, and the heavy mineral fraction was separated by centrifugation using sodium polytungstate with a density of 2.83–2.88 $\text{g}\times\text{cm}^{-3}$ and embedded in synthetic mounts using a bonding epoxy. The mounts were grounded with silicon carbide abrasive paper and polished in five steps with Al_2O_3 abrasives in water suspension up to the finest step with a particle size of 0.05 μm .

**Table Appendix 2-A 1:
Coordinates of modern sand sampling locations**

Sample	Northing	Easting	Creek/River	
			width	Type
JS-Erz-3s	50.74352°	13.24847°	~1.5 m	mixed sample (~5 m sector)
JS-Erz-5s	50.73924°	13.26169°	~3.0 m	mixed sample (~10 m sector)
JS-Erz-6s	50.73537°	13.29782°	~1.0 m	mixed sample (~20 m sector)
JS-Erz-8s	50.74233°	13.30458°	~1.0 m	mixed sample (~10 m sector)
JS-Erz-9s	50.72633°	13.25883°	~1.5 m	mixed sample (~10 m sector)
JS-Erz-13s	50.74862°	13.19472°	~4.0 m	mixed sample (~10 m sector)
JS-Erz-14s	50.76142°	13.17091°	~20.0 m	mixed sample (~60 m sector)

Raman spectroscopy

From each of the seven samples, all mineral inclusions $\geq 2 \mu\text{m}$ were identified in 100 detrital garnets (those without mineral inclusions $\geq 2 \mu\text{m}$ were not considered) by using a Horiba Jobin Yvon XploRA Plus Raman spectrometer equipped with an Olympus BX41 microscope at the University of Göttingen (Geosciences Center, Department of Sedimentology and Environmental Geology). The obtained inclusion spectra were compared with the RRUFF database (Lafuente et al. 2015). Measurements were performed using a 532 nm laser ($\sim 11 \text{ mW}$ at sample surface), a $1800 \text{ l}\times\text{mm}^{-1}$ grating, an $100\times$ LWD objective with a numerical aperture of 0.8, and a confocal hole diameter and slit of $100 \mu\text{m}$. The spectrometer was calibrated on the 520.7 cm^{-1} line of silicon, and the recorded spectrum was centered at 840 cm^{-1} , covering a spectral field between $\sim 70 \text{ cm}^{-1}$ and $\sim 1650 \text{ cm}^{-1}$. The method of inclusion identification and the classification of inclusion types are described in Schönig et al. (2018b). In this study, we did not discriminate between apatite and monazite due to their similar Raman spectra and the limited significance for source rock characterization. However, randomly we checked the OH-region between 3000 and 4000 cm^{-1} of the inclusion spectra and note the presence or absence of OH under remarks in Electronic Appendix 2e-A.

To determine the position of the main bands of diamond and coesite inclusions, the Raman spectra of all identified inclusions were captured again using a specific calibration and correction method. The $2400 \text{ l}\times\text{mm}^{-1}$ grating was used to achieve the highest resolution. For diamond inclusions the spectrometer was calibrated on the 1331.7 cm^{-1} line of diamond, and for coesite inclusions on the 520.7 cm^{-1} line of silicon. The center of the spectrum was left in the same position like during the calibration, i.e., 1331.74 cm^{-1} and 520.62 cm^{-1} , respectively. These positions are close to the positions of the diamond ($\sim 1331.7 \text{ cm}^{-1}$) and coesite ($\sim 520.7 \text{ cm}^{-1}$) main bands at atmospheric pressure and room temperature (e.g., Krishnamurti 1954; Schönig et al. 2018a). Due to possible small inaccuracies of the calibration, a possible drift during the measurement sessions and/or a possible stretching or compression of the spectral field, a correction of the main band positions was performed using distinctive spectral lines of a neon glow lamp as reference positions. The light of the neon glow lamp was captured simultaneously with the spectrum from every inclusion by using a laser power of $\sim 0.04\text{--}4.44 \text{ mW}$ and an acquisition time of $600\text{--}1200 \text{ s}$. Spectra evaluation was performed within the Labspec 6.4.4 software by subtracting the background by a polynomial baseline fit, adding Gaussian Lorentzian mixed functions (pseudo-Voigt) at up to four selected neon reference line positions and the diamond/coesite

main band, and fitting the functions to the captured spectra. Selected neon reference line positions are Ne #1 at 568.982 nm (i.e., 1214.667 cm^{-1} relative), Ne #2 at 571.923 nm (i.e., 1305.044 cm^{-1} relative), Ne #3 at 574.830 nm (i.e., 1393.475 cm^{-1} relative), and Ne #4 at 576.442 nm (i.e., 1442.126 cm^{-1} relative) for diamond; and Ne #1 at 540.065 nm (i.e., 273.336 cm^{-1} relative), Ne #2 at 541.265 nm (i.e., 314.684 cm^{-1} relative), Ne #3 at 543.365 nm (i.e., 386.093 cm^{-1} relative), and Ne #4 556.277 nm (i.e., 813.263 cm^{-1} relative) for coesite. The measured main band position of every diamond/coesite was corrected by a quadratic regression function (linear when only two neon lines are considered) based on the difference between the measured neon line positions compared to their reference positions. Based on the determined diamond main band positions compared to the positions at atmospheric pressure and room temperature, inclusion pressures were calculated by using the experimentally ratio of 1 GPa per 2.64 cm^{-1} for diamond (Tardieu et al. 1990). Results are given in Electronic Appendix 2e-B and Electronic Appendix 2e-C.

Inclusion sizes were determined within the Labspec software using the 100 \times LWD objective. Stated are the long and short axes (0.5 μm steps) in a two-dimensional (plane) view as situated in the garnet grains and embedded in the epoxy. The closest distance to the garnet surface was determined by focusing through the grain, which can be slightly imprecise if the closest distance is in direction of the lower surface.

Electron Microprobe

After inclusion analysis by Raman spectroscopy, the chemical composition of all analyzed garnets that contain inclusions $\geq 2 \mu\text{m}$ was determined by wavelength-dispersive spectroscopy (Electronic Appendix 2e-D). Measurements were performed at the University of Göttingen (Geosciences Center, Department

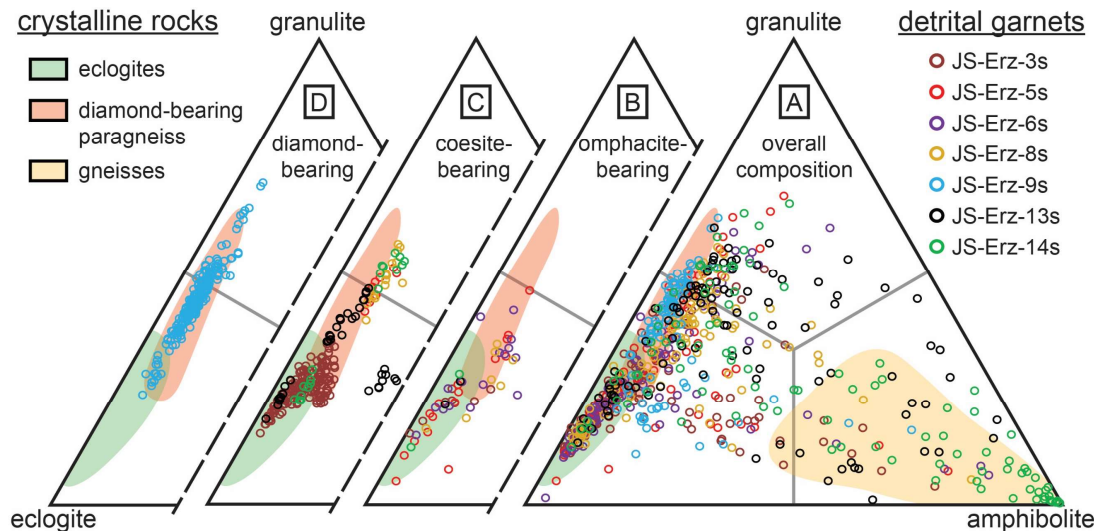


Figure Appendix 2-A 1: Geochemical classification of detrital garnets after Tolosana-Delgado et al. (2018) showing the probabilities of being derived from eclogite-, granulite-, or amphibolite-facies rocks. The entire electron microprobe dataset is given in Electronic Appendix 2e-D. A: Probabilities of all detrital garnets (n = 696; one spot per grain). B: Probabilities of omphacite-bearing garnets (n = 51; one spot per grain; one outlier not shown). C: Probabilities of coesite-bearing garnets (n = 234; 9 spots per grain). D: Probabilities of diamond-bearing garnets (n = 198; 9 spots per grain). For comparison, garnet data of local crystalline rocks are shown as envelopes (Electronic Appendix 2e-E).

of Geochemistry) using a JEOL JXA 8900 RL electron microprobe equipped with five wavelength dispersive spectrometers. Before analysis, all samples were coated with carbon to ensure conductivity. Measurement conditions include an accelerating voltage of 15 kV and a beam current of 20 nA. Counting times were 15 s for Si, Mg, Ca, Fe and Al, and 30 s for Ti, Cr and Mn. The spot of the electron beam was adjusted to the center of the garnet grains except for grains with fractures or inclusions at the center, where the beam spot was adjusted to an undisturbed garnet mantle position. From the 700 analyzed garnets, four measurement results were discarded (totals not close to 100 wt% or interference with inclusions). The composition of diamond- and coesite-bearing garnets was determined at nine spots of each garnet: one at the center, four at the mantle, and four at the rim (in each case two in horizontal (x) direction and two in vertical (y) direction). For garnet classification, besides the molar proportions plotted in Figure 2.4-1, also multivariate statistics after Tolosana-Delgado et al. (2018) were performed using the prior probability 'equal-M' (Figure Appendix 2-A 1). The results support the trends observed in the Figure 2.4-1.

Supplementary Information – Chapter 3

Electronic Appendix 3e-A

Mineral inclusion assemblages and compositions of coesite-, diamond-, cristobalite-, kokchetavite-, and kumdykolite-bearing garnet grains

– *schoenig_2021_PhD_thesis_electronic_appendix_3e-A.xlsx*

Electronic Appendix 3e-B

Garnet composition of local crystalline rocks

– *schoenig_2021_PhD_thesis_electronic_appendix_3e-B.xlsx*

Appendix 3-A

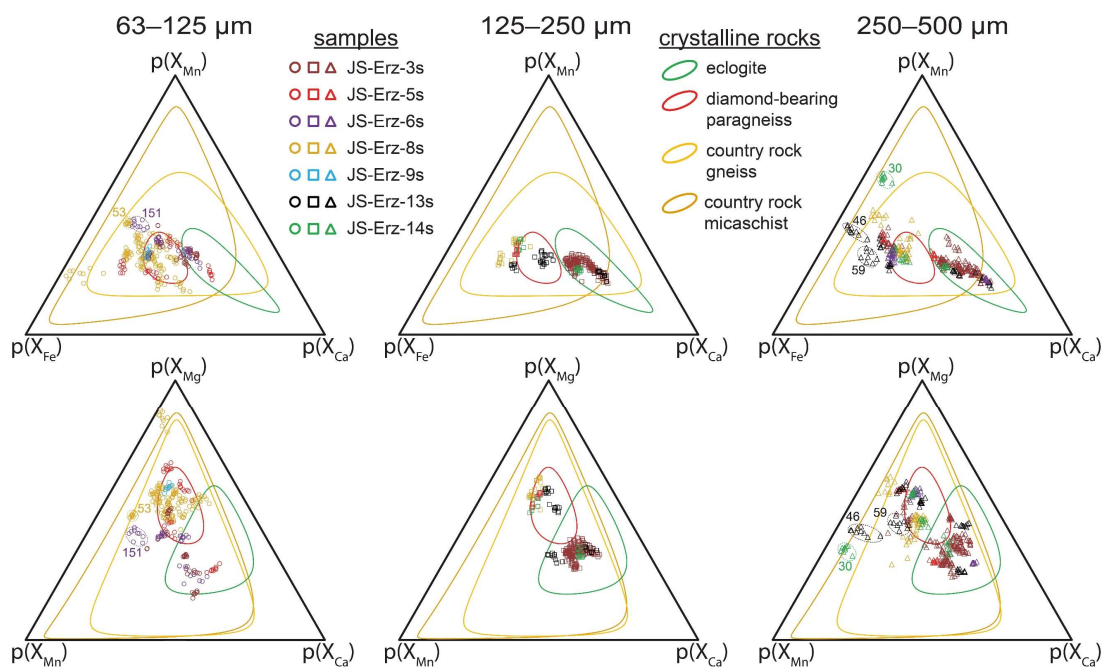


Figure Appendix 3-A 1: Chemistry of coesite-bearing detrital garnet grains shown in perturbed ternary plots. Perturbation after von Eynatten et al. (2002).

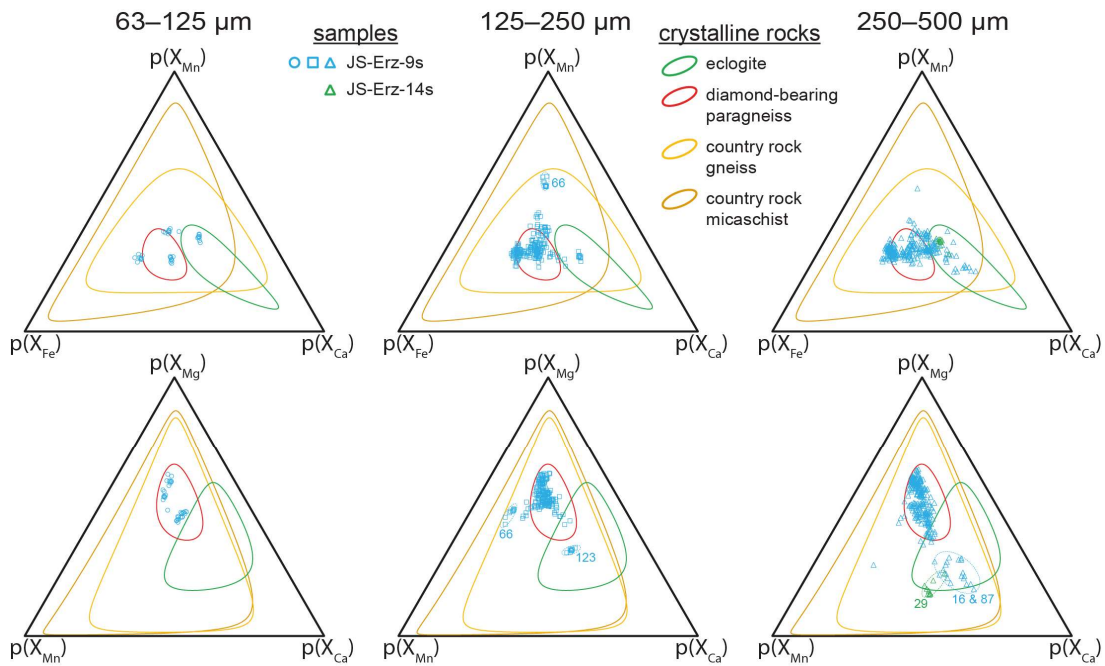


Figure Appendix 3-A 2: Chemistry of diamond-bearing detrital garnet grains shown in perturbed ternary plots. Perturbation after von Eynatten et al. (2002).

Supplementary Information – Chapter 4

Electronic Appendix 4e-A

Detrital garnet compositions and their inclusion suites

– *schoenig_2021_PhD_thesis_electronic_appendix_4e-A.xlsx*

Electronic Appendix 4e-B

Garnet compositions from basement rocks and their inclusion suites. Samples are from the catchment area of the placer deposit, southern Goodenough Island

– *schoenig_2021_PhD_thesis_electronic_appendix_4e-B.xlsx*

Electronic Appendix 4e-C

Compilation of garnet compositions for D'Entrecasteaux Islands basement rocks

– *schoenig_2021_PhD_thesis_electronic_appendix_4e-C.xlsx*

Electronic Appendix 4e-D

Quartz-in-garnet and zircon-in-garnet elastic thermobarometric data for detrital garnets

– *schoenig_2021_PhD_thesis_electronic_appendix_4e-D.xlsx*

Supplementary Information – Chapter 5

Electronic Appendix 5e-A

Mineral inclusions and garnet composition

– schoenig_2021_PhD_thesis_electronic_appendix_5e-A.xlsx

Appendix 5-A

Detailed information on rutile-bearing garnet

Rutile, the most frequent inclusion type, occurs in garnet of all compositions (Figure Appendix 5-A 1). Comparing the kernel density plots of rutile-bearing garnet grains with that of all inclusion-bearing garnet grains (Figure 5.4-1), the distribution pattern is rather similar and there are only minor variations with rutile-bearing garnet being slightly more frequent in garnet from high-grade metamorphic sources. Between the samples, there is a minor variation with regard to rutile-bearing garnet abundance and most samples show amounts ~60 %, except JS-Erz-3s which shows a significantly lower frequency (Figure Appendix 5-A 1, bar chart). However, rutile-bearing garnet frequency and source rock composition do not correlate because samples from catchments being dominated by felsic rocks (JS-Erz-8s, JS-Erz-9s, and JS-Erz-13s) as well as catchments with higher proportions of eclogite (JS-Erz-3s, JS-Erz-5s, and JS-Erz-6s) internally show significant variation in rutile-bearing garnet frequency.

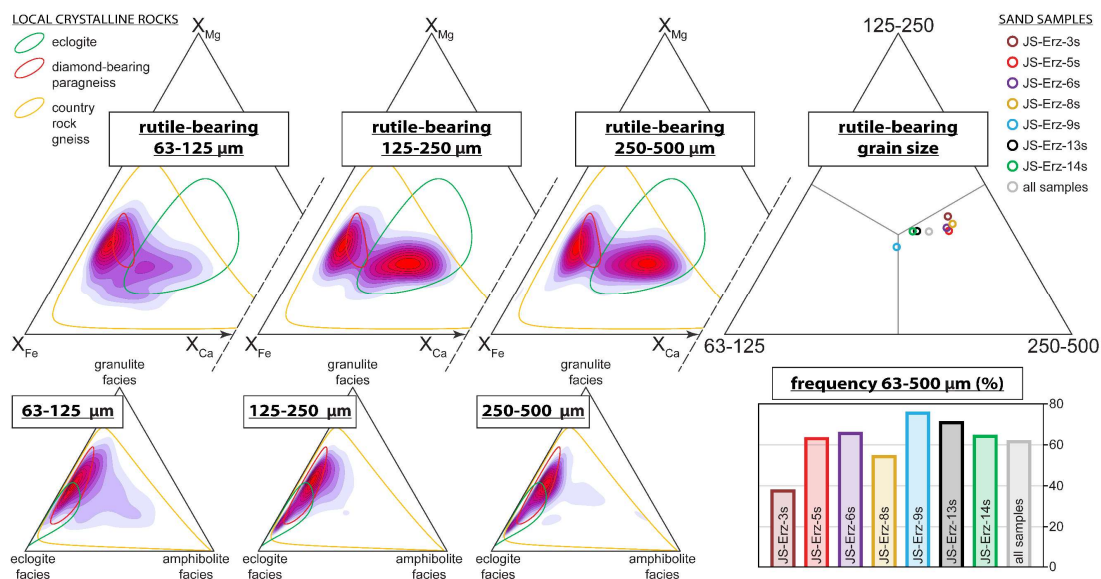


Figure Appendix 5-A 1: Composition, grain-size distribution, and frequency of rutile-bearing detrital garnet. Compositional distributions are shown for the three grain-size fractions as kernel density estimate heatmaps in the X_{Fe} – X_{Mg} – X_{Ca} ternary plots and in the probability ternary plots of metamorphic garnet after multivariate discrimination (Tolosana-Delgado et al. 2018). See Electronic Appendix 5e-A for the dataset. For comparison, garnet composition of local crystalline rocks compiled by Schönig et al. (2020) are shown as 95 % confidence ellipsoids. Grain-size distributions of rutile-bearing garnet for the individual samples are illustrated in a ternary plot showing relative proportions for the number of grains in each analyzed grain-size fraction. The frequencies of rutile-bearing garnet for the individual samples of the entire analyzed grain-size window of 63–500 μm are shown in a bar plot.

In the ternary grain-size distribution plot of rutile-bearing garnet in Figure Appendix 5-A 1, it is shown that rutile-bearing garnet is slightly enriched in the 125–250 μm and even more in the 250–500 μm fraction compared to the 63–125 μm fraction. In addition, samples having lower abundancies in rutile-bearing garnet (JS-Erz-3s, JS-Erz-5s, and JS-Erz-8s) are even more enriched in the coarse fractions. Thus, it can be concluded that the amount of garnet containing a specific inclusion type generally increases with increasing grain size and that this source rock independent effect is more pronounced for inclusion types occurring in lower proportions. This effect is caused by the increasing garnet volume analyzed with increasing grain size, making it more likely to contain a specific inclusion type, in particular when the inclusion frequency of this mineral phase is rather low.

Detailed information on omphacite-bearing garnet

Omphacite co-existing with garnet is the diagnostic mineral assemblage of eclogite-facies metamorphism. Potentially, omphacite-bearing garnet could derive from felsic eclogite-facies rocks but in the investigated area omphacite inclusions in garnet as well symplectites after omphacite in felsic rocks occur occasionally (Willner et al. 1997). Thus, omphacite-bearing garnet seems to be an appropriate indicator for the mafic high-grade source rocks (i.e., eclogites), which is supported by the composition of detrital garnet grains containing omphacite, which almost exclusively matching with the 95 % confidence ellipsoid for the composition of garnet from local eclogite (Figure Appendix 5-A 2). Only in the 63–125 μm fraction minor proportions of omphacite-bearing garnet point to felsic affinity.

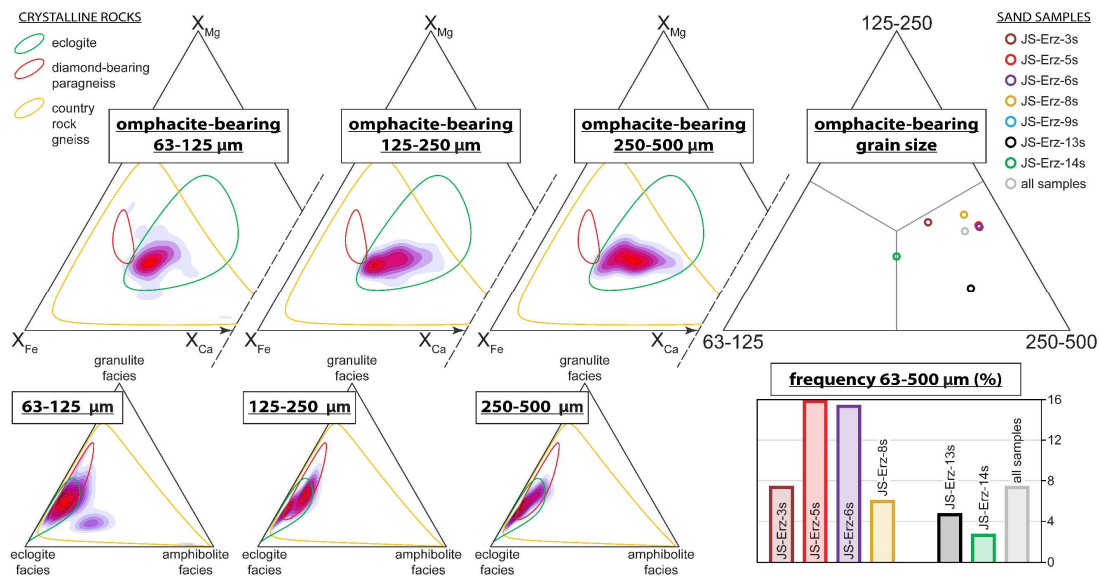


Figure Appendix 5-A 2: Composition, grain-size distribution, and frequency of omphacite-bearing detrital garnet. Compositional distributions are shown for the three grain-size fractions as kernel density estimate heatmaps in the $X_{\text{Fe}}-X_{\text{Mg}}-X_{\text{Ca}}$ ternary plots and in the probability ternary plots of metamorphic garnet after multivariate discrimination (Tolosana-Delgado et al. 2018). See Electronic Appendix 5e-A for the dataset. For comparison, garnet composition of local crystalline rocks compiled by Schönig et al. (2020) are shown as 95 % confidence ellipsoids. Grain-size distributions of omphacite-bearing garnet for the individual samples are illustrated in a ternary plot showing relative proportions for the number of grains in each analyzed grain-size fraction. The frequencies of omphacite-bearing garnet for the individual samples of the entire analyzed grain-size window of 63–500 μm are shown in a bar plot.

Considering the frequency of garnet grains containing omphacite inclusions, the high proportion of eclogite occurring in the catchments of samples JS-Erz-3s, JS-Erz-5s, and JS-Erz-6s is well-reflected, although JS-Erz-3s shows lower amounts than the two latter (Figure Appendix 5-A 2, bar plot). In contrast, the dominantly felsic composition of country rocks in catchments from samples JS-Erz-8s, JS-Erz-9s, and JS-Erz-13s is reflected by lower omphacite-bearing garnet frequencies, although JS-Erz-8s shows higher amounts than the latter two. In addition, the dilution effect by garnet grains from lower-grade metamorphic rocks in sample JS-Erz-14s as implied by garnet chemistry (see Section 5.4.1) is also supported by low proportions of omphacite-bearing garnet. In the grain-size distribution plot of omphacite-bearing garnet in Figure Appendix 5-A 2, it is clearly indicated that garnet containing omphacite is enriched in the coarse fraction independently from the proportion of eclogite occurring in the catchment. This agrees with previous observations of an increasing metamorphic grade with increasing garnet grain size (Figure 5.1-1), and the typical large garnet crystal size in eclogite leading to a grain-size inheritance effect.

Detailed information on graphite-bearing garnet

Contrary to omphacite-bearing garnet, garnet containing inclusions of graphite are a characteristic feature of felsic para-metamorphic rocks. This is supported by their compositional variation covering the entire range of local felsic rocks and only marginally overlap with that of eclogite reflecting the general compositional overlap of felsic and eclogitic rocks (Figure Appendix 5-A 3). Graphite-bearing garnet frequency correlates negatively with that of omphacite-bearing garnet, and thus again well reflect

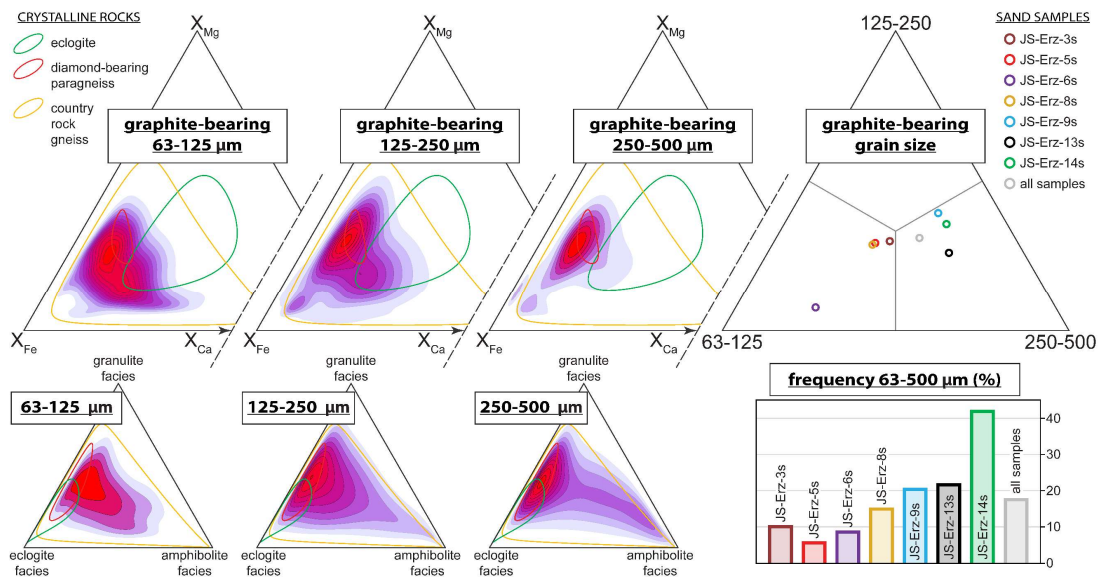


Figure Appendix 5-A 3: Composition, grain-size distribution, and frequency of graphite-bearing detrital garnet. Compositional distributions are shown for the three grain-size fractions as kernel density estimate heatmaps in the $X_{Fe}-X_{Mg}-X_{Ca}$ ternary plots and in the probability ternary plots of metamorphic garnet after multivariate discrimination (Tolosana-Delgado et al. 2018). See Electronic Appendix 5e-A for the dataset. For comparison, garnet composition of local crystalline rocks compiled by Schönig et al. (2020) are shown as 95 % confidence ellipsoids. Grain-size distributions of graphite-bearing garnet for the individual samples are illustrated in a ternary plot showing relative proportions for the number of grains in each analyzed grain-size fraction. The frequencies of graphite-bearing garnet for the individual samples of the entire analyzed grain-size window of 63–500 μm are shown in a bar plot.

the geological framework of the catchments (Figure Appendix 5-A 3, bar plots). Compared to the grain-size distributions of rutile- and omphacite-bearing garnet, which internally have a quite similar pattern for almost all samples, graphite-bearing garnet in the individual samples show strong variations regarding grain size (cf. Figure Appendix 5-A 1, Figure Appendix 5-A 2, and Figure Appendix 5-A 3, grain-size plots). Samples JS-Erz-9s, JS-Erz-13s, and JS-Erz-14s show an increase of graphite-bearing garnet with increasing grain size. In contrast, in particular sample JS-Erz-6s but also JS-Erz-3s, JS-Erz-5s, and JS-Erz-8s show enrichment of graphite-bearing garnet in the 63–125 μm fraction. These grain-size relations are caused by the dominant occurrence of omphacite-bearing garnet in the coarse fractions (125–250 and 250–500 μm) diluting the amount of graphite-bearing garnet. Samples containing minor amounts of omphacite-bearing garnet due to the low proportion of eclogitic sources, i.e., JS-Erz-9s, JS-Erz-13s, and JS-Erz-14s, show an increase of graphite-bearing garnet with increasing grain size due to the larger garnet volume analyzed as discussed for rutile-bearing garnet (see above). In contrast, samples containing higher amounts of omphacite-bearing garnet like JS-Erz-5s and JS-Erz-6s, but also JS-Erz-3s and JS-Erz-8s, show enrichment of graphite-bearing garnet in the 63–125 μm fraction. This dilution effect can be best observed by following the development of omphacite- and graphite-bearing garnet from sample JS-Erz-8s (upstream) to sample JS-Erz-6s (downstream, Figure 5.2-1b). Compared to the other samples, JS-Erz-8s shows an intermediate amount of omphacite-bearing garnet enriched in the coarse fractions and an intermediate amount of graphite-bearing garnet slightly enriched in the fine fraction (Figure Appendix 5-A 2 and Figure Appendix 5-A 3). Farther downstream, the catchment of the sampled creek drains a large eclogite body at its western site leading to a significant increase of omphacite-bearing garnet in JS-Erz-6s being even stronger enriched in the coarse fraction (Figure Appendix 5-A 2), and a decrease of graphite-bearing garnet being highly enriched in the fine fraction (Figure Appendix 5-A 3).

Detailed information on quartz- and kyanite-bearing garnet

As graphite-bearing garnet represents the entire range of exclusively felsic sources and its grain-size distribution is highly affected by the proportion of eclogitic source rocks (see above), graphite-bearing garnet is not suitable to evaluate the grain-size distribution of garnet from lower grade felsic sources, i.e., country rock gneiss, compared to high-grade felsic sources similar to the diamond-bearing paragneiss. For that, the distribution of garnet containing inclusions of quartz and kyanite are more suitable. Both inclusion types are mainly a feature of the felsic sources (e.g., Willner et al. 1997; Nasdala & Massonne 2000), which is supported by garnet chemistry from all grain-size fractions (Figure Appendix 5-A 4). However, both types subordinately also occur in eclogite (e.g., Schmädicke et al. 1992; Gose & Schmädicke 2018), as supported by smaller populations matching with the composition of garnet from local eclogite (Figure Appendix 5-A 4). Thus, quartz- and kyanite-bearing garnet mainly represent felsic sources and their grain-size distribution is less affected by varying proportions of eclogitic sources. In addition, detrital garnet composition reveals that the amount of quartz-bearing garnet is more pronounced for lower-grade felsic sources (i.e., country rock gneisses), whereas the amount of kyanite-bearing garnet is more pronounced for high-grade felsic sources (Figure Appendix 5-A 4).

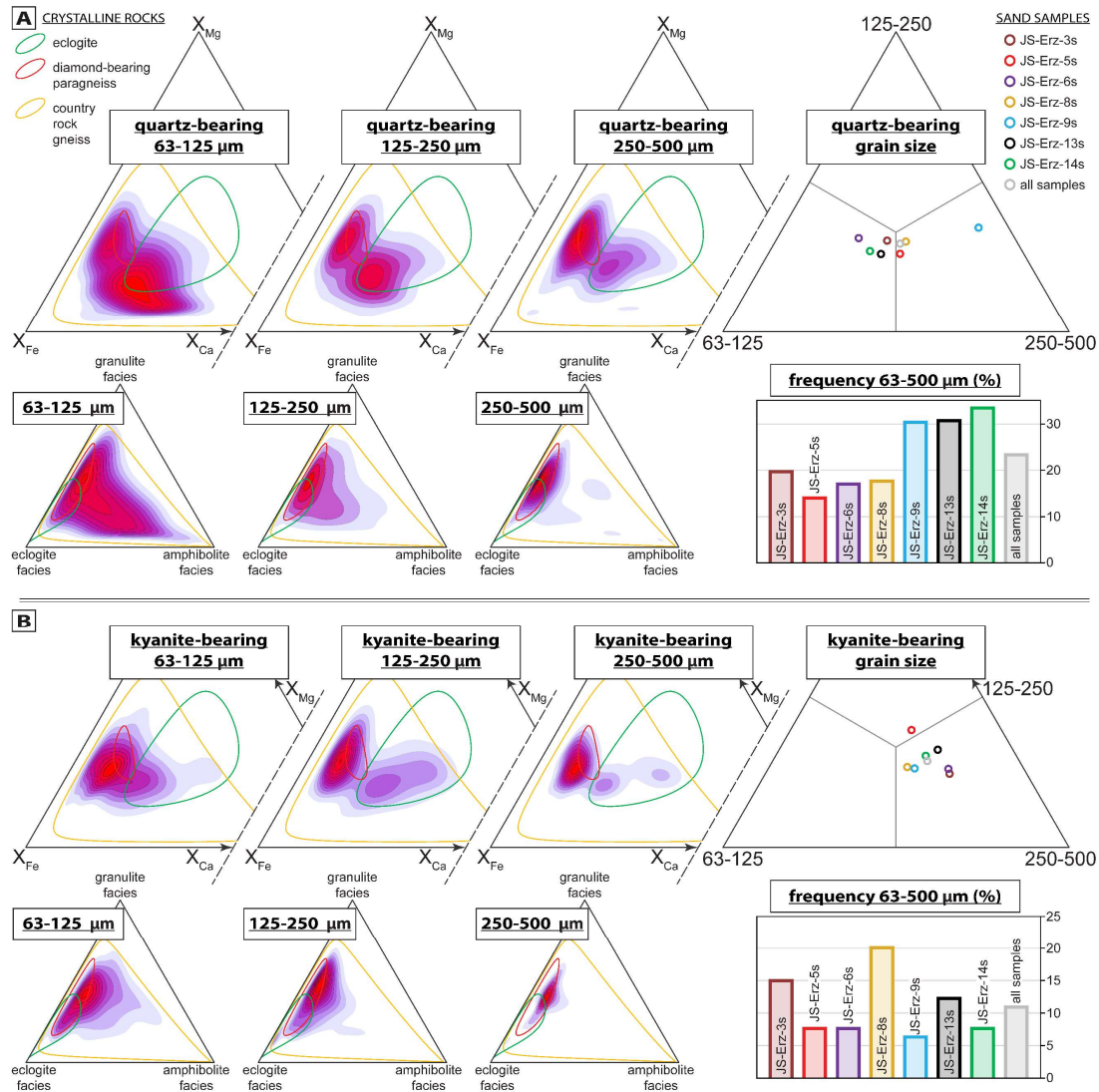


Figure Appendix 5-A 4: Composition, grain-size distribution, and frequency of (A) quartz- and (B) kyanite-bearing detrital garnet. Compositional distributions are shown for the three grain-size fractions as kernel density estimate heatmaps in the $X_{Fe}-X_{Mg}-X_{Ca}$ ternary plots and in the probability ternary plots of metamorphic garnet after multivariate discrimination (Tolosana-Delgado et al. 2018). See Electronic Appendix 5e-A for the dataset. For comparison, garnet composition of local crystalline rocks compiled by Schönig et al. (2020) are shown as 95 % confidence ellipsoids. Grain-size distributions of quartz- and kyanite-bearing garnet for the individual samples are illustrated in ternary plots showing relative proportions for the number of grains in each analyzed grain-size fraction. The frequencies of quartz- and kyanite-bearing garnet for the individual samples of the analyzed grain-size window of 63–500 μm are shown in bar plots.

Considering the frequency of quartz-bearing garnet, it again well reflects the dominantly felsic framework of the catchments from samples JS-Erz-9s, JS-Erz-13s, and JS-Erz-14s (Figure Appendix 5-A 4A, bar plot), as already shown by the frequency of graphite-bearing garnet (Figure Appendix 5-A 3, bar plot). In contrast, the frequency of kyanite-bearing garnet is more heterogeneous and indicates significant inputs from high-grade felsic source rocks for samples JS-Erz-3s and especially JS-Erz-8s, but also for JS-Erz-13s. Obviously, the grain-size distribution plots show enrichment of quartz-bearing garnet in the 63–125 μm fraction overcoming the effect of the increasing garnet volume analyzed with increasing grain size, except for garnet of sample JS-Erz-9s which is exclusively shed from

homogeneous felsic rocks (Figure Appendix 5-A 4A). In contrast, kyanite-bearing garnet is clearly enriched in the coarsest fraction (Figure Appendix 5-A 4B). Thus, it can be concluded that high-grade metamorphic rocks of both mafic (see above) and felsic composition primarily supply large garnet crystals to the sedimentary system leading to an enrichment in the coarser detrital garnet fractions due to an inherited grain size from source to sink. Notably, sample JS-Erz-8s shows a similar grain-size distribution of quartz- and kyanite-bearing garnet contrary to all other samples, implying that another process controlling the grain-size distribution of this sample is involved.

Appendix 5-B

Details of step-wise garnet discrimination

To assign the individual coesite-bearing garnet grains to their most likely source, i.e., felsic or mafic, a step-wise classification is performed by comparing their chemistry and mineral inclusion assemblage with that of garnet from crystalline rocks in the catchment areas. In the first four steps, the molar proportions of X_{Ca} , X_{Fe} , and X_{Mg} are considered (Figure 5.4-5). For step I, it seems reasonable to assume that garnet grains matching with the 50 % confidence ellipsoid of diamond-bearing paragneiss are of felsic origin, whereas those matching with the 50 % confidence ellipsoid of eclogite are derived from mafic rocks. By this means, 21 out of the 93 coesite-bearing garnet grains are assigned to their source. For step II, the boxplot of the X_{Ca} component in terms of the local crystalline rocks shows that all garnet from eclogite contains $X_{Ca} \geq 0.186$. Thus, all coesite-bearing garnet grains with a lower amount of the X_{Ca} component can be assigned to a felsic source (45 out of the 72 remaining unclassified coesite-bearing garnet grains after step I). With regard to the X_{Fe} component, garnet of local eclogite has values ≤ 0.585 and felsic rocks show values ≥ 0.449 . Based on these limits, in step III, all coesite-bearing garnet grains with $X_{Fe} > 0.585$ are assigned to a felsic source and grains with $X_{Fe} < 0.449$ to a mafic source, leading to an assignment of 5 out of the 27 remaining after step II. One additional coesite-bearing garnet can be assigned to a felsic source in step IV based on the low X_{Mg} component, which is ≥ 0.180 for garnet of local eclogite. In summary, after step IV, 72 out of the 93 coesite-bearing garnet grains (~77 %) are assigned to their most likely source, whereby one quarter belongs to a mafic and three quarters belong to a felsic source.

The 21 remaining coesite-bearing garnet grains after step IV are more difficult to assign as they show strong overlap with compositions of garnet from both country rock gneiss and eclogite. To tackle this issue, at first, a principal component analysis was performed on the, so far, unassigned grains. For that, all measured oxide weight percentages were used, except Cr_2O_3 due to amounts that are exclusively below the detection limit. Prior analysis, the data was centered log-ratio transformed. Based on the biplot, the log ratios of the variables $FeO/(CaO+MgO)$ and CaO/MgO are most suitable for further analysis (Figure Appendix 5-B 1).

For step V, the composition of the coesite-bearing garnet grains is shown in a scatter plot using the afore-mentioned ratios in comparison to mineral inclusion assemblages co-existing with coesite (Figure 5.4-6). As discussed in Section 5.4.2, inclusions of omphacite are characteristic of an eclogitic source. This is again supported by omphacite inclusions occurring together with coesite in two out of the 18

garnet grains assigned to a mafic source in the steps before, and the absence of omphacite inclusions in all coesite-bearing grains assigned to a felsic source. Thus, three of the unclassified grains containing coesite co-existing with omphacite and overlapping with the 95 % confidence ellipsoid of local eclogite can be confidently assigned to a mafic source. In contrast, garnet containing graphite inclusions point to a felsic source, which is again supported by their occurrence in 13 out of the 54 coesite-bearing garnet grains previously assigned to a felsic source, and their absence in mafic coesite-bearing garnet. In addition, inclusions of alkali feldspar, phlogopite–biotite, and cristobalite solely occur in coesite-bearing garnet assigned to a felsic source, and quartz inclusions dominantly occur in felsic garnet. These inclusion types furthermore often form mineral assemblages in the coesite-bearing detrital garnet grains of felsic affinity. Thus, considering these inclusion types, seven of the hitherto unclassified grains can be assigned to a felsic source (Figure 5.4-6).

From the remaining 11 not-assigned coesite-bearing grains after step V, five show a compositional contrast to local eclogite and compositions similar to garnet previously assigned to a felsic source (Figure 5.4-6). These five grains are assigned to a felsic source in step VI, ending up with a total of 87 out of the 93 coesite-bearing garnet grains (~94 %) assigned to their most likely source. From these 87 grains, 66 (~76 %) were assigned to a felsic and 21 (~24 %) to a mafic source. Their frequency and grain-size relations for the seven sediment samples are shown in Figure 5.4-7. For some of the remaining six coesite-bearing grains unassigned after step VI, there are subordinate indications for belonging to a felsic origin like inclusions of apatite and kyanite, which often occur in the coesite-bearing felsic grains (Figure Appendix 5-B 3b). However, both inclusion types are also present in some of the mafic grains, and compositionally they do not clearly favor a felsic or mafic source. In either

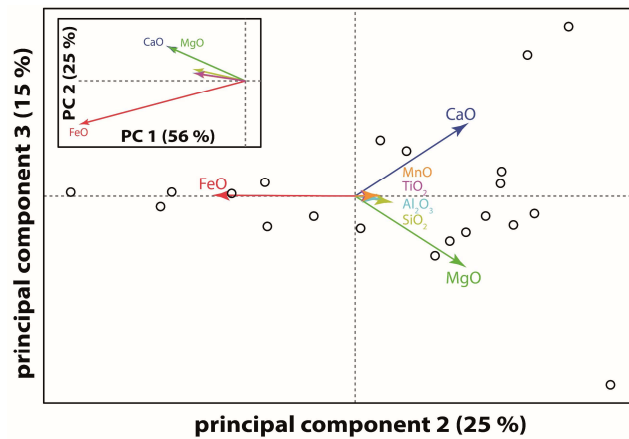


Figure Appendix 5-B 1: Biplot showing principal components two and three of the centered log-ratio transformed compositional data of the unassigned coesite-bearing garnet grains after classification step IV. Inset shows principal components one and two.

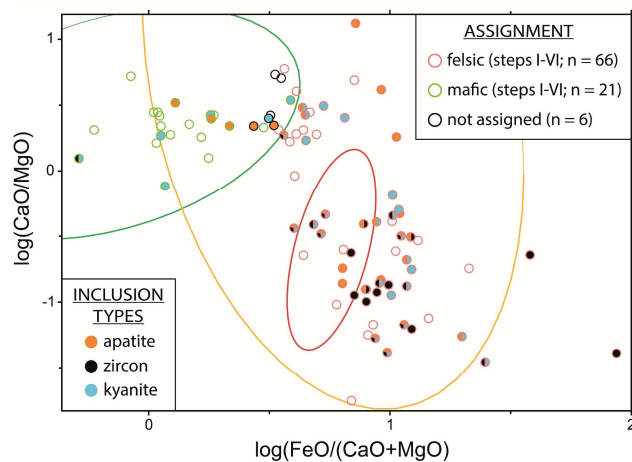


Figure Appendix 5-B 2: Assignment of coesite-bearing garnet to their most likely source after step VI based on log-ratio plots in comparison with mineral inclusion assemblages. Log-ratios are chosen based on the principal component analysis biplot shown in Figure Appendix 5-B 1. For comparison, garnet composition of local crystalline rocks compiled by Schönig et al. (2020) are shown as 95 % confidence ellipsoids with colors similar to Figure 5.4-5.

Appendix 5-C

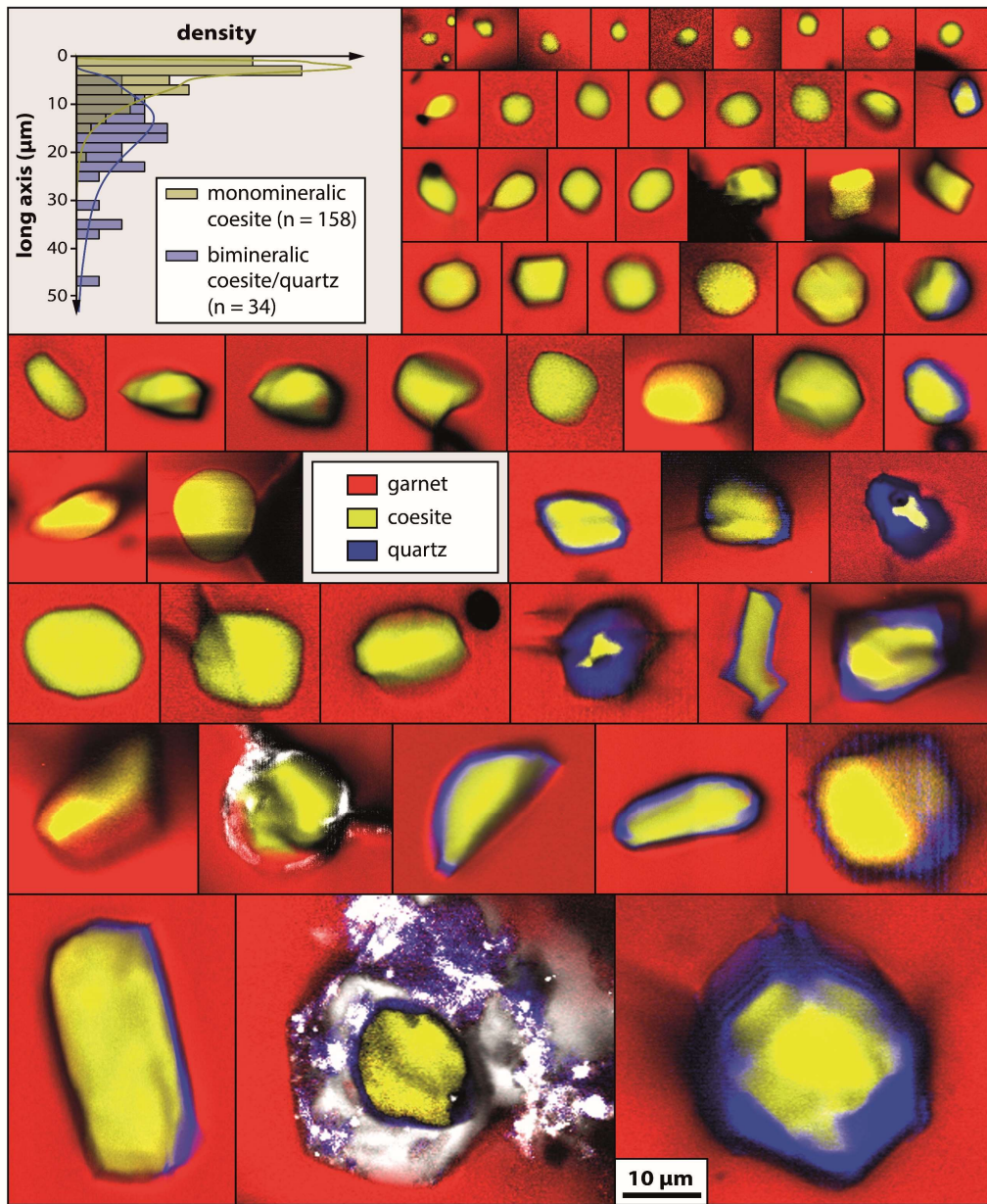


Figure Appendix 5-C 1: Monomineralic coesite and bimineralic coesite/quartz inclusions compared to inclusion size. Upper left diagram shows a histogram and kernel density estimates of all coesite inclusions, except one inclusion of sample JS-Erz-9s due to its polyphase character. Two-dimensional Raman images show a selection of coesite inclusions at the same scale ordered with regard to inclusion size. Colors correspond to Raman mode intensities of the garnet (red), coesite (yellow), quartz (blue), and embedding medium (white) components.

Appendix 5-D

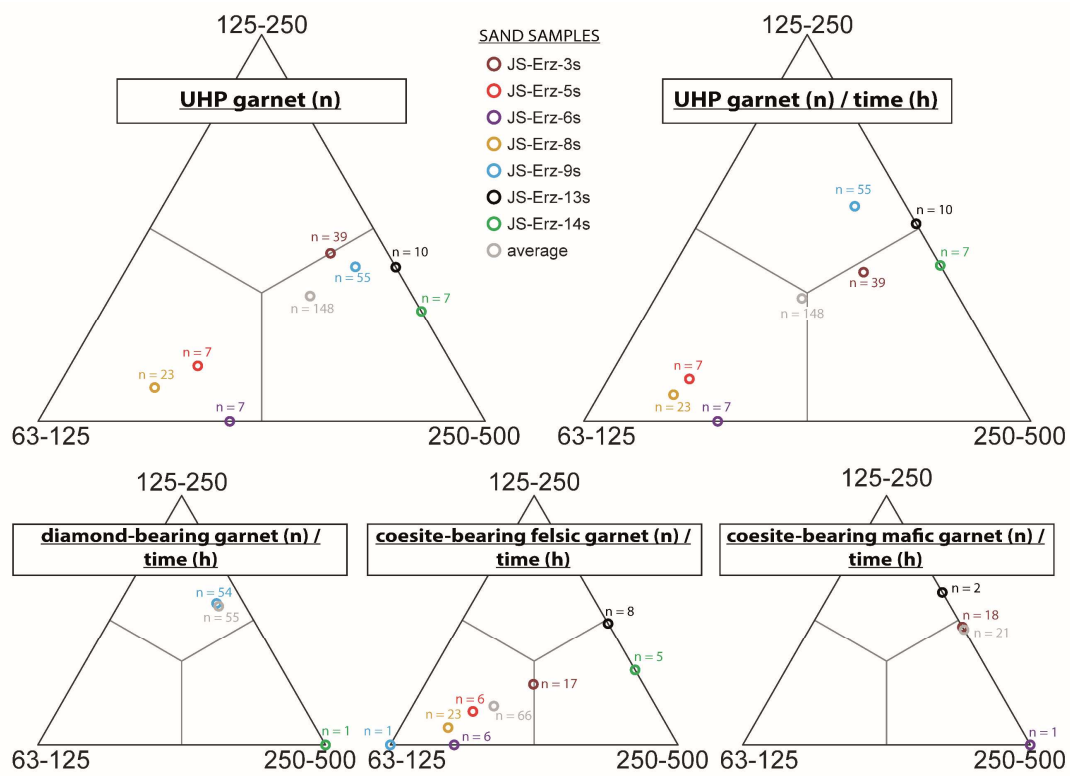


Figure Appendix 5-D 1: Relation of the number of garnet grains per sample containing UHP mineral inclusions (n) in comparison to the analytical time needed (h) with regard to the grain-size fraction. The upper ternary plots show the number of UHP garnet grains containing coesite and diamond inclusions (n), and the number of UHP garnet grains divided by the analytical time needed (n/h). Three ternary plots below show separately the number of diamond-bearing garnet, felsic coesite-bearing garnet, and mafic coesite-bearing garnet divided by the analytical time needed (n/h).

Supplementary Information – Chapter 6

Electronic Appendix 6e-A

Garnet major-element chemistry database

– *schoenig_2021_PhD_thesis_electronic_appendix_6e-A.xlsx*

Appendix 6-A

Extended information to Section 6.3

Random forest is a machine learning algorithm for supervised classification and regression developed by Breiman (2001). To understand the decisions made during the development of the garnet discrimination model (see Section 6.3), a description of the principle of the random forest classifier is given here. For a more detailed and mathematically based explanation, the reader is referred to the original work of Breiman (2001) and reviews treating this topic (Boulesteix et al. 2012; Ziegler & König 2014; Belgiu & Drăgut 2016; Biau & Scornet 2016).

The basis of the random forest algorithm are decision trees. Instead of growing a single tree trained on the classes of a dataset, though, an ensemble of trees is created, that is, a forest. Figure Appendix 6-A 1 shows a flow chart that illustrates the principle of creating a random forest classification model on a simplified example. The example model is based on a database comprising 50 observations, each described by numerical values of ten variables. At first, the user has to split the dataset by defining classes that are aimed to be predicted by the model, here A, B, and C (step (a) in Figure Appendix 6-A 1). The number of observations in each class may be highly imbalanced as exemplified with a range from five (class “B”) to 30 observations (class “A”).

For a tree to be grown, the algorithm picks a random sample of observations (eventually, with repetition) from the defined classes of the dataset (step (b) in Figure Appendix 6-A 1). Afterwards, the sample is passed back to the dataset and a new random sample is taken for the next tree. Consequently, the random samples of the individual trees can resample observations included in the samples of other trees, like highlighted with the red color-coded observations in the random samples 0001 and 1000 (Figure Appendix 6-A 1). As class “B” has five observations only, this holds for all trees in the example. This procedure, called bootstrapping, is repeated until the user defined number of trees to be grown (‘ntree’ parameter) is reached, here 1000. The number of observations taken for each sample from each of the classes can be the full number of observations available or can be defined by the ‘sampsize’ parameter, that is the size of samples to be drawn. In most cases, the overall classification success is higher when the total number of observations is considered for each sample. However, for an imbalanced dataset like the example, this high classification success may result from a preferred correct classification of the class with the highest number of observations. For instance, a classification success of 90 % corresponds to correctly predicted classes for 45 of the 50 observations, which could be generated by perfect prediction of “A” (30 of 30, i.e., 100 %), a fair prediction of “C” (13 of 15, i.e., 87 %), and poor prediction of “B” (2 of 5, i.e., 40 %). To avoid such high discrepancies, in the example the ‘sampsize’

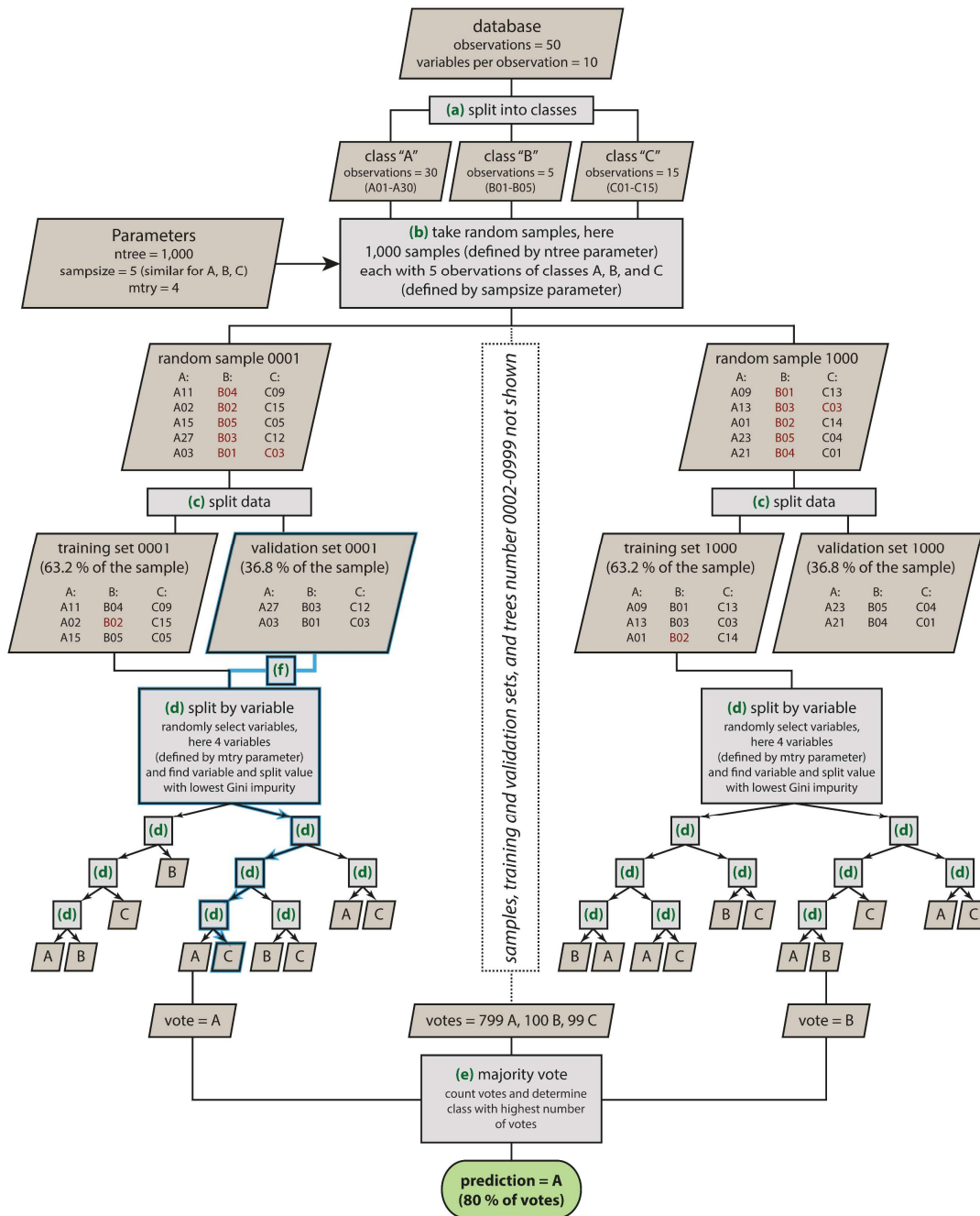


Figure Appendix 6-A 1: Flow chart of a simplified example to create a random forest classification model, inspired by Belgiu & Drăgut (2016).

parameter is chosen to be equal to the number of observations in the class with the lowest number of observations, that is class “B” with five observations. This approach usually results in a slightly lower classification success for the entire dataset, but more balanced success rates for the individual classes (Chen et al. 2004).

After a training sample is taken for a tree (step (b) in Figure Appendix 6-A 1), a validation set is constructed (step (c) in Figure Appendix 6-A 1), containing all observations excluded from the training

set. The training set is used to grow the tree, while the validation set is used to evaluate its performance. At each node of the tree, the algorithm randomly picks a subset of variables from the dataset defined by the 'mtry' parameter, that is the number of variables randomly sampled and considered as candidates at each split. For classification, the default of 'mtry' is defined as the square root of the number of observations (Liaw & Wiener 2002). In the example, 'mtry' was chosen by the user to be four. From these variable candidates, the algorithm selects one variable at a time from the variable subset and a threshold for this variable that shows the highest decrease in Gini impurity is computed (step (d) in Figure Appendix 6-A 1). Gini impurity measures the expected probability of incorrectly classifying a randomly chosen element in the dataset if it were randomly labelled according to the class distribution in the dataset (Breiman et al. 1984). Then, the algorithm picks the variable and the threshold that split the data with the highest reduction of the Gini impurity. This splitting produces two branches. The step is repeated branch by branch, creating new nodes in a hierarchical scheme, until all samples are assigned to their true class (with end branches called then leaves), resulting in a deep tree without pruning (optionally trees can be pruned to save computation time by increasing the 'nodesize' parameter, that is the minimum number of observations on each terminal node). Subsequently, an ensemble of trees, that is the forest, is created based on the training sets of all random samples taken defined by the 'ntree' parameter (step (b) in Figure Appendix 6-A 1).

The random selection of a subset of variables at each node makes the difference between trees grown using the random forest algorithm and trees grown using classification and regression trees (CART, Breiman et al. 1984). In CART, the best split variable is chosen from the entire set of variables. Thus, trees for the samples grown by CART can share high similarities, i.e., have a high correlation, because the best splitting variables are often the same. By contrast, trees grown by random forest show a much lower correlation, which becomes powerful in the last step of the random forest algorithm called bagging, or bootstrap aggregation. When predicting the class of an unknown observation, the sample will run through all of the trained trees. The prediction of a certain observation for a class made by a tree is called a 'vote'. Finally, the votes of all trees are counted and the class with the highest number of votes wins, that is the majority vote (step (e) in Figure Appendix 6-A 1, in this case 800 A, 101 B, 99 C). Similarly, the validation sets created are used to estimate the performance of the random forest model created by the training sets (step (f) in Figure Appendix 6-A 1, blue path). That is, a certain observation contributes either to the training or to the validation of each tree. The samples that have not contributed to the training of a certain tree are called out-of-bag (OOB) samples. The OOB error is defined by the sum of misclassified OOB observations divided by the total number of observations.

Appendix 6-B

Bare-bone version of the code for reproducing the classification models

set working directory

give path to your working directory including the file
"schoenig_2021_PhD_thesis_electronic_appendix_6e-A.xlsx"

```
setwd("C:/Users/49176/Documents/work_backup/schoenig_2021_PhD_thesis/electronic_appendix")
```

import database

before importing "schoenig_2021_PhD_thesis_electronic_appendix_6e-A.xlsx", replace all values <0.03 by -0.03 and all NAs by blanks

```
dt.0 = read_xlsx("schoenig_2021_PhD_thesis_electronic_appendix_6e-A.xlsx",  
sheet = "Electronic Appendix 6e-A", range = "B5:S13622") %>%  
as.data.frame()  
names(dt.0)[1] = "class_setting_facies"  
names(dt.0)[2] = "class_composition"  
dt.0 = select(dt.0, c(class_setting_facies, class_composition, SiO2:CaO))  
summary(dt.0)
```

pair-wise log-ratio function

```
mypwlr = function(X) {  
X[X < 0] = 0  
ids = combn(colnames(X), m = 2)  
Xpwlr = log(X[, ids[1, ]]) - log(X[, ids[2, ]])  
colnames(Xpwlr) = paste(ids[1, ], ids[2, ], sep = ".")  
auxfun = function(i) {  
x = Xpwlr[, i]  
mn = min(x[is.finite(x)]) - 1  
mx = max(x[is.finite(x)]) + 1  
ifelse(is.finite(x), x, ifelse(is.na(x), NA, ifelse(x > 0, mx,  
mn)))  
}  
Xpwlr = sapply(colnames(Xpwlr), auxfun)  
return(Xpwlr)  
}
```

create variable dataset

```
X.0 = dt.0 %>% select(SiO2:CaO)
```

setting and facies model

assign classes

```
classes_setting_facies = factor(dt.0[, "class_setting_facies"])  
summary(classes_setting_facies)
```


compute model

parameter tuning has been performed outside of this reproducible example by a formal exhaustive cross-validation (long runtime). Note, misclassification rates are subject to slight fluctuations as a result of the random sampling procedure

```
rf_setting_facies = randomForest(classes_setting_facies ~ ., data = mypwlr(X.0),  
ntree = 3400, mtry = 5, nodesize = 1, sampsize = c(1200, 1011, 1100,  
1011, 1011, 1011, 826), importance = TRUE, na.action = "na.roughfix")  
rf_setting_facies
```

composition model

assign classes

```
classes_composition = factor(dt.0[, "class_composition"])  
summary(classes_composition)
```

compute model

parameter tuning has been performed outside of this reproducible example by a formal exhaustive cross-validation (long runtime). Note, misclassification rates are subject to slight fluctuations as a result of the random sampling procedure

```
rf_composition = randomForest(classes_composition ~ ., data = mypwlr(X.0),  
ntree = 3200, mtry = 6, nodesize = 1, sampsize = c(89, 1196, 2100,  
2600, 1777), importance = TRUE, na.action = "na.roughfix")  
rf_composition
```

Appendix 6-C

Performance of the discrimination scheme after Mange & Morton (2007)

The discrimination scheme of Mange & Morton (2007) was originally developed to discriminate different source regions of garnet-bearing sedimentary rocks in the North Sea and Norwegian Sea (Morton 1985; Morton et al. 2004, 2005a, 2005b). The approach was to compare the composition of detrital garnet grains with that of potential surrounding source regions including Norway, Scotland, and Greenland. It was demonstrated that the major-element chemistry of detrital garnet is useful to trace back sediment from sink to source, with grains being derived from units dominantly consisting of amphibolite-facies rocks showing low Mg contents, those from mafic granulite- and eclogite-facies rocks showing high Mg and high Ca, and those from metasedimentary granulite-facies rocks having high Mg and low Ca. By considering several other garnet host rocks, Mange & Morton (2007) defined six different garnet types (A, Bi, Bii, Ci, Cii, and D) in a graphical ternary discrimination scheme based on the molar proportions of Fe+Mn, Mg, and Ca.

Figure Appendix 6-C 1 shows the performance of this scheme based on the garnet database presented here (Electronic Appendix 6e-A). In Figure Appendix 6-C 1a the performance of the classification scheme is evaluated solely for garnet compositions from host rocks which have been considered by Mange & Morton (2007). Results are represented splitting the data according to the classes defined in

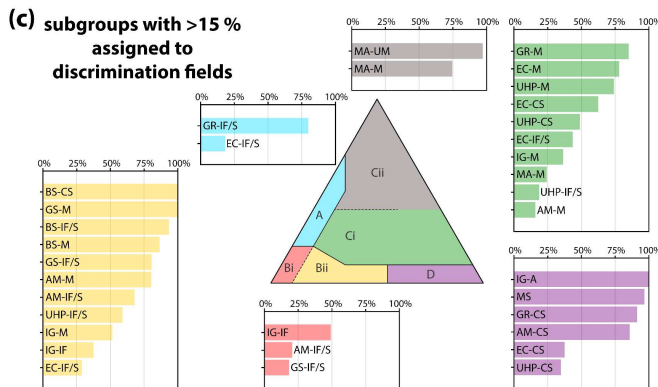
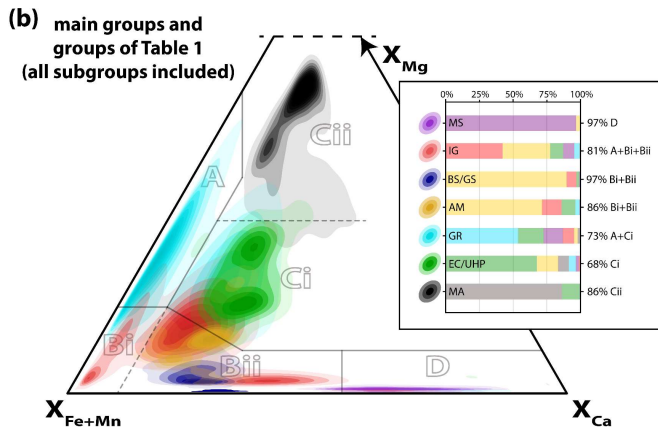
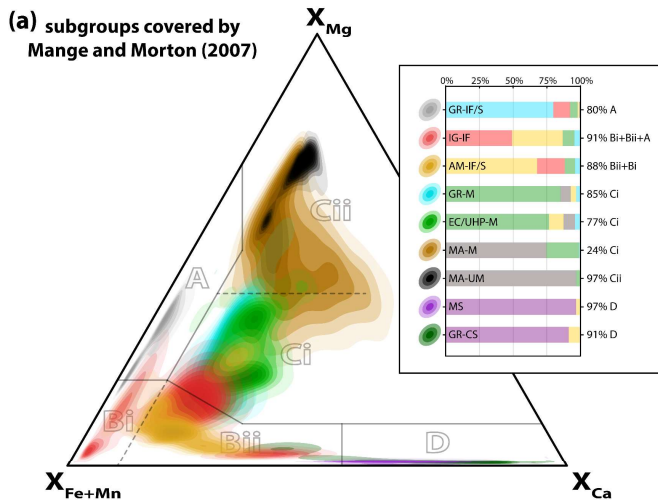


Figure Appendix 6-C 1: Performance of the garnet discrimination scheme after Mange & Morton (2007). Discrimination fields correspond to type A – mainly derived from high-grade granulite-facies metasedimentary rocks or charnockites, but can also be supplied from intermediate-felsic igneous rocks; type B – mainly derived from amphibolite-facies metasedimentary rocks. Populations plotting exclusively in Bi suggest derivation from intermediate-felsic igneous rocks; Type C – derived mainly from high-grade metamafic rocks. High Mg contents (Type Cii) imply sourcing from ultramafic rocks; Type D – derived from metasomatic rocks, very low-grade metamafic rocks, or ultrahigh-temperature calc-silicate. (a) performance for all subgroups of Table 6.2-1 considered by Mange & Morton (2007); (b) performance for all groups of Table 6.2-1; (c) proportions of individual subgroups given in Table 6.2-1 that are assigned to the specific discrimination fields, solely amounts >15% are shown. Compositions are given in molar proportions and shown as kernel density estimate maps in ternary diagrams, with bandwidth calculated after Venables & Ripley (2002). Assignments to garnet types are shown as barplots, color coding corresponds to ternary diagram in (c), percentage to the right of the bars indicate assignment to the respective type(s) according to the scheme.

the present contribution: both probability density maps (showing the location and spread of the garnet composition belonging to each group) and performance barplots (showing the proportion of garnets from these group being classified on the classes of Mange and Morton

(2007)) are displayed. From these barplots it is obvious that only mafic mantle garnets (MA-M) are not well represented by the respective compositional field. All other groups show a discrimination success of between 77% and 97%, with 88% on average (i.e., the frequency of correctly classified garnets). Consequently, the scheme performs well for the application it was designed for.

The main limitation of the Mange & Morton (2007) scheme for provenance analysis refers to the usage as a petrogenetic indicator that arises from the wide range of host rocks represented by each defined

garnet type and the fact that garnets from several specific host rocks are represented by more than one defined type. This is highlighted by the kernel density maps shown in Figure Appendix 6-C 1a and even more clearly in Figure Appendix 6-C 1b when reporting all subgroups included in the database into groups (Table 6.2-1). High compositional overlaps are given for granulite- and eclogite-facies garnet, in particular for mafic host-rock compositions, as well as for blueschist-/greenschist- and amphibolite-facies garnet. In addition, compositions of igneous garnet spread over a large part of the ternary plot and strongly overlap with compositions of blueschist-/greenschist- and amphibolite-facies garnet, but also overlap with higher-grade metamorphic garnet and metasomatic garnet.

Implications of the compositional overlaps for provenance interpretations are evaluated in Figure Appendix 6-C 1c, which shows how many subgroups of the database are represented in significant proportions >15 % by each of the six garnet types defined by Mange & Morton (2007). The best performance is given by type Cii garnet (mantle garnet), followed by type A garnet mostly indicative for intermediate–felsic/metasedimentary granulite-facies sources and lower but significant amounts of intermediate–felsic/metasedimentary eclogite-facies sources. Type Bi mostly represents garnet from intermediate–felsic igneous host rocks, followed by significant proportions of greenschist- and amphibolite-facies intermediate–felsic/metasedimentary garnet. Most critical is type Bii garnet. Although most of the type Bii garnet belongs to lower grade metamorphic source rocks, i.e., greenschist, blueschist, and amphibolite facies, high amounts of intermediate–felsic/metasedimentary eclogite- and ultrahigh-pressure-facies garnets are also assigned to type Bii, as well as igneous garnet of intermediate–felsic to mafic composition. Conversely, most of Ci type garnet belongs to high-grade metamorphic source rocks, i.e., granulite, eclogite, and ultrahigh-pressure facies, but significant amounts of mafic igneous, mantle, and amphibolite-facies garnet are also represented by type Ci. Type D garnet represents metasomatic, alkaline igneous, and calcsilicate metamorphic garnet ranging from amphibolite to ultrahigh-pressure facies.

In conclusion, although changes in garnet composition observed in the $X_{\text{Fe+Mn}}-X_{\text{Mg}}-X_{\text{Ca}}$ ternary plot can imply a change in provenance, the large compositional overlaps from a wide range of garnet host rocks make it difficult to attribute these changes to the setting, geodynamic context, or protolith composition. For instance, only prominent changes like sediment containing dominantly type Bi and Bii garnets that is stratigraphically overlain by strata containing dominantly type A and Ci garnets may indicate the ongoing exhumation of deeper crustal units. Nevertheless, even such an interpretation is vulnerable considering that a similar trend of changing garnet composition could be produced by a change in protolith composition from intermediate–felsic/metasedimentary to mafic for high-grade metamorphic rocks. This becomes even more challenging given the strong overlap with garnet from igneous rocks.

Performance of the discrimination scheme after Hardman et al. (2018)

To reduce costs in diamond exploration campaigns, first surveys often focus on the identification of diamond/kimberlite indicator minerals like chromite, clinopyroxene, and garnet in modern sediments derived from potential target areas, which are by far more frequent than diamond (Nowicki et al. 2007). Garnet is of particular importance due to its occurrence in all dominant diamond-bearing lithologies. Thus, a robust geochemical tool to discriminate between mantle and crustal garnet is of economic

interest. Ultramafic mantle garnet can be confidently discriminated from crustal garnet by the higher Cr₂O₃ component (e.g., Grütter et al. 2004) and its MgO enrichment relative to FeO (e.g., Schulze 2003; Tolosana-Delgado et al. 2018). In contrast, garnet of low-chromium (<1 wt% Cr₂O₃) mantle eclogite compositionally overlap with crustal garnet, especially with granulite- and eclogite-facies metamorphic garnet (Hardman et al. 2018). This leads to high misclassifications in the most applied graphical scheme for mantle versus crustal garnet after Schulze (2003), as demonstrated in Hardman et al. (2018; see their fig. 2).

Hardman et al. (2018) addressed the problem of discriminating low-chromium mantle and crustal garnet by a more robust database and a multivariate approach using linear discriminant analysis and logistic regression, resulting in a classification success of 93 to 94 %. The application requires knowledge of the Na₂O component, which is not covered by our database because Na₂O is often not reported, not measured or below detection limit, in particular for garnet of crustal origin. Thus, the graphical scheme of Hardman et al. (2018) is evaluated here, which is based on the natural logarithmic ratio of Ti to Si versus Mg to Fe, and reported to provide a high discrimination success of 90 %.

Figure Appendix 6-C 2 shows the performance of the graphical scheme after Hardman et al. (2018) for main and subgroups of mantle garnet as well as groups of metamorphic garnet (Table 6.2-1). Mantle versus crustal garnet are correctly classified in 95 % of the cases (average). Even those groups presenting more difficulties to other schemes due to their lower wt% Cr₂O₃, that are garnet of mafic mantle rocks (98 % of observations <1 wt% Cr₂O₃) versus metamorphic eclogite- and ultrahigh-pressure garnet (100 % of observations <1 wt% Cr₂O₃), show a high classification success of on average 91 %. This also holds for low-chromium garnet from the group of ultramafic mantle rocks (36 % of observations <1 wt% Cr₂O₃), which are correctly classified in 95 % of the cases.

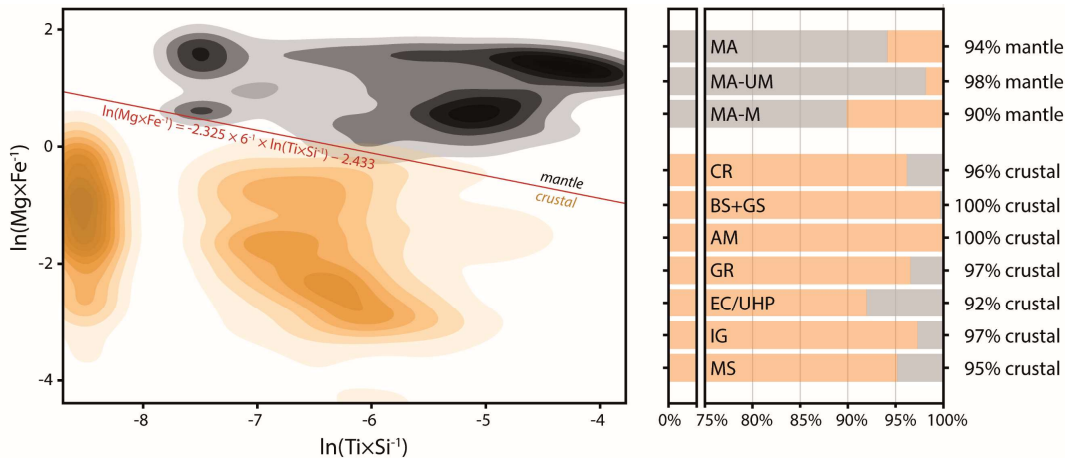


Figure Appendix 6-C 2: Performance of the graphical mantle-versus-crustal garnet discrimination scheme after Hardman et al. (2018). Decision boundary with the highest overall classification success was chosen. As many observations of the database show TiO₂ values below detection limit (<0.03 wt%), TiO₂ values of crustal and mantle garnets have been replaced by 0.01 wt% and 0.03 wt%, respectively (most optimistic approach). Compositions are given as log-ratios of atomic proportions and are shown as kernel density estimate heatmaps, with bandwidth calculated after Venables & Ripley (2002). Assignments to crustal-versus-mantle sources are shown as barplots.

Performance of the discrimination scheme after Tolosana-Delgado et al. (2018)

To tackle the uncertainty derived from the large compositional overlaps, strict discrimination fields, and the usage of fewer variables than available, Tolosana-Delgado et al. (2018) applied a multivariate approach based on linear discriminant analysis to provide probabilities for detrital garnet of belonging to specific host rocks. In three hierarchical steps, the discrimination scheme first predicts probabilities for an ultramafic source, followed by an igneous source, and finally gives probabilities for metamorphic garnet of belonging to amphibolite-, granulite-, and eclogite-facies sources. Because Tolosana-Delgado et al. (2018) used a threshold of 0.02 wt% for Cr₂O₃ to apply the linear discriminant function for separating ultramafic garnet, which is not covered by the database detection limit of 0.03 wt%, and considered only the most abundant igneous garnet-bearing rock type, that is felsic plutonic, we focus here on the performance in discriminating metamorphic garnet sources into facies types, which is most challenging. The scheme requires a prior probability (see Tolosana-Delgado et al. 2018). Due to the unbalanced number of observations for the various groups included in the database (Table 6.2-1), a customized prior based on the number of observations turned out to favor the correct classification of eclogite-facies garnet (including ultrahigh-pressure) but strongly reduces the classification of granulite-facies garnet (only 10 % are correctly classified). To not promote a specific metamorphic group, the prior probability 'equal-M' was chosen (equal proportions of metamorphic host-rock types) for the following performance assessment, that is 30 % for A (eclogite facies), 30 % for B (amphibolite facies), 30 % for C (granulite facies), 5 % for D (ultramafic), and 5 % for E (felsic plutonic).

Figure Appendix 6-C 3 shows the scheme performance based on the garnet database presented here (Electronic Appendix 6e-A), using density maps and barplots as in Figure Appendix 6-C 1. In Figure Appendix 6-C 3a solely garnet compositions from subgroups of Table 6.2-1 are tested which have been included in Tolosana-Delgado et al. (2018) with >33 observations. Barplots indicate that the majority of garnet from all subgroups show the highest probability for their respective host rock; on average 69 % classification success. Eclogite- and amphibolite-facies garnets are much better classified than granulite-facies garnet. By considering all groups of the database, the average success rate is 65 % (Figure Appendix 6-C 3b).

Although the classification success rates are lower compared to the classification after Mange & Morton (2007), the value of information in terms of the geodynamic context is higher. Giving probabilities instead of strict assignments is the major strength of the scheme. This makes better use of the available space in the ternary plot as shown by the kernel density maps (Figure Appendix 6-C 3a and b). Notably, most misclassified grains show almost equal probabilities for two host-rock groups, and thus variations in detrital garnet composition can be more confidently related to metamorphic facies with less influence of protolith composition on the results. However, significant amounts of eclogite-facies and mafic mantle garnet are incorrectly assigned to a granulite-facies source, those of mafic granulite facies to eclogite facies, and those of granulite, eclogite, and ultrahigh-pressure facies to amphibolite facies (see framed bars in Figure Appendix 6-C 3c). In addition, high proportions of metamorphic garnets are misclassified as felsic plutonic, in particular those of calcisilicate protolith composition and greenschist, blueschist, and amphibolite facies (not shown in Figure Appendix 6-C 3).

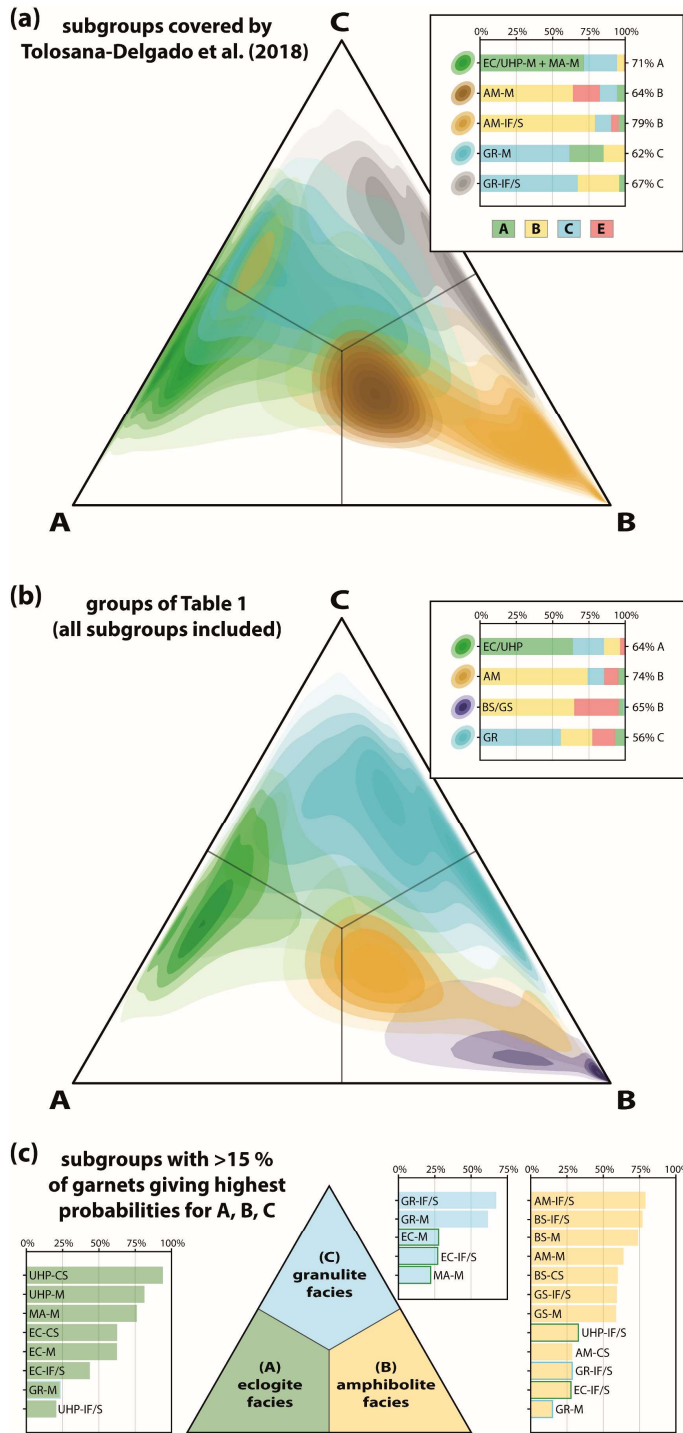


Figure Appendix 6-C 3: Performance of the garnet discrimination scheme after Tolosana-Delgado et al. (2018) using the prior probability 'equal-M'. Host-rock types correspond to type A – eclogite facies; B – amphibolite facies; type C – granulite facies. (a) performance for all subgroups of Table 6.2-1 considered by Tolosana-Delgado et al. (2018); (b) performance for all groups of Table 6.2-1; (c) proportions of individual subgroups given in Table 6.2-1 that give the highest probability for individual host-rock types, solely amounts >15 % are shown. Probabilities are shown as kernel density estimate heatmaps in ternary diagrams, with bandwidth calculated after Venables & Ripley (2002). Assignments to host-rock types are shown as barplots, color coding (frame: true class; filling: predicted class) corresponds to ternary diagram in (c) and type E (igneous) is shown in red.

Appendix 6-D

Effect of pressure and temperature on votes

A reflection of a continuous change in garnet composition with changing P - T conditions by voting results is highlighted in Figure Appendix 6-D 1, which shows the internal distribution of votes within the individual metamorphic classes as a function of pressure and temperature for garnet in the database where P - T information is available. Classes BS/GS and EC/UHP are most sensitive to temperature. Garnets from class BS/GS show a continuous decrease in votes for BS/GS with increasing temperature, while votes for AM and, less clearly, EC/UHP increase (Figure Appendix 6-D 1a). This is exemplified by comparing BS/GS garnets that formed at $T \geq 500$ °C having a higher misclassification rate (28%) compared to $T < 500$ °C (18%). Contrarily, garnets from class EC/UHP show a significant decrease in votes for EC/UHP at $T < 600$ °C along with an increase for BS/GS and AM (Figure Appendix 6-D 1b).

Classes AM and GR are more sensitive to pressure. At $P > 10$ kbar a significant decrease in AM votes for garnets from class AM is observed, while votes for EC/UHP strongly increase simultaneously with a minor increase in GR and BS/GS votes (Figure Appendix 6-D 1c). Votes for garnets from class GR show a two-fold distribution with garnets crystallized at $P < 4$ kbar being more prone to be

Figure Appendix 6-D 1: Votes within the individual metamorphic classes as a function of temperature (a, b) or pressure (c, d). As trends are not obvious from the highly scattered data, vote regression curves are fitted and smoothed using local regression (locally estimated scatterplot smoothing) for classes (a) BS/GS ($n = 662$; 55 % of database observations), (b) EC/UHP ($n = 3,186$; 92 % of database observations), (c) AM ($n = 1,327$; 51 % of database observations), and (d) GR ($n = 856$; 85 % of database observations). Grey area indicates the distribution of observations given as kernel density estimate on a reverse relative scale (sample density distribution). Note that 95 % confidence intervals correspond to the estimated regression curve.

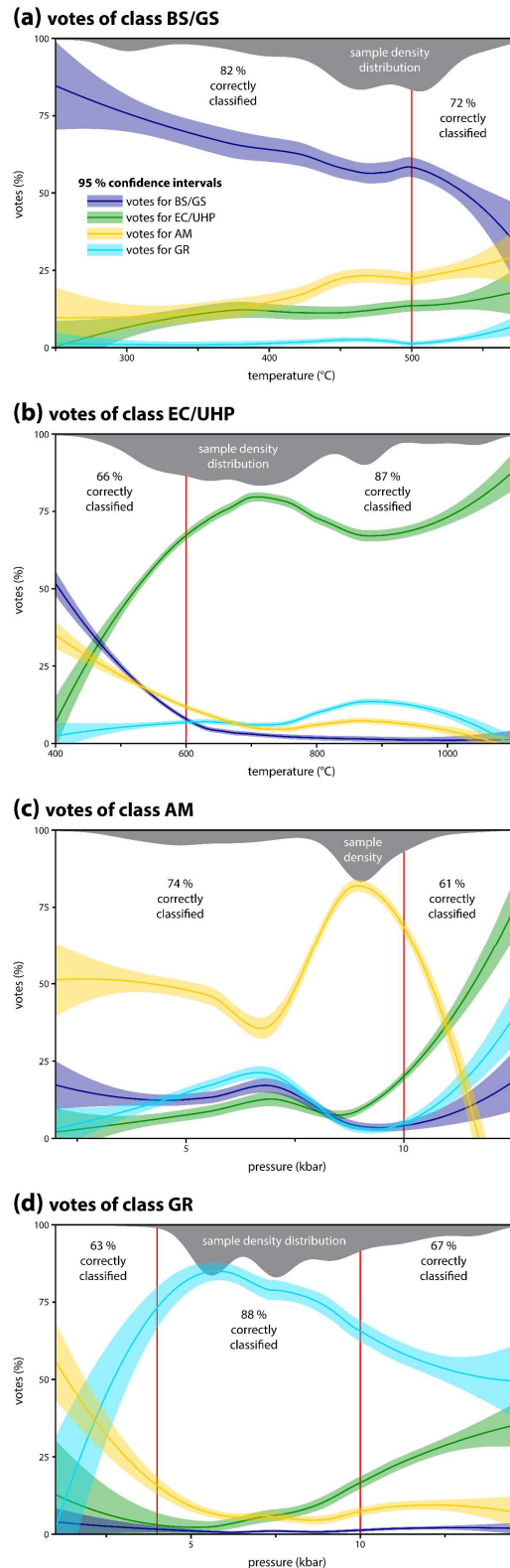
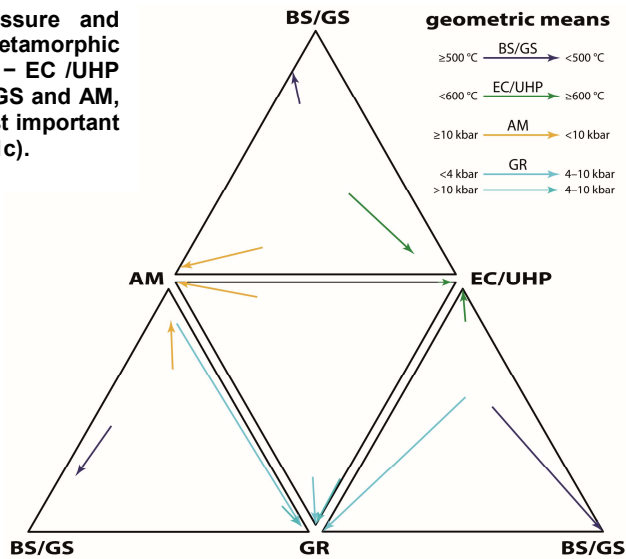


Figure Appendix 6-D 2: Effect of pressure and temperature on geometric mean votes of metamorphic facies classes. Note that the AM – BS/GS – EC /UHP diagram is most important for classes BS/GS and AM, and the EC/UHP – GR – AM diagram is most important for classes EC/UHP and GR (cf. Figure 6.4-1c).

misclassified as AM and those crystallized at $P > 10$ kbar being more prone to be misclassified as EC/UHP (Figure Appendix 6-D 1d). The effect of pressure and temperature is highlighted for the individual metamorphic classes in the respective ternary plots by comparing the geometric means (Figure Appendix 6-D 2).



Appendix 6-E

Consequences on misclassification rates for individual classes of the 'setting and metamorphic facies' model by excluding individual oxides

The highest influence on misclassification rates of class MA is observed by excluding TiO_2 , followed by MnO and Cr_2O_3 (Figure 6.5-2, black line). In comparison to the full model (all eight oxides used), the vast majority of newly misclassified MA garnets are mafic (92 % for TiO_2 excluded, 81 % for MnO , and 75 % for Cr_2O_3) and now assigned to class EC/UHP (97 % for TiO_2 excluded, 93 % for MnO , and 91 % for Cr_2O_3). Thus, TiO_2 , MnO , and Cr_2O_3 are important variables for discriminating between mantle eclogites (subgroup MA-M) and crustal eclogites (subgroup EC/UHP-M).

For class MS, misclassification rates show the highest increase by excluding MgO (consistent with observations based on Gini impurity), followed by MnO and TiO_2 (Figure 6.5-2, purple line). Excluding each of the three oxides mainly leads to newly misclassified MS garnets as GR (79 % for MgO , 54 % for MnO , and 76 % for TiO_2), followed by IG (31 % for MnO) and BS/GS (15 % for MnO , and 12 % for TiO_2). This indicates the importance of MgO , MnO , and TiO_2 for discriminating between metasomatic and low-pressure metamorphic as well as igneous garnet.

Variables TiO_2 and CaO have furthermore high importance for the correct classification of IG garnet, followed by MnO (Figure 6.5-2, red line). The increase in misclassification rate by excluding TiO_2 is not only related to titanium-rich garnet of alkaline igneous rocks (16 % of newly misclassified garnets), but also to garnet of intermediate-felsic (77 %) and mafic (5 %) host-rock composition. In addition, although most of them are now assigned to AM (35 %), all other metamorphic classes are affected (22 % EC/UHP, 14 % GR, and 12 % BS/GS) as well as MS (17 %). Misclassifications by excluding CaO and MnO are mainly related to intermediate-felsic/metasedimentary host-rock compositions (97 % for CaO , and 93 % for MnO). CaO is most important for the discrimination to AM (51 %),

followed by BS/GS (33 %). MnO is also most important for the discrimination to AM (63 %), followed by BS/GS and GR (both 11 %).

The highest influence on misclassification rates of class BS/GS are observed by excluding MgO, followed by CaO, and also FeO_{total} and Al₂O₃ show considerable importance (Figure 6.5-2, dark-blue line). In comparison to the full model, the newly misclassified BS/GS garnets correspond to both intermediate–felsic/metasedimentary as well as mafic host-rock compositions. All four oxides are of particular value for the discrimination of BS/GS to AM (54 % of newly misclassified garnets for MgO, 58 % for CaO, 47 % for FeO_{total}, and 84 % for Al₂O₃). For the discrimination to EC/UHP, MgO is most important (26 %), followed by FeO_{total} (22 %), Al₂O₃ (16 %), and CaO (11 %). Conversely, CaO is most important for the discrimination to IG (30 %), followed by FeO_{total} (25 %) and MgO (17 %), but Al₂O₃ does not affect the classification success.

For class AM, misclassification rates show the highest increase by excluding MnO and MgO, followed by TiO₂ (Figure 6.5-2, yellow line). In comparison to the full model, newly misclassified AM garnets are mainly intermediate–felsic/metasedimentary (70 % for MnO excluded, 80 % for MgO, and 65 % for TiO₂) and mafic garnet constitute the subordinate portion. All three oxides show high importance for the discrimination of AM garnet to all other metamorphic classes. MnO is most important for the discrimination to EC/UHP, followed by BS/GS and GR, and MgO and TiO₂ are most important for BS/GS, followed by EC/UHP and GR. In addition, all three oxides affect the distinction of AM and IG, with TiO₂ being most important, followed by MnO and MgO.

The highest influence on misclassification rates of class GR are observed by excluding MnO, followed by CaO, and also MgO and TiO₂ show considerable importance (Figure 6.5-2, sky-blue line). In comparison to the full model, the majority of newly misclassified GR garnets correspond to mafic host-rock compositions. All four oxides are of particular value for the discrimination of GR to EC/UHP (80 % of newly misclassified garnets for MnO, 51 % for CaO, 34 % for MgO, and 29 % for TiO₂). Considerable importance is also given for the discrimination of GR to AM (10 % for MnO, 36 % for CaO, 18 % for MgO, and 17 % for TiO₂). As observed for class MS, TiO₂ and MgO are important to distinguish GR garnet from MS garnet, with TiO₂ being also important for the discrimination to IG.

As for class GR, MnO, CaO, MgO, and TiO₂ are also important for the discrimination of EC/UHP versus all other metamorphic classes as well as MA (Figure 6.5-2, green line). In addition, Cr₂O₃ shows considerable importance. To distinguish EC/UHP garnet from MA garnet, Cr₂O₃ is the most important oxide (49 % of newly misclassified garnets by excluding Cr₂O₃), followed by TiO₂ (40 %), MgO (19 %), and MnO (17 %). For the discrimination to GR garnet, CaO is most important (44 %), followed by MnO (26 %), Cr₂O₃ (21 %), TiO₂ (16 %), and MgO (13 %). MgO is most important for the discrimination to AM (39 %), followed by MnO (32 %), and CaO as well as TiO₂ (both 17 %). For the discrimination to BS/GS, CaO is most important (27 %), followed by Cr₂O₃ (22 %), MgO (21 %), TiO₂ (15 %), and MnO (14 %).

Consequences on misclassification rates for individual classes of the 'composition' model by excluding individual oxides

The log-ratios including TiO₂ are placed in a subordinate role for the mean decrease in Gini impurity and accuracy (Figure 6.5-3, upper). In contrast, excluding TiO₂ when developing the 'composition' discrimination model leads to the highest increase in misclassification rates, followed by CaO, MgO, MnO, Cr₂O₃, FeO_{total}, SiO₂, and Al₂O₃ in decreasing order of importance (Figure 6.5-4).

This is particularly related to the distinction of A and CS garnet (Figure 6.5-3, lower), whereby the misclassification rate for A is 3.5 times higher when TiO₂ is excluded (Figure 6.5-4, red line). In addition, TiO₂ is important for the classification success of IF/S and M (Figure 6.5-4, yellow and green lines), although compositional differences are rather small (Figure 6.5-3, lower). Excluding TiO₂ leads to misclassifications of IF/S as M, and M as IF/S for crustal garnet as well as M as UM for mantle garnet (see below).

Besides TiO₂, the highest influence on misclassification rates is given by excluding CaO, followed by MgO, MnO, Cr₂O₃, FeO_{total}, SiO₂, and Al₂O₃ in decreasing order of importance (Figure 6.5-4, bold grey line). Class UM is least affected by excluding oxides and solely the exclusion of MnO and FeO_{total} leads to a considerable increase in the misclassification rate (Figure 6.5-4, black line), whereby UM garnet being misclassified as M (92 % of newly misclassified garnets).

For class M, misclassification rates show the highest increase by excluding TiO₂ (see above), followed by CaO, Cr₂O₃, MgO, and MnO (Figure 6.5-4, green line). The exclusion of these oxides mainly leads to misclassification of crustal M garnets as IF/S (52 % of newly misclassified garnets for TiO₂, 77 % for CaO, 24 % for Cr₂O₃, 88 % for MgO, and 71 % for MnO), and of mantle M garnets as UM (45 % for TiO₂, 23 % for CaO, 76 % for Cr₂O₃, 12 % for MgO, and 25 % for MnO).

The highest influence on misclassification rates of class IF/S is observed by excluding MgO, followed by TiO₂, MnO, Al₂O₃, and CaO (Figure 6.5-4, yellow line). By excluding these oxides, newly misclassified IF/S garnets belong to igneous and metamorphic host-rocks of all grades, except granulite facies. The vast majority of those garnets are now assigned to class M (93 % for MgO, 97 % for TiO₂, 91 % for MnO, 89 % for Al₂O₃, and 92 % for CaO).

For class A, misclassification rates strongly increase by excluding TiO₂, followed by FeO_{total}, CaO, and Al₂O₃, all leading to misclassifications as CS. Remarkably, the exclusion of MgO results in lower misclassifications, that are caused by A garnet previously assigned to CS. Conversely, the oxides CaO, MnO, and MgO have the highest influence on misclassification rates of CS garnet. The exclusion of these oxides results in both, the assignment of MS-CS garnet as A (17 % for CaO, 57 % for MnO, and 33 % for FeO_{total}) and metamorphic CS garnets to all other composition classes (83 % for CaO, 43 % for MnO, and 67 % for FeO_{total}).

Appendix 6-F

Detailed exploration of main discriminators for individual subgroups

Garnet of class MS in the ‘setting and metamorphic facies’ model shows the highest classification success (Table 6.4-1), reflecting its distinct chemical composition. MS garnet is very high in CaO and very low in MgO. In addition, garnet of class MS shows a broad range for $\ln(\text{SiO}_2 \times \text{Al}_2\text{O}_3^{-1})$ and higher values compared to all other classes. Consequently, a scatter plot of $\ln(\text{Al}_2\text{O}_3 \times \text{CaO}^{-1})$ versus $\ln(\text{SiO}_2 \times \text{MgO}^{-1})$ well discriminates MS garnet from most other classes (Figure Appendix 6-F 1a). For the remaining subgroups, IG-A can be discriminated based on the high TiO_2 content (Figure Appendix 6-F 1b), while the distinction from the various metamorphic facies subgroups of CS composition is more difficult. However, the tight range of $\ln(\text{SiO}_2 \times \text{CaO}^{-1})$ enables the separation to most CS garnets from classes BS/GS, AM, and GR. Considering additionally the low values for $\ln(\text{FeO}_{\text{total}} \times \text{MgO}^{-1})$ is useful to discriminate EC/UHP-CS garnet (Figure Appendix 6-F 1c).

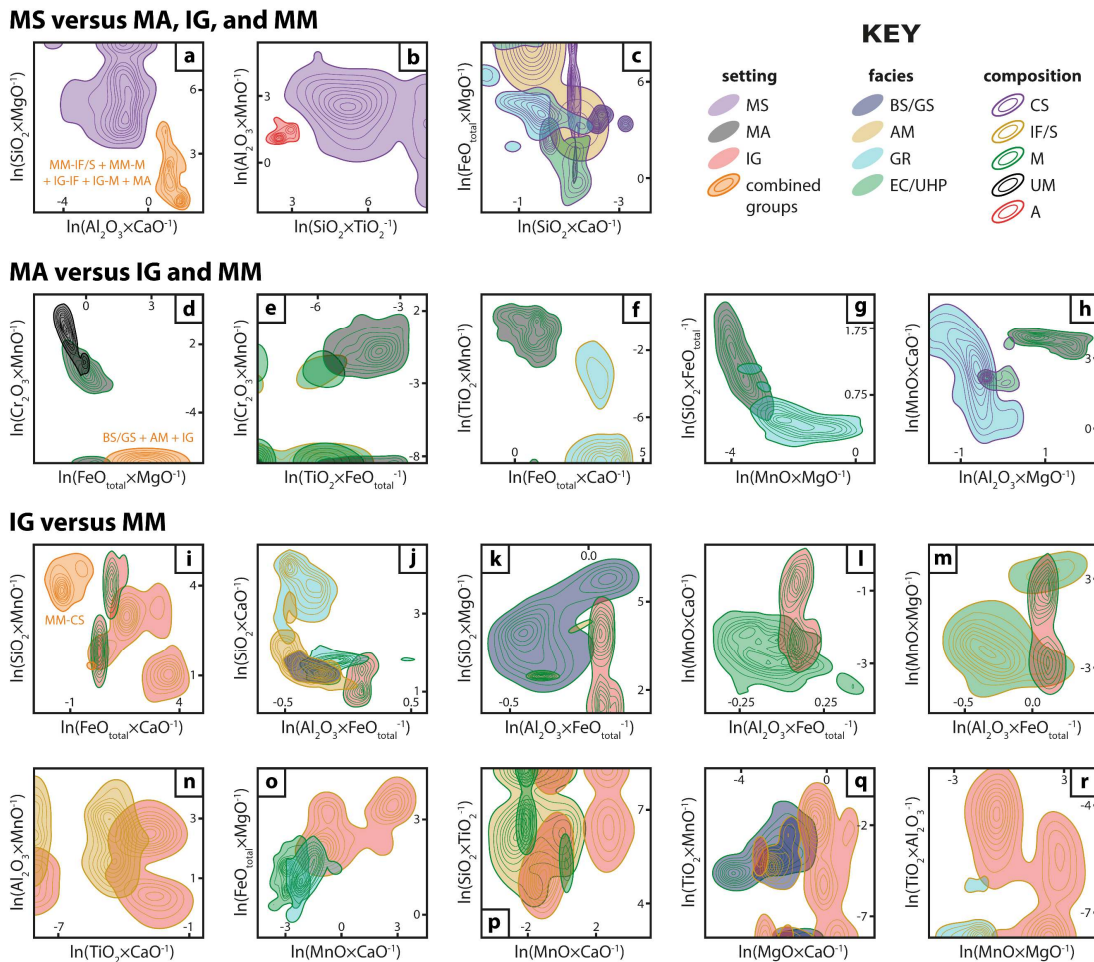


Figure Appendix 6-F 1: Main discriminators to separate individual classes, groups, and subgroups of the ‘setting’ scheme. (a–c) separation of MS garnet from MA, IG, and MM garnet. (d–h) separation of MA garnet from IG and MM. (i–r) separation of IG garnet from MM. Note that individual fields are marked by the combination of color fill (indicating setting/facies) and coloured contours (indicating composition).

The distinct composition of MS garnet is strongly related to the formation environment. Although skarn garnet can form in a wide range of settings and protolith compositions, by far the most are associated with igneous activity that leads to contact metamorphism of carbonates by heat supply and infiltrating metasomatic fluids at depth <12 km (e.g., Meinert 1992). Garnet mainly forms at the prograde anhydrous stage together with clinopyroxene, both being high in Ca^{2+} due to the availability given by protolith composition. Furthermore, high oxygen fugacity enables the stabilization of andradite (end member composition: $\text{Ca}_3\text{Fe}_2\text{Si}_3\text{O}_{12}$), that is the replacement of Al^{3+} by Fe^{3+} compared to grossular ($\text{Ca}_3\text{Al}_2\text{Si}_3\text{O}_{12}$), resulting in a garnet solid solution rich in grossular-andradite (e.g., Zhang & Saxena 1991). In contrast, clinopyroxenes crystallize mainly as solid solutions between diopside ($\text{CaMgSi}_2\text{O}_6$) and hedenbergite ($\text{CaFeSi}_2\text{O}_6$), and thus much of the available Mg^{2+} and Fe^{2+} are incorporated in clinopyroxene (Bin & Barton 1988). An exceptional case are skarns with low oxygen fugacity like those forming tungsten and tin deposits, where some garnet populations are rich in Al^{3+} (e.g., Zhang & Saxena 1991; Meinert 1992). However, considering recently published compositions of garnets from these reduced environments (Duan et al. 2020; Im et al. 2020), >87 % of the garnets are correctly classified as MS, and the remaining are mainly classified as GR garnet of CS composition.

Garnet of class MA shows the second-highest classification success in the ‘setting and metamorphic facies’ model (Table 6.4-1). Due to the relatively high content of MgO and low content of $\text{FeO}_{\text{total}}$ in mantle rocks compared to crustal rocks, the $\ln(\text{FeO}_{\text{total}} \times \text{MgO}^{-1})$ represent the main discriminator. In combination with $\ln(\text{Cr}_2\text{O}_3 \times \text{MnO}^{-1})$ this enables almost perfect discrimination of garnet of subgroup MA-UM from those of crustal affinity (Figure Appendix 6-F 1d). The enrichment of Cr in MA garnet is mainly related to the lithophile behavior of Cr, resulting in the accumulation of Cr in mantle mineral phases like chromium-spinel during partial melting of the upper mantle (e.g., Matrosova et al. 2020), while spinel is replaced by garnet at greater depths (e.g., Klemme et al. 2009). This also holds for garnet of subgroup MA-M versus most crustal garnets, except some overlap with garnet of subgroups EC/UHP-M, EC/UHP-CS, GR-M, and GR-IF/S. In addition, caution should be taken for some rare UHP-IF/S garnets that can have extremely high MgO contents (Chopin 1984) leading to misclassification as MA garnet.

The additional consideration of $\ln(\text{TiO}_2 \times \text{FeO}_{\text{total}}^{-1})$ helps in discriminating EC/UHP garnet (Figure Appendix 6-F 1e) and the consideration of $\ln(\text{FeO}_{\text{total}} \times \text{CaO}^{-1})$ combined with $\ln(\text{TiO}_2 \times \text{MnO}^{-1})$ is very useful to discriminate GR-IF/S garnet from MA-M garnet (Figure Appendix 6-F 1f). The importance of TiO_2 has also been observed by Hardman et al. (2018), but TiO_2 is not considered in most previous garnet provenance discrimination schemes. The higher TiO_2 content in MA-M compared to EC/UHP and GR-IF/S is most likely related to higher temperatures experienced by MA-M, resulting in increasing solubility of Ti in garnet (Aulbach 2020). This can explain the increasing misclassification rates for MA garnet when TiO_2 is excluded (Figure 6.5-2). Furthermore, variables $\ln(\text{MnO} \times \text{MgO}^{-1})$ versus $\ln(\text{SiO}_2 \times \text{FeO}_{\text{total}}^{-1})$ enable better discrimination of GR-M and MA-M garnet (Figure Appendix 6-F 1g), and $\ln(\text{Al}_2\text{O}_3 \times \text{MgO}^{-1})$ versus $\ln(\text{MnO} \times \text{CaO}^{-1})$ enable better discrimination of GR-CS and EC/UHP-CS from MA-M (Figure Appendix 6-F 1h).

Compared to MS and MA garnet, the discrimination of IG versus MM garnet is more challenging. Very distinct are only IG garnets of alkaline composition (IG-A), which can be separated by considering the low values for $\ln(\text{Al}_2\text{O}_3 \times \text{CaO}^{-1})$, $\ln(\text{SiO}_2 \times \text{MgO}^{-1})$, and $\ln(\text{SiO}_2 \times \text{TiO}_2^{-1})$ compared to MM garnet, given

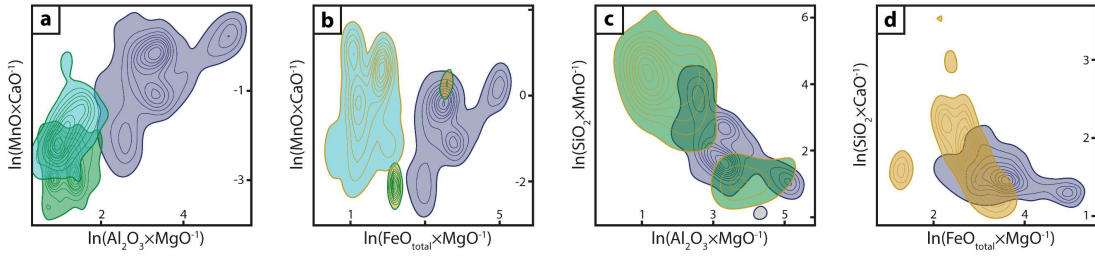
by the high andradite (Fe^{3+}) component resulting in lower amounts of Al_2O_3 along with high TiO_2 (Figure Appendix 6-F 1a and b). This agrees with the increasing incorporation of Ti into garnet with decreasing silica activity and oxygen fugacity (e.g., Russell et al. 1999). Most important for discriminating IG garnet from MM garnet are $\ln(\text{MnO} \times \text{CaO}^{-1})$ and $\ln(\text{SiO}_2 \times \text{MgO}^{-1})$, showing that IG garnet is enriched in MnO but depleted in CaO and MgO compared to MM garnet of similar protolith composition (Figure Appendix 6-F 1c). Probably the typically higher temperature–pressure gradient in igneous systems is the main driver. However, several subpopulations of IG garnet reflect a high chemical variability, reinforcing the need of considering multiple variables for a sufficient distinction to MM garnet.

Due to the distinct protolith composition, both IG-M and IG-IF garnet are decently separated from metamorphic garnet of calcsilicate composition (MM-CS) by $\ln(\text{FeO}_{\text{total}} \times \text{CaO}^{-1})$ and $\ln(\text{SiO}_2 \times \text{MnO}^{-1})$ (Figure Appendix 6-F 1i). To discriminate IG-M garnet from MM garnet of M and IF/S composition, $\ln(\text{Al}_2\text{O}_3 \times \text{FeO}_{\text{total}}^{-1})$ represents the most important variable (Figure Appendix 6-F 1j, k, l, m). This may be related to the high crystallization temperatures of IG-M garnet that leads to the relatively preferred incorporation of Fe into minerals co-existing with garnet like pyroxenes and biotite (e.g., Ferry & Spear 1978; Ganguly 1979; Dahl 1980). Combining $\ln(\text{Al}_2\text{O}_3 \times \text{FeO}_{\text{total}}^{-1})$ with $\ln(\text{SiO}_2 \times \text{CaO}^{-1})$ and $\ln(\text{SiO}_2 \times \text{MgO}^{-1})$ enables the discrimination of IG-M from most MM garnets (Figure Appendix 6-F 1j and k), except those from EC/UHP rocks. The difficulties are mainly related to the higher CaO content of mafic host-rock compositions and the preferred partitioning of Mg into chlorite and chloritoid compared to garnet grown at low temperatures (e.g., Perchuk 1991). To discriminate IG-M from EC/UHP garnet, it is more useful to combine $\ln(\text{Al}_2\text{O}_3 \times \text{FeO}_{\text{total}}^{-1})$ with $\ln(\text{MnO} \times \text{CaO}^{-1})$ or $\ln(\text{MnO} \times \text{MgO}^{-1})$ but some overlaps remain (Figure Appendix 6-F 1l and m), making their separation less pronounced (cf. Figure 6.4-1d).

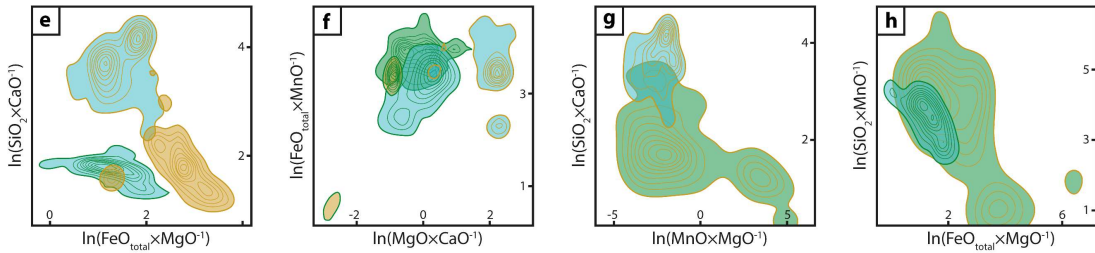
For the discrimination of IG-IF and MM garnet, ln-ratios including CaO, MnO, MgO, and TiO_2 are most important (Figure Appendix 6-F 1n, o, p, q, r). CaO is particularly high in mafic MM garnet due to protolith composition, but it is also higher in the other MM classes. This relates to the higher-pressure conditions of MM garnet formation and Ca-rich garnet in igneous rocks only occurs when deeply emplaced (e.g., Anderson 2008). In contrast, MnO is often higher in IG-IF garnet, which reflects the abundant crystallization from highly fractionated Al- and Mn-rich magmas (e.g., Dahlquist 2007), enabling garnet growth at pressures as low as 3 kbar (e.g., Green 1977). In addition, at crystallization temperatures of IF melts, Mg is partitioning into the melt compared to garnet, resulting in low-Mg garnet (Green 1977). Most difficult is the separation of IG-IF garnet from AM garnet, reflecting the often more similar temperature and pressure conditions during garnet growth. The consideration of TiO_2 significantly enhances this discrimination, reflecting a higher average content of TiO_2 in IG-IF compared to AM (Figure Appendix 6-F 1n). Understanding the partitioning of Ti in garnet of igneous versus metamorphic systems is not straight forward, but the observed preferred incorporation of Ti into igneous biotite may contribute to this trend (Samadi et al. 2021).

The most important variable combinations to discriminate different metamorphic classes and subgroups are shown in Figure Appendix 6-F 2. The absence of ln-ratios that include TiO_2 shows its much lower importance for discrimination within the metamorphic classes (cf. Figure 6.5-2). For class BS/GS, differences between IF/S and M composition are not highly pronounced and thus considered together.

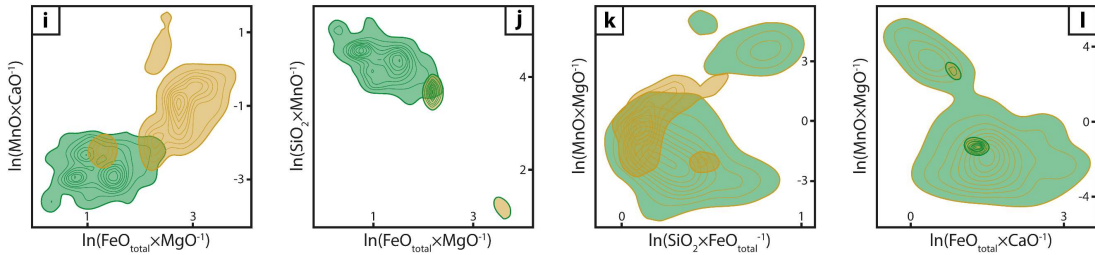
BS/GS versus AM, GR and EC/UHP



GR versus AM and EC/UHP



AM versus EC/UHP



KEY BS/GS AM GR EC/UHP IF/S M IF/S + M

Figure Appendix 6-F 2: Main discriminators to separate individual classes, groups, and subgroups of the ‘metamorphic facies’ scheme. (a–d) separation of BS/GS garnet from AM, GR, and EC/UHP garnet. (e–h) separation of GR garnet from AM and EC/UHP. (i–l) separation AM garnet from EC/UHP. Note that individual fields are marked by the combination of color fill (indicating setting/facies) and coloured contours (indicating composition).

The most important variables to separate BS/GS from other metamorphic classes include MgO in the denominator with Al₂O₃ or FeO_{total} in the nominator, whereby BS/GS garnet shows the highest values due to the low MgO content (Figure Appendix 6-F 2a, b, c, d). This agrees with the low-temperature conditions during garnet growth and the many exchange thermometers that imply increasing Fe×Mg⁻¹ with decreasing temperature (Reverdatto et al. 2019, and references therein). In addition, high contents of MnO in BS/GS garnet improve the discrimination, in particular for AM-M, GR-M, EC-M, and EC-IF/S (Figure Appendix 6-F 2a, b, c). This is consistent with the increasing stability field of garnet to lower pressure–temperature conditions with increasing MnO content of the protolith. Thus, earliest grown garnet typically shows highest MnO contents (e.g., Carlson 1989) and removes MnO from the effective bulk composition leading to an up-temperature shift of garnet stability and bell-shaped Mn-zoning patterns (Evans 2004). For BS/GS garnet versus other MM garnet of M composition, ln(MnO×CaO⁻¹) further increases the distance given by the higher CaO content of mafic protoliths (Figure Appendix 6-F 2a and b). Remarkable overlaps remain for BS/GS and AM-IF/S as well as EC-IF/S (Figure Appendix 6-F 2c and d).

In class GR, most distinct is the low CaO content of GR-IF/S garnet that enables almost perfect discrimination to AM-IF/S (Figure Appendix 6-F 2e), AM-M and EC-M (Figure Appendix 6-F 2f), as well as good discrimination to EC-IF/S (Figure Appendix 6-F 2g). This highlights the fundamentals of the garnet–aluminosilicate–plagioclase–quartz geothermobarometer based on the higher stability of anorthite at high-temperature/low-pressure compared to the higher stability of grossular + aluminosilicate + quartz at low-temperature/high-pressure (e.g., Ghent 1976; Koziol & Newton 1988). GR-M garnet can be discriminated from AM garnet by the higher MgO contents compared to $\text{FeO}_{\text{total}}$ or CaO, whereby the separation is higher for AM-IF/S (Figure Appendix 6-F 2e) than AM-M (Figure Appendix 6-F 2f). More difficult is the discrimination of GR-M garnet from EC/UHP garnet (Figure Appendix 6-F 2g and h), leading to higher misclassification rates (cf. Figure 6.4-1d). Similarly, EC/UHP-M garnet can be separated from AM garnet by the lower $\ln(\text{FeO}_{\text{total}} \times \text{MgO}^{-1})$ and consideration of MnO and CaO (Figure Appendix 6-F 2i and j), but the discrimination of EC-IF/S from AM garnet is difficult, at least by looking at two variables only (Figure Appendix 6-F 2k and l).

Concerning composition, class CS shows the highest discrimination success, followed by A (Table 6.4-2). CS and A garnet are well separated from all other classes by their higher CaO content (Figure Appendix 6-F 3a), reflecting the high host-rock CaO content. The high TiO_2 content of A garnet allows the discrimination to CS (Figure Appendix 6-F 1b). Furthermore, UM garnet separates from IF/S and M garnet by the higher MgO and Cr_2O_3 content in combination with the lower $\text{FeO}_{\text{total}}$ content (Figure Appendix 6-F 3b and c), in line with the element availability defined by the host-rock composition as well as the high-temperature formation conditions of mantle rocks. The similar formation conditions of MA-UM and MA-M make their discrimination most difficult, but particularly the higher CaO content of MA-M (basaltic) enables reasonable separation, although overlaps remain (Figure Appendix 6-F 3d).

For the discrimination of IF/S and M garnet, $\ln(\text{FeO}_{\text{total}} \times \text{MgO}^{-1})$ and $\ln(\text{MnO} \times \text{CaO}^{-1})$ are the most important variables, both being higher for IF/S compared to M garnet (Fig. 8d). Although these ratios represent the superordinate trend, they insufficiently split subpopulations, calling for a case-wise consideration. To separate IG-IF from MM-M garnet, Figures S-7o, S-7p, and S-7q show that the higher MnO and $\text{FeO}_{\text{total}}$ content as well as the lower CaO and MgO content are most important, agreeing with the superordinate trend. For the discrimination of IG-IF from IG-M, it is more useful to solely consider the higher $\text{FeO}_{\text{total}}$ content of IG-IF compared to IG-M (Fig. S-9e), in line with the lower crystallization temperatures.

The discrimination of metamorphic IF/S from M garnet is most distinct for GR-IF/S, which is well separated from all M subgroups by $\ln(\text{FeO}_{\text{total}} \times \text{CaO}^{-1})$ (Fig. S-9f). Although this is mainly a temperature effect as discussed before, it also enables the discrimination of GR-IF/S and GR-M, and thus reflects the higher CaO content of the mafic protolith. BS/GS-IF/S can be well separated from AM-M, GR-M, EC/UHP-M, and MA-M by the higher MnO and lower MgO content (Fig. S-9g), underlining the necessity of a higher MnO content of the protolith to stabilize garnet at low temperatures. As this is similar for IF/S and M protoliths, BS/GS-IF/S is difficult to be distinguished from BS/GS-M, where the superordinate trend of $\ln(\text{FeO}_{\text{total}} \times \text{MgO}^{-1})$ combined with $\ln(\text{MnO} \times \text{CaO}^{-1})$ is most important (Fig. S-9h). Variable $\ln(\text{FeO}_{\text{total}} \times \text{MgO}^{-1})$ also best separates AM-IF/S from M subgroups, whereby GR-M, EC/UHP-M and MA-M show higher values due to average higher temperatures, while BS-M shows lower values due to lower temperatures (Figs. S-9i and S-9j). The protolith effect is mainly given by

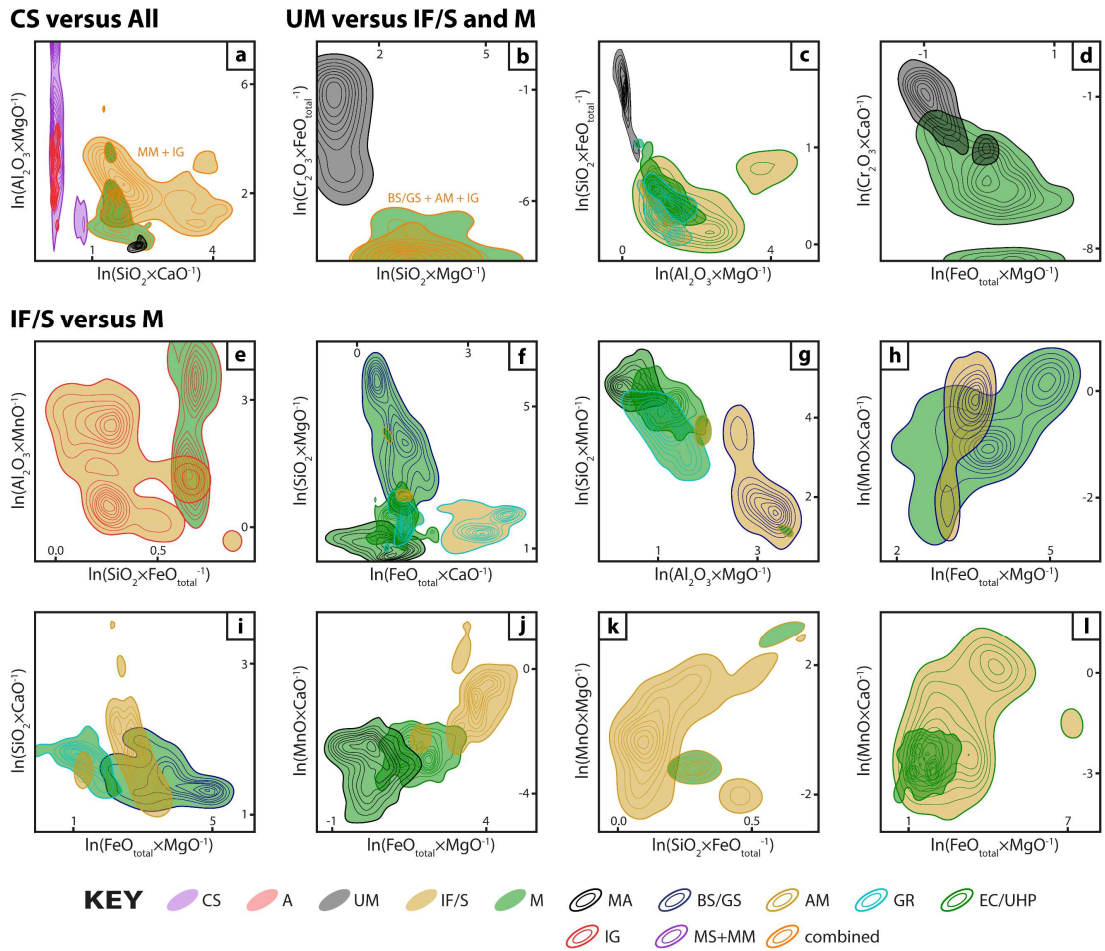


Figure Appendix 6-F 3: Main discriminators to separate individual classes, groups, and subgroups of the 'composition' scheme. (a) separation of CS garnet from UM, IF/S, and M. (b–d) separation of UM garnet from IF/S and M. (e–l) separation IF/S garnet from M. Note that individual fields are marked by the combination of color fill (indicating composition) and coloured contours (indicating setting/facies).

higher CaO of M garnet, whereby the separation to EC/UHP-M and MA-M garnet is getting enhanced by their lower MnO content (Fig. S-9j). Best discrimination of AM-IF/S from AM-M garnet is given by the often lower FeO_{total} and higher MnO of IF/S garnet (Fig. S-9k). Significantly higher overlaps are given for separating EC/UHP-IF/S from M garnet. Lower TiO₂ and Cr₂O₃ are most important to separate EC/UHP-IF/S from MA-M (Fig. S-7e). Higher MgO and lower MnO are most important to separate EC/UHP-IF/S from BS-M (Fig. S-8c) and GR-M (Fig. S-8h). A broader range in ln(FeO_{total}×CaO⁻¹) and ln(MnO×MgO⁻¹) is most important to separate EC/UHP-IF/S from AM-M (Fig. S-8l), and a higher ln(MnO×CaO⁻¹) value separates a subpopulation from EC/UHP-M garnet (Fig. S-9l).

Curriculum Vitae

JAN SCHÖNIG

born in Germany (Burgwedel), 26th July 1988

jan.schoenig@uni-goettingen.de

+49 176 9833 1097

EDUCATION

PhD Candidate Geosciences	November 2018 – present	Georg-August-University, Göttingen
	<i>Thesis:</i>	<i>Deep subduction in Earth history: Seeking for traces in the sedimentary record</i>
Master of Science Geosciences	August 2017	Georg-August-University, Göttingen
	<i>Thesis:</i>	<i>Application and limits of Raman spectroscopy in garnet single-grain analysis: Examples from the UHP Western Gneiss Region, SW Norway</i>
Bachelor of Science Geosciences	December 2014	Georg-August-University, Göttingen
	<i>Thesis:</i>	<i>Heavy-mineral analysis of modern river sands and crystalline rocks from the Almklovdalen area, SW Norway</i>

PROFESSIONAL APPOINTMENTS

Research Assistant	October 2017 – October 2018	Georg-August-University, Göttingen, Dept. Sedimentology & Environmental Geology
Student Assistant	February 2013 – September 2014	Georg-August-University, Göttingen, Dept. Sedimentology & Environmental Geology

TEACHING

Master Thesis, M.Sc. (supervision)	2021	<i>Topic: Screening for traces of Paleoproterozoic (ultra)high-pressure metamorphism in Western Greenland: Clues from modern sand heavy-mineral assemblages and garnet chemistry</i>
Geology-Project, M.Sc. (supervision)	2021	<i>Topic: Semi-Automated Heavy-Mineral Analysis by Raman Spectroscopy: Detailed Manual Control of the Automated Evaluation and its Implications for Provenance Analysis</i>
Fieldtrip, B.Sc.	2020	Regional Geology of the vicinity of Göttingen (2 Days)

PUBLICATIONS

Schönig J, von Eynatten H, Tolosana-Delgado R, Meinhold G (in press): Garnet major-element composition as an indicator of host-rock type: A machine-learning approach using the random forest classifier. *Contributions to Mineralogy and Petrology* (not yet issued), <https://doi.org/10.1007/s00410-021-01854-w>.

Pei Y, Duda JP, **Schönig J**, Luo C, Reitner J (2021): Late Anisian microbe-metazoan build-ups in the Germanic Basin: aftermath of the Permian–Triassic crisis. *Lethaia*, <https://doi.org/10.1111/let.12442>.

Schönig J, von Eynatten H, Meinhold G, Lünsdorf NK (2021): Life-cycle analysis of coesite-bearing garnet. *Geological Magazine* 158, 1421–1440, <https://doi.org/10.1017/S0016756821000017>.

Baldwin SL, **Schönig J**, Gonzalez JP, Davies H, von Eynatten H (2021): Garnet sand reveals rock recycling processes in the youngest exhumed high- and ultrahigh-pressure terrane on Earth. *Proceedings of the National Academy of Sciences* 118, e2017231118, <https://doi.org/10.1073/pnas.2017231118>.

Schönig J, von Eynatten H, Meinhold G, Lünsdorf NK, Willner AP, Schulz B (2021): Reply to comment on “Deep subduction of felsic rocks hosting UHP lenses in the central Saxonian Erzgebirge: Implications for UHP terrane exhumation”. *Gondwana Research* 98, 320–323, <https://doi.org/10.1016/j.gr.2020.12.029>.

Schönig J, von Eynatten H, Meinhold G, Lünsdorf NK, Willner AP, Schulz B (2020): Deep subduction of felsic rocks hosting UHP lenses in the central Saxonian Erzgebirge: Implications for UHP terrane exhumation. *Gondwana Research* 87, 320–329, <https://doi.org/10.1016/j.gr.2020.06.020>.

Dunkl *et al.* (2020): Comparability of heavy mineral data – The first interlaboratory round robin test. *Earth-Science Reviews* 211, 103210, <https://doi.org/10.1016/j.earscirev.2020.103210>.

Schönig J, von Eynatten H, Meinhold G, Lünsdorf NK (2019): Diamond and coesite inclusions in detrital garnet of the Saxonian Erzgebirge, Germany. *Geology* 47, 715–718, <https://doi.org/10.1130/G46253.1>.

Schönig J, Meinhold G, von Eynatten H, Lünsdorf NK (2018): Provenance information recorded by mineral inclusions in detrital garnet. *Sedimentary Geology* 376, 32–49, <https://doi.org/10.1016/j.sedgeo.2018.07.009>.

Schönig J, Meinhold G, von Eynatten H, Lünsdorf NK (2018a): Tracing ultrahigh-pressure metamorphism at the catchment scale. *Scientific Reports* 8, 2931, <https://doi.org/10.1038/s41598-018-21262-8>.

Krippner A, Meinhold G, Morton AC, **Schönig J**, von Eynatten H (2016): Heavy minerals and garnet geochemistry of stream sediments and bedrocks from the Almklovdalen area, Western Gneiss Region, SW Norway: Implications for provenance analysis. *Sedimentary Geology* 336, 96–105, <https://doi.org/10.1016/j.sedgeo.2015.09.009>.

PRESENTATIONS

Schönig J (2021): Mineral inclusions in detrital garnet: An excellent petrogenetic tool. *GeoKarlsruhe 2021, Karlsruhe Institute for Technology, Germany. Oral Presentation.*

Schönig J, von Eynatten H, Tolosana-Delgado R, Meinhold G (2021): A machine-learning approach for detrital garnet host-rock discrimination. *Seminar on Sedimentary Petrology and Environmental Geology, Geosciences Center Göttingen, Germany*. **Oral Presentation.**

Schönig J, von Eynatten H, Meinhold G, Lünsdorf NK (2020): The potential of detrital garnet in UHP research as exemplified by the central Saxonian Erzgebirge. *GeoUtrecht 2020, University of Utrecht, Netherlands*. **Oral Presentation.**

Schönig J, von Eynatten H, Meinhold G, Lünsdorf NK (2020): The Potential of Mineral Inclusions in Garnet Provenance Analysis. *Seminar on Sedimentary Petrology and Environmental Geology, Geosciences Center Göttingen, Germany*. **Oral Presentation.**

Schönig J, von Eynatten H, Meinhold G, Lünsdorf NK (2020): The application of mineral inclusions in detrital garnet as provenance indicator. *Provenance Meeting, Geosciences Center Göttingen, Germany*. **Oral Presentation.**

Schönig J, von Eynatten H, Meinhold G, Lünsdorf NK (2019): Grain-size distribution and 'life cycle' of detrital ultrahigh-pressure garnet. *Seminar on Sedimentary Petrology and Environmental Geology, Geosciences Center Göttingen, Germany*. **Oral Presentation.**

Schönig J, von Eynatten H, Meinhold G, Lünsdorf NK (2019): Dispersed occurrence of mafic and felsic ultrahigh-pressure rocks in the central Saxonian Erzgebirge (Germany) revealed by diamond and coesite inclusions in detrital garnet. *GeoMünster 2019, University of Münster, Germany*. **Oral Presentation.**

Schönig J, von Eynatten H, Meinhold G, Lünsdorf NK (2019): The 'life cycle' of coesite-bearing garnet. *GeoMünster 2019, University of Münster, Germany*. **Poster Presentation.**

Schönig J, von Eynatten H, Meinhold G, Lünsdorf NK (2019): Inclusions in detrital garnet as tracer of UHP metamorphism. *WAGGS 2019, Syracuse University, New York, USA*. **Oral Presentation.**

Schönig J, von Eynatten H, Meinhold G, Lünsdorf NK (2019): Inclusions in detrital garnet as tracer of UHP metamorphism. *Seminar on Sedimentary Petrology and Environmental Geology, Geosciences Center Göttingen, Germany*. **Oral Presentation.**

Schönig J, Meinhold G, von Eynatten H, Lünsdorf NK (2018): Advances in garnet single-grain analysis: Mineral inclusions record HP/UHP provenance. *GeoBonn 2018, University of Bonn, Germany*. **Oral Presentation.**

Schönig J, Meinhold G, von Eynatten H, Lünsdorf NK (2018): Sedimentary provenance analysis meets ultrahigh-pressure research. *Working Group on Sediment Generation Meeting, Trinity College Dublin, Ireland*. **Oral Presentation.**

Schönig J, Meinhold G, von Eynatten H, Lünsdorf NK (2018): Provenance information recorded by mineral inclusions in detrital garnet: An example from the HP/UHP Western Gneiss Region of SW Norway. *Early Career Sedimentologist Meeting, University of Hannover, Germany*. **Oral Presentation.**

Schönig J, Meinhold G, von Eynatten H, Lünsdorf NK (2018): Tracing ultrahigh-pressure metamorphism at the catchment scale. *Heavy Mineral School, University of Milano-Bicocca, Italy*. **Poster Presentation.**

Schönig J, Meinhold G, von Eynatten H, Lünsdorf NK (2017): Application and limits of Raman spectroscopy in garnet single-grain analysis: Examples from the UHP Western Gneiss Region, SW Norway. *GZG Colloquium, Geosciences Center Göttingen, Germany*. **Oral Presentation.**

Schönig J, Meinhold G, von Eynatten H, Lünsdorf NK (2017): Application and limits of Raman spectroscopy in garnet single-grain analysis: Examples from the UHP Western Gneiss Region, SW Norway.

AWARDS

2021 **Bernd-Rendel-Prize**
of the 'German Research Foundation (DFG)'
for promising and original geoscientific research at the beginning of the career

2020 **Best Students' Paper Award**
of the 'DGGV' and 'KNGMG' at the GeoUtrecht 2020 Conference
for an outstanding presentation

2017 **Adolf-von-Koenen-Prize**
of the 'Freunde der Geowissenschaften der Universität Göttingen e.V.'
for the best master thesis of the year

ADDITIONAL QUALIFICATIONS

2019 Short Course – R for Geoscientists at the Helmholtz Institute Freiberg, Germany
Lecturers: Tolosana-Delgado R, van den Boogart KG

2019 Short Course – School of Provenance Analysis at the Geosciences Center Göttingen, Germany
Lecturers: von Eynatten H, Dunkl I, Meinhold G, Lünsdorf NK, Weltje GJ

2018 Short Course – Electron Microprobe and Electron Microscopy
Lecturer: Kronz A

2018 Short Course – Heavy Mineral School at the University of Milano-Bicocca, Italy
Lecturers: Andò S, Garzanti E, Vezzoli G, Resentini A

LANGUAGES

German native speaker

English fluent in text and speech

Göttingen, 3rd November 2021